



National Library
of Canada

Acquisitions and
Bibliographic Services Branch

395 Wellington Street
Ottawa, Ontario
K1A 0N4

Bibliothèque nationale
du Canada

Direction des acquisitions et
des services bibliographiques

395, rue Wellington
Ottawa (Ontario)
K1A 0N4

Your file - Votre référence

Our file - Notre référence

NOTICE

The quality of this microform is heavily dependent upon the quality of the original thesis submitted for microfilming. Every effort has been made to ensure the highest quality of reproduction possible.

If pages are missing, contact the university which granted the degree.

Some pages may have indistinct print especially if the original pages were typed with a poor typewriter ribbon or if the university sent us an inferior photocopy.

Reproduction in full or in part of this microform is governed by the Canadian Copyright Act, R.S.C. 1970, c. C-30, and subsequent amendments.

AVIS

La qualité de cette microforme dépend grandement de la qualité de la thèse soumise au microfilmage. Nous avons tout fait pour assurer une qualité supérieure de reproduction.

S'il manque des pages, veuillez communiquer avec l'université qui a conféré le grade.

La qualité d'impression de certaines pages peut laisser à désirer, surtout si les pages originales ont été dactylographiées à l'aide d'un ruban usé ou si l'université nous a fait parvenir une photocopie de qualité inférieure.

La reproduction, même partielle, de cette microforme est soumise à la Loi canadienne sur le droit d'auteur, SRC 1970, c. C-30, et ses amendements subséquents.

Canada

**Numerical Prediction of Gas-Solid Particle Flows Over
a Wide Range of Concentration in Irregular Geometries**

by

Christian Masson

Thesis submitted to the Faculty of Graduate Studies and Research
in partial fulfilment of the requirements for the degree of
Doctor of Philosophy

Department of Mechanical Engineering
McGill University
Montréal, Canada.

© Christian Masson, Montréal, Canada, 1993.



National Library
of Canada

Acquisitions and
Bibliographic Services Branch

395 Wellington Street
Ottawa, Ontario
K1A 0N4

Bibliothèque nationale
du Canada

Direction des acquisitions et
des services bibliographiques

395, rue Wellington
Ottawa (Ontario)
K1A 0N4

Your file *Votre référence*

Our file *Notre référence*

The author has granted an irrevocable non-exclusive licence allowing the National Library of Canada to reproduce, loan, distribute or sell copies of his/her thesis by any means and in any form or format, making this thesis available to interested persons.

The author retains ownership of the copyright in his/her thesis. Neither the thesis nor substantial extracts from it may be printed or otherwise reproduced without his/her permission.

L'auteur a accordé une licence irrévocable et non exclusive permettant à la Bibliothèque nationale du Canada de reproduire, prêter, distribuer ou vendre des copies de sa thèse de quelque manière et sous quelque forme que ce soit pour mettre des exemplaires de cette thèse à la disposition des personnes intéressées.

L'auteur conserve la propriété du droit d'auteur qui protège sa thèse. Ni la thèse ni des extraits substantiels de celle-ci ne doivent être imprimés ou autrement reproduits sans son autorisation.

ISBN 0-315-94682-2

Canada

**Numerical Prediction of Gas-Solid
Particle Flows in Irregular Geometries**
(Shortened Title)

by

Christian Masson

Thesis submitted to the Faculty of Graduate Studies and Research
in partial fulfilment of the requirements for the degree of
Doctor of Philosophy

Department of Mechanical Engineering
McGill University
Montréal, Canada.

A Marie,
et à mes parents

Abstract

The formulation of a co-located equal-order Control-Volume-based Finite Element Method (CVFEM) for the solution of two-fluid models of two-dimensional, planar or axisymmetric, incompressible, gas-solid particle flows is presented in this thesis. The main focus is on the development of a numerical method that allows computer simulation of gas-solid particle flows over a wide range of solid-phase volume concentration in complex irregular geometries.

A general two-fluid mathematical model is presented. This model is essentially borrowed from published works in the area of granular flows. It is established here that this model is applicable to gas-solid flows over a wide range of solid-phase concentration. The governing equations of the fluid phase are obtained by volume averaging the Navier-Stokes equations for an incompressible fluid. The solid-phase macroscopic equations are derived using an approach that has been successfully used earlier for the description of granular materials, and is based on the kinetic theory of dense gases. This approach accounts for particle/particle collisions, and permits the determination of the solid-phase macroscopic properties such as viscosity and pressure.

The proposed CVFEM is formulated by borrowing and extending ideas put forward in earlier CVFEMs for single-phase flows. In axisymmetric problems, the calculation domain is discretized into torus-shaped elements and control volumes: in a longitudinal cross-sectional plane, or in planar problems, these elements are three-node triangles, and the control volumes are polygons obtained by joining the centroids of the three-node triangles to the midpoints of the sides. In each element, mass-weighted skew upwind functions are used to interpolate the volume concentrations. An iterative variable adjustment algorithm is used to solve the discretized equations.

The chosen mathematical model, along with its specializations to single-phase flows and dilute gas-solid flows, and the proposed CVFEM have been applied to

several test problems and some demonstration problems. These test and demonstration problems include single-phase flows, dilute-concentration gas-solid particle flows and dense-concentration gas-solid particle flows. The CVFEM results have been compared with results of independent numerical and experimental investigations whenever possible. These comparisons and the results of the demonstration problems are quite encouraging.

Sommaire

La formulation d'une Méthode aux Eléments Finis/Volumes de Contrôle (CVFEM) pour les écoulements diphasés et bidimensionnels est présentée dans cette thèse. Cette méthode à colocation d'ordre égal est établie pour les écoulements de gaz avec particules solides, et utilise le système de coordonnées cartésien et cylindrique. Une attention particulière est portée sur le développement d'une méthode numérique permettant la simulation d'écoulements diphasés de gaz avec particules solides, sur une grande étendue de concentration, et à l'intérieur de domaines complexes et irréguliers.

Un modèle mathématique général, utilisant sur une formulation eulérienne pour les deux phases, est présenté. Ce modèle est basé essentiellement sur certains travaux publiés dans le domaine des écoulements granulaires. Dans cet ouvrage, il est établi que ce modèle est applicable pour les écoulements diphasés de gaz avec particules solides, sur une grande étendue de concentration de la phase solide. Les équations gouvernant la phase fluide sont obtenues en moyennant sur un volume les équations de Navier-Stokes pour fluides incompressibles. Les équations macroscopiques de la phase solide sont dérivées à l'aide d'une approche utilisée avec succès pour la description de matériaux granulaires. Etant basée sur la théorie dynamique des gaz où les effets des collisions entre particules sont inclus, cette approche permet la détermination des propriétés macroscopiques de la phase solide telles que la viscosité et la pression.

La formulation de la CVFEM proposée se base sur l'extension de certaines idées utilisées dans les récentes CVFEMs pour écoulements monophasés. Pour les problèmes axisymétriques, le domaine de calcul est discrétisé en éléments et volumes de contrôle en forme de tore: dans une tranche plane longitudinale, ou dans les problèmes plans cartésiens, ces éléments sont des triangles à trois noeuds, et les volumes de contrôle sont des polygones obtenus en unissant le centroïde des triangles à trois noeuds au centre de leurs côtés. Dans chaque élément, des fonctions

dités amont moyennées sur la masse sont utilisées pour interpoler la concentration volumétrique. Une procédure itérative est utilisée pour la solution des équations discrétisées.

Le modèle mathématique choisi, les spécialisations pour écoulements monophasés et écoulements diphasés de gaz avec particules solides en faible concentration, de même que la CVFEM proposée ont été appliqués sur plusieurs cas typiques et sur certains problèmes de démonstration. Ces derniers représentent des écoulements monophasés, des écoulements diphasés de gaz avec particules solides en faible concentration, et des écoulements diphasés de gaz avec particules solides en forte concentration. Les résultats de la CVFEM ont été comparés avec les résultats numériques et expérimentaux d'investigations indépendantes lorsque cela était possible. Ces comparaisons et les résultats des problèmes de démonstration sont bien encourageants.

Acknowledgement

The work presented in this thesis would not be possible without the implication of several people. I would like to first stress the outstanding participation of my supervisor, Prof. B.R. Baliga. He was always available, though sometimes at strange hours, and his advice and comments were always very useful and pertinent. I would like to thank him for his guidance and support. He succeeded in transmitting his thirst for knowledge and his quest for perfection.

I would like to express my gratitude to Prof. S.B. Savage who introduced me to the fascinating world of granular flows and made his most recent advances available to me.

The everyday support, encouragement and love of Marie and my parents helped me a great deal to manage to do my research with the appropriate state of mind and a positive spirit even during the most frustrating parts of my work. I gratefully recognize their essential and important contributions.

The support of the Natural Sciences and Engineering Research Council of Canada (NSERC), the "Fonds pour la Formation des Chercheurs et l'Aide à la Recherche" (FCAR), and Hydro Québec are gratefully acknowledged.

Ecole Polytechnique, and especially Charles A. Laberge, allowed me to remain focused on my research by inviting me to join the "Programme de relève de l'Ecole Polytechnique". I express my gratitude.

Finally, the numerous days spent at Mc Gill University were much more pleasant with the exchanges and discussions during work hours, lunches and coffee breaks with my friends Stéphane Cyr, Nabil Elkouh, Wadood Hamad, Nasrollah Monshi, Vinhson Nguyen, Daniel Rousse, John Saabas, Simone Sebben, and Victor Storm.

Thank you all.

Table of Contents

Abstract	iii
Sommaire	v
Acknowledgement	vii
Table of Contents	viii
List of Figures	xi
List of Tables	xiv
Nomenclature	xvi
1 Introduction	1
1.1 Aims and Scope of this Work	1
1.2 Two-Phase Flows	2
1.3 Organization of the Thesis	4
2 Literature Review	6
2.1 Mathematical Models of Gas-Solid Particle Flows	6
2.2 Numerical Solution of the Mathematical Models	12
3 Mathematical Model	21
3.1 Dynamics of a Single Particle in a Fluid Flow	23
3.2 Multiple Spherical Particles in a Fluid Flow	25
3.3 Solid-Phase Macroscopic Equations	26
3.3.1 Terminology/Definitions	27
3.3.2 Boltzmann Equation	28
3.3.3 Macroscopic Equation	29
3.3.4 Binary Encounter Dynamics	30
3.3.5 Hydrodynamic Equations	34

3.3.6	Velocity Distribution Function	35
3.4	Solid-Phase Boundary Conditions	36
3.5	Fluid-Phase Governing Equations	37
3.5.1	Local Volume Average of the Fluid-Phase Continuity Equation	38
3.5.2	Local Volume Average of the Fluid-Phase Momentum Equation	39
3.6	Fluid-Phase Boundary Conditions	42
3.7	Two-Dimensional Axisymmetric Gas-Solid Particle Flows: Summary .	43
3.7.1	Governing Equations	43
3.7.2	Constitutive and Auxiliary Equations	45
3.7.3	Specializations	47
4	Numerical Model	51
4.1	General Equation	52
4.2	Domain Discretization	54
4.3	Integral Conservation Equation	55
4.4	Interpolation Functions	55
4.4.1	Diffusion Coefficients, Density, and Sources	57
4.4.2	Mass Flow Rates	58
4.4.3	ϕ in Diffusion Terms	58
4.4.4	ϕ in Convection Terms	59
4.4.5	Fluid-Phase Pressure p^f and Solid-Phase Pressure p^s	62
4.4.6	Volume Concentrations	63
4.5	Discretization Equations	63
4.5.1	Discretization Equation for ϕ	64
4.5.2	Discretized Momentum Equations	67
4.5.3	Discretized Solid-Phase Fluctuating Kinetic Energy Equation	73
4.5.4	Discretized Equations for p^f and α	75
4.6	Boundary Conditions	80
4.6.1	Specified Value	80
4.6.2	Specified Gradient	80
4.6.3	Special Treatments	82
4.7	Overall Solution Algorithm	82
5	Single-Phase Flow Simulations	85
5.1	Developing Laminar Flow in a Pipe	86

5.2	Laminar Flow in a Pipe with a Sudden Contraction	88
5.3	Laminar Natural Convection in a Cylindrical Enclosure	92
5.4	Laminar Flow in a Replica Segment of a Coronary Artery	99
6	Dilute Gas-Solid Particle Flow Simulations	103
6.1	Non-Dimensional Parameters	104
6.2	Specified Solution in a Cartesian Domain	105
6.3	Flow in a Channel with a Restriction	107
6.4	Split-Flow Inertial Separator	112
7	Dense Gas-Solid Particle Flow Simulations	124
7.1	Specified Solution in a Cartesian Geometry	125
7.2	Specified Solution in a Cylindrical Geometry	128
7.3	Vertical Pipe Flow	130
7.4	Flow in an Annular Shear Cell Apparatus	145
7.5	Fluidized Bed	156
7.6	Flow in a Channel with a Restriction	163
7.7	Split-Flow Inertial Separator	167
8	Conclusion	171
8.1	Review of the Thesis	171
8.2	Contributions of the Thesis	174
8.3	Recommendations for Further Work	175
	References	177
A	Ensemble Averages and Collisional Integrals	195
A.1	Solid-Phase Stress Tensor	195
	A.1.1 Kinetic Contribution	195
	A.1.2 Collisional Contribution	195
A.2	Interaction Force Term	196
A.3	Solid-Phase Heat Flux Vector	196
	A.3.1 Kinetic Contribution	196
	A.3.2 Collisional Contribution	196
A.4	Collisional Dissipation	197
A.5	Interaction-Force Dissipation	197
A.6	Energy Transfer Term	197

B	Some Details of the Implementation of the Proposed CVFEM	198
B.1	Implementation of the MAW Scheme	198
B.2	Implementation of the Modified MAW Scheme	199
B.3	Element Contribution of Diffusion Terms	200
B.4	Element Contribution to Convection Terms	202
B.4.1	FLO Scheme	202
B.4.2	MAW Scheme	203
B.5	Element Contribution to the Mass Flow Rates	204
B.5.1	Contribution to the Fluid-Phase Pressure Equation	204
B.5.2	Contribution to the Volume Concentration Equation	205
B.6	Calculation of Element Volumes	205
C	Linearization of the Momentum Coupling Source Term	208
C.1	Linearization (<i>i</i>)	209
C.2	Linearization (<i>ii</i>)	210
C.3	Linearization (<i>iii</i>)	210
D	Implied Source Terms of the Specified Solutions	212
D.1	Dense Concentration - Specified Solution in a Cartesian Geometry . .	212
D.2	Dense Concentration - Specified Solution in a Cylindrical Geometry .	213

List of Figures

3.1	Binary collision	31
4.1	Discretization of the longitudinal cross-section of a calculation domain	54
4.2	Typical control volumes surrounding (a) an internal node; and (b) a boundary node	56
4.3	Typical triangular element: (a) global and local coordinate systems; (b) unit normals	56
5.1	Streamline patterns for laminar flow in a pipe with a sudden contraction: (a) $Re_D = 196$; (b) $Re_D = 968$	89
5.2	Laminar flow in a pipe with a sudden contraction for $Re_D = 196$: (a) axial velocity ; (b) radial velocity	90
5.3	Laminar flow in a pipe with a sudden contraction for $Re_D = 968$: (a) axial velocity ; (b) radial velocity	91
5.4	Schematic representation of laminar natural convection in a cylindrical enclosure	92
5.5	Temperature distribution along $r/R = 0.5$ in laminar natural convection in a cylindrical enclosure: grid-independence study for the case of upflow using FLO and MAW	95
5.6	Temperature distribution in laminar natural convection in a cylindrical enclosure: (a) upflow ; (b) downflow	96
5.7	Straight axisymmetric analogue casting of a coronary artery and the grid used in the CVFEM simulations: scale in radial direction is ten times that in the axial direction.	99
5.8	Laminar flow in a replica segment of a coronary artery: pressure-change coefficient for different grids	101
5.9	Laminar flow in a replica segment of a coronary artery: pressure-change coefficient for different Reynolds numbers	102

6.1	Geometry of the channel with a restriction	107
6.2	Flow in a channel with a restriction: variation of fluid-phase velocity along the centerline	110
6.3	Flow in a channel with a restriction: variation of solid-phase velocity along the centerline	110
6.4	Flow in a channel with a restriction: variation of fluid-phase pressure along the centerline	111
6.5	Flow in a channel with a restriction: variation of solid-phase concen- tration along the centerline	111
6.6	Geometry of the separator	113
6.7	Results pertaining to $\gamma = 10^3$ and $\alpha_{in} = 10^{-3}$: (a) separator efficiency; (b) static-pressure drop in the main duct; (c) static-pressure drop in the bypass duct	119
6.8	Results pertaining to $\gamma = 10^2$ and $\alpha_{in} = 10^{-3}$: (a) separator efficiency; (b) static-pressure drop in the main duct; (c) static-pressure drop in the bypass duct	120
6.9	Results pertaining to $\gamma = 10^3$ and $\alpha_{in} = 10^{-4}$: (a) separator efficiency; (b) static-pressure drop in the main duct; (c) static-pressure drop in the bypass duct	121
6.10	Velocity and concentration profiles pertaining to $\gamma = 10^3$, $\alpha_{in} = 10^{-3}$ and $b = 10\%$: (a) $Sk = 2 \times 10^{-2}$; (b) $Sk = 6 \times 10^{-2}$	122
6.11	Velocity and concentration profiles pertaining to $\gamma = 10^3$, $\alpha_{in} = 10^{-3}$ and $b = 30\%$: (a) $Sk = 2 \times 10^{-2}$; (b) $Sk = 2 \times 10^{-1}$	123
7.1	Specified solution in the Cartesian geometry: solid-phase velocity in the y -direction along the centerline ($x/L = 0.5$) of the calculation domain.	127
7.2	Specified solution in the Cartesian geometry: solid-phase pressure along the centerline ($x/L = 0.5$) of the calculation domain.	127
7.3	Vertical pipe	131
7.4	Vertical pipe flow : $\frac{d\tilde{P}}{dz} = -0.2$; $e = 1.0$; $\tilde{Q}^s = 0.34$	138
7.5	Vertical pipe flow : $\frac{d\tilde{P}}{dz} = -0.2$; $e = 1.0$; $\tilde{Q}^s = 0.04$	139
7.6	Vertical pipe flow : $\frac{d\tilde{P}}{dz} = -0.2$; $e = 1.0$; $\tilde{Q}^s = -0.15$	140
7.7	Vertical pipe flow : $\frac{d\tilde{P}}{dz} = -0.2$; $e = 1.0$; $\tilde{Q}^s = -0.34$	141
7.8	Vertical pipe flow : $\frac{d\tilde{P}}{dz} = -0.2$; $e = 1.0$; $\tilde{Q}^s = -0.62$	142

7.9	Vertical pipe flow : $\frac{d\bar{P}}{dz} = -0.2$; $e = .99$; $\tilde{Q}^s = -2.10$	143
7.10	Two-dimensional vertical pipe flow : $\frac{d\bar{P}}{dz} = -0.2$; $e = 1.0$; $\tilde{Q}^s = 0.34$	144
7.11	(a) Annular shear cell apparatus (Fig. 1 of Ref. [150]); (b) Plane shearing model	146
7.12	Flow in annular shear cell - parametric study : $\bar{\alpha} = 0.477$; $\left(\frac{d}{g}\right)^{\frac{1}{2}} \frac{u_w}{H} = 2.0$	152
7.13	Flow in annular shear cell - velocity, concentration and temperature profiles : $\bar{\alpha} = 0.477$; $\left(\frac{d}{g}\right)^{\frac{1}{2}} \frac{u_w}{H} = 2.0$	153
7.14	Flow in annular shear cell - shear and normal stresses : $e = 0.89$; $e_w = 0.50$; $\phi' = 0.60$	154
7.15	Flow in annular shear cell - shear and normal stresses : $e = 0.95$; $e_w = 0.95$; no-slip	155
7.16	Typical fluidized-bed geometry	157
7.17	Results of the fluidized-bed problem: (a) fluid-phase velocity; (b) solid-phase velocity	161
7.18	Results of the fluidized-bed problem: distribution of the solid-phase concentration along the axis	162
7.19	Flow in a channel with a restriction: variation of fluid-phase velocity along the centerline	165
7.20	Flow in a channel with a restriction: variation of solid-phase velocity along the centerline	165
7.21	Flow in a channel with a restriction: variation of fluid-phase pressure along the centerline	166
7.22	Flow in a channel with a restriction: variation of solid-phase concentration along the centerline	166
7.23	Results pertaining to $b = 20\%$, $\gamma = 10^3$ and $\alpha_{in} = 10^{-3}$: (a) separator efficiency; (b) static-pressure drop in the main duct; (c) static-pressure drop in the bypass duct	170
B.1	Typical triangular element - general notation	201
B.2	Typical triangular element - volume calculation	206

List of Tables

3.1	Examples of $C_D Re^3$ relations	50
3.2	Examples of $\mu_r^f(\alpha)$ relations	50
3.3	Examples of g_0 relations	50
4.1	Specific forms of the general equation	53
5.1	Developing laminar flow in a pipe: u_{\min}^f and u_{\max}^f values	87
5.2	Developing laminar flow in a pipe: nondimensional hydrodynamic entrance length	87
5.3	Laminar natural convection in a cylindrical enclosure: number of iterations and CPU times	97
5.4	Laminar natural convection in a cylindrical enclosure: average Nus- selt number results	98
6.1	Values of parameters for flow in a channel with a restriction	108
7.1	Specified solution in a cylindrical geometry: absolute values of aver- age relative errors(%).	129
7.2	Vertical pipe flow: comparative study	135
7.3	Flow in annular shear cell: various parameters	145
7.4	Results of the fluidized-bed problem: bed height in <i>mm</i>	160
C.1	Iterative process for the low concentration problem	210
C.2	Iterative process for the high concentration problem	210
C.3	Iterative process for the low concentration problem	211
C.4	Iterative process for the high concentration problem	211

Nomenclature

a_0	constant appearing in the evaluation of B_{ij}
a_1, a_2, a_3	functions appearing in the evaluation of $f(\vec{c}, \vec{x}, t)$
ac_i^p, ac_{nb}^p, b^p	coefficients in the algebraic discretization pressure equation
ac_i^T, ac_{nb}^T, b^T	coefficients in the algebraic discretization granular temperature equation
ac_i^u, ac_{nb}^u, b^u	coefficients in the algebraic discretization z -momentum equation
ac_i^v, ac_{nb}^v, b^v	coefficients in the algebraic discretization r -momentum equation
$ac_i^\phi, ac_{nb}^\phi, b^\phi$	coefficients in the algebraic discretization equation for ϕ
$ac_i^\alpha, ac_{nb}^\alpha, b^\alpha$	coefficients in the algebraic discretization equation for α
A, B, C	coefficients in the interpolation of ϕ
B_{ij}	specific kinetic energy transfer tensor
c_i	single particle velocity component in the i -direction
\vec{c}	single particle velocity vector
\vec{c}_1	velocity vector of particle labelled 1
\vec{c}_2	velocity vector of particle labelled 2
\vec{c}_{12}	relative velocity vector of particle labelled 1 with respect to particle 2
C_D	particle drag coefficient
C_i	solid-phase velocity fluctuation in the i -direction
C_s	constant appearing in the evaluation of the Reynolds Stress
d	particle diameter
d^f, e^f, f^f	coefficients in the interpolation of the fluid-phase pressure
d^s, e^s, f^s	coefficients in the interpolation of the solid-phase pressure
d^{uf}	pressure-gradient coefficient for u
d^{vf}	pressure-gradient coefficient for v
D	particle drag force
$\frac{D}{Dt}$	substantial derivative
e	coefficient of restitution for particle/particle collision
e_w	coefficient of restitution for particle/wall collision
f^o	Maxwellian velocity distribution function
f^+, f^-	mass-weighted function
$f(\vec{c}, \vec{x}, t)$	velocity distribution function
F_i^{ext}	sum of the external forces applied on a single particle per unit mass
F_i^f	force per unit mass applied by the fluid phase on a single particle
g_i	gravitational acceleration in the i -direction
g_0	equilibrium radial distribution

\vec{G}	centre of mass velocity
\vec{i}, \vec{j}	units vectors in the z and r direction
\vec{J}	combined convection-diffusion flux
\vec{J}_D	diffusion flux
\vec{J}_{DS}	diffusion-source flux
\vec{J}_C	convection flux
\vec{J}_α	concentration-diffusion flux
k_T^s	granular thermal conductivity related to temperature gradient
k_α^s	granular thermal conductivity related to concentration gradient
\vec{k}	unit vector along the line of the centres of the particles at collision
m^p	mass of a single particle
\dot{m}	mass flow rate
\dot{M}	material mass flow rate
M	mass of a two-particle system
n	particle number density
n_i	unit normal component in the i -direction
\vec{n}	unit normal vector
p	pressure
Pe_Δ	elemental Peclet number
q_i^s	solid-phase fluctuating kinetic energy flux vector
r	radial coordinate in the polar coordinate system
Re	Reynolds number
Re^s	particle Reynolds number
s	length
Sk	Stokes number
S	volumetric source term
S_α	concentration-diffusion source term
S	surface
S^p	surface of a single particle
t	time
T	granular temperature
u	velocity in the z -direction
u_i	velocity in the i -direction
\hat{u}_i	z -component of the pseudo-velocity at node i
v	velocity in the r -direction
\hat{v}_i	r -component of the pseudo-velocity at node i
v_t	terminal velocity of fall of a single particle under gravity
\vec{V}	velocity vector
\mathcal{V}	volume
\mathcal{V}^p	volume of a particle
W_p	solid-phase pressure work source term
x	local coordinate
x_i	coordinate in the i -direction

\vec{x}	vector position
X	local flow-oriented coordinate
y	local coordinate
Y	local flow-oriented coordinate
z	axial coordinate in the polar coordinate system

Greek Symbols

α	solid-phase volume concentration
β	volume concentration
δ_{ij}	Kronecker delta
Δ	linear measure of the grid size
Δt	time step
ϵ	fluid-phase volume concentration
ε	dummy variable
γ	density ratio
γ_c	solid-phase fluctuating kinetic energy dissipation due to inelastic collisions
γ_B	solid-phase fluctuating kinetic energy transfer term
γ_D	solid-phase fluctuating kinetic energy dissipation due to drag
Γ_b	bulk diffusion coefficient
Γ_e	effective diffusion coefficient
μ	dynamic viscosity
μ_e	effective viscosity
μ_b	bulk viscosity
μ_a^f	fluid-phase apparent viscosity
μ_r^f	fluid-phase relative viscosity
ϕ	single-particle property or dependent variable
ϕ'	specularity factor
Φ^s	dissipation function
π	3.1415926
ρ	density
σ_{ij}	surface stress tensor
ξ	exponential variable of the local flow-oriented coordinate system
ζ_D	specific fluid friction coefficient

Superscripts

f	pertains to the fluid phase
int	pertains to the fluid-solid interface
m	pertains to the mass-flow related velocity
p	pertains to a single particle
s	pertains to the solid phase
*	pertains to the previous time step
l	pertains to conditions after collisions or to local point variable
//	pertains to the fluctuation

Subscripts

a, b, c	pertains to points a, b, c , respectively
av	pertains to element average quantities
cv	pertains to the control volume
ele	pertains to the element
i	index used in tensor notation, and refers to a node in the grid
j	index used in tensor notation, and refers to a node in the grid
MX	related to maximum packing condition
o	pertains to the centroid of the element
r	pertains to the r -component equation or to point r
s, t	pertains to points s and t , respectively
SP	pertains to specified value
z	pertains to the z -component equation
ϕ	pertains to the dependent variable ϕ

Chapter 1

Introduction

1.1 Aims and Scope of this Work

This work is primarily concerned with the numerical solution of the mathematical models of laminar gas-solid particle flows. Both dilute and dense gas-solid particle flows have been modelled in the past, but there have been only a few recent efforts to analyze flows of medium concentration. Furthermore, most of the published works on this subject involve gas-solid particle flows in regular-shaped geometries, or calculation domains whose boundaries lie along commonly used orthogonal coordinate axes. In this work, the focus is on the computer simulation of gas-solid particle flows over a *wide range of concentration* in two-dimensional planar and axisymmetric *irregular* geometries.

Several mathematical models of gas-solid particle flows can be found in the literature, but it is still not clear if any one set of equations is appropriate for all problems of interest [42]. The aim in this work is not to determine the most appropriate set of governing equations, but to provide a general numerical method capable of solving such sets of equations in irregular geometries. To justify the scope of this work, it is useful to cite Steward and Wendroff [172]: “It may seem rash to solve a set of equations which are not known to be correct in detail. The effort is justified in many cases because numerical solutions yield information of practical value even admitting some uncertainty. More basically, numerical solutions help evaluate the uncertainty and improve the model”. Thus the motivation behind the proposed

numerical method is to provide a useful tool to improve the mathematical models of gas-solid particle flows. It represents a first step towards a long-term objective of designing efficient computer simulation tools to solve practical problems involving gas-solid particle flows.

The numerical method proposed in this thesis belongs to the family of Control-Volume Finite Element Methods (CVFEMs) [13], which provides the geometrical flexibility of Finite Element Methods (FEMs) along with the physically meaningful numerical formulation traditionally associated with Finite Volume Methods (FVMs) [130].

1.2 Two-Phase Flows

This section is intended to *briefly introduce* some fundamental concepts of two-phase flows. This will be done by defining some terms typically used in the description of two-phase flows, discussing some of the phenomena encountered in such flows, and, finally, listing some applications.

A *phase* is simply one of the states of matter, which can be either a gas, a liquid or a solid. Thus, two-phase flow implies the simultaneous flow of two phases. In the subject of two-phase flows, however, the word *phase* is used in a more general sense: the simultaneous flow of two immiscible liquids, such as water and oil, is also called two-phase flow, even though each substance is liquid, because the mathematical models that are used to describe actual two-phase and such two-component flows are similar.

The subject of two-phase flows is very broad. It includes flow of liquid-liquid, gas-liquid, gas-solid particles, and liquid-solid particles, with and without chemical reaction and/or change of phase. Each type of two-phase flow has its own special physical characteristics, such as thermal, momentum, and mass coupling between the phases. A satisfactory general mathematical description of all physical phenomena that occur in two-phase flows is unavailable, and, perhaps, hardly possible. The interested reader is referred to detailed physical and mathematical discussions of two-phase flows in books by Hetsroni [78], Ishii [89], Soo [169] and Wallis [186], and papers by Bedford and Drumheller [18], Drew [48] and Stewart and Wendroff [172],

for example. The discussion in the remainder of this section will be restricted to *gas-solid particle* flows, or flows of a mixture of gas and solid particles. A review of the mathematical models of such flows is presented in Chapter 2, and details of the mathematical model used in this work are given in Chapter 3.

Gas-solid particle flows are commonly encountered in the environment and in the power-generation, chemical, process, food and aeronautics industries. Environmental examples include dust and sand storms, and transport of pollutants in the atmosphere. Industrial applications include flows in pneumatic conveyor systems, pulverized coal fired furnaces, cyclone separators, fluidized beds, and split-flow inertial separators for air intakes of helicopter gas-turbine engines.

Many of the available mathematical models of gas-solid particle flows are based on some form of averaging where each phase is considered as a continuum occupying the same region in space [47, 89, 124]. Such models require definitions of the volume concentration and the bulk density of the two phases. The volume concentration of a particular phase is the ratio of the volume occupied by the phase to the volume of the mixture. Correspondingly, the bulk density of a particular phase is the mass of the phase divided by the volume of the mixture.

The definition of the bulk density leads to the notion of *loading* which is the ratio of the solid-phase bulk density and the fluid-phase bulk density. The loading is an important parameter that characterizes the coupling between the phases. At low loading, the coupling can be assumed to be *one-way* [41], because the dynamics of the solid phase depend on the fluid-phase flow field, while the latter is only weakly influenced by the flow of the solid phase: in other words, the amount of particles under low-loading conditions is assumed to be so small that the fluid-phase flow field is not affected by the presence of the particles, but the particle trajectories are strongly influenced by the fluid-phase flow field. At larger loadings, the flow of the fluid phase may be significantly influenced by the dynamics of the solid phase, and vice versa [41, 42, 48].

Each phase has its own characteristic time scale. The ratio of the solid-phase time scale and the fluid-phase time scale is the *Stokes number* [41]. The fluid-phase time scale is defined by the ratio of a characteristic length and a characteristic fluid-phase velocity. In the case of gas-solid particle flow, the solid-phase time scale

is typically taken to be the single particle relaxation time [118, 148]. The Stokes number characterizes the dynamic equilibrium between the phases. At low Stokes numbers, the solid phase responds very rapidly to the fluid-phase flow field and, therefore, is essentially always in dynamic equilibrium with the fluid phase. The flow of such a mixture is called homogeneous equilibrium flow [186]: the fluid- and solid-phase velocities have the same value, therefore the two-phase mixture can be treated as a single-phase substance by defining proper average properties. However, at large Stokes numbers, the fluid and solid phases are usually not in dynamic equilibrium.

The dynamics of gas-solid particle flows are also influenced by the volume concentration of the solid phase. At low concentration, the dynamic coupling between the phases is governed by aerodynamic forces, and the number of particle collisions and their influence are negligible. At high concentration, particle collisions have significant effects on the dynamics of both phases. In summary, when the dynamics of the solid phase is primarily controlled by the aerodynamic forces that they experience, the flow is said to be *dilute*, while a *dense* gas-solid particle flow is mainly influenced by collisions between the particles [41].

The importance of particle collisions cannot be assessed solely on the basis of the solid-phase concentration. When the solid phase consists of particles of non-uniform size (polydispersed particles), for example, collisions may be promoted since particles of different size respond differently to the aerodynamics forces, resulting in relative velocity between the particles and preferential accumulation of particles in certain regions of the flow.

1.3 Organization of the Thesis

The development of the numerical method proposed in this work was realized in three major steps. At each step, a particular aspect of the numerical model was developed, implemented and validated. The first step was the formulation, implementation, and testing of a Control-Volume Finite Element Method (CVFEM) for two-dimensional planar and axisymmetric (Cartesian/cylindrical) single-phase fluid flow. This Cartesian/cylindrical formulation is a very useful feature of the proposed

CVFEM, because it allows its application to a wide variety of test cases and problems of interest. The second step was the formulation, incorporation and testing of a dilute gas-solid particle flow model. The last step was the formulation and incorporation of a more general model for gas-solid particle flows, in which the effects of particle collisions are accounted for through a solid viscosity and pressure in the solid-phase governing equations.

The structure of this thesis reflects this step-by-step evolution of the proposed numerical method. In Chapter 2, various relevant, existing mathematical and numerical models are reviewed. The description of the chosen mathematical model follows in Chapter 3. The presentation in this chapter is focused on a general model, which is capable of handling a wide range of solid-phase concentration. At the end of Chapter 3, specializations of this general mathematical model for single-phase flows and dilute gas-solid particle flows are presented. The proposed numerical method, described in Chapter 4, is also presented in the context of the general mathematical model applicable to a wide range of concentration. Chapters 5, 6, and 7 present the validations and results for the various specializations of the mathematical model, which also correspond to the step-by-step evolution described previously. In Chapter 8, the contributions of this thesis are reviewed and some suggestions are presented for the extensions of this work.

Chapter 2

Literature Review

Two-phase flow is a very broad subject and an exhaustive literature review is a formidable task: only on the subject of gas-liquid flow prior to 1966, more than 5000 references were indexed [68]. A general review of the subject of two-phase flow is beyond the scope of this work. Fairly detailed discussions of two-phase flow are available in books by Hetsroni [78], Ishii [89], Soo [169] and Wallis [186], and in papers by Bedford and Drumheller [18], Drew [48] and Stewart and Wendroff [172], for example. This literature review is intended to present only the works primarily related or significant to *gas-solid particle* flows.

2.1 Mathematical Models of Gas-Solid Particle Flows

The most detailed model for gas-solid particle flows is the so-called complete local description [172], or exact formulation [18]. This approach deals with the dynamics of each phase and the interface on the basis of first principles [78]. At each point of the domain of interest, only one phase exists at a time, and, therefore, the appropriate governing equations are solved at those points. To be more precise, in the case of two immiscible Newtonian fluids flowing simultaneously, for example, the complete local description consists of two sets of Navier-Stokes equations along with appropriate interphase boundary conditions. Such a complete local description *exactly* models the flow of interest. However, the solution of practical problems

using this model is usually beyond the capabilities of available computers [42], and some simplifications are needed to obtain a tractable model.

Practical models can be obtained by introducing the notion of volume concentration in the context of superimposed continua: each phase is treated as a continuum, occupying simultaneously the same region in space. The governing equations can be postulated or obtained by some averaging processes. The early models were postulated. Example includes the works of (i) Rudinger and Chang [147], who derived one-dimensional two-phase flow equations, and studied expansion and shock waves in pipes; (ii) Zuber [198], who proposed a mathematical model of laminar gas-solid particle flow consisting of a continuity equation for each phase, a mixture momentum equation, and the equation of motion of a single particle that is used to compute the slip between the gas and the solid phases; and (iii) Marble [112], who proposed a set of governing equations, the so-called dusty-gas model, consisting of a continuity and a momentum equation for each phase. The model of Marble is limited to dilute concentration of the solid phase, and, therefore, the fluid-phase is governed by the well-known single-phase Navier-Stokes equations with an additional term that represents the fluid-solid interactions.

More rigorous derivations of mathematical models of two-phase flows are based on averaging procedures. The early works in averaging theories, such as Anderson and Jackson [5], Murray [122], Panton [128], and Buyevich [24] are related to applications involving gas-solid particle flows. The works of Slattery [166] and Whitaker [192] for porous media are based on the technique of volume averaging. Averaging formulations of a more general multiphase system can be found in the works of Drew [47], Ishii [89], and Nigmatulin [124]. Ishii's [89] and Nigmatulin's [124] formulations are both based on the averaging of the local instantaneous governing equations of each phase, along with the local instantaneous jump conditions at the interfaces. The difference between these two formulations is in the type of averaging procedure. Ishii [89] applied time averaging while Nigmatulin [124] used volume averaging. The volume-averaging procedure naturally introduces the volume fraction, or volume concentration, in the resulting average equations. In the time-average formulation of Ishii [89], however, the local time fraction has to be equated to the volume concentration, and this step is not founded on any rigorous argument [18]. Ishii's and Nigmatulin's formulations lead to equivalent

averaged equations, but the macroscopic variables have different interpretations: Ishii's equations deal with time-averaged variables, while the macroscopic variables in the formulation of Nigmatulin are volume-averaged quantities.

A more sophisticated averaging procedure has been suggested by Drew [47] in which two spatial and two time averages are applied, not on the local governing equations, but on their corresponding integral formulation. This four-step averaging procedure was applied to obtain a formulation whose solutions have smooth derivatives. A statistical approach has been used by Buyevich [24] to derive the governing equation for dilute-concentration suspensions of mono-disperse particles. Delhaye and Achard [43] derived average equations based on ensemble averaging. These various cited averaging procedures vary significantly. However, they lead to essentially equivalent form of averaged balance equations [18]. These average descriptions are also called continuum-mechanical approaches [48], or continuum model of immiscible mixture [18], and are useful in problems where the exact details of the flow, such as those obtainable from the complete local description, are not needed.

In the average models, in addition to the specification of how each phase interacts with itself through stresses, the mutual interaction of the two phases has to be included. These additional terms are modelled based on basic rules of physics and empirical data applicable for a specific flow topology (stratified flow, dispersed flow, etc.). Such models represent the major source of uncertainties in the average formulations. Several models, developed for specific applications, exist in the literature. Anderson and Jackson [5], and Murray [122] used volume averaging to obtain a description of fluidized beds. Panton [128] based his gas-solid particle equations on a combination of volume and time averaging. Jiang et al. [94] applied volume averaging techniques to obtain a model for the suspension of neutrally buoyant particles. More recently, ensemble averaging has been applied to gas-solid particle flows by Liljegren [104].

In the formulation of the fluid-phase momentum equations using the averaging approach, terms involving the velocity fluctuations appear. These terms are similar to the so-called Reynolds-stress terms that appear in the time-averaged momentum equations of single-phase turbulent flow. Several names have been given to these terms in the literature: Anderson and Jackson [5] use the term *Reynolds stresses*;

Buyevich [24] calls them the *pseudo-turbulent stresses*; Drew [48] prefers the term *turbulent stresses*; and *fluctuating stresses* is used by Nigmatulin [124]. In the early models [147, 198, 112], these additional stresses were not considered. However, in many gas-solid flows of interest, these additional stresses need to be modelled, and a large amount of works on this subject is available in the relatively recent literature [56, 32, 163, 96]. Crowe [42] has presented a review of the various available turbulence models for dispersed two-phase flows.

Averaged models based on the so-called Eulerian approach use an Eulerian formulation both for the fluid and the solid phases. The solid phase can alternatively be modelled by using a Lagrangian formulation [3, 39, 50] where the dynamics of individual particles are modelled by the particle equation of motion: this formulation is referred to as the Lagrangian approach. Practically, it is impossible to track all the particles, even in dilute concentration, and, therefore, the incoming particle flow is represented by a finite number of “computational” particles [42]. Each “computational” particle represents a group of particles having the same properties in terms of size, density, and starting position. This formulation facilitates implementation of the wall boundary conditions, through particle/wall collisions, and the incorporation of a distribution of particle sizes is relatively straightforward [168]. However, the volume concentration is not an integral part of the formulation, and, therefore, additional treatments are needed to obtain the volume concentration required in the fluid-phase governing equations. Furthermore, the Lagrangian approach can become very expensive computationally when particle/particle collisions are important.

Most of the mathematical models of gas-solid particle flow described so far in this review are limited to dilute concentration of the solid phase. This limitation is not related to the averaging process, but is due to the assumption that the particles have negligible effects on each other. However, as the solid concentration increases, the interaction between the fluid and the solid phases is no longer the only mechanism that must be taken into account, since particles start to interact with each other. One of the earliest works on dense-concentration flows is the experimental investigation by Bagnold [9]. He observed two flow regimes, namely, *low shear rates* flow and *high shear rates* flow. His experimental results show that at high shear rates, the normal and shear stresses are both quadratic functions of the shear rate, while at low shear rates, the variations are linear. This change in behaviour can be

explained by noting that the transport process is dominated by collisional interactions at high shear rates and by viscous fluid flow effects at low shear rates. These two regimes were accordingly called the *grain-inertia* regime and the *macro-viscous* regime. In the grain-inertia regime, the fluid plays a negligible role in comparison to particle/particle interactions.

Bagnold's interpretation of the importance of the particle collisions in the grain-inertia regime lead Savage and co-workers [58, 91, 106, 108, 109, 150] to propose mathematical models of dry granular materials (or collection of discrete solid particles with no interstitial fluid). Using an analogy with the kinetic theory of dense gases [31], the momentum exchange in granular materials is assumed to occur primarily through binary collisions of hard spheres. However, in the kinetic theory of dry granular materials, an energy dissipation process is included through inelastic collisions. These collisions are characterized by a coefficient of restitution. Using similar averaging techniques as in the kinetic theory of gases, a macroscopic description of dry granular materials can be obtained. The resulting macroscopic equations consist of a continuity equation, a momentum equation, and an equation governing the transport of the specific kinetic energy of the solid-particle velocity fluctuations, which has become known as the granular temperature [152]. This model, called the granular temperature model, has the advantage of giving a microscopic interpretation of the various macroscopic (average) transport properties of the solid phase such as viscosity and conductivity.

Campbell [28] and Savage [152] have recently reviewed the works related to granular flows. Therefore, only a brief discussion of some of the contributions to the kinetic theory of granular materials is presented here. The early models [150, 91, 106] were developed for the case of uniform, nearly elastic, smooth, spherical particles. The effects of particle surface roughness [92, 109], the effects of impact velocity-dependent coefficient of restitution [107], and the effects of highly inelastic particles [146] are among the advances included in later works on the kinetic theory of dry granular materials. There have also been some recent efforts to include the effects of the interstitial fluid, and develop granular-flow kinetic theories involving binary mixtures of particles having different sizes [58, 93]. Adapting the granular-flow kinetic theory, Sinclair and Jackson [165] analyzed fully-developed gas-solid particle flow in a pipe. The effects of the fluid were modelled through a drag

force appearing in the solid- and fluid-phase momentum equations. The solid-phase constitutive equations were simply based on the dry granular kinetic theory of Lun et al. [106]. A similar model has been developed by Ding and Gidaspow [45] and applied to fluidized beds. Lun [107] and Lun and Savage [110] have rigorously developed a kinetic theory for gas-solid particle mixtures. In their framework, the particles are governed by Newton's laws of motion: the forces acting on the particles come from the fluid phase/particle interactions, particle/particle collisions, and the gravity field; and the effects of the fluid phase are systematically introduced in the solid- and fluid-phase governing equations, and also in the solid-phase constitutive equations.

The physical behaviour of granular flows has also been studied through *numerical experiments* [25]. Typically, the dynamics of a finite amount of particles is computed using Newton's laws of motion and appropriate interaction models. This idea of *numerical experiments* has been successfully used in the simulation of granular flows, to investigate both the macroscopic and microscopic aspects of such flows. It is a complete description of a multi-body problem where instantaneous particle positions, velocities and forces are computed. Averaging processes are then applied to obtain macroscopic properties such as stresses. These simulations are completely deterministic [152] and are used to verify the various assumptions of the kinetic theory of granular flows. However, numerical experiments are currently limited to relatively simple flows, such as Couette and chute flows, and need to use special techniques, such as periodic boundary conditions, in order to limit the number of particles involved in the calculation. It should be also noted that the results of these simulations depend on the model used for the particle interactions. Campbell [26, 27] and Savage [153] treat the particles as hard spheres, and the particle collisions are assumed to be instantaneous and binary. Other simulations by Walton [187, 188] and Haff and Werner [71] assume particle interactions of finite durations.

Leighton and Acrivos [102] have also proposed a mathematical model for dense-concentration particulate flows based on experimental observations of particle diffusion in shear flows. This model, called diffusive flux model, is based on a macroscopic shear induced diffusivity which is a function of the shear rate and the concentration gradient.

2.2 Numerical Solution of the Mathematical Models

The mathematical models of the multitude of fluid flow phenomena in engineering and the environment are, in general, not amenable to analytical solution techniques. Consequently, alternative solution procedures such as numerical methods have been proposed and used successfully. In this section, some of the numerical methods used for the solution of the mathematical models of single-phase and gas-solid particle flows are reviewed.

Numerical methods for the prediction of such flows are based on vorticity/stream-function [61, 67], vorticity/vector velocity potential [6], or primitive-variable formulations [130]. In two-dimensional problems, methods based on vorticity/stream-function formulation offer a number of advantages: pressure is eliminated from the governing equations; and in single-phase flows, three governing equations, the continuity and two momentum equations, are replaced by two governing equations, one for vorticity and one for stream function. However, the vorticity/stream-function formulation is limited to two-dimensional problems. The vorticity/vector velocity potential formulation is suitable for three-dimensional problems, and it too eliminates pressure from the governing equations; however, in single-phase flows, six dependent variables are involved, three components of the vorticity vector and three components of the vector velocity potential, in contrast to four dependent variables, three components of velocity and pressure, in the primitive-variable formulation. In all vorticity-based formulations, the value of vorticity at walls has to be specified iteratively, and this feature often leads to convergence difficulties [130]. It should also be noted that it is difficult to specify boundary conditions on stream function in problems with multiply-connected domains. For these reasons, the primitive-variable formulation is favoured in the solution of practical problems. In this thesis, the primitive-variable formulation is preferred.

In primitive-variable formulations of incompressible flows, there is no explicit governing equation for pressure: when the correct pressure field is substituted into the momentum equations, and then these equations are solved, the resulting velocity field satisfies the continuity equation [130]. This indirect specification of pressure does not pose any difficulties in numerical methods if the discretized momentum and

continuity equations are solved *simultaneously*. However, direct solution of the discretized, coupled momentum and continuity equations requires very large computer storage: thus, this approach is impractical in three-dimensional problems and in the solution of multiphase flows. To overcome this problem, alternative sequential solution algorithms, such as the Semi-Implicit Method for Pressure-Linked Equations (SIMPLE), SIMPLE-Revised (SIMPLER), and SIMPLE-Consistent (SIMPLEC), have been proposed [130, 184]. In these sequential algorithms, discretized equations for pressure and/or pressure correction are obtained by using the discretized momentum equations in the discretized continuity equations, and then the sets of discretized equations for the velocity components, pressure and/or pressure correction are solved sequentially. Other options for the solution of coupled momentum and continuity equations include iterative coupled solution algorithms, such as the Simultaneous Variable Adjustment (SIVA) method of Caretto et al. [29] and the Coupled-Equation Line Solver (CELS) of Galpin et al. [62]. In this work, ideas from SIMPLER and CELS are borrowed to construct an iterative variable adjustment algorithm. Details are given in Chapter 4.

Another difficulty encountered in primitive-variable formulations of incompressible flows is the following: if the velocity components and pressure are stored at the same nodes (co-located) and interpolated by similar functions (equal-order), then physically unrealistic checkerboard-type pressure distributions could be admitted as solutions [130]. One way to avoid this difficulty is to use staggered grids for the velocity components and pressure [74, 130]. However, the use of staggered grids is not an attractive option when nonorthogonal structured or unstructured grids are used [14, 149, 162]. In finite element methods, mixed or unequal-order interpolation of the velocity components and pressure is often used to avoid the aforementioned difficulty of checkerboard-type pressure distributions [10, 81, 87]. Yet another approach to overcome this difficulty in co-located, equal-order, primitive-variable formulations is to use special interpolation functions for the velocity components when discretizing mass-flux terms. Examples of this approach can be found in the works of Prakash and Patankar [135], Rice and Schnipke [145], Peric et al. [131], and Saabas [149]. This approach is also used in the numerical methods proposed in this thesis: details are presented in Chapter 4.

The discretization of the governing equations can be achieved using finite dif-

ference methods (FDMs) [4], finite volume methods (FVMs) [74, 129, 139], finite element methods (FEMs) [126, 178, 196] or control-volume finite element methods (CVFEMs) [11, 12, 13, 14, 15, 134, 135, 136, 137, 141, 156, 157]. FDMs and FVMs have been applied very successfully to complex fluid flow phenomena in regular-shaped calculation domains. General orthogonal grids [179] can be used to extend the applicability of FDMs and FVMs to irregular geometries. Examples of FVMs and FDMs based on general orthogonal and nonorthogonal grids can be found in the works of Raithby and co-workers [140, 70, 183], Shyy and Vu [162], Acharya et al. [1], and Pope [133]. However, methods based on finite-element discretizations seem to be better suited for the solution of fluid flow problems in complex irregular domains.

In the mid-seventies, the desire and the need to extend the capabilities of the successful marker and cell (MAC) method of Harlow and Welch [74], and the FVMs of Patankar and Spalding [129], and Raithby [139] to irregular geometries provided the motivation for the CVFEMs of Baliga [11], Ramadhyani [141] and Prakash [134]. These early CVFEMs were formulated by combining and extending concepts borrowed from the aforementioned FVMs, the work of Winslow [194], and the FEMs of Zienkiewicz [196], Oden [126], and Taylor and Hood [178]. Today, many papers dealing with the formulation and application of CVFEMs for conduction, convection-diffusion, and single-phase fluid flow problems are available in published literature. Examples include the works of Baliga and Patankar [12, 13, 14], Prakash and Patankar [135], LeDain-Muir and Baliga [100], Prakash [136], Hookey and Baliga [83], Schneider and Raw [156, 157], Costa and Oliviera [34], and Elkaim et al. [57]. The combination of finite element and finite volume approaches can also be found in the works of Choudhury and Nicolaides [33], van Leer [185], Jameson and Mavriplis [90], Lahrman [99], and Swaminathan and Voller [175].

Recent reviews of CVFEMs for two- and three-dimensional viscous fluid flows are available in the works of Hookey [84], Saabas [149], and Baliga and Saabas [15]. Most of the CVFEMs proposed in the seventies and eighties have intrinsic difficulties that restrict the scope of their applicability to practical problems. CVFEMs based on flow-oriented upwind schemes [13, 100, 136] are successful in reducing the false diffusion that afflicts locally one-dimensional upwind schemes used in FVMs [130], but they can encounter difficulties caused by negative coefficients in the discretization

equations. These difficulties can become quite serious when obtuse angled triangular elements, or tetrahedral elements with a solid angle exceeding $\pi/2$ steradians, are used in problems that involve high Peclet numbers [15, 149]: furthermore, for these conditions, additional difficulties related to indeterminate coefficients in the interpolation functions may be encountered [149]. Some of the two-dimensional CVFEMs based on unequal-order and equal-order co-located formulations are successful in avoiding checkboard-type pressure distributions in incompressible flow problems, but they suffer from other difficulties: the unequal-order formulation of Baliga and Patankar [13] can suffer a loss of accuracy in problems with high Reynolds numbers, and its extension to three-dimensions would be quite cumbersome; the co-located equal-order formulations of Prakash [136] and Hookey and Baliga [83] require over-specification of boundary conditions and encounter convergence difficulties in problems with inflow and outflow boundaries [149]. Schneider and Raw [156, 157] have proposed a co-located equal-order CVFEM based a mass-weighted upwind scheme. This method ensures that the discretized convection transport terms contribute positively to the coefficients in the discretization equations, and it avoids spurious oscillations in the computed pressure field. However, this CVFEM [156, 157] is based on planar quadrilateral elements, and its behaviour in problems with inflow and outflow boundaries has not been discussed in detail in the published literature.

The recently completed work of Saabas [149] was aimed at overcoming some of the difficulties mentioned in the previous paragraph. It has resulted in an equal-order co-located CVFEM that deals directly with primitive variables and is capable of solving steady, multidimensional, laminar and turbulent, incompressible, viscous single-phase fluid flow problems in irregular-shaped geometries, with or without inflow and outflow boundaries [15, 149]. More recently, the CVFEM proposed by Saabas [149] has been adapted and extended for the solution of two-dimensional axisymmetric single-phase fluid flow problems by Masson et al. [116].

CVFEMs have proved successful in the solution of single-phase fluid flow and heat transfer problems in two- and three-dimensional geometries. Recently, Masson and Baliga [114, 115, 117] have proposed a CVFEM for dilute gas-solid particle flows: this CVFEM was developed as a part of the work reported in this thesis. In this numerical method all of the dependent variables are stored at the same nodes (co-located) and interpolated over the same elements (equal-order). This numerical

method was constructed by adapting ideas from earlier CVFEMs for incompressible single-phase fluid flows proposed by Baliga and Patankar [14], Prakash and Patankar [135], Schneider and Raw [156, 157], Saabas [149], and Masson et al. [116].

In dilute gas-solid particle flows, if dynamic and thermal equilibrium between the fluid and solid phases can be assumed, then the gas-solid mixture can be considered as a single-phase homogeneous fluid, with suitable thermophysical properties that account for the presence of the particles. The corresponding mathematical formulation can be solved using available numerical methods for single-phase flows. However, in general, the fluid and solid phases cannot be assumed to be in equilibrium, and, therefore, it is not always appropriate to consider the gas-solid mixture as a homogeneous fluid. The early numerical models for non-equilibrium dilute particulate flows, such as those proposed by Marshall and Seltzer [113], Hotchkiss and Hirt [86], Morsi and Alexander [121], Gauvin et al. [63], and Westbrook [191], are Eulerian-Lagrangian formulations based on *one-way coupling*: the fluid-phase flow field is computed on a fixed grid, without accounting for the influence of the solid phase; then particle trajectories are calculated by integrating the particle-motion equation, with the previously calculated flow field as a known input. The Eulerian formulations of Hamed and Tabakoff [72], and Eldighidy et al. [55], where, after suitable averaging, the solid particles are considered as a continuum, are also based on the one-way formulation. The solution of such models is straightforward, because existing numerical methods developed for single-phase flows can be used with only little or no modifications. One-way coupling models have been used to predict multiphase flows in split-flow particle separators [22], cyclone separators [180], liquid-fuel spray nozzles [191], and ventury scrubbers [19]. They have also been used in studies of dispersion of atmospheric pollutants [86], turbine blade erosions [176], and spray drying [63, 113].

In most of the applications involving gas-solid mixtures, even at low concentration, the solid-phase mass flow rate is of the same order as the fluid-phase mass flow rate, because the density of the solid phase is usually much higher than that of the gas. At such high loadings, a more general technique for the simulation of dilute gas-solid particle flows, namely, the *two-way coupling* model, in which both particle/gas and gas/particle interactions are taken into account, is required. Again, the implementation of this model can be done either by using a Lagrangian or an

Eulerian description for the solid phase. The fluid phase is always described in an Eulerian manner.

In two-way coupling models, the effects of the solid-phase can be introduced as implied sources of mass, momentum, and energy in the continuum description of the fluid phase, as was first proposed by Migdal and Agosta [119]. Using the Lagrangian description of the particulate phase and the implied-source concept of Migdal and Agosta [119], Crowe and Pratt [36, 37], Crowe et al. [39], Stock and Crowe [173], and Amsden and Hirt [3] have predicted particle trajectories in the continuous phase. Their procedures consist first in solving the fluid flow assuming that no particles are present, using either the vorticity/stream-function [38] or primitive-variable formulations [39] and an appropriate numerical method, if required. Particle trajectories are then predicted, and used to calculate the implied sources of mass and momentum in the governing equations of the fluid phase. The fluid-phase flow is recalculated using these computed, implied sources, and the process is repeated until convergence. A popular scheme based on such a Lagrangian approach is the PSI-CELL model first proposed by Crowe et al. [39]; similar models have been applied to various problems such as cyclone separator [37], liquid fuel combustion [54], pneumatic transport [101], orifice and venturi [160], swirling flow [161], spray drying [40], electrostatic precipitation [181], swirl combustion chamber [138], and pipe flow [51]. Early Lagrangian models [3, 119] are well suited for dilute-concentration liquid-solid particle flow simulations. However, for gas-solid particle flow simulation at high loading, prohibitively small time steps are needed, and the strong fluid-solid momentum coupling could cause convergence difficulties [50, 51]. These convergence difficulties are associated with the explicit treatment of the momentum coupling term: during the calculation of the fluid-phase velocity, the solid-phase velocity that appears in the momentum coupling term is assumed to be the corresponding value taken at the previous time step. To remove the necessity of small time steps and alleviate the aforementioned convergence problems, Crowe et al. [39] have introduced an implicit treatment of the momentum coupling term, resulting in an iterative process at each time step. Dukowicz [50] used a time-splitting technique that allows implicit, noniterative, computation of the momentum-coupling term.

Numerical models based on Eulerian formulations of the particles, such as those proposed by Di Giacinto et al. [44], Durst et al. [51], and Simonin [164], are very

similar to the corresponding two-fluid flow models developed by Carver [30], Harlow and Amsden [76], Shah et al. [159], and Spalding [170]. Most of these two-fluid models have been used in conjunction with established single-phase finite-volume methods that employ staggered grids for the velocity component and pressure [74, 129]. A co-located, equal-order CVFEM based on a two-fluid model of dilute gas-solid particle flows has been recently proposed by Masson and Baliga [114, 115, 117]. Again, it should be noted that this CVFEM [114, 115, 117] was developed as a part of the work reported in this thesis. Two sets of governing equations, one for the fluid phase and one for the solid phase, with appropriate interaction terms have to be solved in such models. Most of these formulations in the literature use upwind interpolation of the volume concentration, but differ in the derivation of the pressure equation (or pressure correction equation): the pressure correction equation is based on the overall mixture continuity equation in the algorithm of Shah et al. [159]; Carver [30] derived a pressure correction equation based on the *volumetric* continuity equation of the mixture; and the pressure correction equation employed by Spalding [170] is based on the imbalance of volume concentrations.

The pressure correction equation of Carver [30] is based on volumetric flow rates instead of mass flow rates, and is more appropriate than the pressure correction equation of Shah et al. [159] in the case of high density ratios (which is typical of gas-solid particle mixtures). Carver [30] has also implemented an equation for the pressure, that is similar to his pressure correction equation, and arrived at a SIMPLER-type algorithm [130]. The imbalance of volume concentrations defined by Spalding [170] is computed from the individual continuity equations. Each continuity equation allows the calculation of the volume concentration of the corresponding phase. Since the mixture occupies the entire domain, the volume concentrations should add to unity, but during the iterative solution procedure, the volume concentrations computed from the individual continuity equations do not necessarily do so, and, therefore, there is a imbalance of volume concentration. The pressure correction equation of Spalding [170], which is obtained by requiring an elimination of this imbalance, includes the effects of available volume concentrations and velocities. The form of the volume concentration equation also differs between these various formulation. Spalding [170] and Shah et al. [159] use the continuity equation of one of the phases to construct the volume concentration equation. Carver [30] notes that such a volume concentration equation does not explicitly incorporate the

influence of the other phase: his equation for volume concentration is based on a linear combination of the two continuity equations, one for each phase. In later work, Spalding [171] has also explicitly included the effects of both phases by constructing the volume concentration equation using a combination of the continuity equations of both phases.

The Lagrangian approach is based on the solution of the parabolic equations of motion of a large number of particles. In this formulation, the handling of boundary conditions, though quite demanding computationally, is straightforward once the wall/particle collision properties are known. It can also handle polydispersed particle size distribution [51] more efficiently than the Eulerian formulation. However, the volume concentration does not appear directly in the Lagrangian formulation, and, therefore, special treatments need to be applied [50] in order to obtain the volume concentration required in the equations that govern the motion of the fluid phase. This can adversely affect the effectiveness of the solution procedure at high solid-phase volume concentration. It has also been observed that the Eulerian formulation often converges more easily at high loading than the Lagrangian model, as has been discussed by Durst et al. [51]. Furthermore, at high particle concentrations, particle collisions can occur, and these are difficult to take into account in the Lagrangian formulation. However, recently, Lagrangian formulations have been proposed by Tanaka and Tsuji [177], and Oesterle and Petitjean [127], in which the particle collision effects are included.

The granular-temperature models and numerical simulations of Johnson and Jackson [95], Nott and Brady [125], Sinclair and Jackson [165], and Wang and Ni [123, 190, 189], or diffusion-flux models of Nott and Brady [125], and Schaffinger and Acrivos [154], are examples of Eulerian formulations in which the interparticle collisions are included. The aforementioned numerical simulations are based on one-dimensional formulations. Recent efforts to implement granular-temperature models in multi-dimensional numerical simulations of high-concentration gas-solid particle flows include the works of Gidaspow and co-workers [45, 66, 65]. These numerical models use a staggered-grid finite volume formulation based on the ICE algorithm developed by Harlow and Amsden [76]. Gidaspow and co-workers have successfully used these methods for some fluidized bed calculations.

The method proposed in this thesis is a CVFEM that is designed to solve two-

fluid models of gas-solid particle flows over a wide range of concentrations in complex two-dimensional domains. Some aspects of this CVFEM, pertaining to single-phase flows and dilute-concentration gas-solid particle flows, have been published recently [114, 115, 116, 117]. Details of this CVFEM are presented in Chapter 4 of this thesis.

Chapter 3

Mathematical Model

The equations that govern single-phase Newtonian fluid flows, the Navier-Stokes equations, are well established. However, in the case of gas-solid particle flows, the situation is not the same. Several derivations of the governing and constitutive equations are available in the literature, but arguments still exist on the most appropriate form of these equations. The methodology proposed by Savage and Jeffrey [150], Jenkins and Savage [91], and Lun et al. [106] for the modelling of granular flows, in which the solid-particle phase is modelled using a theory similar to the kinetic theory of gases, appears to be a promising technique for the derivation of the governing and constitutive equations in two-fluid models of gas-solid particle flows. Lun [107], and Lun and Savage [110] have proposed the first model of fluid-solid particle flows that uses the so-called granular-temperature concept. This model [107] is appropriate for a wide range of concentration, is based on fundamental principles of the kinetic theory of gases, and allows a microscopic interpretation of the constitutive equations. Thus the granular temperature methodology proposed by Lun [107], and Lun and Savage [110], will be used in this chapter to derive the governing and constitutive equations.

Ding and Gidaspow [45] have also used the granular-temperature approach to derive a mathematical model of gas-solid particle flows, but their model is only valid at dense concentrations. Using a similar approach, Koch [97] has also derived a mathematical model for monodisperse gas-solid suspensions. In his study, the inertia of the fluid was neglected.

In this chapter, the major steps involved in the derivation of the solid-particle phase governing equations and constitutive relations, as proposed by Lun [107] and Lun and Savage [110], are presented. First, the dynamics of a single particle, which is simply governed by Newton's law of motion, is discussed. Then the dynamics of multiple spherical particles in a fluid is presented. Following that, the averaging procedure that is used to obtain the macroscopic equations is described, along with a direct particle/particle interaction model based on simple hard-sphere binary collisions. The aforementioned averaging procedure is similar to that used to obtain the macroscopic governing equations of single-phase fluid flow from the Boltzmann equation [31].

In principle, the motion of the fluid phase is governed by the Navier-Stokes equations, which must be satisfied at each point in the fluid regions, and the dynamics of each particle is governed by Newton's laws of motion. Suitable boundary conditions can also be prescribed at the interfaces between the solid particles and the fluid. These equations together constitute an exact local description model. However, for a large number of particles, the exact topology is far too complex, so numerical solutions of the exact local description model are impractical. To simplify this local description, point variables which vary rapidly on the scale of the particle spacing are averaged over regions that are large compared with that spacing, but small compared with the domain of interest. The resulting average equations describe the fluid and solid phases as two interpenetrating continua. The volume averaging procedure of Anderson and Jackson [5] and Jiang et al. [94] is also described in this chapter. Finally, the resulting governing equations for two-dimensional axisymmetric flows are presented, along with specializations for single-phase flows, and dilute gas-solid particle flows.

The Einstein notation is used in most of the developments presented in this chapter. However, in the derivation of the solid-phase governing equations, the vectorial notation is sometimes used for the sake of conciseness and clarity. At the end of the chapter, the expanded equations are presented for two-dimensional, axisymmetric problems.

It should be noted here, again, that the objective in this thesis is *not* the comparative evaluation of the many models of gas-solid flows that are available in the published literature, as reviewed in Chapter 2. Rather, the goal here is to select

a model that allows the simulation of gas-solid particle flows over a wide range of concentration, and has the general features that are commonly found in other available models, and then propose a suitable numerical method for the solution of such mathematical models in complex two-dimensional domains.

It should be noted at this stage that the models discussed in this chapter are based on the following assumptions: the solid phase is composed of hard, spherical, smooth, elastic or slightly inelastic particles of uniform size; the mass density of the particles is much larger than the fluid-phase mass density; the rotation of the particles is neglected; the fluid is Newtonian and incompressible; and the flow is laminar.

3.1 Dynamics of a Single Particle in a Fluid Flow

Often, the dynamics of particles in a fluid flow is typically modelled using the Newton's second law of motion of a single spherical particle [80, 118, 148]. Considering a spherical particle of diameter d and density ρ^s in a Newtonian fluid having a density ρ^f , dynamic viscosity μ^f , and velocity component, u_i^f , in the i direction the equation of motion of the particle is given by [80, 118, 148]:

$$\begin{aligned} \mathcal{V}^p \rho^s \frac{Du_i^s}{Dt} = \mathcal{V}^p \rho^s g_i + \frac{\pi}{8} \mu^f d C_D \text{Re}^s (u_i^f - u_i^s) - \mathcal{V}^p \frac{\partial p^f}{\partial x_i} + \frac{1}{2} \mathcal{V}^p \rho^f \left(\frac{Du_i^f}{Dt} - \frac{Du_i^s}{Dt} \right) \\ + \frac{3}{2} d^2 \sqrt{\pi \rho^f \mu^f} \int_0^t \frac{\frac{Du_i^f}{Dt'} - \frac{Du_i^s}{Dt'}}{\sqrt{t-t'}} dt' \end{aligned} \quad (3.1)$$

where u_i^s is the particle velocity component in the i direction, Re^s is the particle Reynolds number, and \mathcal{V}^p is the volume of the particle.

$$\text{Re}^s = \frac{\rho^f d \sqrt{u_i^{f2} - 2u_i^f u_i^s + u_i^{s2}}}{\mu^f} \quad (3.2)$$

$$\mathcal{V}^p = \frac{\pi d^3}{6} \quad (3.3)$$

In this equation of motion, side forces, such as the Magnus and Saffman forces, are neglected since they are small compared with the viscous drag [118] under the

assumptions presented at the beginning of this chapter. The right-hand side of this equation of motion of the particle consists of the various external forces in the i direction experienced by the particle, namely, the gravitational force, the viscous drag, the overall fluid pressure gradient force, the apparent mass force, and the Basset force. The pressure force represents the effects of the global pressure gradient. This pressure gradient can be caused by viscous shear stresses at solid boundaries, the gravitational field, and acceleration/deceleration of the fluid. In the case of the gravitational field, the overall pressure gradient force is simply the buoyancy force. The apparent mass force is that needed to accelerate the mass of fluid displaced by the particle. The Basset force accounts for effects such as boundary layer growth, which are functions of the entire history of the particle trajectory [148].

In most practical applications of gas-solid particle flows, the particle density is much higher than the fluid density, and, therefore, the only forces on the particle which are significant are the gravitational, pressure, and viscous drag forces [118, 148]. The equation of motion of a particle for high values of the density ratio, $\frac{\rho_s}{\rho_f}$, simplifies to:

$$\frac{Du_i^s}{Dt} = g_i + \zeta_D (u_i^f - u_i^s) - \frac{1}{\rho^s} \frac{\partial p^f}{\partial x_i} \quad (3.4)$$

where

$$\zeta_D = \frac{3}{4} \frac{\mu^f}{\rho^s d^2} C_D \text{Re}^s \quad (3.5)$$

One of the first solutions of the flow field around a spherical particle, with uniform flow far from the particle, is the so-called Stokes solution [155]. Using creeping flow assumptions, Stokes obtained a solution of the Navier-Stokes equations and computed the drag force, D , applied on the particle by the fluid. The Stokes solution is

$$D = \frac{\pi}{8} \mu^f d C_D \text{Re}^s (u_i^f - u_i^s) \quad (3.6)$$

with

$$C_D \text{Re}^s = 24 \quad (3.7)$$

One third of the drag given by Eq.(3.6) is due to pressure force, and the remainder is attributable to viscous effects [155].

The creeping flow assumption limits the applicability of Stokes solution to $Re^s \ll 1$. An improvement of this expression was obtained by Oseen [155], who retained linearized convection terms in the Navier-Stokes equations. Oseen's expression for the drag force, valid for $Re^s \leq 5$, is

$$C_D Re^s = 24 + \frac{9}{2} Re^s \quad (3.8)$$

At high Re^s , the Stokes and Oseen solutions are inappropriate, and empirical relations are typically used. Wallis [186] has reported a well-accepted empirical expression :

$$C_D Re^s = \begin{cases} 24 + 3.6(Re^s)^{-0.687} & \text{if } Re^s \leq 1000 \\ 0.44 Re^s & \text{if } Re^s > 1000 \end{cases} \quad (3.9)$$

3.2 Multiple Spherical Particles in a Fluid Flow

In the case of multiple particles in a fluid flow, particle/particle effects could be important. At low solid-phase volume concentration, direct particle/particle interactions such as collisions are negligible, but the presence of a particle in the vicinity of another modifies the flow field around it significantly with respect to the single-particle problem. These effects in a suspension of solid particles in a fluid was first studied by Einstein [53]. In Einstein's work, the suspension was treated as a homogeneous mixture of fluid and particles, and the problem was of finding the appropriate homogeneous-mixture viscosity as a function of the solid-phase volume concentration. This viscosity is called the apparent viscosity of the suspension: it will be denoted by the symbol μ_a^f . The ratio of the apparent viscosity μ_a^f and the fluid viscosity μ^f is called the relative viscosity μ_r^f . Therefore, the apparent viscosity is given by:

$$\mu_a^f = \mu^f \mu_r^f(\alpha) \quad (3.10)$$

where α is the solid-phase volume concentration.

The following expression for the relative viscosity, derived by Einstein, is valid for dilute suspensions at low Reynolds numbers.

$$\mu_r^f(\alpha) = 1 + \frac{5}{2}\alpha \quad (3.11)$$

Several other derivations of the apparent viscosity can be found in the literature [17, 182]. Using the expression given by Vand [182] and estimating the associated free parameter, Lun and Savage [110] suggest the following expression:

$$\mu_r^f(\alpha) = (1 - \alpha - 0.33\alpha^2)^{-\frac{5}{2}} \quad (3.12)$$

This last expression has been derived for dense suspensions, but it is also applicable to dilute concentrations. It will, therefore, be used in this work.

This functional form of the apparent viscosity leads naturally to a modified drag force expression for a particle in a suspension of the following form [107]:

$$D = \frac{\pi}{8} \mu_a^f d C_D \text{Re}^s (u_i^f - u_i^s) \quad (3.13)$$

Other derivations of the drag of a particle in a suspension have been proposed for fluidized beds. For example, using the Ergun equation [98], Gidaspow [65] proposed the following relation to compute the drag of a particle in a dense suspension:

$$C_D \text{Re}^s = \frac{4}{3} (150\alpha + 1.75\text{Re}^s) \quad \text{if } \alpha > 0.2 \quad (3.14)$$

3.3 Solid-Phase Macroscopic Equations

The complete description of gas-solid particle flows must include boundary conditions at the interface and the interactions between the phases. Moreover, this phenomena is usually unsteady and three dimensional. As was mentioned earlier, the complete local description of gas-solid particle flows is not a viable option for the solution of practical problems. In order to obtain a tractable model for the solution of practical problems, averaging procedures, such as statistical methods, are used to

derive macroscopic governing equations along with their constitutive relations. Following the works of Lun [107] and Lun and Savage [110], the motion of the particles in a gas-solid particle flow can be assumed to be analogous to the random motion of the molecules of a gas. Therefore, a macroscopic description of the solid-particle phase can be obtained following closely the kinetic theory of dense gases [31]. This model is based on the prescription of a velocity distribution function. The velocity distribution function is governed by the Boltzmann equation, in which the external forces applied to the particles and a collisional term appear. The collisional term models the direct particle/particle interactions. Using appropriate averaging procedures, the so-called hydrodynamic equations of the solid-particle phase are obtained.

3.3.1 Terminology/Definitions

The distribution of particle velocities, \vec{c} , among the large number, $n d\vec{x}$, of particles in the volume $d\vec{x}$ at time t is represented by the *velocity distribution function* $f(\vec{c}, \vec{x}, t)$. The statistically definite number-density of the $n d\vec{x}$ particles in the velocity-space is denoted by $f(\vec{c}, \vec{x}, t) d\vec{c}$. This implies that the probable number of particles which, at time t , are situated at \vec{x} in the volume $d\vec{x}$ and have velocities in the range $[\vec{c}, \vec{c} + d\vec{c}]$ is $f(\vec{c}, \vec{x}, t) d\vec{c} d\vec{x}$. Therefore, the number of particle per unit volume, n , situated at \vec{x} is expressed by:

$$n = \int_{\vec{c}} f(\vec{c}, \vec{x}, t) d\vec{c} \quad (3.15)$$

This integral is performed over the entire velocity space. If m^p is the mass of a single particle and ρ^s is the density of the particle, the solid-phase volume concentration, α , can be expressed as:

$$\alpha \rho^s = n m^p \quad (3.16)$$

The distribution function, $f(\vec{c}, \vec{x}, t)$, contains detailed information on the motion of the particles. The evaluation of averaged quantities can be determined once $f(\vec{c}, \vec{x}, t)$ is known. These average quantities are obtained by integration of the

product of the distribution function and a single-particle property ϕ over the entire velocity space as follows:

$$\langle \phi \rangle = \frac{1}{n} \int_{\vec{c}} \phi f(\vec{c}, \vec{x}, t) d\vec{c} \quad (3.17)$$

where $\langle \phi \rangle$ denotes the average of ϕ . The solid-phase average velocity, $\langle c_i \rangle$, is denoted by u_i^s . The solid-phase velocity fluctuation, C_i , is the difference between the velocity, c_i , and the averaged velocity u_i^s . This definition leads to the important concept of granular temperature, which is a measure of the fluctuating kinetic energy of the solid particles [107, 110]. Using an analogy with the temperature of a gas, the granular temperature is denoted by T and it is defined as:

$$\frac{3}{2}T = \frac{1}{2} \langle C_i^2 \rangle \quad (3.18)$$

where

$$C_i = c_i - u_i^s \quad (3.19)$$

$$u_i^s = \langle c_i \rangle \quad (3.20)$$

3.3.2 Boltzmann Equation

The velocity distribution function is governed by the Boltzmann equation [31]:

$$\frac{\partial f}{\partial t} + c_i \frac{\partial f}{\partial x_i} + F_i^{\text{ext}} \frac{\partial f}{\partial c_i} = \left(\frac{\partial f}{\partial t} \right)_c \quad (3.21)$$

F_i^{ext} is the sum of the external forces per unit mass of particle, such as the gravitational force, applied on a single particle of mass m^p , and is independent of c_i . The force applied by the surrounding fluid on the particle is not included in F_i^{ext} . $\left(\frac{\partial f}{\partial t} \right)_c$ accounts for the changes in the particle velocity resulting from collisions. In the two-phase system under study, two types of collisions can occur [144]: (i) particle/particle collisions, and (ii) fluid molecules/particle collisions. Therefore,

$$\left(\frac{\partial f}{\partial t} \right)_c = \left(\frac{\partial f}{\partial t} \right)_c^{\text{H}} + \left(\frac{\partial f}{\partial t} \right)_c^{\text{S}} \quad (3.22)$$

The term representing collisions between solid particles, $\left(\frac{\partial f}{\partial t}\right)_c^H$, will be modelled using the assumption of binary encounters of inelastic hard spheres [106] and will, therefore, be called the *hard-sphere collisional term*. The contribution of collisions between solid particles and fluid molecules, represented by $\left(\frac{\partial f}{\partial t}\right)_c^S$, are computed using the Fokker-Planck collisional term [107, 110] and will be called the *soft collisional term*:

$$\left(\frac{\partial f}{\partial t}\right)_c^S = \frac{\partial}{\partial c_i} \left(-F_i^f f + \frac{\partial}{\partial c_j} (B_{ij} f) \right) \quad (3.23)$$

F_i^f is the force per unit mass of particle applied by the surrounding fluid on the particle:

$$F_i^f = \zeta_D (u_i^f - c_i) - \frac{1}{\rho^s} \frac{\partial p^f}{\partial x_i} \quad (3.24)$$

The first term of the Fokker-Planck collisional term represents the rate of change of $f(\vec{c}, \vec{x}, t)$ due to momentum transfer by F_i^f . The second term accounts for the rate of change of $f(\vec{c}, \vec{x}, t)$ due to energy transfer from the fluid to the solid phase and is expressed as a function of the specific kinetic energy transfer tensor, B_{ij} . Lun [107] has proven that the specific kinetic energy transfer tensor can be related to the force applied by the fluid on the particle. The form of the specific kinetic energy transfer tensor proposed by Lun and Savage [110] is used in this work:

$$B_{ij} = \left(1 - a_0 \alpha^{\frac{3}{2}}\right) \zeta_D T \delta_{ij} \quad (3.25)$$

where a_0 is a constant which depends on the phenomenon being considered. Based on a fluidized bed experiment, Lun and Savage [110] suggested $a_0 = 0.88$.

3.3.3 Macroscopic Equation

A macroscopic equation may be derived by multiplying the Boltzmann equation by the single-particle property ϕ and integrating over the velocity space. The resulting equation is called the equation of change of the single-particle property:

$$\frac{\partial}{\partial t} (n \langle \phi \rangle) + \frac{\partial}{\partial x_i} (n \langle \phi c_i \rangle) - n \left[\left\langle \frac{\partial \phi}{\partial t} \right\rangle + \left\langle c_i \frac{\partial \phi}{\partial x_i} \right\rangle + \left\langle F_i^{\text{ext}} \frac{\partial \phi}{\partial c_i} \right\rangle \right] = \Phi_c \quad (3.26)$$

Φ_c is the collisional rate of increase of $\langle \phi \rangle$ per unit volume of the mixture and can be split into hard-sphere collisional and soft collisional contributions. It is expressed as:

$$\Phi_c = \Phi_c^H + \Phi_c^S = \int_{\vec{c}} \phi \left(\frac{\partial f}{\partial t} \right)_c d\vec{c} \quad (3.27)$$

where

$$\Phi_c^H = \int_{\vec{c}} \phi \left(\frac{\partial f}{\partial t} \right)_c^H d\vec{c} \quad (3.28)$$

$$\Phi_c^S = \left\langle n F_i' \frac{\partial \phi}{\partial c_i} \right\rangle + \left\langle n B_{ij} \frac{\partial}{\partial c_i} \left(\frac{\partial \phi}{\partial c_j} \right) \right\rangle \quad (3.29)$$

3.3.4 Binary Encounter Dynamics

A more explicit expression for Φ_c^H is obtained by considering binary collisions between hard, smooth, but inelastic spherical particles of uniform diameter d . Lun et al. [106] found that the hard-sphere collisional term can be expressed as:

$$\Phi_c^H(\phi) = \mathcal{X}(\phi) - \frac{\partial \theta_i(\phi)}{\partial x_i} \quad (3.30)$$

where

$$\mathcal{X}(\phi) = \frac{d^2}{2} \int_{\vec{c}_{12} \cdot \vec{k} > 0} (\phi'_1 + \phi'_2 - \phi_1 - \phi_2) (\vec{c}_{12} \cdot \vec{k}) f(\vec{c}_1, \vec{x} - d\vec{k}, t) f(\vec{c}_2, \vec{x}, t) g_0 d\vec{k} d\vec{c}_1 d\vec{c}_2 \quad (3.31)$$

$$\theta_i(\phi) = -\frac{d^3}{2} \int_{\vec{c}_{12} \cdot \vec{k} > 0} (\phi'_1 - \phi_1) (\vec{c}_{12} \cdot \vec{k}) f(\vec{c}_1, \vec{x} - \frac{d}{2}\vec{k}, t) f(\vec{c}_2, \vec{x} + \frac{d}{2}\vec{k}, t) g_0 k_i d\vec{k} d\vec{c}_1 d\vec{c}_2 \quad (3.32)$$

These expressions were derived by considering two spherical particles, labelled 1 and 2, having velocity \vec{c}_1 and \vec{c}_2 prior to the collision. The velocities of the two particles after the collisions are represented by \vec{c}'_1 and \vec{c}'_2 . At the instant of the collision, the particle labelled 2 is located at \vec{x} and the particle labelled 1 is located at $\vec{x} - d\vec{k}$, where \vec{k} is the unit vector along the line of centres from O_1 to O_2 (Fig. 3.1). \vec{c}_{12} is the relative velocity of particle 1 with respect to particle 2. g_0 is the equilibrium radial distribution which takes into account the finite dimensions of the particles. ϕ_1 and ϕ_2 are the single-particle property of particle 1 and 2, respectively, *prior* to the collision and ϕ'_1 and ϕ'_2 are the single-particle property of particle 1 and 2, respectively, *after* the collision.

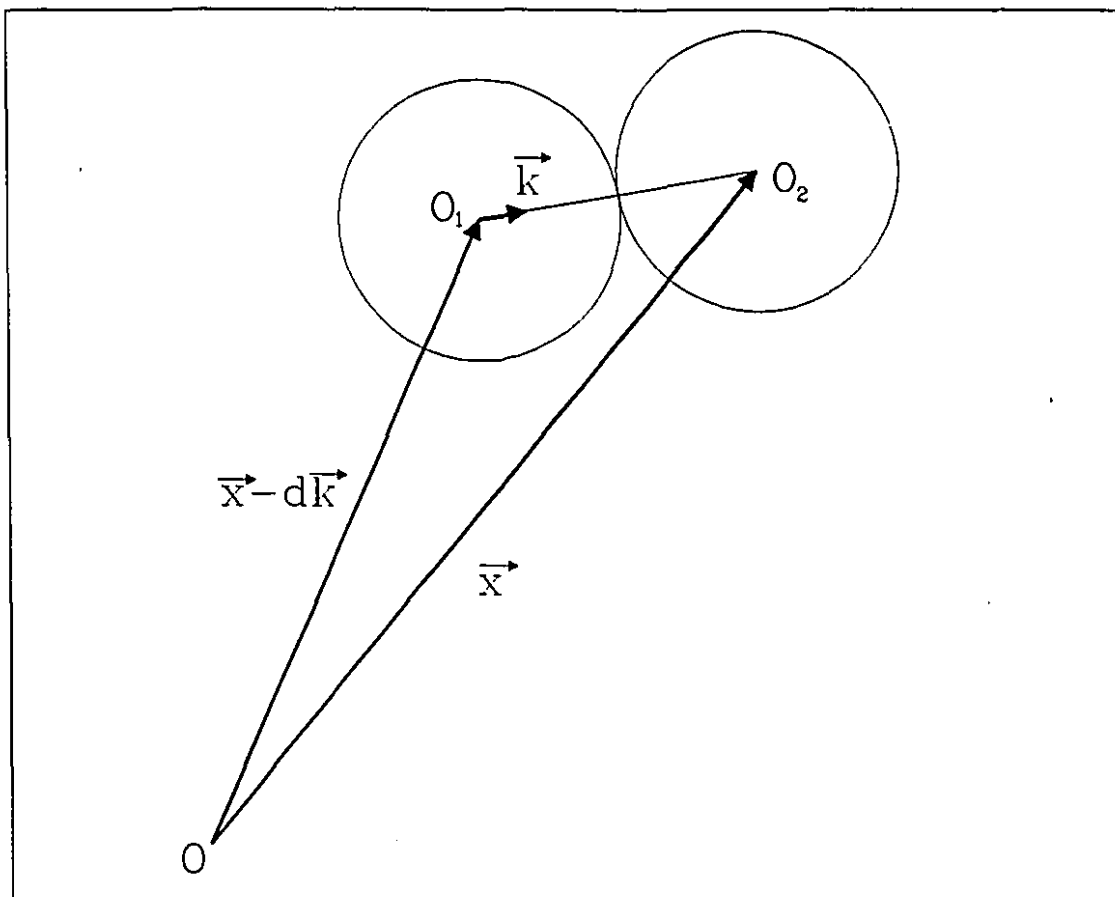


Figure 3.1: Binary collision

In order to evaluate these integrals, a relationship between the particle velocity prior to and after the collision is needed.

Elastic Particles

Using the principle of conservation of momentum, the following equation is obtained:

$$m^p \vec{c}_1 + m^p \vec{c}_2 = m^p \vec{c}'_1 + m^p \vec{c}'_2 \quad (3.33)$$

The mass of the system is $M = 2m^p$ and its velocity, called the centre of mass velocity, \vec{G} , is given by

$$\vec{G} = \frac{m^p \vec{c}_1 + m^p \vec{c}_2}{M} \quad (3.34)$$

From the momentum conservation principle, it follows that the centre-of-mass of the two particles moves uniformly throughout the encounter:

$$\vec{G} = \vec{G}' \quad (3.35)$$

This equation simply states that the centre-of-mass velocity prior to the collision is equal to the centre-of-mass velocity after the collision.

The relative velocities before and after the collision are, respectively:

$$\vec{c}_{12} = \vec{c}_1 - \vec{c}_2 \quad (3.36)$$

$$\vec{c}'_{12} = \vec{c}'_1 - \vec{c}'_2 \quad (3.37)$$

Using the definitions of the centre-of-mass velocity and relative velocity, it can be shown that:

$$\vec{c}_1 = \vec{G} + \frac{m^p}{M} \vec{c}_{12} \quad \vec{c}_2 = \vec{G} - \frac{m^p}{M} \vec{c}_{12} \quad (3.38)$$

$$\vec{c}'_1 = \vec{G}' + \frac{m^p}{M} \vec{c}'_{12} \quad \vec{c}'_2 = \vec{G}' - \frac{m^p}{M} \vec{c}'_{12} \quad (3.39)$$

The second conservation principle that applies in an elastic collision is the conservation of kinetic energy during the encounter:

$$\frac{1}{2} m^p \vec{c}_1 \cdot \vec{c}_1 + \frac{1}{2} m^p \vec{c}_2 \cdot \vec{c}_2 = \frac{1}{2} m^p \vec{c}'_1 \cdot \vec{c}'_1 + \frac{1}{2} m^p \vec{c}'_2 \cdot \vec{c}'_2 \quad (3.40)$$

Using Eqs.(3.38)-(3.39), one can obtain:

$$\frac{1}{2} m^p \vec{c}_1 \cdot \vec{c}_1 + \frac{1}{2} m^p \vec{c}_2 \cdot \vec{c}_2 = m^p \left[\vec{G} \cdot \vec{G} + \left(\frac{m^p}{M} \right)^2 \vec{c}_{12} \cdot \vec{c}_{12} \right] \quad (3.41)$$

$$\frac{1}{2} m^p \vec{c}'_1 \cdot \vec{c}'_1 + \frac{1}{2} m^p \vec{c}'_2 \cdot \vec{c}'_2 = m^p \left[\vec{G}' \cdot \vec{G}' + \left(\frac{m^p}{M} \right)^2 \vec{c}'_{12} \cdot \vec{c}'_{12} \right] \quad (3.42)$$

Since the centre-of-mass velocity is constant throughout the encounter, it follows that

$$\vec{c}_{12} \cdot \vec{c}_{12} = \vec{c}'_{12} \cdot \vec{c}'_{12} \quad (3.43)$$

This means that the relative velocity between the two particles is changed only in direction, and not in magnitude. If \vec{k} denotes the unit vector along the line of the centres of the *smooth spherical* particles at the instant of collision, then the relative velocity component normal to \vec{k} is not changed during the collision, and the relative velocity component in the direction of \vec{k} before and after the collision are equal but opposite in sign:

$$\vec{c}_{12} - \vec{c}'_{12} = (\vec{c}_{12} \cdot \vec{k})\vec{k} - (\vec{c}'_{12} \cdot \vec{k})\vec{k} \quad (3.44)$$

$$\vec{c}_{12} \cdot \vec{k} = -\vec{c}'_{12} \cdot \vec{k} \quad (3.45)$$

Therefore,

$$\vec{c}_{12} - \vec{c}'_{12} = 2(\vec{c}_{12} \cdot \vec{k})\vec{k} \quad (3.46)$$

and, finally, the following relations can be obtained:

$$\vec{c}'_1 = \vec{c}_1 - (\vec{c}_{12} \cdot \vec{k})\vec{k} \quad (3.47)$$

$$\vec{c}'_2 = \vec{c}_2 + (\vec{c}_{12} \cdot \vec{k})\vec{k} \quad (3.48)$$

Inelastic Particles

In the case of inelastic particles, a coefficient of restitution e is defined such that:

$$\vec{c}'_{12} \cdot \vec{k} = -e(\vec{c}_{12} \cdot \vec{k}) \quad (3.49)$$

Therefore,

$$\vec{c}_{12} - \vec{c}'_{12} = (1 + e)(\vec{c}_{12} \cdot \vec{k})\vec{k} \quad (3.50)$$

and the following relations can be obtained:

$$\vec{c}'_1 = \vec{c}_1 - \frac{1 + e}{2}(\vec{c}_{12} \cdot \vec{k})\vec{k} \quad (3.51)$$

$$\vec{c}'_2 = \vec{c}_2 + \frac{1 + e}{2}(\vec{c}_{12} \cdot \vec{k})\vec{k} \quad (3.52)$$

3.3.5 Hydrodynamic Equations

The hydrodynamic equations of the solid phase are obtained from the general macroscopic equation, Eq. (3.26), by assigning specific interpretations of the single-particle property, ϕ . The solid-phase continuity, momentum and fluctuating kinetic energy equations are obtained by setting $\phi = m^p$, $\phi = m^p c_i$, and $\phi = \frac{1}{2} m^p c_i^2$, respectively. The resulting hydrodynamic equations can be expressed as [107, 110]:

Continuity Equation

$$\frac{\partial}{\partial t} (\alpha \rho^s) + \frac{\partial}{\partial x_i} (\alpha \rho^s u_i^s) = 0 \quad (3.53)$$

Momentum Equation

$$\frac{\partial}{\partial t} (\alpha \rho^s u_j^s) + \frac{\partial}{\partial x_i} (\alpha \rho^s u_i^s u_j^s) = \frac{\partial \sigma_{ij}^s}{\partial x_i} + \alpha \rho^s \langle F_j^f \rangle + \alpha \rho^s F_j^{\text{ext}} \quad (3.54)$$

Fluctuating Kinetic Energy Equation

$$\frac{3}{2} \left[\frac{\partial}{\partial t} (\alpha \rho^s T) + \frac{\partial}{\partial x_i} (\alpha \rho^s u_i^s T) \right] = \sigma_{ij}^s \frac{\partial u_j^s}{\partial x_i} - \frac{\partial q_i^s}{\partial x_i} - \gamma_c + \alpha \rho^s \langle F_i^f C_i \rangle + \alpha \rho^s \langle B_{ij} \delta_{ij} \rangle \quad (3.55)$$

where

$$\sigma_{ij}^s = -\theta_i (m^p C_j) - \alpha \rho^s \langle C_i C_j \rangle \quad (3.56)$$

$$q_i^s = \theta_i \left(\frac{1}{2} m^p C_j^2 \right) + \alpha \rho^s \frac{1}{2} \langle C_i C_j^2 \rangle \quad (3.57)$$

$$\gamma_c = -\mathcal{X} \left(\frac{1}{2} m^p c_i^2 \right) \quad (3.58)$$

σ_{ij}^s is the solid-phase stress tensor. The first term in Eq.(3.56) is the collisional contribution, and the term involving the ensemble average represents the kinetic contribution. The two last terms of the momentum equation, Eq.(3.54), represent the forces due to fluid-solid interactions and body forces, such as the gravity, respectively. The first term on the right-hand side of the fluctuating kinetic energy equation is the work done by the solid-phase stress tensor. In Eqs. (3.55) and (3.57), q_i^s is the solid-phase fluctuating kinetic energy flux vector. Similarly to the solid-phase stress tensor, it is composed of a collisional and kinetic part. γ_c is the solid-phase fluctuating kinetic energy dissipation due to inelastic particle/particle collisions. In Eq. (3.55), $\alpha \rho^s \langle F_i^f C_i \rangle$ is the energy dissipation due to the fluid-solid interaction forces. Finally, the last term on the right-hand side of Eq. (3.55) represents the transfer of energy from the fluid to the solid phases during the soft collisions.

3.3.6 Velocity Distribution Function

Explicit expressions of the solid-phase stress tensor, fluctuating kinetic energy flux vector, dissipation rate of fluctuating kinetic energy, and the various ensemble average terms appearing in the hydrodynamic equations can be obtained once the velocity distribution function $f(\vec{c}, \vec{x}, t)$ is known. The velocity distribution function is obtained by solving the Boltzmann equation. Lun [107] has assumed the following functional form for $f(\vec{c}, \vec{x}, t)$:

$$f(\vec{c}, \vec{x}, t) = f^\circ (1 + \psi) \quad (3.59)$$

where

$$f^\circ = \frac{n}{(2\pi T)^{\frac{3}{2}}} \exp\left(-\frac{C_i^2}{2T}\right) \quad (3.60)$$

$$\psi = a_1 \left[\left(C_i C_j - \frac{1}{3} C_k^2 \delta_{ij} \right) \frac{\partial u_j^s}{\partial x_i} \right] + \left[\frac{5}{2} - \frac{C_k^2}{2T} \right] \left[a_2 \left(C_i \frac{\partial}{\partial x_i} (\ln T) \right) + a_3 \left(C_i \frac{\partial}{\partial x_i} (\ln n) \right) \right] \quad (3.61)$$

f° is the Maxwellian velocity distribution function which describes local equilibrium conditions. When this assumed form of $f(\vec{c}, \vec{x}, t)$ is substituted into the Boltzmann equation, it is found that no choice of a_1 , a_2 and a_3 will exactly satisfy the equation for *all* values of \vec{c} . Nevertheless, as discussed by Lun [107], the assumed functional form of $f(\vec{c}, \vec{x}, t)$ will be appropriate if an optimum choice of a_1 , a_2 and a_3 is made. One systematic way of making this choice is to replace the task of satisfying the Boltzmann equation by the weaker requirement of satisfying the macroscopic equation, Eq. (3.26). This equation has been integrated over \vec{c} and is, therefore, independent of \vec{c} . By choosing a set of three single-particle properties, ϕ_1 , ϕ_2 , and ϕ_3 , and trying to satisfy the resulting set of three equations, a system of three equations and three unknowns is obtained. This method, called the moment method, has been used by Lun [107] to obtain the following expressions for a_1 , a_2 and a_3 :

$$a_1 = -\frac{\mu^{s*}}{\alpha \rho^s g_0 T^2} \left[1 + \frac{8}{5} \eta (3\eta - 2) \alpha g_0 \right] \quad (3.62)$$

$$a_2 = -\frac{2k^{s*}}{5\alpha \rho^s g_0 T} \left[1 + \frac{12}{5} \eta^2 (4\eta - 3) \alpha g_0 \right] \quad (3.63)$$

$$a_3 = -\frac{24k^{s*}}{25\alpha \rho^s g_0 T} (2\eta - 1)(\eta - 1) \frac{d}{d\alpha} (\alpha^2 g_0) \quad (3.64)$$

where

$$\mu^{s*} = \frac{\mu^{s'}}{1 + \frac{2\zeta_D \mu^{s'}}{\alpha \rho^s g_0 T}} \quad \mu^{s'} = \frac{\mu^s}{\eta(2 - \eta)} \quad \mu^s = \frac{5m^p \left(\frac{T}{\pi}\right)^{\frac{1}{2}}}{16d^2} \quad (3.65)$$

$$k^{s*} = \frac{k^{s'}}{1 + \frac{6\zeta_D k^{s'}}{5\alpha\rho^s g_0 T}} \quad k^{s'} = \frac{8k^s}{\eta(41 - 33\eta)} \quad k^s = \frac{75m^p \left(\frac{T}{\pi}\right)^{\frac{1}{2}}}{64d^2} \quad (3.66)$$

$$\eta = \frac{1 + e}{2} \quad (3.67)$$

The evaluations of the various collisional integrals and ensemble averages appearing in Eqs. (3.53)-(3.58) involve a large amount of mathematical operations. Sufficient information to evaluate the various collisional integrals and ensemble averages is available in Chapman and Cowling [31, Chapters 1 and 16]. Therefore, only the results are presented in Appendix A.

3.4 Solid-Phase Boundary Conditions

The complete physical description of the solid phase requires the prescription of suitable boundary conditions. In many practical internal flow problems, the boundaries of a domain of interest consist primarily of inflow/outflow boundaries and walls. At inflow boundaries, usually all quantities of interest, such as solid-phase concentration, velocity and granular temperature, are specified. Outflow boundaries are most often situated in a region of the flow where the downstream influence is negligible, thereby allowing the assumption of negligible transport by diffusion normal to the boundary. At walls, special treatments are needed since the particles interact with the wall through inelastic collisions. During the collision of a particle with a wall, the particle kinetic energy is lost through inelastic deformation. When the wall surface is rough, there is a transfer of lateral momentum from the particle to the wall. Microscopically, in the Lagrangian formulation, the treatment of the wall is realized through a collision model between a single particle and the wall. This formulation introduces empirical parameters, such as the wall coefficient of restitution, which lead to the prescription of the particle velocity after collision as a function of the particle velocity prior to the collision. Macroscopically, in the Eulerian formulation, the wall treatment is expressed through the prescription of appropriate solid-phase shear stress and fluctuating kinetic energy flux at this boundary. Several proposals for the estimation of solid-phase wall shear stress and fluctuating kinetic energy flux can be found in the literature [88, 95]. For particles that are of small or comparable size with respect to the wall roughness, Hui et al. [88] have proven that the prescription of no-slip condition and zero granular temperature at walls is a good

approximation. The prescription of appropriate boundary conditions depends on the problem of interest and, therefore, more explicit descriptions are delayed until Chapters 5, 6, and 7 where the results of some specific applications are presented.

3.5 Fluid-Phase Governing Equations

The motion of a Newtonian fluid phase is governed by the Navier-Stokes equations, which must be satisfied at each point of the continuous phase: appropriate boundary conditions at the domain boundaries and the interface between the particles and the fluid phase complete the description of the mathematical model. For large number of particles, the exact topology is far too complex to allow modelling based on such an exact local formulation. To simplify the description, point variables which vary rapidly on the scale of the particle spacing are averaged over regions that are large compared with this spacing but small compared with the domain of interest. The resulting average equations describe the fluid and solid phases as two interpenetrating continua.

In this section, the fluid-phase point dependent variables, the velocities u^f, v^f and the pressure p^f , are replaced by appropriate mean variables, obtained by averaging over volumes containing a large number of particles. However, these volumes are small in comparison with the macroscopic scale. The resulting mean variables are assumed to be smooth functions of position and time, and are considered to be defined at all points of the domain of interest. This procedure is called volume averaging, and several variants can be found in the literature [5, 35, 48, 89, 94, 124, 172].

Let \mathcal{V}^T denote a volume around a specific point in space such that it contains a large amount of particles, but has a characteristic dimension small with respect to the characteristic dimension of the macroscopic flow. \mathcal{V}^f and \mathcal{V}^s are the parts of \mathcal{V}^T occupied by the fluid and solid phase, respectively. The fluid- and solid-phase volume concentrations are defined by

$$\epsilon = \frac{\mathcal{V}^f}{\mathcal{V}^T} \quad \alpha = \frac{\mathcal{V}^s}{\mathcal{V}^T} \quad (3.68)$$

If ϕ^f is a fluid-phase point dependent variable, the fluid-phase *intrinsic* volume

average variable, ϕ , is defined by [94]:

$$\epsilon\phi = \frac{1}{\mathcal{V}^T} \int_{\mathcal{V}^f} \phi' d\mathcal{V} \quad (3.69)$$

A similar expression can be defined for the solid-phase intrinsic volume average. During such a volume averaging of the fluid-phase point governing equations, the local volume averages of space and time derivatives are encountered frequently. Therefore, it is useful to introduced the theorems for local volume averages of a space and of a time derivative of a scalar variable associated with a dispersed flow [94]:

$$\frac{1}{\mathcal{V}^T} \int_{\mathcal{V}^f} \frac{\partial \phi'}{\partial t} d\mathcal{V} = \frac{\partial}{\partial t} (\epsilon\phi) + \frac{1}{\mathcal{V}^T} \int_{\mathcal{S}^{\text{int}}} \phi' u_i^{\text{int}} n_i^{\text{int}} d\mathcal{S} \quad (3.70)$$

$$\frac{1}{\mathcal{V}^T} \int_{\mathcal{V}^f} \frac{\partial \phi'}{\partial x_i} d\mathcal{V} = \frac{\partial}{\partial x_i} (\epsilon\phi) - \frac{1}{\mathcal{V}^T} \int_{\mathcal{S}^{\text{int}}} \phi' n_i^{\text{int}} d\mathcal{S} \quad (3.71)$$

where \mathcal{S}^{int} is the union of the interface surfaces in \mathcal{V}^T ; n_i^{int} is the i -component of the unit normal vector to the interface pointing into the fluid phase; and u_i^{int} is the i -component of the velocity of the interface.

3.5.1 Local Volume Average of the Fluid-Phase Continuity Equation

The fluid-phase point continuity equation is given by:

$$\frac{\partial}{\partial t} (\rho^f) + \frac{\partial}{\partial x_i} (\rho^f u_i^f) = 0 \quad (3.72)$$

Integrating this equation over \mathcal{V}^f and dividing by \mathcal{V}^T yields

$$\frac{1}{\mathcal{V}^T} \int_{\mathcal{V}^f} \frac{\partial}{\partial t} (\rho^f) d\mathcal{V} + \frac{1}{\mathcal{V}^T} \int_{\mathcal{V}^f} \frac{\partial}{\partial x_i} (\rho^f u_i^f) d\mathcal{V} = 0 \quad (3.73)$$

Using Eq. (3.70) with $\phi' = \rho^f$ and Eq. (3.71) with $\phi' = \rho^f u_i^f$, the following equation is obtained:

$$\frac{\partial}{\partial t} (\epsilon\rho^f) + \frac{\partial}{\partial x_i} (\epsilon\rho^f u_i^f) + \frac{1}{\mathcal{V}^T} \int_{\mathcal{S}^{\text{int}}} \rho^f u_i^{\text{int}} n_i^{\text{int}} d\mathcal{S} - \frac{1}{\mathcal{V}^T} \int_{\mathcal{S}^{\text{int}}} \rho^f u_i^f n_i^{\text{int}} d\mathcal{S} = 0 \quad (3.74)$$

In the problems of interest in this work, there is no change of phase or chemical reaction, and the particles have impermeable boundary, therefore, at the particle surfaces, $u_i^{\text{int}} n_i^{\text{int}} = u_i^{f'} n_i^{\text{int}}$. Thus, the local volume average continuity equation is simply:

$$\frac{\partial}{\partial t} (\epsilon \rho^f) + \frac{\partial}{\partial x_i} (\epsilon \rho^f u_i^f) = 0 \quad (3.75)$$

3.5.2 Local Volume Average of the Fluid-Phase Momentum Equation

The fluid-phase point momentum equation is given by:

$$\frac{\partial}{\partial t} (\rho^f u_j^{f'}) + \frac{\partial}{\partial x_i} (\rho^f u_i^{f'} u_j^{f'}) = \frac{\partial \sigma_{ij}^{f'}}{\partial x_i} + \rho^f g_j \quad (3.76)$$

$\sigma_{ij}^{f'}$ is the point fluid-phase surface stress tensor. Integrating this equation over \mathcal{V}^f and dividing by \mathcal{V}^T yields

$$\frac{1}{\mathcal{V}^T} \left[\int_{\mathcal{V}^f} \frac{\partial}{\partial t} (\rho^f u_j^{f'}) d\mathcal{V} + \int_{\mathcal{V}^f} \frac{\partial}{\partial x_i} (\rho^f u_i^{f'} u_j^{f'}) d\mathcal{V} \right] = \frac{1}{\mathcal{V}^T} \left[\int_{\mathcal{V}^f} \frac{\partial \sigma_{ij}^{f'}}{\partial x_i} d\mathcal{V} + \int_{\mathcal{V}^f} \rho^f g_j d\mathcal{V} \right] \quad (3.77)$$

Using Eq. (3.70) with $\phi' = \rho^f u_j^{f'}$ and Eq. (3.71) with $\phi' = \rho^f u_i^{f'} u_j^{f'}$, the left-hand side of the previous equation can be expressed as:

$$\frac{\partial}{\partial t} (\epsilon \rho^f u_j^f) + \frac{\partial}{\partial x_i} \left(\frac{1}{\mathcal{V}^T} \int_{\mathcal{V}^f} \rho^f u_i^{f'} u_j^{f'} d\mathcal{V} \right) + \frac{1}{\mathcal{V}^T} \int_{S^{\text{int}}} \rho^f u_j^{f'} (u_i^{\text{int}} - u_i^{f'}) n_i^{\text{int}} dS \quad (3.78)$$

Again, in the problems considered here, $u_i^{\text{int}} n_i^{\text{int}} = u_i^{f'} n_i^{\text{int}}$, so the left-hand side simplifies to:

$$\frac{\partial}{\partial t} (\epsilon \rho^f u_j^f) + \frac{\partial}{\partial x_i} \left(\frac{1}{\mathcal{V}^T} \int_{\mathcal{V}^f} \rho^f u_i^{f'} u_j^{f'} d\mathcal{V} \right) \quad (3.79)$$

The fluid-phase point velocity $u_i^{f'}$ can be expressed as the sum of the intrinsic volume average of the fluid-phase velocity u_i^f and a fluctuating component $u_i^{f''}$. Therefore

$$\begin{aligned} \frac{\partial}{\partial x_i} \left(\frac{1}{\mathcal{V}^T} \int_{\mathcal{V}^f} \rho^f u_i^{f'} u_j^{f'} d\mathcal{V} \right) &= \frac{\partial}{\partial x_i} \left(\frac{1}{\mathcal{V}^T} \int_{\mathcal{V}^f} \rho^f u_i^f u_j^f d\mathcal{V} \right) + \frac{\partial}{\partial x_i} \left(\frac{1}{\mathcal{V}^T} \int_{\mathcal{V}^f} \rho^f u_i^{f''} u_j^{f''} d\mathcal{V} \right) \\ &\quad + \frac{\partial}{\partial x_i} \left(\frac{1}{\mathcal{V}^T} \int_{\mathcal{V}^f} \rho^f (u_i^f u_j^{f''} + u_j^f u_i^{f''}) d\mathcal{V} \right) \end{aligned} \quad (3.80)$$

u_i^f , the intrinsic volume average, varies little within \mathcal{V}^f [5], so it can be taken out of the volume integrals. Therefore

$$\begin{aligned} \frac{\partial}{\partial x_i} \left(\frac{1}{\mathcal{V}^T} \int_{\mathcal{V}^f} \rho^f u_i^{f'} u_j^{f'} d\mathcal{V} \right) &= \frac{\partial}{\partial x_i} (\epsilon \rho^f u_i^f u_j^f) + \frac{\partial \sigma_{ij}^{f''}}{\partial x_i} + \frac{\partial}{\partial x_i} \left(\frac{u_i^f}{\mathcal{V}^T} \int_{\mathcal{V}^f} \rho^f u_j^{f''} d\mathcal{V} \right) \\ &+ \frac{\partial}{\partial x_i} \left(\frac{u_j^f}{\mathcal{V}^T} \int_{\mathcal{V}^f} \rho^f u_i^{f''} d\mathcal{V} \right) \end{aligned} \quad (3.81)$$

where

$$\sigma_{ij}^{f'''} = \frac{1}{\mathcal{V}^T} \int_{\mathcal{V}^f} \rho^f u_i^{f''} u_j^{f''} d\mathcal{V} \quad (3.82)$$

As discussed by Anderson and Jackson [5], the third and fourth terms of the right-hand side of Eq. (3.81) involve integration of the fluctuation and are negligibly small. Therefore, the left-hand side of the local volume average momentum equation is

$$\frac{\partial}{\partial t} (\epsilon \rho^f u_j^f) + \frac{\partial}{\partial x_i} (\epsilon \rho^f u_i^f u_j^f) + \frac{\partial \sigma_{ij}^{f''}}{\partial x_i} \quad (3.83)$$

The right hand-side of the local volume average momentum equation (Eq. (3.77)) is composed of two terms. The first term involves the fluid-phase stress tensor and the second term represents the effect of gravity. The gravity term can be easily integrated and is given by:

$$\frac{1}{\mathcal{V}^T} \int_{\mathcal{V}^f} \rho^f g_j d\mathcal{V} = \epsilon \rho^f g_j \quad (3.84)$$

Using Eq. (3.71) with $\phi' = \sigma_{ij}^{f'}$, the stress-tensor term is given by

$$\frac{1}{\mathcal{V}^T} \int_{\mathcal{V}^f} \frac{\partial \sigma_{ij}^{f'}}{\partial x_i} d\mathcal{V} = \frac{\partial}{\partial x_i} (\epsilon \sigma_{ij}^{f'}) - \frac{1}{\mathcal{V}^T} \int_{\mathcal{S}^{\text{int}}} \sigma_{ij}^{f'} n_i^{\text{int}} d\mathcal{S} \quad (3.85)$$

Neglecting the contribution of incomplete (only portions of, not whole) particles lying in \mathcal{V}^T , the interface can be expressed as the sum of the surface of the complete particles within \mathcal{V}^T . Therefore:

$$\frac{1}{\mathcal{V}^T} \int_{\mathcal{S}^{\text{int}}} \sigma_{ij}^{f'} n_i^{\text{int}} d\mathcal{S} = \frac{1}{\mathcal{V}^T} \sum_p \int_{\mathcal{S}_p} \sigma_{ij}^{f'} n_i^{\text{int}} d\mathcal{S} \quad (3.86)$$

where \mathcal{S}^p is the surface of a single particle; and \sum_p means a summation over all the complete particles within the volume \mathcal{V}^T . The surface integral involving the fluid-phase local stress tensor can be related to the aerodynamic force $m^p F_j^f$ applied to a single particle [5] where m^p is the mass of a single particle. The aerodynamic force applied on a particle comes from the fluid stresses at the particle surface:

$$m^p F_j^f = \int_{\mathcal{S}^p} \sigma_{ij}^f n_i^{\text{int}} d\mathcal{S} \quad (3.87)$$

Summing over all particles in \mathcal{V}^T yields

$$\frac{1}{\mathcal{V}^T} \sum_p \int_{\mathcal{S}^p} \sigma_{ij}^f n_i^{\text{int}} d\mathcal{S} = \frac{m^p}{\mathcal{V}^T} \sum_p F_j^f \quad (3.88)$$

The stress-tensor term is, therefore, given by:

$$\frac{1}{\mathcal{V}^T} \int_{\mathcal{V}^T} \frac{\partial \sigma_{ij}^f}{\partial x_i} d\mathcal{V} = \frac{\partial}{\partial x_i} (\epsilon \sigma_{ij}^f) - \frac{m^p}{\mathcal{V}^T} \sum_p F_j^f \quad (3.89)$$

$\frac{m^p}{\mathcal{V}^T} \sum_p F_j^f$ represents the rate of momentum transfer between the fluid and solid phases. An equivalent term can be found in the solid-phase momentum equation (Eq. (3.54)), and it should be noted that

$$\frac{m^p}{\mathcal{V}^T} \sum_p F_j^f = \alpha \rho^s \langle F_j^f \rangle \quad (3.90)$$

This equation is equivalent to the local volume average of the force balance at the interface [94]. The following local volume average fluid-phase momentum equation can be readily derived from the various expressions given so far in this section:

$$\frac{\partial}{\partial t} (\epsilon \rho^f u_j^f) + \frac{\partial}{\partial x_i} (\epsilon \rho^f u_i^f u_j^f) = \frac{\partial}{\partial x_i} (\epsilon \sigma_{ij}^f) - \frac{\partial \sigma_{ij}^f}{\partial x_i} - \alpha \rho^s \langle F_j^f \rangle + \epsilon \rho^f g_j \quad (3.91)$$

$\epsilon \sigma_{ij}^f$ is the local volume average Newtonian fluid stress tensor. Jiang et al. [94] have derived an expression for the local volume average of the Newtonian fluid stress tensor based on an idealized model for the flow within the averaging volume \mathcal{V}^T . This model yields a resulting system of 18 equations with 18 unknowns, which is a

very large system to solve even in two dimensions. Furthermore, the model proposed by Jiang et al. [94] is limited to dilute concentration. Following the proposals of Anderson and Jackson [5] and Lun and Savage [110], in the proposed mathematical model, the local volume average Newtonian fluid stress is assumed to be given in terms of the intrinsic fluid variables, by an expression similar to that for the single-phase Newtonian stress tensor:

$$\epsilon \sigma_{ij}^f = -p^f \delta_{ij} + \left(\mu_b^f - \frac{2}{3} \mu_a^f \right) \frac{\partial u_k^f}{\partial x_k} \delta_{ij} + \mu_a^f \left(\frac{\partial u_i^f}{\partial x_j} + \frac{\partial u_j^f}{\partial x_i} \right) \quad (3.92)$$

where p^f is the intrinsic volume average fluid-phase pressure, μ_a^f is the apparent fluid-phase viscosity, and μ_b^f is the apparent fluid-phase bulk viscosity.

$\sigma_{ij}^{f''}$ is analogous to the to the subgrid-scale Reynolds stress tensor, which is used to simulate the drainage of energy from the large-scale motions due to the small-scale ones in the volume-average descriptions of turbulent flows [5]. Therefore, it seems reasonable to use approximations similar to those used in the Smagorinsky model developed in the context of Large Eddy Simulations (LES) [66]:

$$\sigma_{ij}^{f''} = -\rho^f (C_s \Delta)^2 S \left(\frac{\partial u_i^f}{\partial x_j} + \frac{\partial u_j^f}{\partial x_i} - \frac{2}{3} \frac{\partial u_k^f}{\partial x_k} \delta_{ij} \right) \quad (3.93)$$

where C_s lies between 0.1 (for coarse grid) and 0.2 (for fine grid) [132]; Δ is a linear measure of the grid size; and

$$S = \left[\frac{1}{2} \left(\frac{\partial u_i^f}{\partial x_j} + \frac{\partial u_j^f}{\partial x_i} - \frac{2}{3} \frac{\partial u_k^f}{\partial x_k} \delta_{ij} \right) \left(\frac{\partial u_i^f}{\partial x_j} + \frac{\partial u_j^f}{\partial x_i} - \frac{2}{3} \frac{\partial u_k^f}{\partial x_k} \delta_{ij} \right) \right]^{\frac{1}{2}} \quad (3.94)$$

3.6 Fluid-Phase Boundary Conditions

The fluid phase is composed of molecules which are much smaller than the macroscopic length scale. Therefore, it is appropriate to assume no slip of the velocity at walls for the fluid phase. However, some researchers [95, 165] argue that since the fluid-phase velocity that appears in the governing equations is a volume-average

velocity, the no-slip condition is not strictly valid, and, therefore, an appropriate condition on stress at the wall has to be evaluated. Johnson and Jackson [95] have proposed an approximation of the fluid-phase stress at walls. Their derivation is ad-hoc and there is no evidence of whether it is more appropriate to use the simple no-slip condition or their evaluation of the fluid-phase wall stress. Therefore, the simple no-slip condition at walls is used in most of the calculations presented in Chapters 5, 6 and 7.

3.7 Two-Dimensional Axisymmetric Gas-Solid Particle Flows: Summary

This section presents the governing and constitutive equations, obtained using the theory described in this chapter, for two-dimensional axisymmetric gas-solid particle flows. Finally, several specializations of the general mathematical model are given.

3.7.1 Governing Equations

Solid Phase

Continuity Equation

$$\frac{\partial}{\partial t}(\alpha\rho^s) + \frac{\partial}{\partial z}(\alpha\rho^s u^s) + \frac{1}{r} \frac{\partial}{\partial r}(r\alpha\rho^s v^s) = 0 \quad (3.95)$$

z-Momentum Equation

$$\begin{aligned} \frac{\partial}{\partial t}(\alpha\rho^s u^s) + \frac{\partial}{\partial z}(\alpha\rho^s u^s u^s) + \frac{1}{r} \frac{\partial}{\partial r}(r\alpha\rho^s v^s u^s) = & -\alpha \frac{\partial p^f}{\partial z} + \alpha\rho^s \zeta_D (u^f - u^s) + S_z^s \\ & + \frac{\partial}{\partial z} \left(\mu_c^s \frac{\partial u^s}{\partial z} \right) + \frac{1}{r} \frac{\partial}{\partial r} \left(r\mu_c^s \frac{\partial u^s}{\partial r} \right) - \frac{\partial p^s}{\partial z} \\ & + \frac{\partial}{\partial z} \left(\mu_c^s \frac{\partial u^s}{\partial z} \right) + \frac{1}{r} \frac{\partial}{\partial r} \left(r\mu_c^s \frac{\partial v^s}{\partial z} \right) \\ & + \frac{\partial}{\partial z} \left(\left(\mu_b^s - \frac{2}{3}\mu_c^s \right) \left(\frac{\partial u^s}{\partial z} + \frac{1}{r} \frac{\partial}{\partial r}(rv^s) \right) \right) \end{aligned} \quad (3.96)$$

r-Momentum Equation

$$\frac{\partial}{\partial t}(\alpha\rho^s v^s) + \frac{\partial}{\partial z}(\alpha\rho^s u^s v^s) + \frac{1}{r} \frac{\partial}{\partial r}(r\alpha\rho^s v^s v^s) = -\alpha \frac{\partial p^f}{\partial r} + \alpha\rho^s \zeta_D (v^f - v^s) + S_r^s$$

$$\begin{aligned}
& + \frac{\partial}{\partial z} \left(\mu_c^s \frac{\partial v^s}{\partial z} \right) + \frac{1}{r} \frac{\partial}{\partial r} \left(r \mu_c^s \frac{\partial v^s}{\partial r} \right) - \mu_c^s \frac{v^s}{r^2} - \frac{\partial p^s}{\partial r} \\
& + \frac{\partial}{\partial z} \left(\mu_c^s \frac{\partial u^s}{\partial r} \right) + \frac{1}{r} \frac{\partial}{\partial r} \left(r \mu_c^s \frac{\partial v^s}{\partial r} \right) - \mu_c^s \frac{v^s}{r^2} \\
& + \frac{\partial}{\partial r} \left(\left(\mu_b^s - \frac{2}{3} \mu_c^s \right) \left(\frac{\partial u^s}{\partial z} + \frac{1}{r} \frac{\partial}{\partial r} (r v^s) \right) \right) \quad (3.97)
\end{aligned}$$

Fluctuating Kinetic Energy Equation

$$\begin{aligned}
\frac{3}{2} \left[\frac{\partial}{\partial t} (\alpha \rho^s T) + \frac{\partial}{\partial z} (\alpha \rho^s u^s T) + \frac{1}{r} \frac{\partial}{\partial r} (r \alpha \rho^s v^s T) \right] &= -p^s \left(\frac{\partial u^s}{\partial z} + \frac{1}{r} \frac{\partial}{\partial r} (r v^s) \right) + S_T^s \\
& + \frac{\partial}{\partial z} \left(k_T^s \frac{\partial T}{\partial z} \right) + \frac{1}{r} \frac{\partial}{\partial r} \left(r k_T^s \frac{\partial T}{\partial r} \right) + \frac{\partial}{\partial z} \left(k_\alpha^s \frac{\partial \alpha}{\partial z} \right) + \frac{1}{r} \frac{\partial}{\partial r} \left(r k_\alpha^s \frac{\partial \alpha}{\partial r} \right) \\
& + \Phi^s - \gamma_c - \gamma_D + \gamma_B \quad (3.98)
\end{aligned}$$

Fluid Phase

Continuity Equation

$$\frac{\partial}{\partial t} (\epsilon \rho^f) + \frac{\partial}{\partial z} (\epsilon \rho^f u^f) + \frac{1}{r} \frac{\partial}{\partial r} (r \epsilon \rho^f v^f) = 0 \quad (3.99)$$

z-Momentum Equation

$$\begin{aligned}
\frac{\partial}{\partial t} (\epsilon \rho^f u^f) + \frac{\partial}{\partial z} (\epsilon \rho^f u^f u^f) + \frac{1}{r} \frac{\partial}{\partial r} (r \epsilon \rho^f v^f u^f) &= -\epsilon \frac{\partial p^f}{\partial z} - \alpha \rho^s \zeta_D (u^f - u^s) + S_z^f \\
& + \frac{\partial}{\partial z} \left(\mu_c^f \frac{\partial u^f}{\partial z} \right) + \frac{1}{r} \frac{\partial}{\partial r} \left(r \mu_c^f \frac{\partial u^f}{\partial r} \right) \\
& + \frac{\partial}{\partial z} \left(\mu_c^f \frac{\partial u^f}{\partial z} \right) + \frac{1}{r} \frac{\partial}{\partial r} \left(r \mu_c^f \frac{\partial v^f}{\partial z} \right) \\
& + \frac{\partial}{\partial z} \left(\left(\mu_b^f - \frac{2}{3} \mu_c^f \right) \left(\frac{\partial u^f}{\partial z} + \frac{1}{r} \frac{\partial}{\partial r} (r v^f) \right) \right) \quad (3.100)
\end{aligned}$$

r-Momentum Equation

$$\begin{aligned}
\frac{\partial}{\partial t} (\epsilon \rho^f v^f) + \frac{\partial}{\partial z} (\epsilon \rho^f u^f v^f) + \frac{1}{r} \frac{\partial}{\partial r} (r \epsilon \rho^f v^f v^f) &= -\epsilon \frac{\partial p^f}{\partial r} - \alpha \rho^s \zeta_D (v^f - v^s) + S_r^f \\
& + \frac{\partial}{\partial z} \left(\mu_c^f \frac{\partial v^f}{\partial z} \right) + \frac{1}{r} \frac{\partial}{\partial r} \left(r \mu_c^f \frac{\partial v^f}{\partial r} \right) - \mu_c^f \frac{v^f}{r^2} \\
& + \frac{\partial}{\partial z} \left(\mu_c^f \frac{\partial u^f}{\partial r} \right) + \frac{1}{r} \frac{\partial}{\partial r} \left(r \mu_c^f \frac{\partial v^f}{\partial r} \right) - \mu_c^f \frac{v^f}{r^2} \\
& + \frac{\partial}{\partial r} \left(\left(\mu_b^f - \frac{2}{3} \mu_c^f \right) \left(\frac{\partial u^f}{\partial z} + \frac{1}{r} \frac{\partial}{\partial r} (r v^f) \right) \right) \quad (3.101)
\end{aligned}$$

These equations have been written in a form that is similar to that of the Navier-Stokes equations of a single-phase Newtonian fluid. Additional comments are needed on the form of the viscous stresses. The viscous stresses are divided into two parts, which will be called the diffusion term and the pseudo-diffusion term. In the solid-phase z-momentum equation, for example, the diffusion term is given by:

$$\frac{\partial}{\partial z} \left(\mu_e^s \frac{\partial u^s}{\partial z} \right) + \frac{1}{r} \frac{\partial}{\partial r} \left(r \mu_e^s \frac{\partial u^s}{\partial r} \right) \quad (3.102)$$

the pseudo-diffusion term is given by:

$$\frac{\partial}{\partial z} \left(\mu_e^s \frac{\partial u^s}{\partial z} \right) + \frac{1}{r} \frac{\partial}{\partial r} \left(r \mu_e^s \frac{\partial v^s}{\partial z} \right) + \frac{\partial}{\partial z} \left(\left(\mu_b^s - \frac{2}{3} \mu_e^s \right) \left(\frac{\partial u^s}{\partial z} + \frac{1}{r} \frac{\partial}{\partial r} (r v^s) \right) \right) \quad (3.103)$$

Terms similar to the pseudo-diffusion term also appear in the Navier-Stokes equations for single-phase flow. However, in many single-phase applications, the viscosity and the density may be treated as constant, and these terms cancel out. In two-phase flow, even with constant viscosity and density, the pseudo-diffusion term is not zero since, in general, the volume concentration varies. This term, together with the diffusion term, are needed to model the complete viscous stresses. This distinction between these two contributions has been introduced here in the interest of clarity and ease in the formulation of the numerical method.

Φ^s is the dissipation function representing the rate of conversion of mechanical energy to fluctuating kinetic energy due to the solid-phase viscous stresses; γ_c and γ_D are the rate of dissipation due to inelastic collisions and drag force exerted by the fluid on the particles, respectively; and finally, γ_B represents the rate of transfer of energy of the fluid phase into fluctuating kinetic energy of the solid phase.

3.7.2 Constitutive and Auxiliary Equations

Solid Phase

$$\zeta_D = \frac{3}{4} \frac{\mu^f}{\rho^s d^2} C_D \text{Re}^s \quad (3.104)$$

$$\gamma_c = 48\eta(1 - \eta) \frac{\alpha^2 \rho^s g_0}{d} \left(\frac{T}{\pi} \right)^{\frac{1}{2}} T \quad (3.105)$$

$$\gamma_D = 3\alpha\rho^s\zeta_D T' \quad (3.106)$$

$$\gamma_B = \left(1 + a_0\alpha^{\frac{3}{2}}\right) \gamma_D \quad (3.107)$$

$$\begin{aligned} \Phi^s = & \left(\mu_b^s - \frac{2}{3}\mu_c^s\right) \left(\frac{\partial u^s}{\partial z} + \frac{1}{r}\frac{\partial}{\partial r}(rv^s)\right)^2 + 2\mu_c^s \left(\left(\frac{\partial v^s}{\partial r}\right)^2 + \left(\frac{v^s}{r}\right)^2 + \left(\frac{\partial u^s}{\partial z}\right)^2\right) \\ & + \mu_c^s \left(\frac{\partial u^s}{\partial r} + \frac{\partial v^s}{\partial z}\right)^2 \end{aligned} \quad (3.108)$$

$$p^s = \alpha\rho^s T (1 + 4\eta g_0\alpha) \quad (3.109)$$

$$\mu_b^s = \frac{16m^p\alpha^2\eta g_0}{\pi d^2} \left(\frac{T}{\pi}\right)^{\frac{1}{2}} \quad (3.110)$$

$$\mu_c^s = \frac{\mu^{s*}}{g_0} \left(1 + \frac{8}{5}\eta g_0\alpha\right) \left(1 + \frac{8}{5}\eta(3\eta - 2)g_0\alpha\right) + \frac{3}{5}\mu_b^s \quad (3.111)$$

$$k_T^s = \frac{k^{s*}}{g_0} \left(1 + \frac{12}{5}\eta g_0\alpha\right) \left(1 + \frac{12}{5}\eta^2(4\eta - 3)g_0\alpha\right) + \frac{3}{2}\mu_b^s \quad (3.112)$$

$$k_\alpha^s = \frac{k^{s*}}{g_0} \left(1 + \frac{12}{5}\eta g_0\alpha\right) \frac{12}{5}\eta(2\eta - 1)(\eta - 1) \frac{d}{d\alpha} (\alpha^2 g_0) \frac{T}{\alpha} \quad (3.113)$$

Fluid Phase

$$\mu_c^f = \mu_a^f + \mu_F^f \quad (3.114)$$

$$\mu_a^f = \mu^f \mu_r^f(\alpha) \quad (3.115)$$

$$\mu_F^f = \rho^f (C_s \Delta)^2 S \quad (3.116)$$

$$\mu_b^f = 0 \quad (3.117)$$

$$S = \left\{ 2 \left[\left(\frac{\partial u^f}{\partial z}\right)^2 + \left(\frac{\partial v^f}{\partial r}\right)^2 + \left(\frac{v^f}{r}\right)^2 \right] + \left[\frac{\partial u^f}{\partial r} + \frac{\partial v^f}{\partial z} \right]^2 - \frac{2}{3} \left[\frac{\partial u^f}{\partial z} + \frac{1}{r}\frac{\partial}{\partial r}(rv^f) \right]^2 \right\}^{\frac{1}{2}} \quad (3.118)$$

This mathematical model is valid for a wide range of concentration of the solid phase, from dilute concentration to high concentration. The high-concentration limit is restricted to flows where particles interact mainly through binary collisions. Situations where particles interact through sliding, which occurs in situations close to maximum packing, are not properly modelled, because the associated frictional contribution to the solid-phase stress is not included. Various expressions for $C_D \text{Re}^s$, $\mu_r^f(\alpha)$ and g_0 can be found in the literature (please see Tables 3.1, 3.2 and 3.3): the particular expressions used in this work are specified in Chapters 5, 6 and 7.

The resulting governing equations are very similar to the models proposed by Lun [107] and Lun and Savage [110]. However, in the early work of Lun [107], the

Reynolds stress tensor $\sigma_{ij}^{f''}$ is neglected. In the recent work of Lun and Savage [110], the Reynolds stress tensor is included and evaluated through an additional equation, corresponding to the fluctuating kinetic energy transport equation of the fluid phase. Lun and Savage [110] allow the treatment of low density ratios $\frac{\rho^s}{\rho^f}$ by including different particle coefficients of restitution in the fluid and in vacuum. In the proposed formulation, it is assumed that the fluid density is much smaller than the particle density. Therefore, the coefficient of restitution of a particle in a fluid is essentially equal to the coefficient of restitution in vacuum. The Smagorinsky model is used in this work for the evaluation of the Reynolds stresses. This removes the need for solving the fluid-phase fluctuating kinetic energy transport equation derived by Lun and Savage [110].

Using the granular temperature approach, Gidaspow and co-workers [46, 45, 65] have derived solid-phase governing equations similar to the ones proposed in this work. The main differences in the derivations of Lun and Savage [110] and Gidaspow and co-workers [46, 45, 65] come from the assumed form of the velocity distribution function $f(\vec{c}, \vec{x}, t)$. In the works of Gidaspow and co-workers, the velocity distribution function is approximated as the Maxwellian velocity distribution f^o . Using this assumption, the kinetic contributions to the solid-phase stress tensor, σ_{ij}^s , and fluctuating kinetic energy flux, q_i^s , are zero. Since the kinetic transport is the dominant process at low concentration, the resulting governing equations proposed by Gidaspow and co-workers are not adequate for dilute gas-solid particle flows.

The general mathematical model so far in this section can be easily simplified to describe the various problems of interest in this work. These specializations are described next.

3.7.3 Specializations

Single-Phase Flow

The general governing equations presented in the last sub-section can be easily specialized to model laminar flow of single-phase Newtonian fluids by setting the fluid-phase concentration, ϵ , equal to one and, correspondingly, the solid-phase concentration, α , to zero. In the context of laminar single-phase flow, the Reynolds

stress has no meaning and is, therefore, set to zero. The corresponding governing equations consist of the continuity equation and two momentum equations, as follows:

Continuity Equation

$$\frac{\partial}{\partial t} (\rho^f) + \frac{\partial}{\partial z} (\rho^f u^f) + \frac{1}{r} \frac{\partial}{\partial r} (r \rho^f v^f) = 0 \quad (3.119)$$

z-Momentum Equation

$$\begin{aligned} \frac{\partial}{\partial t} (\rho^f u^f) + \frac{\partial}{\partial z} (\rho^f u^f u^f) + \frac{1}{r} \frac{\partial}{\partial r} (r \rho^f v^f u^f) = -\frac{\partial p^f}{\partial z} + S_z^f \\ + \frac{\partial}{\partial z} \left(\mu^f \frac{\partial u^f}{\partial z} \right) + \frac{1}{r} \frac{\partial}{\partial r} \left(r \mu^f \frac{\partial u^f}{\partial r} \right) \end{aligned} \quad (3.120)$$

r-Momentum Equation

$$\begin{aligned} \frac{\partial}{\partial t} (\rho^f v^f) + \frac{\partial}{\partial z} (\rho^f u^f v^f) + \frac{1}{r} \frac{\partial}{\partial r} (r \rho^f v^f v^f) = -\frac{\partial p^f}{\partial r} + S_r^f \\ + \frac{\partial}{\partial z} \left(\mu^f \frac{\partial v^f}{\partial z} \right) + \frac{1}{r} \frac{\partial}{\partial r} \left(r \mu^f \frac{\partial v^f}{\partial r} \right) - \mu^f \frac{v^f}{r^2} \end{aligned} \quad (3.121)$$

Dilute Gas-Solid Particle Flow

A model for dilute gas-solid particle flow can be obtained from the general governing equations by assuming negligible solid-phase pressure and viscosities; setting the fluid-phase effective viscosity equal to the apparent fluid viscosity; and by neglecting the third term of the pseudo-diffusion term (Eq. (3.103)). Using these assumptions, the granular temperature is not needed, and the resulting model consists of two continuity equations, and two sets of two-component momentum equations, as follows:

Solid Phase

Continuity Equation

$$\frac{\partial}{\partial t} (\alpha \rho^s) + \frac{\partial}{\partial z} (\alpha \rho^s u^s) + \frac{1}{r} \frac{\partial}{\partial r} (r \alpha \rho^s v^s) = 0 \quad (3.122)$$

z-Momentum Equation

$$\frac{\partial}{\partial t} (\alpha \rho^s u^s) + \frac{\partial}{\partial z} (\alpha \rho^s u^s u^s) + \frac{1}{r} \frac{\partial}{\partial r} (r \alpha \rho^s v^s u^s) = -\alpha \frac{\partial p^f}{\partial z} + \alpha \rho^s \zeta_D (u^f - u^s) + S_z^s \quad (3.123)$$

r-Momentum Equation

$$\frac{\partial}{\partial t} (\alpha \rho^s v^s) + \frac{\partial}{\partial z} (\alpha \rho^s u^s v^s) + \frac{1}{r} \frac{\partial}{\partial r} (r \alpha \rho^s v^s v^s) = -\alpha \frac{\partial p^f}{\partial r} + \alpha \rho^s \zeta_D (v^f - v^s) + S_r^s \quad (3.124)$$

Fluid Phase

Continuity Equation

$$\frac{\partial}{\partial t} (\epsilon \rho^f) + \frac{\partial}{\partial z} (\epsilon \rho^f u^f) + \frac{1}{r} \frac{\partial}{\partial r} (r \epsilon \rho^f v^f) = 0 \quad (3.125)$$

z-Momentum Equation

$$\begin{aligned} \frac{\partial}{\partial t} (\epsilon \rho^f u^f) + \frac{\partial}{\partial z} (\epsilon \rho^f u^f u^f) + \frac{1}{r} \frac{\partial}{\partial r} (r \epsilon \rho^f v^f u^f) &= -\epsilon \frac{\partial p^f}{\partial z} - \alpha \rho^s \zeta_D (u^f - u^s) + S_z^f \\ &+ \frac{\partial}{\partial z} \left(\mu_c^f \frac{\partial u^f}{\partial z} \right) + \frac{1}{r} \frac{\partial}{\partial r} \left(r \mu_c^f \frac{\partial u^f}{\partial r} \right) \\ &+ \frac{\partial}{\partial z} \left(\mu_c^f \frac{\partial v^f}{\partial z} \right) + \frac{1}{r} \frac{\partial}{\partial r} \left(r \mu_c^f \frac{\partial v^f}{\partial r} \right) \end{aligned} \quad (3.126)$$

r-Momentum Equation

$$\begin{aligned} \frac{\partial}{\partial t} (\epsilon \rho^f v^f) + \frac{\partial}{\partial z} (\epsilon \rho^f u^f v^f) + \frac{1}{r} \frac{\partial}{\partial r} (r \epsilon \rho^f v^f v^f) &= -\epsilon \frac{\partial p^f}{\partial r} - \alpha \rho^s \zeta_D (v^f - v^s) + S_r^f \\ &+ \frac{\partial}{\partial z} \left(\mu_c^f \frac{\partial v^f}{\partial z} \right) + \frac{1}{r} \frac{\partial}{\partial r} \left(r \mu_c^f \frac{\partial v^f}{\partial r} \right) - \mu_c^f \frac{v^f}{r^2} \\ &+ \frac{\partial}{\partial z} \left(\mu_c^f \frac{\partial u^f}{\partial r} \right) + \frac{1}{r} \frac{\partial}{\partial r} \left(r \mu_c^f \frac{\partial u^f}{\partial r} \right) - \mu_c^f \frac{v^f}{r^2} \end{aligned} \quad (3.127)$$

This dilute model *slightly* differs from other simple models available in the literature [44, 51]. The model proposed by DiGiacinto et al. [44] is obtained by setting $\epsilon = 1$ in Eqs.(3.125)-(3.127). To derive the model used by Durst et al. [51], the fluid effective viscosity μ_c^f in Eqs.(3.126)-(3.127) has to be replaced by $\epsilon \mu^f$. Since $\epsilon \approx 1$ at dilute concentration, the three models produce similar results.

Investigators	$C_D Re^s$	Remarks
Stoke Solution [155]	24	$Re^s < 1$
Oseen Solution [155]	$24 + \frac{9}{2} Re^s$	$Re^s < 5$
Wallis [186]	$24 + \frac{18}{5} (Re^s)^{.687}$	$Re^s < 1000$
Di Giacinto et al. [44]	$24 + 4 (Re^s)^{\frac{2}{3}}$	$Re^s < 1000$
Sinclair & Jackson [165]	$\frac{4}{3} \frac{\rho^s d^2 g}{\mu^s v_t (1-\alpha)^2}$	v_t is the terminal velocity of fall of a single particle under the influence of gravity
Syamlal & O'Brien [174]	$\frac{Re^s}{v_r^2} (0.63 + 4.8 \sqrt{\frac{v_r}{Re^s}})^2$	v_r is the ratio of the terminal velocity of multiple particles to that of a single particle
Ding & Gidaspow [45]	$\frac{4}{3} (150\alpha + 1.75 Re^s)$	$\alpha > 0.2$

Table 3.1: Examples of $C_D Re^s$ relations

Investigators	$\mu_r^f(\alpha)$
Einstein [53]	$1 + \frac{5}{2}\alpha$
Batchelor [17]	$1 + \frac{5}{2}\alpha + 5.2\alpha^2$
Lun [107]	$(1 - \alpha)^{-\frac{5}{2}}$
Lun & Savage [110]	$(1 - \alpha - 0.33\alpha^2)^{-\frac{5}{2}}$

Table 3.2: Examples of $\mu_r^f(\alpha)$ relations

Investigators	g_0
Sinclair & Jackson [165]	$\frac{1}{1 - \left(\frac{\alpha}{\alpha_{MX}}\right)^{\frac{1}{3}}}$
Ding & Gidaspow [45]	$\frac{0.6}{1 - \left(\frac{\alpha}{\alpha_{MX}}\right)^{\frac{1}{3}}}$
Lun & Savage [110], Lun [107], Ding et al. [46]	$\frac{1}{\left(1 - \frac{\alpha}{\alpha_{MX}}\right)^{2.5\alpha_{MX}}}$

Table 3.3: Examples of g_0 relations

Chapter 4

Numerical Model

The formulation of a control-volume-based finite element method (CVFEM) for two-dimensional, axisymmetric or planar, gas-solid particle flows is presented in this chapter. The proposed method is based on a primitive-variables, co-located, equal-order formulation: it works directly with the velocity components, pressure and temperature; these dependent variables are stored at the same nodes in the finite element mesh; and they are interpolated over the same elements. This CVFEM is constructed by adapting and extending ideas from earlier CVFEMs for single-phase incompressible fluid flows proposed by Baliga and Patankar [13, 14], Prakash and Patankar [135], Schneider and Raw [156, 157], and Saabas [149].

The formulation of control-volume-based finite element methods (CVFEMs) for fluid flow typically involves five basic steps: *(i)* discretization of the calculation domain into elements; *(ii)* further discretization of the calculation domain into control volumes that surround the nodes in the finite element mesh; *(iii)* prescription of element-based interpolation functions for the dependent variables and the thermo-physical properties of the phases; *(iv)* use of subdomain, or control-volume-based, method of weighted residuals [59] and an element-by-element procedure to derive and assemble algebraic approximations to the governing equations; and *(v)* prescription of a procedure to solve these algebraic equations. Thus CVFEMs combine concepts native to finite volume methods (FVMs) and finite element methods (FEMs). Indeed, following the views of Finlayson and Scriven [59] and Zienkiewicz [196], FVMs, FEMs and CVFEMs can all be regarded as particular cases of the method of weighted residuals (MWR).

The description of the proposed numerical method is given for two-dimensional axisymmetric problems. However, it is presented in a general manner, with respect to the two-dimensional cylindrical and Cartesian coordinate systems. The discretized equations are written in a form that allows both the two-dimensional axisymmetric and planar (Cartesian) formulations to be obtained easily. The proposed expressions are appropriate for two-dimensional axisymmetric problems; and by setting $r = 1$ in the various discretized expressions, the two-dimensional planar (Cartesian) formulation is obtained. Concise descriptions of the various steps involved in the formulation of the proposed CVFEM are presented in this section, with suitable emphasis on features that are of particular interest in simulations of gas-solid particle flows in complex geometries.

4.1 General Equation

In two-dimensional axisymmetric problems, the proposed mathematical model consists of a set of seven differential equations: a continuity equation and two momentum equations for each of the two phases, and a fluctuating kinetic energy equation for the solid phase. The seven dependent variables are u^f , v^f , p^f , u^s , v^s , α and T . The superscripts f and s refer to the gas (fluid) and particulate (solid particle) phases, respectively. The volume concentration of the solid phase is denoted by α . The volume concentration of the fluid phase, ϵ , is related to α by $\alpha + \epsilon = 1$.

With respect to the cylindrical coordinate system (r, θ, z) , axisymmetric gas-solid particle flows can be represented by the following general formulation:

$$\frac{\partial}{\partial t} (\beta \rho \phi) + \frac{\partial}{\partial z} (\beta \rho u \phi) + \frac{1}{r} \frac{\partial}{\partial r} (r \beta \rho v \phi) = \frac{\partial}{\partial z} \left(\Gamma_\epsilon \frac{\partial \phi}{\partial z} \right) + \frac{1}{r} \frac{\partial}{\partial r} \left(r \Gamma_\epsilon \frac{\partial \phi}{\partial r} \right) + S_\phi \quad (4.1)$$

The appropriate governing equations can be obtained from Eq.(4.1) by defining the dependent variable, ϕ , the volume concentration, β , the diffusion coefficient, Γ_ϵ , the mass density, ρ , the z -component of velocity, u , the r -component of velocity, v , and the volumetric source term, S_ϕ , according to Table 4.1, where

$$S_{\Gamma_z} = \frac{\partial}{\partial z} \left(\Gamma_\epsilon \frac{\partial u}{\partial z} + \left(\Gamma_b - \frac{2}{3} \Gamma_\epsilon \right) \left(\frac{\partial u}{\partial z} + \frac{1}{r} \frac{\partial}{\partial r} (r v) \right) \right) + \frac{1}{r} \frac{\partial}{\partial r} \left(r \Gamma_\epsilon \frac{\partial v}{\partial z} \right) \quad (4.2)$$

$$S_{\Gamma r} = \frac{\partial}{\partial z} \left(\Gamma_\epsilon \frac{\partial u}{\partial r} \right) + \frac{1}{r} \frac{\partial}{\partial r} \left(r \left(\Gamma_\epsilon \frac{\partial v}{\partial r} + \left(\Gamma_b - \frac{2}{3} \Gamma_\epsilon \right) \left(\frac{\partial u}{\partial z} + \frac{1}{r} \frac{\partial}{\partial r} (rv) \right) \right) \right) \quad (4.3)$$

$$S_{\text{cyl}} = - \frac{\left(\Gamma_b - \frac{2}{3} \Gamma_\epsilon \right) \left(\frac{\partial u}{\partial z} + \frac{1}{r} \frac{\partial}{\partial r} (rv) \right)}{r} - 2 \Gamma_\epsilon \frac{v}{r^2} \quad (4.4)$$

$$S_{Dz} = \alpha \rho^s \zeta_D (u^f - u^s) \quad (4.5)$$

$$S_{Dr} = \alpha \rho^s \zeta_D (v^f - v^s) \quad (4.6)$$

$$S_\alpha = \frac{\partial}{\partial z} \left(k_\alpha^s \frac{\partial \alpha}{\partial z} \right) + \frac{1}{r} \frac{\partial}{\partial r} \left(r k_\alpha^s \frac{\partial \alpha}{\partial r} \right) \quad (4.7)$$

$$W_p = -p^s \left(\frac{\partial u^s}{\partial z} + \frac{1}{r} \frac{\partial}{\partial r} (rv^s) \right) \quad (4.8)$$

The terms $S_{\Gamma z}$ and $S_{\Gamma r}$ represent part of the pseudo-diffusion term, defined in Chapter 3, and will be called the diffusion-source terms. The remaining part of the pseudo-diffusion term along with a part of the diffusion term, are regrouped in the cylindrical source term S_{cyl} . This splitting has been done only to emphasis the difference between the cylindrical and Cartesian formulations. In the Cartesian formulation, $S_{\text{cyl}} = 0$. The source terms S_{Dz} and S_{Dr} are the mutual z - and r -direction drag forces per unit volume of the mixture, respectively, exerted by the fluid and solid phases on one another. Therefore, these source terms will be referred to as the momentum coupling terms. S_α represents the transport of solid-phase fluctuating kinetic energy because of concentration gradients, and, finally, W_p is the work done by the solid-phase pressure.

	β	ρ	u	v	Γ_ϵ	Γ_b	ϕ	S_ϕ
Fluid Phase								
<i>z-momentum</i>	ϵ	ρ^f	u^f	v^f	μ_ϵ^f	μ_b^f	u^f	$S_{\Gamma z} - S_{Dz} + S_z^f - \epsilon \frac{\partial p^f}{\partial z}$
<i>r-momentum</i>	ϵ	ρ^f	u^f	v^f	μ_ϵ^f	μ_b^f	v^f	$S_{\Gamma r} - S_{Dr} + S_r^f - \epsilon \frac{\partial p^f}{\partial r} + S_{\text{cyl}}$
<i>continuity</i>	ϵ	ρ^f	u^f	v^f	0	0	1	0
Solid Phase								
<i>energy</i>	α	$\frac{3}{2} \rho^s$	u^s	v^s	k_T^s	-	T	$W_p + S_\alpha + \Phi^s - \gamma_c - \gamma_D + \gamma_B$
<i>z-momentum</i>	α	ρ^s	u^s	v^s	μ_ϵ^s	μ_b^s	u^s	$S_{\Gamma z} + S_{Dz} + S_z^s - \alpha \frac{\partial p^f}{\partial z} - \frac{\partial p^s}{\partial z}$
<i>r-momentum</i>	α	ρ^s	u^s	v^s	μ_ϵ^s	μ_b^s	v^s	$S_{\Gamma r} + S_{Dr} + S_r^s - \alpha \frac{\partial p^f}{\partial r} - \frac{\partial p^s}{\partial r} + S_{\text{cyl}}$
<i>continuity</i>	α	ρ^s	u^s	v^s	0	0	1	0

Table 4.1: Specific forms of the general equation

4.2 Domain Discretization

It is convenient to present the domain discretization procedure with respect to a longitudinal cross section of the axisymmetric domain of interest. This cross section is first divided into three-node triangular elements. Then the centroids of the elements are joined to the midpoints of the corresponding sides. This creates polygonal control volumes around each node in the finite element mesh. The longitudinal cross section of a sample domain discretization is shown in Fig. 4.1: the solid lines denote the domain and element boundaries; the dashed lines represent the control-volume faces; and the shaded areas show the control volumes associated with one internal node and one boundary node.

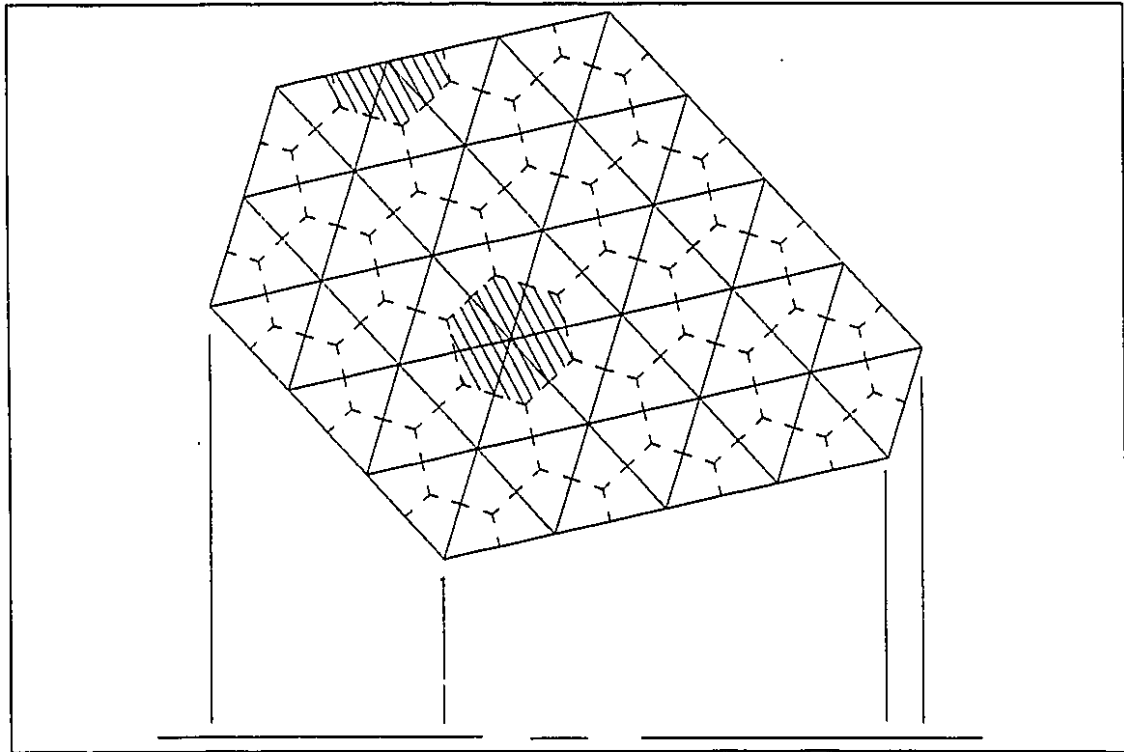


Figure 4.1: Discretization of the longitudinal cross-section of a calculation domain

The discretization of the longitudinal cross section is rotated through 2π radians about the axis of symmetry. The result is a discretization of the axisymmetric calculation domain into torus elements, of triangular cross section, and torus control volumes, of polygonal cross section. In the rest of the thesis, for conciseness in the presentation, the torus elements and torus control volumes will be referred to as

triangular (3-node) elements and polygonal control volumes, respectively.

4.3 Integral Conservation Equation

Consider a typical node i in the calculation domain: it could be an internal node, such as the one shown in Fig. 4.2a, or a boundary node, similar to the one shown in Fig. 4.2b. An integral formulation corresponding to Eq.(4.1) can be obtained by applying the appropriate conservation principle for the dependent variable, ϕ , to a suitably chosen control volume. The resulting integral conservation equation, when applied to the polygonal control volume surrounding node i in Fig. 4.2, can be written as follows:

$$\begin{aligned} & \left[\int_a^o \vec{J} \cdot \vec{n} 2\pi r ds + \int_o^c \vec{J} \cdot \vec{n} 2\pi r ds - \int_{iaoc} S_\phi dV + \int_{iaoc} \frac{\partial}{\partial t} (\beta \rho \phi) dV \right] \\ & + [\text{similar contributions from other elements surrounding node } i] \\ & + [\text{boundary contributions, if applicable}] = 0 \end{aligned} \quad (4.9)$$

where \vec{n} is a unit vector normal to the differential length element, ds , and pointing outward with respect to the control volume. \vec{J} is the combined convection-diffusion flux of ϕ :

$$\vec{J} = \vec{J}_D + \beta \vec{J}_C \quad (4.10)$$

$$\vec{J}_D = -\Gamma_e \nabla \phi \quad (4.11)$$

$$\vec{J}_C = \rho \vec{V} \phi \quad (4.12)$$

The form of Eq.(4.9) emphasizes that it can be assembled by using an element-by-element procedure akin to that used in FEMs.

4.4 Interpolation Functions

The derivation of algebraic approximations to the integral conservation equations requires the specification of element-based interpolation functions for the dependent variable, ϕ , the velocity component, u and v , diffusion coefficients, Γ_e and Γ_b , source term, S_ϕ , mass density, ρ , and volume concentration, β . As was stated earlier, specific forms of ϕ , u , v , Γ_e , Γ_b , ρ , and β are given in Table 4.1.

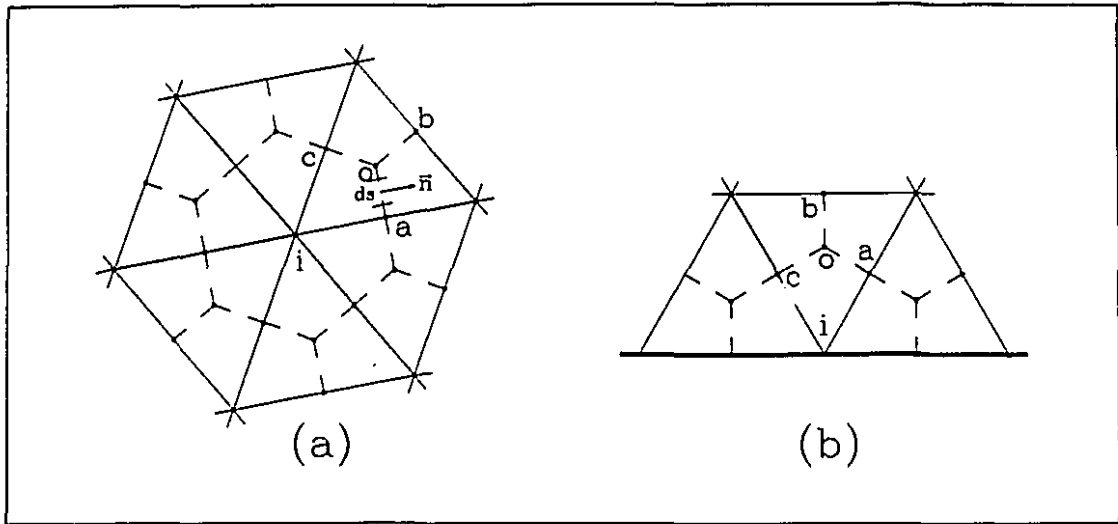


Figure 4.2: Typical control volumes surrounding (a) an internal node; and (b) a boundary node

The interpolation functions are specific to each element. For convenience in the formulation of these functions, in each element, a local (x, y) coordinate system is defined such that the origin is at the centroid of the triangular element, the x axis is in the direction of z , and the y axis is in the direction of r , as shown in Fig. 4.3a. Some of the interpolation functions will be expressed with respect to this local coordinate system.

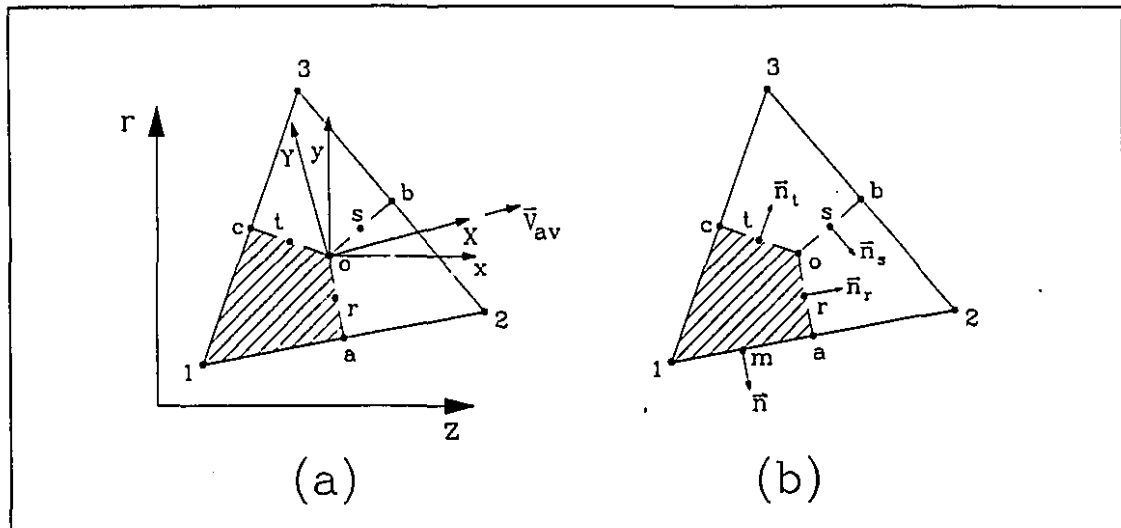


Figure 4.3: Typical triangular element: (a) global and local coordinate systems; (b) unit normals

4.4.1 Diffusion Coefficients, Density, and Sources

The diffusion coefficients, Γ_e and Γ_b , are stored at the vertices of the triangular elements. In the evaluation of the diffusion and diffusion-source fluxes, defined later in this chapter by Eqs.(4.39) and (4.52), respectively, $\bar{\Gamma}_e$ and $\bar{\Gamma}_b$ are assumed to prevail over the corresponding element. $\bar{\Gamma}_e$ and $\bar{\Gamma}_b$ are computed by assuming a linear variation of the diffusion coefficient:

$$\bar{\Gamma}_e = \frac{1}{3}(\Gamma_{e1} + \Gamma_{e2} + \Gamma_{e3}) \quad (4.13)$$

$$\bar{\Gamma}_b = \frac{1}{3}(\Gamma_{b1} + \Gamma_{b2} + \Gamma_{b3}) \quad (4.14)$$

where Γ_{e1} , Γ_{e2} , and Γ_{e3} are the values of Γ_e stored at the vertices 1, 2, and 3, defined in Fig. 4.3. Similar notation is used for Γ_b . This treatment is convenient in this formulation because most of the diffusion coefficients, namely, μ_a^f , μ_b^f , μ_e^s , μ_b^s , k_T^s , and k_α^s , are functions of the dependent variables only and not of their derivatives. In the case where the diffusion coefficient is expressed as a function of space derivatives of the dependent variables, such as for μ_F^f , volume-average space derivatives, associated with each control volume, are used to evaluate the nodal values of μ_F^f . The element contribution of S_{cy1} is evaluated assuming that the values at the vertices prevail over the corresponding portions of the control volumes within that element.

In each triangular element, the centroidal value of ρ is assumed to prevail over the corresponding element.

The source term, S_ϕ , is linearized, if needed, and expressed in the following general form [130]:

$$S_\phi = S_C + S_P\phi \quad (4.15)$$

In each triangular element, the values of S_C and S_P are stored at the vertices, and are assumed to prevail over the corresponding portions of the control volumes within that element. Thus within *each element*, three sets of S_C and S_P are stored: S_{C1} , S_{C2} , S_{C3} , S_{P1} , S_{P2} , and S_{P3} .

4.4.2 Mass Flow Rates

In the calculation of mass flow rates across the control-volume faces, the velocity is denoted by:

$$\vec{V}^m = u^m \vec{i} + v^m \vec{j} \quad (4.16)$$

When mass flow rates of the solid phase are considered, $u^m = u^s$ and $v^m = v^s$, and u^m and v^m are interpolated linearly in each element. However, when the mass flow rates of the fluid phase are considered, a special treatment, borrowed from the works of Prakash and Patankar [135] and Saabas [149], is used to prevent the occurrence of spurious pressure oscillations in the proposed co-located equal-order CVFEM. Similar treatments for the interpolation of the velocity in mass flux terms have been proposed by Peric et al. [131], in the context of finite volume methods, and Rice and Schnipke [145], in the context of finite element methods, for single-phase fluid flow. The development of this special interpolation is based on the discretized fluid-phase momentum conservation equations. Therefore, it will be presented later in this chapter.

4.4.3 ϕ in Diffusion Terms

In the derivation of algebraic approximations to surface integrals of diffusion fluxes, Eqs.(4.9) and (4.11), the dependent variable, ϕ , is interpolated linearly in each element:

$$\phi = Ax + By + C \quad (4.17)$$

Referring to Fig. 4.3a, the constants A , B and C can be uniquely determined in terms of the local (x, y) coordinates of the three nodes (or vertices) and the corresponding values of ϕ . Thus with reference to the element 123 and the local (x, y) coordinate system shown in Fig. 4.3a:

$$A = \frac{(y_2 - y_3)\phi_1 + (y_3 - y_1)\phi_2 + (y_1 - y_2)\phi_3}{\text{DET}} \quad (4.18)$$

$$B = \frac{(x_3 - x_2)\phi_1 + (x_1 - x_3)\phi_2 + (x_2 - x_1)\phi_3}{\text{DET}} \quad (4.19)$$

$$C = \frac{(x_2y_3 - x_3y_2)\phi_1 + (x_3y_1 - x_1y_3)\phi_2 + (x_1y_2 - x_2y_1)\phi_3}{\text{DET}} \quad (4.20)$$

where

$$\text{DET} = (x_1y_2 + x_2y_3 + x_3y_1 - y_1x_2 - y_2x_3 - y_3x_1) \quad (4.21)$$

An equivalent, and perhaps more elegant, development of this linear interpolation on triangular elements could be done using barycentric or area coordinates, traditionally employed in FEMs [196]. Here, however, the above-stated development is preferred in order to be consistent with the derivations in the following sections of this chapter. It should also be noted that with such linear interpolation functions, Delauney triangulation is required to ensure that algebraic approximations of the diffusion transport terms contribute positively to the coefficients in the discretized equations. Barth [16] has presented a formal proof of this statement for two-dimensional planar problems.

4.4.4 ϕ in Convection Terms

In the derivation of algebraic approximations to surface integrals of the convective fluxes, Eqs.(4.9) and (4.12), two different interpolation schemes for ϕ were investigated: a FLOW Oriented upwind scheme (FLO); and a MASS Weighted upwind scheme (MAW).

The FLO scheme is based on the earlier work of Baliga and Patankar [12, 14]. The interpolation function used in this scheme responds appropriately to an element-based Peclet number and to the direction of the element-average velocity vector. This interpolation function for ϕ is defined using a local flow-oriented (X, Y) coordinate system, shown in Fig. 4.3a: the origin of this coordinate system is located at the centroid of the element, and the X axis is oriented along the element average velocity \vec{V}_{av}^m .

$$\phi = A\xi + BY + C \quad (4.22)$$

where

$$\xi = \frac{\bar{\Gamma}_e}{\beta\rho U_{av}^m} \left\{ \exp \left[\frac{\text{Pe}_\Delta (X - X_{\max})}{X_{\max} - X_{\min}} \right] - 1 \right\} \quad (4.23)$$

$$Pe_{\Delta} = \bar{\beta} \rho U_{av}^m \frac{X_{max} - X_{min}}{\Gamma_c} \quad (4.24)$$

$$X_{max} = \max(X_1, X_2, X_3) \quad X_{min} = \min(X_1, X_2, X_3) \quad (4.25)$$

$$U_{av}^m = |\vec{V}_{av}^m| \quad (4.26)$$

$\bar{\beta}$ is evaluated using linear interpolation similar to that used to obtain $\bar{\Gamma}_c$. The constants A , B and C in equation (4.22) can be determined from Eqs. (4.18)-(4.21) with the following modifications: replace x_1 , x_2 and x_3 by ξ_1 , ξ_2 and ξ_3 , respectively; and replace y_1 , y_2 and y_3 by Y_1 , Y_2 and Y_3 , respectively. It should be noted that with reference to the typical element shown in Fig. 4.3a, the element-average value of velocity in Eq.(4.26), \vec{V}_{av}^m , is given by

$$\vec{V}_{av}^m = u_{av}^m \vec{i} + v_{av}^m \vec{j} \quad (4.27)$$

where \vec{i} and \vec{j} are unit vectors in the z and r directions, respectively, and

$$u_{av}^m = \frac{u_1^m + u_2^m + u_3^m}{3} \quad v_{av}^m = \frac{v_1^m + v_2^m + v_3^m}{3} \quad (4.28)$$

In transport equations related to the fluid phase, u_i^m and v_i^m are computed using Eq.(4.93), as discussed in Section 4.5.4. However, in transport equations related to the solid phase, $u_i^m = u_i^s$ and $v_i^m = v_i^s$.

In planar two-dimensional problems that involve acute-angled triangular elements and relatively low element Peclet-numbers, the FLO scheme has proved quite successful [12, 149]. If high values of the element Peclet number are encountered, however, the FLO scheme can lead to negative coefficients in the algebraic discretized equations [149], and this difficulty is compounded when obtuse angled triangular elements are used [149]. These negative coefficients imply that an increase in the value of the transported scalar at a node outside the corresponding control volume could lead to an increase in the net outflow of the scalar from that control volume. This is physically incorrect. In steady-state problems, in the absence of source terms, for a scalar to be transported out of a control volume, it first has to flow into the control volume [77]. The donor-cell scheme of Prakash [137] is one way of ensuring positive coefficients: in this approach, the value of a scalar convected out of a control volume, across its surface, is set equal to the value of the scalar at the node within the control volume. This approach guarantees positive coefficients, but takes little

account of the influence of the direction of the flow. Thus it is prone to considerable false diffusion [137].

The proposed MAW scheme is an adaptation of the positive-coefficient schemes of Schneider and Raw [156] and Saabas [149]. It ensures, at the element level, that the extent to which the dependent variable at a node exterior to a control volume contributes to the convective outflow is less than or equal to its contribution to the inflow by convection. Thus, it is a sufficient condition to ensure that the algebraic approximations to the convective terms in Eq.(4.9) add positively to the discretized equation. It should be noted that the MAW scheme takes better account of the influence of the direction of the flow than the donor-cell scheme of Prakash [137], so it is less prone to false diffusion [137, 149, 156].

The MAW scheme defines a mass-weighted average of ϕ at each of the three control surfaces of a triangular element (Fig. 4.3b), namely, ϕ_r , ϕ_s , ϕ_t , in the following manner: let

$$\dot{m}_r = \int_0^a \beta \rho \vec{V}^m \cdot \vec{n}_r 2\pi r ds \quad \dot{m}_s = \int_0^b \beta \rho \vec{V}^m \cdot \vec{n}_s 2\pi r ds \quad \dot{m}_t = \int_0^c \beta \rho \vec{V}^m \cdot \vec{n}_t 2\pi r ds \quad (4.29)$$

where \vec{n}_r , \vec{n}_s and \vec{n}_t are unit normals, as shown in Fig. 4.3b.

$$\phi_r = \begin{cases} f^+ \phi_t + (1 - f^+) \phi_1 & \text{where } f^+ = \min[\max(-\frac{\dot{m}_t}{\dot{m}_r}, 0), 1] \text{ if } \dot{m}_r > 0 \\ f^- \phi_s + (1 - f^-) \phi_2 & \text{where } f^- = \min[\max(-\frac{\dot{m}_s}{\dot{m}_r}, 0), 1] \text{ if } \dot{m}_r < 0 \end{cases} \quad (4.30)$$

$$\phi_s = \begin{cases} f^+ \phi_t + (1 - f^+) \phi_3 & \text{where } f^+ = \min[\max(\frac{\dot{m}_t}{\dot{m}_s}, 0), 1] \text{ if } \dot{m}_s > 0 \\ f^- \phi_r + (1 - f^-) \phi_2 & \text{where } f^- = \min[\max(-\frac{\dot{m}_r}{\dot{m}_s}, 0), 1] \text{ if } \dot{m}_s < 0 \end{cases} \quad (4.31)$$

$$\phi_t = \begin{cases} f^+ \phi_r + (1 - f^+) \phi_1 & \text{where } f^+ = \min[\max(-\frac{\dot{m}_r}{\dot{m}_t}, 0), 1] \text{ if } \dot{m}_t > 0 \\ f^- \phi_s + (1 - f^-) \phi_3 & \text{where } f^- = \min[\max(\frac{\dot{m}_s}{\dot{m}_t}, 0), 1] \text{ if } \dot{m}_t < 0 \end{cases} \quad (4.32)$$

These mass-weighted averages of ϕ are assumed to prevail over each control surface when the surface integrals of the convection terms, Eqs.(4.9) and (4.12), are evaluated. The algebraic approximations of the mass flow rates in Eq.(4.29) will be discussed later in this chapter. Details of the numerical implementation of the MAW scheme are presented in Appendix B.

In problems with acute-angled triangular elements and relatively low element Peclet numbers, the FLO scheme is more accurate than the MAW scheme. As was mentioned earlier, however, when high element Peclet numbers are involved,

especially in conjunction with obtuse-angled elements, the FLO scheme produces negative coefficients in the discretized equations. Negative coefficients in the discretized equations can lead to the following difficulties: (i) the numerical solutions could exhibit spurious oscillations about the exact solution; (ii) iterative solution algorithms, such as SIMPLE or its variants [130] and CELS [62], that use segregated or coupled equation line-by-line iterative algorithms to solve the linearized sets of discretization equations, could diverge; and (iii) always-positive dependent variables, such as volume concentration of the fluid and solid phases, or the fluctuating kinetic energy of the solid phase, could take on negative values and lead to a failure of the overall solution algorithm. When such difficulties are encountered, the MAW scheme is recommended. Indeed, a formulation that automatically switches from the FLO scheme to the MAW scheme, when necessary, could be conceived, but this is not within the scope of this work.

The MAW scheme defined by Eqs. (4.29)-(4.32) is highly implicit. This does not pose any special difficulties in the proposed derivation of the discretization equations, as presented in the next section, because it is based on successive-substitution, or Picard, linearization of the convective transport terms in the momentum equations. However, the MAW scheme would make Newton-type linearizations very difficult. It should also be noted that in this scheme, to obtain expressions for ϕ_r , ϕ_s , and ϕ_t in terms of ϕ_1 , ϕ_2 , and ϕ_3 , a 3 X 3 matrix of element-interpolation coefficients must be inverted. Further details are available in Appendix B.

4.4.5 Fluid-Phase Pressure p^f and Solid-Phase Pressure p^s

Fluid-phase and solid-phase pressures are interpolated linearly in each element. With respect to the local (x, y) coordinate system shown in Fig. 4.3a:

$$p^f = d^f x + e^f y + f^f \quad (4.33)$$

$$p^s = d^s x + e^s y + f^s \quad (4.34)$$

The constants d^f , e^f and f^f (or d^s , e^s and f^s) can be obtained using procedures similar to those used to determine the constants A , B and C in Eqs. (4.18)-(4.20).

4.4.6 Volume Concentrations

The function used to interpolate α in most of the available finite volume methods for two-phase flows is based on the upwind scheme [30, 44, 51, 76, 159, 170]. The donor-cell scheme of Prakash [137] is one way of implementing this idea in CVFEMs. In this work, an adaptation of the MAW scheme described previously has been implemented. As discussed in the last section, the MAW scheme takes better account of the influence of the direction of the flow than the donor-cell scheme.

The modified MAW scheme defines a material mass-weighted average of β at integration points on each of the three control surfaces of a triangular element (Fig. 4.3b), namely, β_r , β_s , β_t , in the following manner: let

$$\dot{M}_r^s = \int_0^a \rho \vec{V}^s \cdot \vec{n}_r 2\pi r ds \quad \dot{M}_s^s = \int_0^b \rho \vec{V}^s \cdot \vec{n}_s 2\pi r ds \quad \dot{M}_t^s = \int_0^c \rho \vec{V}^s \cdot \vec{n}_t 2\pi r ds \quad (4.35)$$

where \vec{n}_r , \vec{n}_s and \vec{n}_t are the unit-normal vectors shown in Fig. 4.3a.

Then

$$\alpha_r = \begin{cases} f^+ \alpha_t + (1 - f^+) \alpha_1 & \text{where } f^+ = \min[\max(-\frac{\dot{M}_t^s}{\dot{M}_r^s}, 0), 1] \text{ if } \dot{M}_r^s > 0 \\ f^- \alpha_s + (1 - f^-) \alpha_2 & \text{where } f^- = \min[\max(-\frac{\dot{M}_s^s}{\dot{M}_r^s}, 0), 1] \text{ if } \dot{M}_r^s < 0 \end{cases} \quad (4.36)$$

$$\alpha_s = \begin{cases} f^+ \alpha_t + (1 - f^+) \alpha_3 & \text{where } f^+ = \min[\max(\frac{\dot{M}_t^s}{\dot{M}_s^s}, 0), 1] \text{ if } \dot{M}_s^s > 0 \\ f^- \alpha_r + (1 - f^-) \alpha_2 & \text{where } f^- = \min[\max(-\frac{\dot{M}_r^s}{\dot{M}_s^s}, 0), 1] \text{ if } \dot{M}_s^s < 0 \end{cases} \quad (4.37)$$

$$\alpha_t = \begin{cases} f^+ \alpha_r + (1 - f^+) \alpha_1 & \text{where } f^+ = \min[\max(-\frac{\dot{M}_r^s}{\dot{M}_t^s}, 0), 1] \text{ if } \dot{M}_t^s > 0 \\ f^- \alpha_s + (1 - f^-) \alpha_3 & \text{where } f^- = \min[\max(\frac{\dot{M}_s^s}{\dot{M}_t^s}, 0), 1] \text{ if } \dot{M}_t^s < 0 \end{cases} \quad (4.38)$$

ϵ is calculated using $\epsilon + \alpha = 1$. These solid-material mass-weighted averages of α and ϵ are assumed to prevail over each control surface when the mass flow rates in the integral continuity and momentum equations are evaluated.

4.5 Discretization Equations

The discretization equations are obtained by first deriving algebraic approximations to the element contributions and the boundary contributions, if applicable, and then assembling these contributions appropriately.

4.5.1 Discretization Equation for ϕ

The following discussion pertains to node 1 of the element shown in Fig. 4.3. In each element, there are diffusion, convection, source and unsteady contributions. The derivation of algebraic approximations to each of these contributions is presented separately.

Diffusion Contribution

In each element, the diffusion flux, \vec{J}_D , can be expressed in terms of its components in the z and r directions:

$$\vec{J}_D = J_{Dz}\vec{i} + J_{Dr}\vec{j} = \left(-\Gamma_\epsilon \frac{\partial \phi}{\partial z}\right)\vec{i} + \left(-\Gamma_\epsilon \frac{\partial \phi}{\partial r}\right)\vec{j} \quad (4.39)$$

where \vec{i} and \vec{j} are unit vectors in the z and r directions, respectively. The linear interpolation function given by Eq. (4.17) is used to approximate J_{Dz} and J_{Dr} . Thus, with reference to element 123 and the local (x, y) coordinate system in Fig. 4.3a, the diffusion contribution is approximated as follows:

$$\int_a^o \vec{J}_D \cdot \vec{n} 2\pi r ds = 2\pi \bar{\Gamma}_\epsilon \frac{r_o + r_a}{2} [Ay_a - Bx_a] \quad (4.40)$$

$$\int_o^c \vec{J}_D \cdot \vec{n} 2\pi r ds = 2\pi \bar{\Gamma}_\epsilon \frac{r_o + r_c}{2} [Bx_c - Ay_c] \quad (4.41)$$

where A and B are given by Eqs. (4.18) and (4.19), respectively.

Convection Contribution

In each element, the convection flux, \vec{J}_C , can be expressed in terms of its components in the z and r directions:

$$\vec{J}_C = (J_{Cz}\vec{i} + J_{Cr}\vec{j}) = (\rho u^m \phi \vec{i} + \rho v^m \phi \vec{j}) \quad (4.42)$$

where ϕ is given by Eq. (4.22) when the FLO scheme is used, or Eqs. (4.30)-(4.32) when using the MAW scheme. It should be noted here again that u^m and v^m denote components of the velocity vector, \vec{V}^m , in the mass-flux terms.

In the case of the FLO scheme, the interpolation function given in Eq. (4.22) is used to approximate ϕ , β is computed using the modified MAW scheme (Eqs. (4.36)-(4.38)), Eq. (4.93) or (4.97) is used to obtain u^m and v^m , and the convection contribution is evaluated using Simpson's rule as follows:

$$\int_a^o \beta \vec{J}_C \cdot \vec{n} 2\pi r ds = 2\pi \beta_r \left\{ -\frac{y_a}{6} [r_o(J_{Cz})_o + 4r_r(J_{Cz})_r + r_a(J_{Cz})_a] \right. \\ \left. + \frac{x_a}{6} [r_o(J_{Cr})_o + 4r_r(J_{Cr})_r + r_a(J_{Cr})_a] \right\} \quad (4.43)$$

$$\int_o^c \beta \vec{J}_C \cdot \vec{n} 2\pi r ds = 2\pi \beta_t \left\{ +\frac{y_c}{6} [r_o(J_{Cz})_o + 4r_t(J_{Cz})_t + r_c(J_{Cz})_c] \right. \\ \left. - \frac{x_c}{6} [r_o(J_{Cr})_o + 4r_t(J_{Cr})_t + r_c(J_{Cr})_c] \right\} \quad (4.44)$$

When the MAW scheme is used, the convection flux, \vec{J}_C , is computed using ϕ given by Eqs.(4.30)-(4.32), and β obtained from the modified MAW scheme. Therefore, the convection contribution is simply approximated as:

$$\int_a^o \beta \vec{J}_C \cdot \vec{n} 2\pi r ds = \beta_r \dot{M}_r \phi_r \quad \int_o^c \beta \vec{J}_C \cdot \vec{n} 2\pi r ds = \beta_t \dot{M}_t \phi_t \quad (4.45)$$

where

$$\dot{M}_r = \int_a^o \rho \vec{V}^m \cdot \vec{n}_r 2\pi r ds \quad \dot{M}_t = \int_o^c \rho \vec{V}^m \cdot \vec{n}_t 2\pi r ds \quad (4.46)$$

It should be noted that $\beta_r \dot{M}_r$ and $\beta_t \dot{M}_t$ are the mass flow rates \dot{m}_r and \dot{m}_t , respectively; and \dot{m}_r and \dot{m}_t are mass flow rates across the corresponding control surfaces, in the directions of the normals \vec{n}_r and \vec{n}_t , respectively (see Fig. 4.3b), as expressed in Eq. (4.29).

Element Source Contribution

The volume integral involving the source term, S_ϕ , is approximated as follows:

$$\int_{1aoc} S_\phi dV = S_{C1} \mathcal{V}_{1aoc} + S_{P1} \phi_1 \mathcal{V}_{1aoc} \quad (4.47)$$

where S_{C1} , S_{P1} are the stored nodal values *within each element*, and \mathcal{V}_{1aoc} is the volume define by the points 1, a, o, and c:

$$\mathcal{V}_{1aoc} = 2\pi \frac{|\text{DET}|}{36} (2r_1 + 2r_o + r_a + r_c) \quad (4.48)$$

with DET given by Eq. (4.21). The expressions for the various volumes involved in the numerical formulation are developed in Appendix B.

Element Unsteady Contribution

A fully-implicit unsteady formulation [130] is used in this work. It should be noted here that in the proposed method, the solution of steady-state problems is also obtained through the use of a fully-implicit unsteady formulation. This approach is related to the solution of the coupled, non-linear, steady-state equations using iterative methods with under-relaxation [130]. In the two-fluid model considered in this work, there are two sets of governing equations, one related to the fluid phase and one to the solid phase. In the iterative solution of the steady-state equations, it is often necessary to prescribe different relaxation factors for each of the two sets of discretization equations, in order to ensure convergence of the overall algorithm. An early implementation of the proposed CVFEM was based on an iterative method with under-relaxation: the appropriate relaxation factors to ensure convergence had to be changed from one problem to another and were different for each phase; and the choice of the appropriate relaxation factors involved a tedious trial-and-error process. In the unsteady formulation, however, only the time step is needed to be given. This time step will naturally ensure a common evolution of the solution for each set of equations, and this results in a robust numerical solution algorithm. In the choice of a suitable time step, guidance is obtained from physical quantities such as the value of the particle relaxation time [148].

The volume integral involving the unsteady term is approximated as follows:

$$\int_{V_{1aoc}} \frac{\partial}{\partial t} (\beta \rho \phi) dV = \frac{\rho V_{1aoc}}{\Delta t} (\beta_1 \phi_1 - \beta_1^* \phi_1^*) \quad (4.49)$$

where Δt is the time step, and β_1^* and ϕ_1^* are the values of β and ϕ , respectively, at the previous time step.

Discretized ϕ Equation

Adding up the diffusion, convection, source and unsteady contributions, the total contribution of element 123 to the conservation equation for node 1 is obtained. The algebraic approximation to this total element contribution can be compactly expressed as follows:

$$\int_a^o \vec{J} \cdot \vec{n} 2\pi r ds + \int_o^c \vec{J} \cdot \vec{n} 2\pi r ds + \int_{1aoc} \left[\frac{\partial}{\partial t} (\beta \rho \phi) - S_\phi \right] dV = C_1^\phi \phi_1 + C_2^\phi \phi_2 + C_3^\phi \phi_3 + D^\phi \quad (4.50)$$

Details of the derivations pertaining to the element contribution are given in Appendix B. Expressions similar to Eq. (4.50) can be derived for the contributions of all elements associated with the internal node i , shown in Fig. 4.2a. When the total contributions of all elements associated with this internal node i are substituted into Eq.(4.9), the complete discretization equation for this node is obtained. A general representation of this equation can be cast in the following form:

$$ac_i^\phi \phi_i = \sum_{nb} ac_{nb}^\phi \phi_{nb} + b^\phi \quad (4.51)$$

4.5.2 Discretized Momentum Equations

The momentum conservation equations are identical in form to the conservation equation for ϕ . However, additional comments are needed concerning the treatment of the source terms. The momentum source terms are divided into five parts, namely, the diffusion-source terms (S_{Γ_z} , S_{Γ_r}), the momentum-coupling terms (S_{Dz} , S_{Dr}), the body force terms (S_z^f , S_r^f , S_z^s , S_r^s), the pressure gradient terms, and the cylindrical source term (S_{cyl}).

Diffusion-Source Term

The diffusion-source term is integrated similarly to the diffusion term. However, its contribution is included in the source-part of the discretized momentum equation (in b^u or b^v). A diffusion-source flux, $\vec{J}_{DS\epsilon}$, is defined as follows:

$$\begin{aligned} \vec{J}_{DS\epsilon} = & \left[\Gamma_\epsilon \frac{\partial u}{\partial \epsilon} + \left(\Gamma_b - \frac{2}{3} \Gamma_\epsilon \right) \left(\frac{\partial u}{\partial z} + \frac{1}{r} \frac{\partial}{\partial r} (rv) \right) \frac{\partial \epsilon}{\partial z} \right] \vec{i} \\ & + \left[\Gamma_\epsilon \frac{\partial v}{\partial \epsilon} + \left(\Gamma_b - \frac{2}{3} \Gamma_\epsilon \right) \left(\frac{\partial v}{\partial z} + \frac{1}{r} \frac{\partial}{\partial r} (rv) \right) \frac{\partial \epsilon}{\partial r} \right] \vec{j} \end{aligned} \quad (4.52)$$

where ϵ stands for z for the z -momentum equation or r for the r -momentum equation. In the algebraic approximation of $\vec{J}_{DS\epsilon}$, u and v are assumed to vary linearly in

each element. Therefore, the derivatives of u and v that appear in Eq.(4.52) are constants over the element, and the diffusion-source contribution can be approximated as follows:

$$\int_{1aoc} S_{\Gamma_\epsilon} dV = \int_a^o \vec{J}_{DS\epsilon} \cdot \vec{n} 2\pi r ds + \int_o^c \vec{J}_{DS\epsilon} \cdot \vec{n} 2\pi r ds \quad (4.53)$$

$$\int_a^o \vec{J}_{DS\epsilon} \cdot \vec{n} 2\pi r ds = 2\pi \frac{r_o + r_a}{2} \left\{ \left[\Gamma_\epsilon \left(\frac{\partial v}{\partial \epsilon} \right)_{\text{ele}} + \left(\Gamma_b - \frac{2}{3} \Gamma_\epsilon \right) \left(\frac{\partial u}{\partial z} + \frac{1}{r} \frac{\partial}{\partial r} (rv) \right) \right]_o \frac{\partial \epsilon}{\partial r} \right] x_a - \left[\Gamma_\epsilon \left(\frac{\partial u}{\partial \epsilon} \right)_{\text{ele}} + \left(\Gamma_b - \frac{2}{3} \Gamma_\epsilon \right) \left(\frac{\partial u}{\partial z} + \frac{1}{r} \frac{\partial}{\partial r} (rv) \right) \right]_o \frac{\partial \epsilon}{\partial z} \right] y_a \right\} \quad (4.54)$$

$$\int_o^c \vec{J}_{DS\epsilon} \cdot \vec{n} 2\pi r ds = 2\pi \frac{r_o + r_c}{2} \left\{ \left[\Gamma_\epsilon \left(\frac{\partial u}{\partial \epsilon} \right)_{\text{ele}} + \left(\Gamma_b - \frac{2}{3} \Gamma_\epsilon \right) \left(\frac{\partial u}{\partial z} + \frac{1}{r} \frac{\partial}{\partial r} (rv) \right) \right]_o \frac{\partial \epsilon}{\partial z} \right] y_c - \left[\Gamma_\epsilon \left(\frac{\partial v}{\partial \epsilon} \right)_{\text{ele}} + \left(\Gamma_b - \frac{2}{3} \Gamma_\epsilon \right) \left(\frac{\partial u}{\partial z} + \frac{1}{r} \frac{\partial}{\partial r} (rv) \right) \right]_o \frac{\partial \epsilon}{\partial r} \right] x_c \right\} \quad (4.55)$$

where

$$\left(\frac{\partial u}{\partial z} + \frac{1}{r} \frac{\partial}{\partial r} (rv) \right)_o = \left(\frac{\partial u}{\partial z} \right)_{\text{ele}} + \left(\frac{\partial v}{\partial r} \right)_{\text{ele}} + \frac{v_o}{r_o} \quad (4.56)$$

The expression given in Eq.(4.53) is written without the diffusion-source contribution on the surfaces 1 – a and c – 1 (see Fig. 4.3a) because they cancel out when all appropriate element contributions are assembled to approximate the complete integral conservation equation for an internal node; in the case of boundary nodes, one or both of these contributions may need to be included.

Momentum-Coupling Source Term

The integration of the momentum-coupling source term is presented here only for the z -component of the momentum equation, since the treatment of this term in the r -momentum equation is analogous. The z -component momentum-coupling source term is given by:

$$S_{Dz} = K (u^f - u^s) \quad (4.57)$$

where

$$K = \alpha \rho^s \zeta_D \quad (4.58)$$

All the quantities involved in the calculation of the momentum-coupling source term are defined at the vertices (or nodes) of the triangular elements. Therefore, using a simple prevailing assumption over the corresponding portion of the control volume within that element, the volume integration of the momentum-coupling term can be approximated as follows:

$$\int_{1aoc} S_{Dz} dV = K_1 (u_1^f - u_1^s) V_{1aoc} \quad (4.59)$$

The complete contribution of the momentum-coupling source term to the z -momentum equation can be easily obtained:

$$\int_{(V_{cv})_1} S_{Dz} dV = K_1 (u_1^f - u_1^s) (V_{cv})_1 \quad (4.60)$$

where $(V_{cv})_1$ is the volume of the control volume surrounding node 1. While this integration is straightforward, the proper linearization of the momentum-coupling source term is crucial to ensure convergence of the overall algorithm, especially in the context of segregated iterative solution algorithms. The linearization consists in the specification of appropriate expressions for S_C and S_P (see Eq. (4.15)). Before the discussion of the linearization, it is useful to introduce the following notation:

solid-phase momentum-coupling term contribution (4.61)

$$\int_{(V_{cv})_1} S_{Dz} dV = (S_{Dz})_C^s (V_{cv})_1 + (S_{Dz})_P^s u_1^s (V_{cv})_1 \quad (4.62)$$

fluid-phase momentum-coupling term contribution (4.63)

$$- \int_{(V_{cv})_1} S_{Dz} dV = (S_{Dz})_C^f (V_{cv})_1 + (S_{Dz})_P^f u_1^f (V_{cv})_1 \quad (4.64)$$

In this context, a linearization consists in a choice of $(S_{Dz})_C^s$, $(S_{Dz})_P^s$, $(S_{Dz})_C^f$, and $(S_{Dz})_P^f$. A very simple linearization can be obtained by treating the momentum-coupling source term explicitly in each iteration:

$$(S_{Dz})_C^s = K_1 (u_1^f - u_1^s)^* \quad (S_{Dz})_P^s = 0 \quad (4.65)$$

$$(S_{Dz})_C^f = K_1 (u_1^s - u_1^f)^* \quad (S_{Dz})_P^f = 0 \quad (4.66)$$

where $(u_1^f - u_1^s)^*$ and $(u_1^s - u_1^f)^*$ are based on initial values or values from the previous iteration. Implementation of such a linearization in a segregated iterative

algorithm resulted in significant convergence problems at high loading and/or low Stokes number. For a given concentration, as the Stokes number decreases (which can be interpreted as decreasing the size of the particles, for example), the value of K becomes larger, and the resulting momentum equations are source dominated. This results in very slow convergence rates, and, sometimes segregated iterative algorithms may even diverge. In an effort to improve the robustness of the iterative solution algorithm, a treatment could be proposed in which the momentum-coupling source term is treated explicitly in the fluid phase but implicitly in the solid phase, in each iteration:

$$(S_{Dz})_C^s = K_1 (u_1^f)^n \quad (S_{Dz})_P^s = -K_1 \quad (4.67)$$

$$(S_{Dz})_C^f = K_1 (u_1^s - u_1^f)^n \quad (S_{Dz})_P^f = 0 \quad (4.68)$$

This treatment describes the physical interactions between the phases more closely than the above-mentioned fully explicit treatment. As the Stokes number decreases, the particle inertia decreases and, therefore, it follows the fluid closely. This means that the solid-phase velocity is almost equal to the fluid-phase velocity. The implicit treatment of the solid phase ensures, at high Stokes numbers, that the solid-phase velocities will be close to the fluid-phase velocity, because of the domination of the contribution of the momentum-coupling term in comparison to the convection and diffusion contributions. This is the attractive feature of this linearization. However, preliminary computations using this scheme also resulted in converging problems similar to those encountered in the completely explicit formulation.

The proposed linearization is a fully implicit formulation in each iteration, which allows a simultaneous coupled solution of the fluid- and solid-phase momentum equations:

$$(S_{Dz})_C^s = K_1 u_1^f \quad (S_{Dz})_P^s = -K_1 \quad (4.69)$$

$$(S_{Dz})_C^f = K_1 u_1^s \quad (S_{Dz})_P^f = -K_1 \quad (4.70)$$

This linearization has proven to be much less prone to convergence problems than the other two linearization schemes discussed earlier in this section. Numerical examples which illustrate the characteristics of these linearization schemes are presented in Appendix C.

Body-Force Source Term

The integration of the body-force source term is approximated in a similar manner to that used for the source term in the ϕ equation. An example of body-force is the gravity field. In this particular case, no linearization is needed.

Pressure-Gradient Terms

Both the fluid-phase and solid-phase pressures are assumed to vary linearly within an element. Therefore, their gradients are constant within an element, and the corresponding volume integrations are approximated as follows:

$$\int_{1aoc} -\beta \frac{\partial p^f}{\partial \varepsilon} dV = -\beta_1 \left(\frac{\partial p^f}{\partial \varepsilon} \right)_{ele} V_{1aoc} \quad (4.71)$$

$$\int_{1aoc} \frac{\partial p^s}{\partial \varepsilon} dV = \left(\frac{\partial p^s}{\partial \varepsilon} \right)_{ele} V_{1aoc} \quad (4.72)$$

ε stands for z in the z -momentum equation, or r in the r -momentum equations. The pressure gradients in these equations are computed using Eqs. (4.33) and (4.34).

Cylindrical Source Term

The evaluation of the cylindrical source term involves the diffusion coefficients, the radial velocity, and velocity gradients. In the volume integration of this source term, the nodal values of the diffusion coefficients are assumed to prevail over the corresponding portions of the control volume; the radial velocity is also evaluated at the nodal point; and the velocity gradients are evaluated using linear interpolations and these quantities are assumed to prevail over the element. These approximations yield the following expression:

$$\int_{1aoc} S_{cyl} dV = \left[-\frac{(\Gamma_{b1} - \frac{2}{3}\Gamma_{e1}) \left(\frac{\partial u}{\partial z} + \frac{1}{r} \frac{\partial}{\partial r} (rv) \right)_e}{r_1} - 2\Gamma_{e1} \frac{v_1}{r_1^2} \right] V_{1aoc} \quad (4.73)$$

Discretized u^f and v^f Equations

The discretized momentum equations are derived and assembled using element-by-element procedures akin to those used to obtain the discretization equation for ϕ . The resulting u^f and v^f discretization equations for the fluid phase at a node i can be cast in the following forms:

$$\begin{aligned} \left(ac_i^{uf} + K_i \mathcal{V}_{cv} + \frac{\epsilon_i \rho^f \mathcal{V}_{cv}}{\Delta t} \right) u_i^f &= \sum_{nb} ac_{nb}^{uf} u_{nb}^f + b^{uf} + K_i u_i^s \mathcal{V}_{cv} \\ &+ \frac{\epsilon_i^* \rho^f \mathcal{V}_{cv}}{\Delta t} u_i^{f*} + \epsilon_i \mathcal{V}_{cv} \left(-\overline{\frac{\partial p^f}{\partial z}} \right) \end{aligned} \quad (4.74)$$

$$\begin{aligned} \left(ac_i^{vf} + K_i \mathcal{V}_{cv} + \frac{\epsilon_i \rho^f \mathcal{V}_{cv}}{\Delta t} \right) v_i^f &= \sum_{nb} ac_{nb}^{vf} v_{nb}^f + b^{vf} + K_i v_i^s \mathcal{V}_{cv} \\ &+ \frac{\epsilon_i^* \rho^f \mathcal{V}_{cv}}{\Delta t} v_i^{f*} + \epsilon_i \mathcal{V}_{cv} \left(-\overline{\frac{\partial p^f}{\partial r}} \right) \end{aligned} \quad (4.75)$$

The bar over the pressure gradient denotes volume average associated with the control volume \mathcal{V}_{cv} .

Discretized u^s and v^s Equations

Using similar element-by-element procedures, the resulting u^s and v^s discretization equations for the solid phase at a node i can be cast in the following forms:

$$\begin{aligned} \left(ac_i^{us} + K_i \mathcal{V}_{cv} + \frac{\alpha_i \rho^s \mathcal{V}_{cv}}{\Delta t} \right) u_i^s &= \sum_{nb} ac_{nb}^{us} u_{nb}^s + b^{us} + \mathcal{V}_{cv} \left(-\overline{\frac{\partial p^s}{\partial z}} \right) + K_i u_i^f \mathcal{V}_{cv} \\ &+ \frac{\alpha_i^* \rho^s \mathcal{V}_{cv}}{\Delta t} u_i^{s*} + \alpha_i \mathcal{V}_{cv} \left(-\overline{\frac{\partial p^f}{\partial z}} \right) \end{aligned} \quad (4.76)$$

$$\begin{aligned} \left(ac_i^{vs} + K_i \mathcal{V}_{cv} + \frac{\alpha_i \rho^s \mathcal{V}_{cv}}{\Delta t} \right) v_i^s &= \sum_{nb} ac_{nb}^{vs} v_{nb}^s + b^{vs} + \mathcal{V}_{cv} \left(-\overline{\frac{\partial p^s}{\partial r}} \right) + K_i v_i^f \mathcal{V}_{cv} \\ &+ \frac{\alpha_i^* \rho^s \mathcal{V}_{cv}}{\Delta t} v_i^{s*} + \alpha_i \mathcal{V}_{cv} \left(-\overline{\frac{\partial p^f}{\partial r}} \right) \end{aligned} \quad (4.77)$$

The contribution of the momentum interaction term is stated explicitly in these equations in order to clearly represent the coupling between the momentum equations of the two phases. This coupling will be used in the solution procedure presented later. Further manipulations of the unsteady contributions are needed in the

calculation of mass flow rates (see Eqs.(4.91)-(4.92)); therefore, they are also stated explicitly in the previous equations. The solid-phase pressure gradient terms that appear in Eqs.(4.76) and (4.77) are presented as separate terms in the discretized equations for the sake of clarity, however, in the actual implementation, they are included in b^{us} and b^{vs} .

4.5.3 Discretized Solid-Phase Fluctuating Kinetic Energy Equation

For the sake of completeness, the results of the volume integrations of the various source terms in the solid-phase fluctuating kinetic energy equation are presented in this sections. These source terms consist of the work done by the solid-phase pressure, W_p , the viscous-dissipation source term, Φ^s , the diffusion induced by concentration gradient, S_α , the collisional dissipation, γ_c , the drag dissipation, γ_D , and, finally, the transfer of energy between the phases, γ_B .

Solid-Phase Pressure Work Source Term

$$\int_{1aoc} W_p dV = -p_1^s \left(\frac{\partial u^s}{\partial z} + \frac{1}{r} \frac{\partial}{\partial r} (rv^s) \right)_o \mathcal{V}_{1aoc} \quad (4.78)$$

Viscous-Dissipation Source Term

$$\int_{1aoc} \Phi^s dV = \left\{ \left(\mu_{b1}^s - \frac{2}{3} \mu_{e1}^s \right) \left(\frac{\partial u^s}{\partial z} + \frac{1}{r} \frac{\partial}{\partial r} (rv^s) \right)_o^2 + 2\mu_{e1}^s \left(\left(\frac{\partial v^s}{\partial r} \right)_{ele}^2 + \left(\frac{v_o^s}{r_o} \right)^2 + \left(\frac{\partial u^s}{\partial z} \right)_{ele}^2 \right) + \mu_{e1}^s \left(\left(\frac{\partial u^s}{\partial r} \right)_{ele} + \left(\frac{\partial v^s}{\partial z} \right)_{ele} \right)^2 \right\} \mathcal{V}_{1aoc} \quad (4.79)$$

The velocity derivatives are computed using linear interpolations; and

$$\left(\frac{\partial u^s}{\partial z} + \frac{1}{r} \frac{\partial}{\partial r} (rv^s) \right)_o = \left(\frac{\partial u^s}{\partial z} \right)_{ele} + \left(\frac{\partial v^s}{\partial r} \right)_{ele} + \frac{v_o^s}{r_o} \quad (4.80)$$

Concentration-Diffusion Source Term S_α

The diffusion induced by concentration gradient, S_α , is approximated using a derivation similar to that used to approximate the diffusion-source term in the momentum equations. The concentration diffusion flux is given by:

$$\vec{J}_\alpha = \left(k_\alpha^s \frac{\partial \alpha}{\partial z} \right) \vec{i} + \left(k_\alpha^s \frac{\partial \alpha}{\partial r} \right) \vec{j} \quad (4.81)$$

α is assumed to vary linearly within each element. Therefore, the derivatives appearing in Eq.(4.81) are constant over the element, and the concentration-diffusion source contribution can be approximated as follows:

$$\int_{1aoc} S_\alpha dV = \int_a^o \vec{J}_\alpha \cdot \vec{n} 2\pi r ds + \int_o^c \vec{J}_\alpha \cdot \vec{n} 2\pi r ds \quad (4.82)$$

$$\int_a^o \vec{J}_\alpha \cdot \vec{n} 2\pi r ds = 2\pi \frac{r_o + r_a}{2} \left[\overline{k_\alpha^s} \frac{\partial \alpha}{\partial r} x_a - \overline{k_\alpha^s} \frac{\partial \alpha}{\partial z} y_a \right] \quad (4.83)$$

$$\int_o^c \vec{J}_\alpha \cdot \vec{n} 2\pi r ds = 2\pi \frac{r_o + r_c}{2} \left[\overline{k_\alpha^s} \frac{\partial \alpha}{\partial z} y_c - \overline{k_\alpha^s} \frac{\partial \alpha}{\partial r} x_c \right] \quad (4.84)$$

where $\overline{k_\alpha^s}$ is the element average of k_α^s . The expression given in Eq.(4.82) is written without the contribution on the surfaces 1 - a and c - 1 (see Fig. 4.3a) because they cancel out when all appropriate element contributions are assembled to approximate the complete integral conservation equation for an internal node; in the case of boundary nodes, one of both of these contributions may have to be included.

Collisional Dissipation γ_c

$$-\int_{1aoc} \gamma_c dV = -48\eta(1 - \eta) \frac{\alpha_1^2 \rho^s g_{01}}{d} \left(\frac{T_1}{\pi} \right)^{\frac{1}{2}} T_1 \mathcal{V}_{1aoc} \quad (4.85)$$

Drag Dissipation γ_D

$$-\int_{1aoc} \gamma_D dV = -3K_1 T_1 \mathcal{V}_{1aoc} \quad (4.86)$$

Energy Transfer γ_B

$$\int_{1aoc} \gamma_B dV = 3K_1 \left(1 + a_0 \alpha_1^{\frac{3}{2}} \right) T_1 \mathcal{V}_{1aoc} \quad (4.87)$$

Discretized T Equation

The solid-phase fluctuating kinetic energy is always positive. To ensure a positive granular temperature, special attention is needed in the linearization of the source terms. Patankar [130] has suggested the use of positive S_C and negative S_P to ensure that the always-positive dependent variables are indeed positive *during the solution process*. In order to satisfy Patankar's recommendations, the following strategy is adopted in this work: (i) contributions from the collisional and drag dissipation source terms are included in S_P ; (ii) the energy transfer term is included in S_C ; (iii) the solid-phase pressure work, the viscous dissipation, and the diffusion induced by concentration gradients (which may exhibit both positive and negative element contributions) are included either in S_C or S_P , depending on the sign of their respective element contribution. The resulting T discretization equation of the solid phase at a node i can be cast in the following general form:

$$ac_i^T T_i = \sum_{nb} ac_{nb}^T T_{nb} + b^T \quad (4.88)$$

4.5.4 Discretized Equations for p^f and α

Denoting the velocity in the mass-flux terms by \vec{V}^m , the integral mass conservation equation, when applied to the control volume surrounding node i in Fig. 4.2, can be written as follows:

$$\begin{aligned} & \left[\int_a^o \beta \rho \vec{V}^m \cdot \vec{n} 2\pi r ds + \int_o^c \beta \rho \vec{V}^m \cdot \vec{n} 2\pi r ds + \int_{iaoc} \frac{\partial}{\partial t} (\beta \rho) dV \right] \\ & + [\text{similar contributions from other elements surrounding node } i] \quad (4.89) \\ & + [\text{boundary contributions, if applicable}] = 0 \end{aligned}$$

The volume integral involving the unsteady term is approximated using Eq.(4.49) with the specialization $\phi = 1$.

Discretized p^f Equation

In each element, the velocity \vec{V}^m can be expressed in terms of its components in the z and r directions, u^m and v^m , respectively, as shown in Eq. (4.16). Interpolation

functions for u^m and v^m have to be first prescribed in order to approximate the fluid-phase mass flux integrals in Eq. (4.89). First, the fluid-phase discretized momentum equations, Eqs.(4.74) and (4.75), are rewritten in the following manner:

$$u_i^f = \hat{u}_i^f + d_i^{uf} \left(-\frac{\partial p^f}{\partial z} \right) \quad v_i^f = \hat{v}_i^f + d_i^{vf} \left(-\frac{\partial p^f}{\partial r} \right) \quad (4.90)$$

where

$$\hat{u}_i^f = \frac{\sum_{nb} ac_{nb}^{uf} u_{nb}^f + b^{uf} + K_i u_i^f \mathcal{V}_{cv} + \frac{\rho^f \mathcal{V}_{cv}}{\Delta t} (\epsilon_i^* u_i^{f*} - \epsilon_i u_i^f)}{ac_i^{uf} + K_i \mathcal{V}_{cv}} \quad d_i^{uf} = \frac{\epsilon_i \mathcal{V}_{cv}}{ac_i^{uf} + K_i \mathcal{V}_{cv}} \quad (4.91)$$

$$\hat{v}_i^f = \frac{\sum_{nb} ac_{nb}^{vf} v_{nb}^f + b^{vf} + K_i v_i^f \mathcal{V}_{cv} + \frac{\rho^f \mathcal{V}_{cv}}{\Delta t} (\epsilon_i^* v_i^{f*} - \epsilon_i v_i^f)}{ac_i^{vf} + K_i \mathcal{V}_{cv}} \quad d_i^{vf} = \frac{\epsilon_i \mathcal{V}_{cv}}{ac_i^{vf} + K_i \mathcal{V}_{cv}} \quad (4.92)$$

For the evaluation of the fluid-phase mass fluxes on the faces $a-o$ and $o-c$ (Fig. 4.3), the fluid-phase velocity components are written as:

$$u^m = \hat{u}^f + d^{uf} \left(-\frac{\partial p^f}{\partial z} \right)_{ele} \quad v^m = \hat{v}^f + d^{vf} \left(-\frac{\partial p^f}{\partial r} \right)_{ele} \quad (4.93)$$

where \hat{u}^f , \hat{v}^f , d^{uf} and d^{vf} are interpolated linearly from the corresponding values at the vertices of the element. This interpolation for u^m and v^m is borrowed from the work of Prakash and Patankar [135] and Saabas [149]. It prevents the occurrence of spurious pressure oscillations in the proposed CVFEM. Similar interpolation of the velocity components in the mass-flux terms have been successfully used by Rice and Schnipke [145], Peric et al. [131], and Rhie and Chow [143]. It should be noted, however, that this interpolation procedure may not be well-suited for Newton-type linearizations of the convective terms in the fluid-phase momentum equations. In the proposed CVFEM, however, this mass flux interpolation does not pose any problems because successive substitution (or Picard) linearization is used for the convective terms in the fluid-phase momentum equations.

In the derivation of algebraic approximations to integrals of fluid-phase mass flow rates, u^m and v^m are interpolated in each element by the functions given in Eq.(4.93). The same functions are also used to approximate integrals that represent the mass flow rates in the fluid-phase momentum equations. They are also used to compute u_{av}^m and v_{av}^m in Eq.(4.28). Using these interpolation functions to approximate the integrals in Eq.(4.89), the contributions of element 123 (Fig. 4.3) to the fluid-phase

mass conservation equation for the node 1 are expressed as:

$$\int_a^o \epsilon \rho^f \vec{V}^m \cdot \vec{n} 2\pi r ds = 2\pi \frac{\epsilon_r}{6} \{ -y_a [\rho^f u_o^m (r_a + 2r_o) + \rho^f u_a^m (2r_a + r_o)] \\ + x_a [\rho^f v_o^m (r_a + 2r_o) + \rho^f v_a^m (2r_a + r_o)] \} \quad (4.94)$$

$$\int_o^c \epsilon \rho^f \vec{V}^m \cdot \vec{n} 2\pi r ds = 2\pi \frac{\epsilon_t}{6} \{ -x_c [\rho^f v_o^m (r_c + 2r_o) + \rho^f v_c^m (2r_c + r_o)] \\ + y_c [\rho^f u_o^m (r_c + 2r_o) + \rho^f u_c^m (2r_c + r_o)] \} \quad (4.95)$$

where u_o^m , v_o^m , u_a^m , v_a^m , u_c^m and v_c^m are given by Eqs.(4.93) and ϵ_r and ϵ_t are obtained using the modified MAW scheme given by Eqs.(4.36) and (4.38), respectively, and the relation $\alpha + \epsilon = 1$.

Addition of the contributions of the other elements surrounding the point i yields the complete discretized fluid-phase continuity equation.

When explicit expressions for the pressure gradient terms are substituted into the interpolation functions for the mass-flux velocity components (Eq.(4.93)), and then these interpolation functions are used in the element contributions to the discretized fluid-phase continuity equations (Eqs.(4.94) and (4.95)), discretized equations for p^f are obtained.

A compact representation of the discretized p^f equation for a typical node i is the following:

$$ac_i^p p_i^f = \sum_{nb} ac_{nb}^p p_{nb}^f + b^p \quad (4.96)$$

Discretized α Equation

For the evaluation of the solid-phase mass fluxes on the faces $a-o$ and $o-c$ (Fig. 4.3), the mass-flux velocity components are written as:

$$u^m = u^s \quad v^m = v^s \quad (4.97)$$

where u^s , v^s are interpolated linearly from the corresponding values at the vertices of the element. Using these interpolation functions to approximate the integrals in Eq.(4.89), the contributions of element 123 (Fig. 4.3) to the solid-phase mass

conservation equation for the node 1 are expressed as:

$$\int_a^o \alpha \rho^s \vec{V}^s \cdot \vec{n} 2\pi r ds = 2\pi \frac{\alpha_r}{6} \{-y_a[\rho^s u_o^s(r_a + 2r_o) + \rho^s u_a^s(2r_a + r_o)] \\ + x_a[\rho^s v_o^s(r_a + 2r_o) + \rho^s v_a^s(2r_a + r_o)]\} \quad (4.98)$$

$$\int_o^c \alpha \rho^s \vec{V}^s \cdot \vec{n} 2\pi r ds = 2\pi \frac{\alpha_t}{6} \{-x_c[\rho^s v_o^s(r_c + 2r_o) + \rho^s v_c^s(2r_c + r_o)] \\ + y_c[\rho^s u_o^s(r_c + 2r_o) + \rho^s u_c^s(2r_c + r_o)]\} \quad (4.99)$$

where where u_o^s , v_o^s , u_a^s , v_a^s , u_c^s and v_c^s are given by linear interpolation of u^s and v^s values at the vertices, and α_r and α_t are obtained using the modified MAW scheme given by Eqs.(4.36) and (4.38), respectively.

Addition of the contributions of the other elements surrounding the point i yields the complete discretized solid-phase continuity equation. The solid-phase continuity equation provide a set of discretized equations, which are used to compute the solid-phase concentration, α ; ϵ is computed using $\alpha + \epsilon = 1$.

A compact representation of the discretized α equation for a typical node i is the following:

$$ac_i^\alpha \alpha_i = \sum_{nb} ac_{nb}^\alpha \alpha_{nb} + b^\alpha \quad (4.100)$$

Details of the numerical implementation of the element fluid- and solid-phase mass flow rates can be found in Appendix B.

Discussion

Carver [30] suggests subtraction of the fluid-phase continuity equation from the solid-phase continuity equation to derive a discretization equation for α , and an addition of these equations in the derivation of the discretization equation for p^f , so as to explicitly account for the coupling between the phases in the calculation of α and p^f . This treatment is appropriate only when *local* mass conservation is ensured over each control-volume for each phase, individually, as in the finite volume method used by Carver [30]. In the proposed co-located equal-order CVFEM, for problems that involve inflows and outflows, α is prescribed at all nodes located on the inflow boundaries, and p^f is prescribed at one (or more) node(s) located at

the outflow boundaries: thus, for the control volumes surrounding the nodes on the inflow boundaries, *local* mass conservation of the solid phase is not necessarily satisfied; and *local* mass conservation of the fluid phase is not necessarily respected for the control volumes associated with the nodes on the outflow boundaries. Thus, at nodes on the inflow and outflow boundaries, the treatment proposed by Carver [30] could not be incorporated into the proposed CVFEM. Furthermore, the construction of a fluid-phase pressure equation based on the sum of the fluid- and solid-phase continuity equations can be realized only when the solid-phase mass-flow related velocities are calculated using expressions similar to the fluid-phase mass-flow related velocities, Eq.(4.93). The use of such solid-phase mass-flow related velocities have been implemented for the solution of dilute gas-solid particle flows [114, 115, 117] but this approach leads to severe convergence problems at high solid-phase concentrations. Instead, as was described earlier in this section, the discretization equations for α are obtained from the continuity equation for the solid phase, and the solid-phase mass-flow related velocities at the integration points are obtained from linear interpolation of the solid-phase nodal velocities; and only the fluid-phase continuity equation is used to derive the discretization equations for p^f . Therefore, the coupling between the two phases is not directly accounted for in the calculation of α and p^f , but this did not lead to any major difficulties. It should be also noted that in *dilute* gas-solid particle flows, the proposed discretization equations for α do not need any special treatment to ensure physically realistic solutions [114, 115, 117], while the linear combination approach suggested by Carver [30] does: the b^α term of the proposed discretized concentration equation (Eq.(4.100)) is always equal to or greater than zero and so are all the coefficients in this equation. This feature ensures that $\alpha \geq 0$. In addition, since $\alpha \ll 1$ in *dilute* gas-solid particle flows, there is no need to incorporate any special procedures to ensure that $\alpha < 1$ during the iterative solution procedure. However, for problems involving higher solid-phase concentrations, appropriate choice of the time step was needed to ensure that $\alpha \leq \alpha_{MX}$ throughout the solution procedure.

Another important feature of the formulation proposed in this work is that in Eqs.(4.91) and (4.92), the unsteady contribution is *all* included in the numerator of \hat{u}^f and \hat{v}^f : thus, when the steady-state solution is reached, the unsteady contribution is zero, and the mass flux interpolation is *independent of the time step*. Each of these variables can be defined in such a way that parts of the unsteady terms appear in

the numerators of \hat{u}^f and \hat{v}^f , and the other parts are included in the denominators of \hat{u}^f , d^{uf} , \hat{v}^f , and d^{vf} . This would be inappropriate since the mass flux interpolation would then *depend on the time step* even under steady-state conditions.

4.6 Boundary Conditions

In this work, it is assumed that the domain boundaries remain at fixed spatial locations, and they could coincide with solid walls, symmetry surfaces, and fluid-phase and/or solid-phase inlet and outlet regions. All these boundaries can be accounted for in a general formulation by noting that only two types of boundary conditions are encountered: specified value or given gradient. Gas-solid particle flows with free boundaries and/or moving boundaries are not within the scope of this work.

The following derivation pertains to the discretization equation for node 1 of the element 123 shown in Fig. 4.3b. The link between the points 1 and 2 is assumed to coincide with the boundary of the domain of interest.

4.6.1 Specified Value

When the value of the dependent variable, ϕ , is given at the boundary node, and denoted by ϕ_{SP} , the discretization equation associated with that node is written as follows:

$$ac_i^\phi = 1 \quad , \quad ac_{nb}^\phi = 0 \quad , \quad b_i^\phi = \phi_{SP} \quad (4.101)$$

4.6.2 Specified Gradient

When the gradient of the dependent variable normal to the boundary is given, say $\left(\frac{\partial\phi}{\partial n}\right)_{SP}$, the combined convection-diffusion flux of ϕ normal to the boundary is given by:

$$\vec{J} \cdot \vec{n} = \beta\rho V_n \phi - \Gamma_c \left(\frac{\partial\phi}{\partial n}\right)_{SP} \quad (4.102)$$

where V_n is the velocity component normal to the boundary. With reference to node 1 in Fig. 4.3b, the values of β , ρ , Γ_e and $\left(\frac{\partial\phi}{\partial n}\right)_{SP}$ are assumed to be constant on surface 1-a. Thus, the contribution of boundary link 1-a to the conservation equation for the control volume associated with node 1 is given by:

$$\int_1^a \vec{J} \cdot \vec{n} 2\pi r ds = \beta \rho \int_1^a V_n \phi 2\pi r ds - \Gamma_e \left(\frac{\partial\phi}{\partial n}\right)_{SP} \mathcal{A}_{1-a} \quad (4.103)$$

where

$$\mathcal{A}_{1-a} = 2\pi l_{1-a} r_m \quad l_{1-a} = [(r_a - r_1)^2 + (z_a - z_1)^2]^{1/2} \quad (4.104)$$

The convection contribution is evaluated using Simpson's rule. The variations of V_n and β over the link 1-2 are approximated with linear and piecewise prevailing interpolations, respectively. The ϕ -interpolation has to be consistent with the interpolation scheme used in the convection terms: when the FLO scheme is used, ϕ is interpolated linearly; when the MAW scheme is used, the prevailing assumption is appropriate. Therefore, the convection contribution, when the FLO scheme is used, is given by:

$$\int_1^a \beta \rho V_n \phi 2\pi r ds = 2\pi \beta_1 \frac{l_{1-a}}{12} [\phi_1 (2\rho(V_n)_1 r_1 + 6\rho(V_n)_m r_m + \rho(V_n)_a r_a) + \phi_2 (\rho(V_n)_a r_a + 2\rho(V_n)_m r_m)] \quad (4.105)$$

and the convection contribution, when the MAW scheme is used, is given by:

$$\int_1^a \beta \rho V_n \phi 2\pi r ds = 2\pi \beta_1 \phi_1 \frac{l_{1-a}}{6} [\rho(V_n)_1 r_1 + 4\rho(V_n)_m r_m + \rho(V_n)_a r_a] \quad (4.106)$$

This derivation has been done for the general ϕ -equation. A similar treatment is applied to the momentum equations.

For the continuity equation, only boundaries having mass flow crossing them have non-zero contributions. Thus the contribution of boundary link 1-a to the integral mass conservation equation for the control volume associated with node 1 can be expressed as:

$$\int_1^a \beta \rho V_n 2\pi r ds = 2\pi \beta_1 \frac{l_{1-a}}{6} [\rho(V_n)_1 r_1 + 4\rho(V_n)_m r_m + \rho(V_n)_a r_a] \quad (4.107)$$

It should be noted here that the mass flow rates across the *boundary edges*, such as 1-a in Fig. 4.3b, are calculated using the latest available values of the nodal velocity \vec{V} , not \vec{V}^m . Only the mass flow rates across control-volume faces in the interior of the domain are calculated using \vec{V}^m .

4.6.3 Special Treatments

In the proposed CVFEM, special treatments are needed for \hat{u}^f , \hat{v}^f , d^{uf} and d^{vf} on boundaries with prescribed fluid-phase velocities, such as walls and inflow boundaries. At nodes which lie on such boundaries, d^{uf} and d^{vf} are set to zero, and, therefore,

$$\hat{u}^f = u_{SP}^f \quad \hat{v}^f = v_{SP}^f \quad (4.108)$$

At outflow boundaries, the treatment recommended by Patankar [130] is used: it is assumed that convection is the dominant transport process and diffusion is negligible. This is handled by dropping the $-\Gamma_e \left(\frac{\partial \phi}{\partial n} \right)$ term in Eq. (4.102).

4.7 Overall Solution Algorithm

The discretization equations form two sets of coupled nonlinear algebraic equations. In this work, *at each time step*, a modified version of the iterative variable adjustment procedure proposed by Saabas [149] for single-phase flow, and recently applied to dilute gas-solid particle flows by Masson and Baliga [114, 115, 117], was used to solve the mathematical model:

1. Start with guessed or available velocities, fluid-phase pressure, solid-phase concentration and granular temperature fields.
2. Calculate the fluid- and solid-phase diffusion coefficients, and the solid-phase pressure, using the constitutive equations.
3. Calculate coefficients in the discretized unsteady momentum equations *without* including contributions of the fluid-phase pressure-gradient terms.
4. Calculate \hat{u}^f , \hat{v}^f , d^{uf} , and d^{vf} .
5. Calculate coefficients in the discretized fluid-phase pressure equations, and solve these equations to obtain updated values of p^f .

6. Add contributions of the fluid-phase pressure-gradient terms to the appropriate coefficients of the discretized z -momentum equations calculated in Step 3, and solve for u^f and u^s , *simultaneously*.
7. Add contributions of the fluid-phase pressure-gradient terms to the appropriate coefficients of the discretized r -momentum equations calculated in Step 3, and solve for v^f and v^s , *simultaneously*.
8. Calculate coefficients of the discretized equations for α , and solve these equations to obtain updated values of α .
9. Calculate ϵ ($= 1 - \alpha$).
10. Calculate coefficients in the discretized granular temperature equations, and solve these equations to obtain updated values of T .
11. Return to Step 2, and repeat until appropriate convergence criteria are satisfied.

If the unsteady formulation is used only to facilitate the solution of steady-state problems, then it is not necessary to do Step 11 in this procedure. Rather, Steps 2-10 could be repeated until steady-state conditions prevail. In this work, the solution was considered to be converged when the non-dimensional average, absolute, residue for each set of discretization equations was less than 10^{-10} . Depending on the problem, global values, such as the separator efficiency in a problem involving a split-flow inertial separator (Chapter 6), were also monitored, and it was stipulated that the absolute value of the relative change from one iteration to the next (or from one time step to the next in steady-state problems) should be less than 10^{-6} ; in most of the calculations, however, it was found that the convergence criterion based on the non-dimensional average, absolute, residue is the more demanding one.

In this work, in order to facilitate implementation and testing of the proposed CVFEM, structured grids were used: the nodes in the finite element mesh lie along nonorthogonal lines that allow (I,J) indexing. Thus, in steps 5, 8 and 10, a line Gauss-Seidel algorithm based on the tri-diagonal matrix algorithm [130] was used to solve the discretized equations for p^f , α and T , respectively. In steps 6 and 7, a line Gauss-Seidel method based on a coupled-equation line solver [84, 62, 130] was used.

These ideas could be extended to unstructured-grid implementations by employing point, rather than line, Gauss-Seidel methods. More sophisticated approaches, such as direct, or block decomposition, techniques based on sparse matrix algorithms may also prove viable for use with unstructured grids. To improve the rate of convergence, block-correction procedures and multigrid techniques, for example, can be included. In this work, however, these options were not considered.

The proposed linearization of the momentum coupling source terms allows a direct accounting of the coupling between the solid- and fluid-phase momentum equations in the above-mentioned solution algorithm. The simultaneous solution of the solid- and fluid-phase momentum equations in Steps 6 and 7 is an important element in the robustness of the proposed algorithm. The unsteady formulation also contributes significantly to the robustness of the overall solution procedure by ensuring a similar evolution of the solutions of the fluid- and solid-phase sets of equations.

The modified MAW scheme that is used to interpolate the solid-phase concentration ensures positive coefficients in the discretized solid-phase concentration equation. Furthermore, the solid-phase concentration equation is based on the solid-phase continuity equation only: this yields zero values of b^α everywhere in the domain of interest except at points where the concentration is known. Zero b^α , along with positive coefficients, results in discretized equations that admit only positive values of α , which is a physical requirement of the volume concentration. At high solid-phase concentrations, the discretized solid-phase concentration equations can, in principle, admit values larger than the maximum packing limit, α_{MX} . However, when the concentration is large, the solid-phase pressure appearing in the momentum equation tends to disperse the solid particles and, therefore, reduce the solid-phase volume concentration to values below α_{MX} . However, in the context of the above-mentioned iterative solution algorithm, the effects of the solid-phase pressure are not always large enough to prevent α from reaching values equal to or larger than the maximum packing limit, α_{MX} . In such situations, the use of a smaller time step has been found to be useful in alleviating this difficulty.

Chapter 5

Single-Phase Flow Simulations

The validity of the proposed CVFEM for two-dimensional, axisymmetric, *single-phase* [116] fluid flow and heat transfer is demonstrated in this chapter by its application to four problems, and comparisons of the solutions with available numerical and experimental results. In general, the MAW scheme produces discretized equations that are more robust than those obtained with the FLO scheme, with respect to solution with the iterative variable adjustment algorithm discussed in the previous chapter. However, the results obtained with FLO, when it converges, are more accurate than those obtained with MAW, for the same grid. Therefore, most of the results presented here were obtained using the FLO scheme. However, for one of the test problems, involving laminar natural convection in a cylindrical enclosure, results obtained with both FLO and MAW are presented in order to enable a comparative evaluation of these schemes: detailed grid independence checks and CPU times are also presented for this test problem. It should also be noted that at high Reynolds numbers, good initial guess values of the u^f , v^f , and p^f fields were essential for convergence of the FLO scheme: in such cases, a solution obtained with the MAW scheme was fed as the initial guess to the FLO scheme.

5.1 Developing Laminar Flow in a Pipe

Problem Statement

Laminar flow of a constant-property Newtonian fluid in the inlet region of a circular pipe is investigated in this problem. The fluid enters the pipe of radius R with a uniform velocity profile: $u^f = \bar{u}^f$, $v^f = 0$. The ratio of the length to the radius of the pipe is $\frac{L}{R} = 6$. The results obtained with the proposed CVFEM are compared to those of Friedmann et al. [60].

Governing Equations

The governing equations are the continuity, z - and r -momentum equations, Eqs. (3.119)-(3.121). For negligible body force, or for body-force terms that can be absorbed into an effective pressure, the source terms in the momentum equations are the following:

$$S_z^f = S_r^f = 0 \quad (5.1)$$

The boundary conditions are the prescribed uniform velocity profile at the inlet, fully developed conditions at the outlet, and the no-slip condition on the wall.

Results

The Reynolds number, $Re = \frac{\rho^f \bar{u}^f 2R}{\mu^f}$, considered in this problem is 40. A nonuniform grid, with 111 nodes in the z direction and 61 nodes in the r direction, was used in this test. Preliminary test with 40 X 15 and 56 X 31 grids had established that the 111 X 61 grid produces essentially grid independent results: the absolute difference in $\frac{u^f}{\bar{u}^f}$ values produced by 56 X 31 and 111 X 61 grids is less than 0.23%. In the region $0 \leq \frac{z}{R} \leq 1.25$, the u^f velocity profile has a local minimum on the axis of the pipe and a maximum at a value of $r > 0$. This behaviour has been observed experimentally [23]. Table 5.1 presents the local minimum and maximum u^f velocities at several axial locations downstream of the entrance. Table 5.2 presents a comparison of the nondimensional hydrodynamic entrance length, defined

as the distance along the axis where the centerline velocity reaches 99% of its fully developed value. The results obtained with the proposed CVFEM are compared with the finite difference solution of Friedmann et al. [60]. The CVFEM results match the solution of Friedmann et al. [60] very well: the maximum percentage difference in the results presented in Table 5.1 is 0.09%; the nondimensional hydrodynamic entrance lengths presented differ by 0.80%. This simulation illustrates the capabilities of the proposed formulation to accurately capture the fluid flow phenomena encountered in the entrance regions of pipes.

Re	$\frac{z}{R}$	Proposed CVFEM		Friedmann et al. [60]	
		$\frac{u_{min}^f}{\bar{u}^f}$	$\frac{u_{max}^f}{\bar{u}^f}$	$\frac{u_{min}^f}{\bar{u}^f}$	$\frac{u_{max}^f}{\bar{u}^f}$
40	0.25	1.048	1.219	1.048	1.219
	0.50	1.173	1.313	1.174	1.314
	0.75	1.325	1.404	1.326	1.405
	1.00	1.465	1.494	1.466	1.495
	1.25	1.579	1.583	1.580	1.583

Table 5.1: Developing laminar flow in a pipe: u_{min}^f and u_{max}^f values

Re	Proposed CVFEM	Friedmann et al. [60]
40	4.92	4.88

Table 5.2: Developing laminar flow in a pipe: nondimensional hydrodynamic entrance length

5.2 Laminar Flow in a Pipe with a Sudden Contraction

Problem Statement

The behaviour of laminar flow in a straight pipe with a sudden contraction in its diameter is investigated in this problem. This simulation was conducted with the geometry proposed by Durst and Loy [52]. The inlet pipe has a diameter D of 19.1 mm, while the diameter of the pipe after the contraction is 10.2 mm. The computational domain extends 25 mm upstream of the contraction and 20 mm downstream. At the inlet of the pipe, the flow is considered as fully developed. The length of the pipe downstream of the contraction is long enough to ensure that the following outflow treatment is satisfactory: $\frac{\partial u^f}{\partial z} = 0$ and $v^f = 0$.

Governing Equations

The governing equations are the same as the ones presented in the previous section for the problem involving developing laminar flow in a pipe.

The boundary conditions are prescribed fully developed velocity profile at the inlet, outflow treatment at the outlet, and no-slip conditions on the pipe wall.

Results

Simulations were conducted for two values of Reynolds number, Re_D , based on the inlet diameter D and the average inlet velocity \bar{u}^f , namely, 196 and 968. All simulations were done with a 72 X 97 non-uniform grid with a concentration of nodes in the recirculating zones, one upstream and one downstream of the contraction. The presented results consist of streamlines computed using the proposed CVFEM, and comparisons of the computed axial and radial velocity profiles at several axial positions with the experimental data obtained by Durst and Loy [52].

Numerical simulations on 37 X 51, 72 X 97 and 143 X 193 grids established that the 72 X 97 grid produces essentially grid-independent results. The results of this

grid independence study are well-illustrated by the variation of the radial velocity profile at station $z/D = -0.052$ for the three different grids (see Fig. 5.2b): the radial velocity profiles predicted by the 72 X 97 and 143 X 193 grids are so close to each other that it is impossible to distinguish one from the other. All other results showed similar or better grid-independence. Therefore, simulations done on the 72 X 97 grid were used to obtain all other results presented in this section.

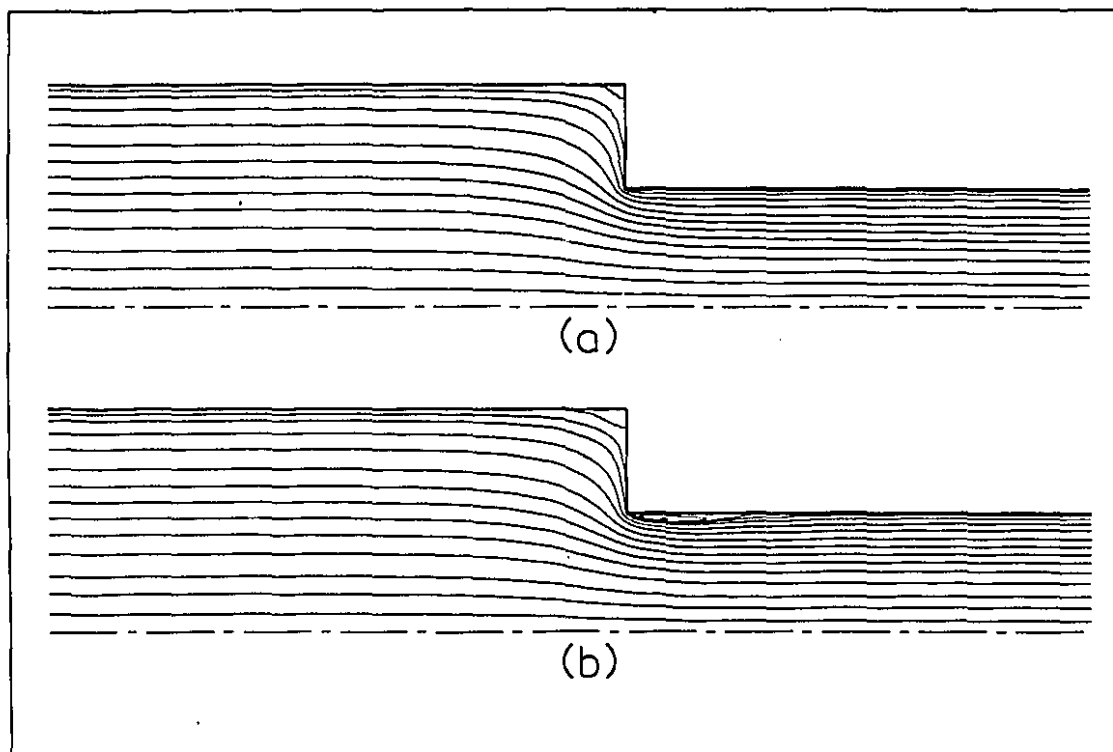


Figure 5.1: Streamline patterns for laminar flow in a pipe with a sudden contraction: (a) $Re_D = 196$; (b) $Re_D = 968$.

For $Re_D = 196$, there is only one recirculating zone situated upstream of the contraction, as can be seen from the streamlines plotted in Fig. 5.1a. However, at $Re_D = 968$, an additional recirculating zone appears just downstream of the contraction (see Fig. 5.1b). For $Re_D = 196$, Fig. 5.2a presents the evolution of the axial velocity profile along the pipe: $\frac{z}{D} = 0$ at the location of the contraction. The agreement with the experimental data of Durst and Loy is very good: both the shape of the profiles and the magnitude of the velocity are well predicted. It is interesting to note the velocity over-shooting phenomena, exhibited by both the numerical and experimental results, just downstream of the contraction. The computed radial

velocity profiles, for $Re_D = 196$, presented in Fig. 5.2b do not agree as well with the experimental data: the difference in the magnitude is up to 50% at the station $z/D = -0.052$.

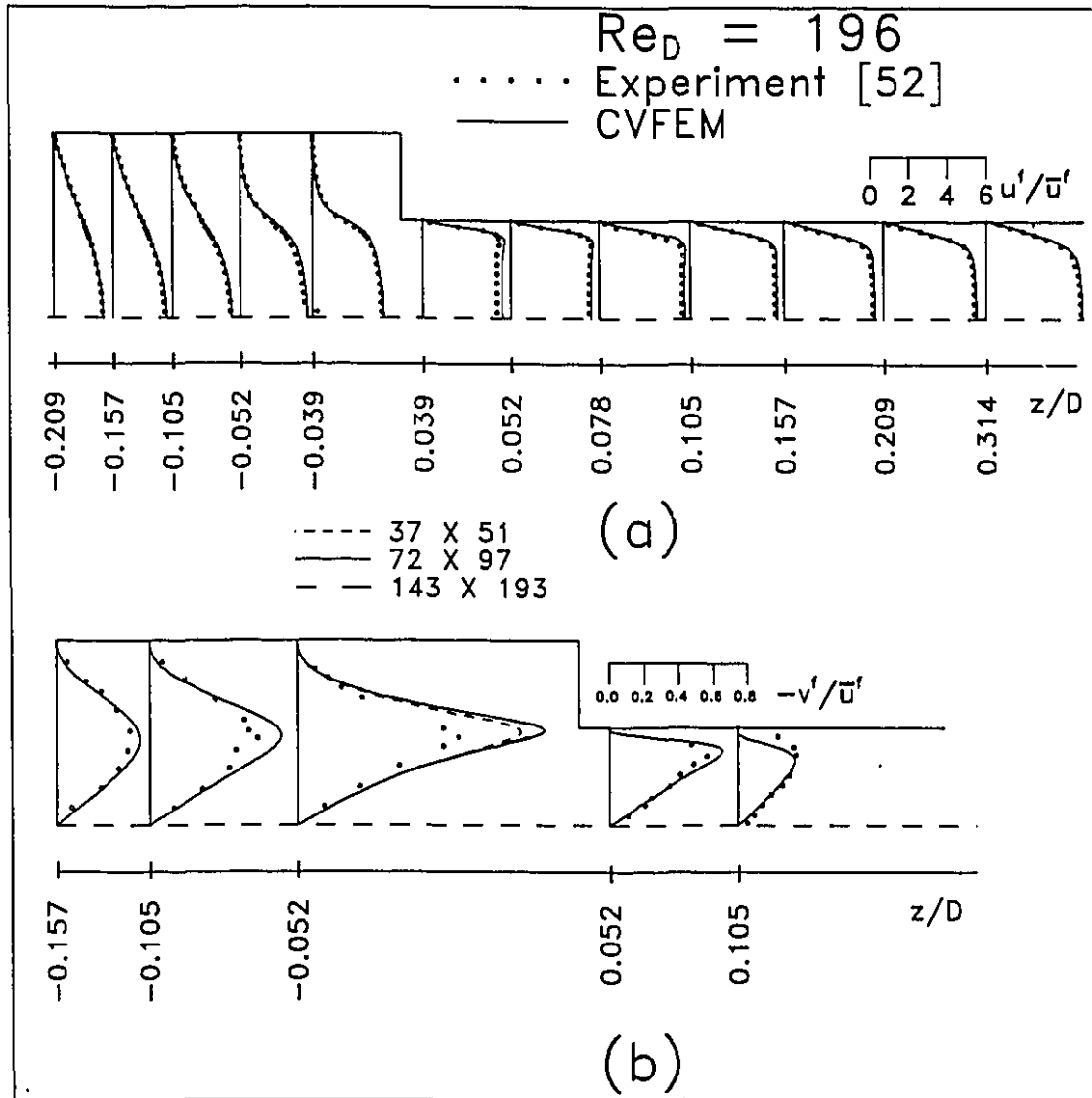


Figure 5.2: Laminar flow in a pipe with a sudden contraction for $Re_D = 196$: (a) axial velocity ; (b) radial velocity

The axial velocity profiles for $Re_D = 968$ are shown in Fig. 5.3a. The proposed CVFEM predicts a recirculating zone downstream of the contraction. This is clearly confirmed by the shape of the axial velocity profiles downstream of the contraction: a zone of negative axial velocity exists near the wall. The computations done by

Durst and Loy [52] also indicates the presence of a recirculating zone downstream of the contraction. No such affirmation can be drawn from their experimental velocity profiles, however, since there are no experimental data close enough to the wall. The agreement between the CVFEM and the experimental results is again good, but not as good as in the case of $Re_D = 196$. The magnitude of the radial velocity profiles, presented in Fig. 5.3b, do not agree very well with the experimental data, but the shapes of these profiles are close to the experimental ones.

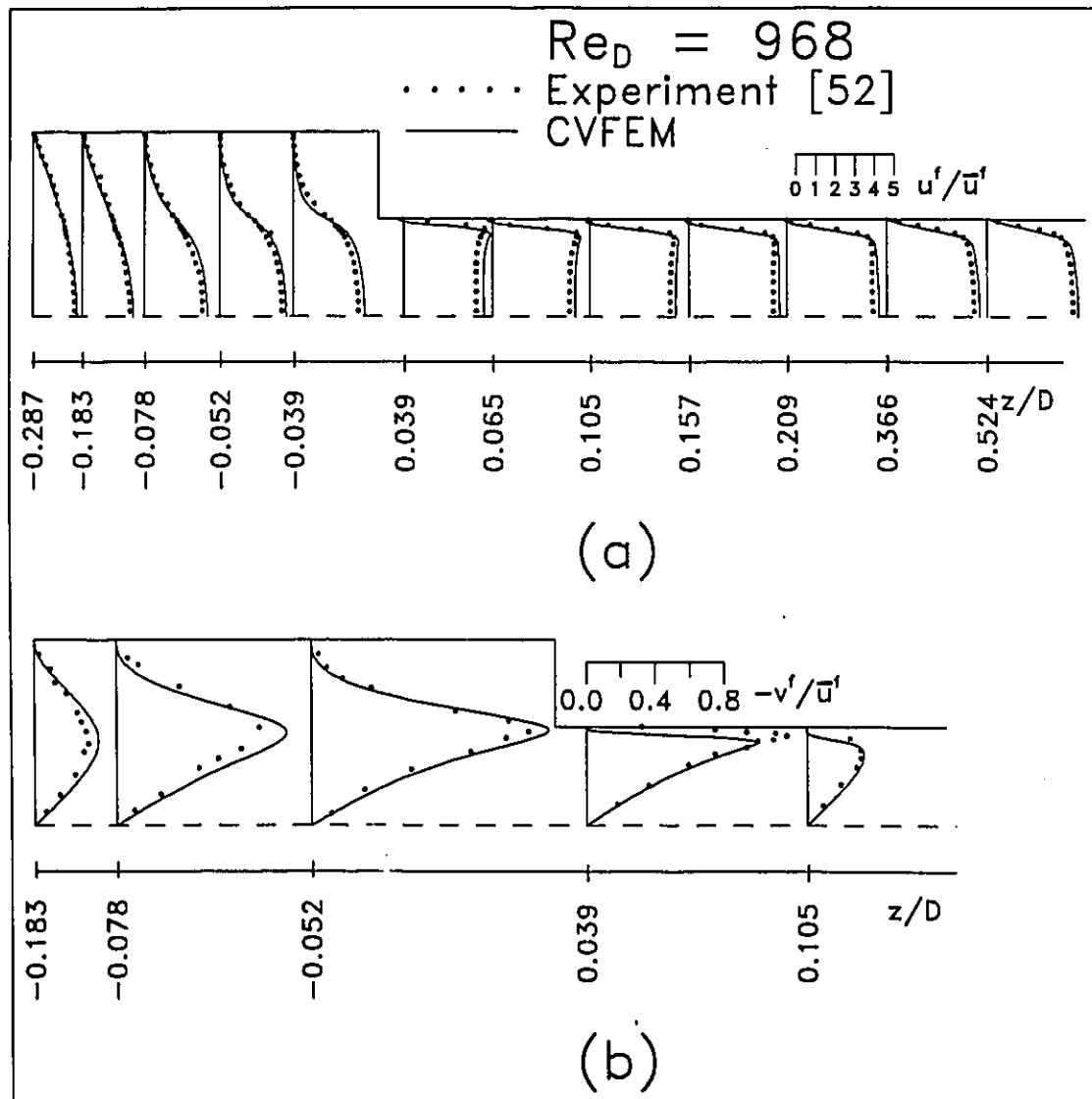


Figure 5.3: Laminar flow in a pipe with a sudden contraction for $Re_D = 968$: (a) axial velocity ; (b) radial velocity

5.3 Laminar Natural Convection in a Cylindrical Enclosure

Problem Statement

Axisymmetric buoyancy-driven laminar flow in a cylindrical cavity is considered in this test problem, schematically illustrated in Fig. 5.4. A Newtonian fluid, with a temperature dependent viscosity, is confined within the cylindrical region $0 \leq r \leq R$, $0 \leq z \leq L$. The lateral boundary, $r = R$, is insulated, and the horizontal surfaces $z = 0$ and $z = L$ are maintained at constant temperatures T_H^f and T_C^f , respectively, where $T_H^f > T_C^f$. The superscript f is used on T to clearly identify it as the fluid thermodynamic temperature, and prevent any confusion with the solid-phase granular temperature introduced earlier in Chapter 3. The acceleration due to gravity, \vec{g} , is directed in the negative z direction. The results obtained with the proposed CVFEM are compared with those obtained by Liang et al. [103] using a finite difference method (FDM).

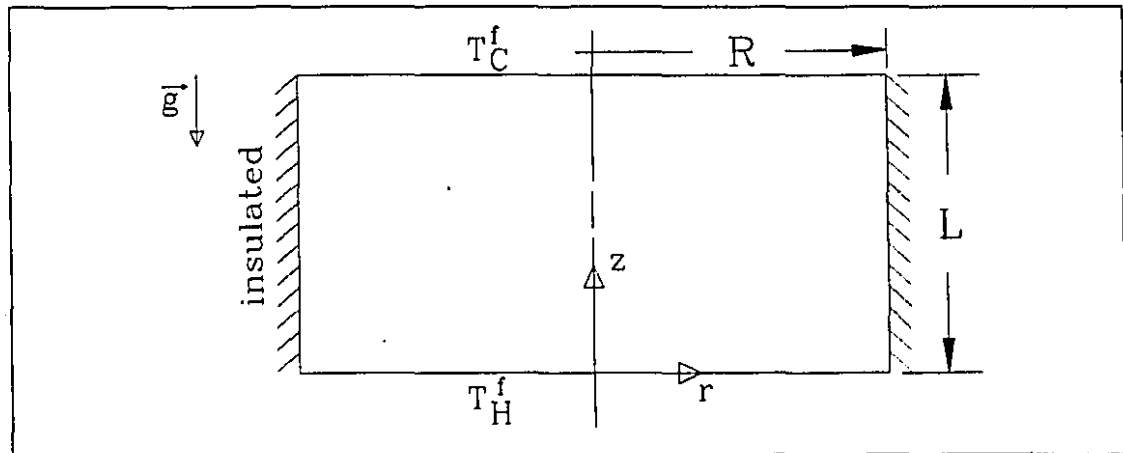


Figure 5.4: Schematic representation of laminar natural convection in a cylindrical enclosure

Governing Equations

In this problem, the governing equations are the z - and r -momentum, continuity and energy equations. The Boussinesq approximation is used: thus, density is

assumed to be a constant, $\rho^f = \rho_o^f$, in all terms, except the buoyancy term in the z momentum equation, in which $\rho^f = \rho_o^f(1 - \zeta^f(T^f - T_H^f))$. Here, ζ^f is the thermal volumetric expansion coefficient of the fluid. The specific heat, C_p^f , and the thermal conductivity, k^f , of the fluid are assumed to remain constant.

The source terms in the momentum equations can be written as follows:

z - momentum

$$S_z^f = -\rho_o^f g + \zeta^f g \rho_o^f (T^f - T_H^f) + \frac{\partial \mu^f}{\partial z} \frac{\partial u^f}{\partial z} + \frac{\partial \mu^f}{\partial r} \frac{\partial v^f}{\partial z} \quad (5.2)$$

r - momentum

$$S_r^f = \frac{\partial \mu^f}{\partial z} \frac{\partial u^f}{\partial r} + \frac{\partial \mu^f}{\partial r} \frac{\partial v^f}{\partial r} \quad (5.3)$$

The temperature distribution is governed by the *energy equation*:

$$\frac{\partial}{\partial z} (\rho_o^f u^f T^f) + \frac{1}{r} \frac{\partial}{\partial r} (r \rho_o^f v^f T^f) = \frac{\partial}{\partial z} \left(\rho_o^f \lambda^f \frac{\partial T^f}{\partial z} \right) + \frac{1}{r} \frac{\partial}{\partial r} \left(r \rho_o^f \lambda^f \frac{\partial T^f}{\partial r} \right) \quad (5.4)$$

where λ^f is the thermal diffusivity of the fluid ($\lambda^f = \frac{k^f}{\rho_o^f C_p^f}$).

In accordance with the assumptions of Liang et al. [103], the viscosity is a function of the temperature, according to the following expression:

$$\mu^f = \mu_C^f \left(1 + \eta^f \frac{T^f - T_C^f}{T_H^f - T_C^f} \right) \quad (5.5)$$

where η^f is a parameter for this problem. The other non-dimensional parameters are $\frac{R}{L}$, the Prandtl number, Pr, and the Grashof number, Gr:

$$\text{Pr} = \frac{\mu_C^f}{\rho_o^f \lambda^f} \quad \text{Gr} = \frac{g \zeta^f (T_H^f - T_C^f) L^3 \rho_o^{f2}}{\mu_C^{f2}} \quad (5.6)$$

Results

In this problem, two steady-state solutions, one with upflow and the other with downflow at the axis, have been found experimentally and numerically [103]. Numerically, a specific steady-state regime can be obtained by using the proper initial temperature distribution: to get upflow at the axis, the lighter fluid (hot fluid) has

to be near the axis initially; for the downflow solution, initially, the heavier fluid (cold fluid) has to be near the axis. The numerical results presented in this section were computed for $\frac{R}{L} = 1$, $Pr = 2500$, $Gr = 2$ and $\eta^f = -0.2$. Preliminary computations on uniform 11 X 11, 31 X 31 and 51 X 51 grids (see Fig. 5.5) demonstrate that the 51 X 51 grid is fine enough to get grid-independent results when the FLO scheme is used. Fig. 5.5 also presents the numerical results obtained with the MAW scheme. As was expected, with the coarse grid (11 X 11), the MAW-scheme solution is not as accurate as that of the FLO scheme. For the grid which is considered to produce grid-independent results with the FLO scheme (51 X 51), the solution obtained with the MAW scheme is in pretty good agreement with the FLO-scheme solution. However, the solution of the MAW scheme on the 51 X 51 grid is not as grid-independent as that of the FLO scheme. In terms of convergence, this test problem is more challenging than the other three test problems presented in this chapter. Accordingly, the number of iterations¹ and the CPU times needed to achieve convergence are presented only for this test problem, both for the FLO and the MAW schemes (see Table 5.3). A Hewlett-Packard HP-720 Unix-based workstation was used to solve this problem, with a HP FORTRAN 77 compiler running at optimization level 3. Convergence was considered to be achieved when both the absolute value of the relative change in the average Nusselt number and the non-dimensional average, absolute, residue of all the equations were less than 10^{-6} and 10^{-10} , respectively. The temperature distributions for the upflow and downflow regimes are presented in Figs. 5.6a and 5.6b. The solutions given by the proposed CVFEM are in good agreement with the numerical results obtained by Liang et al. [103]

Table 5.4 gives a comparison of the average Nusselt numbers, Nu , computed by the proposed CVFEM and the FDM of Liang et al. [103]. The average Nusselt number is given by:

$$Nu = \frac{QL}{\pi R^2 k^f (T_H^f - T_C^f)} \quad (5.7)$$

where Q is the overall rate of heat transfer through the top or bottom surface. The CVFEM Nusselt numbers are grid-independent extrapolated values obtained

¹The calculations presented in this chapter were done using an early version of the proposed CVFEM based on an iterative algorithm with under-relaxation, instead of an unsteady formulation: details are available in Ref. [116].

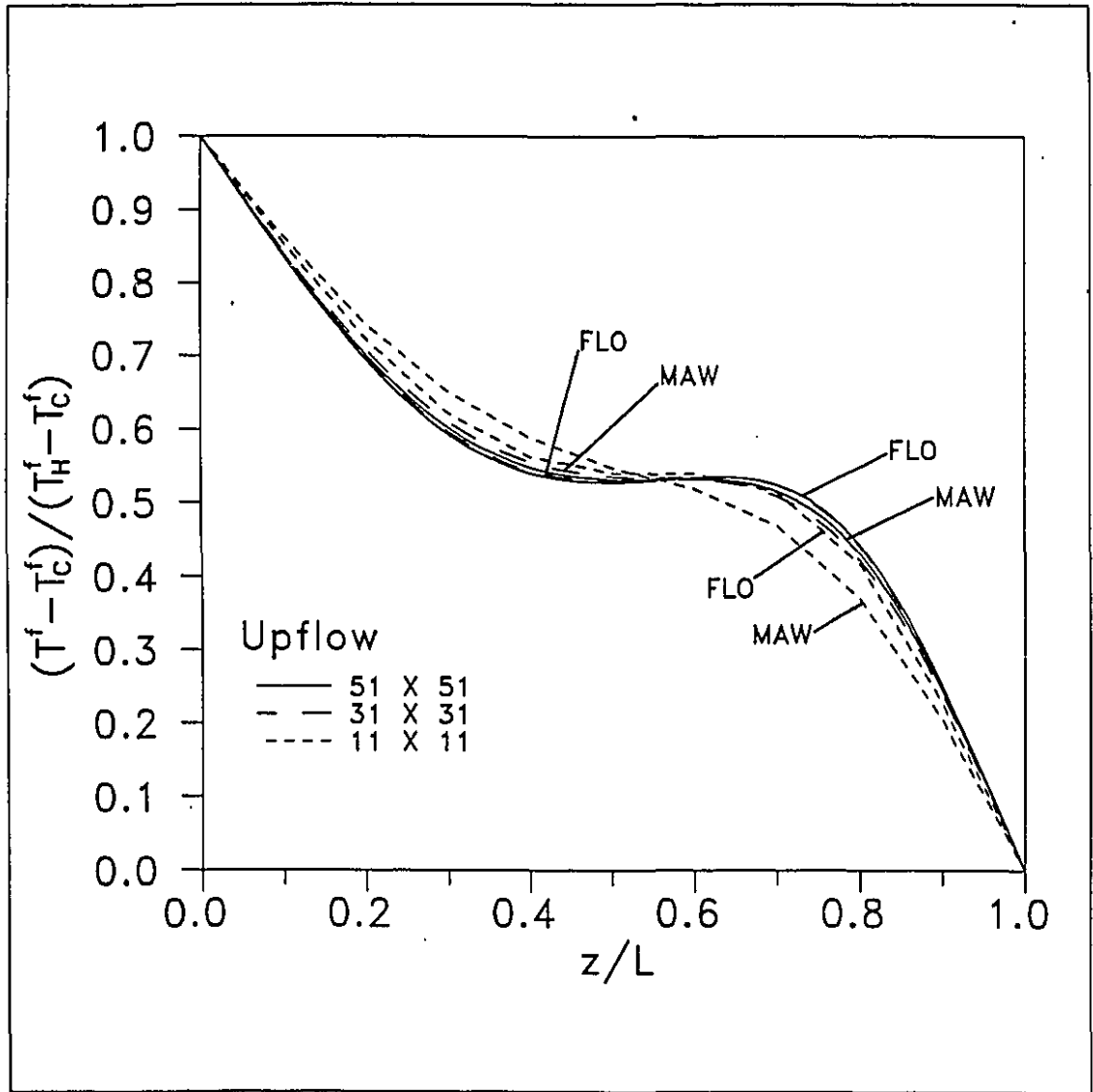


Figure 5.5: Temperature distribution along $r/R = 0.5$ in laminar natural convection in a cylindrical enclosure: grid-independence study for the case of upflow using FLO and MAW

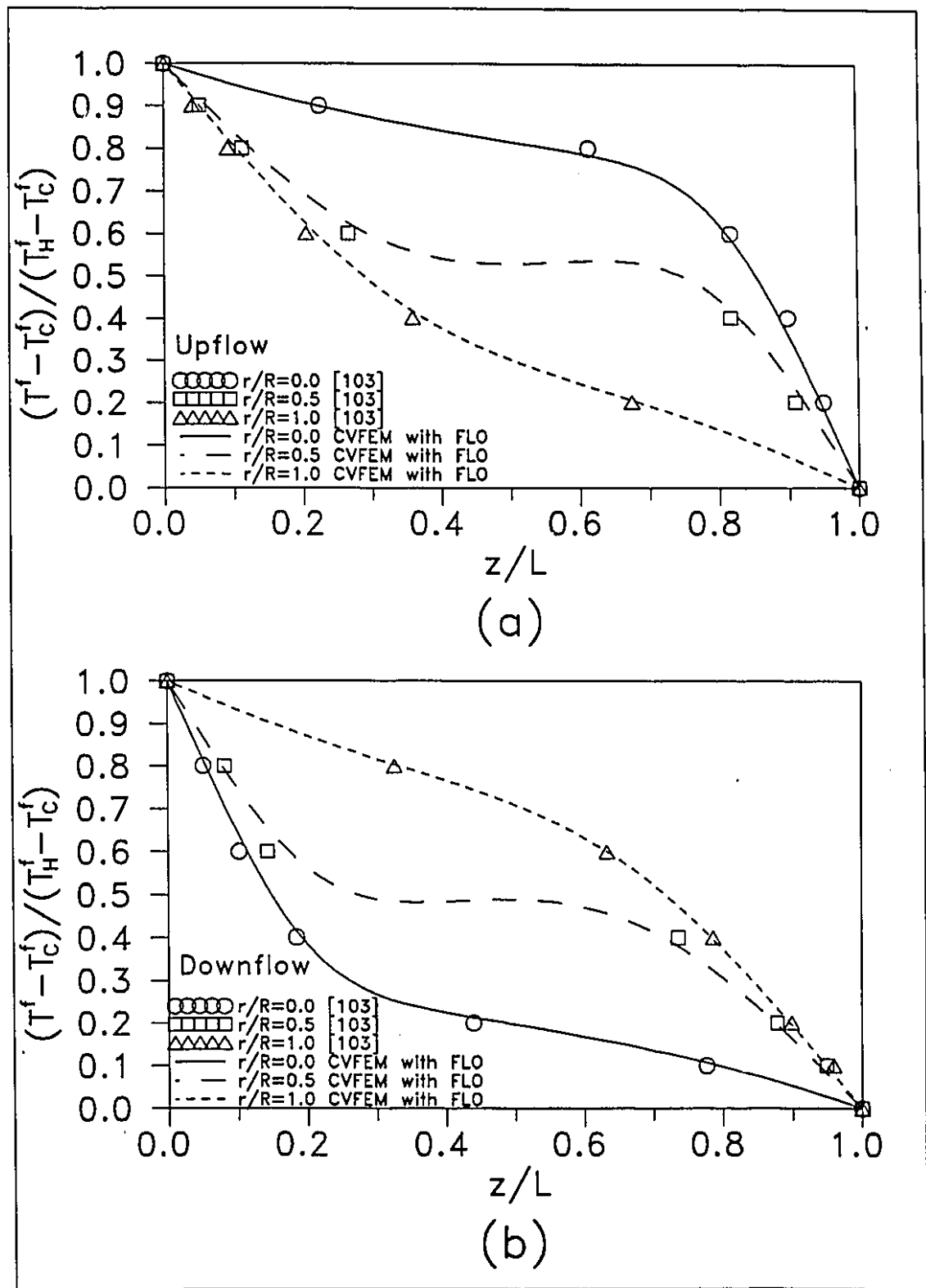


Figure 5.6: Temperature distribution in laminar natural convection in a cylindrical enclosure: (a) upflow ; (b) downflow

as follows:

$$Nu_{gi} = Nu_c + K\delta^n \quad (5.8)$$

where Nu_{gi} is the grid-independent Nusselt number, Nu_c is the computed Nusselt number, and δ is the grid size ($\Delta r = \Delta z = \text{const.}$). For a given set of parameters, the unknowns in this equation are Nu_{gi} , K and n . Therefore, three calculations, on three different grids, provide enough extrapolation equations to find the unknowns. In Eq.(5.8), it is assumed that terms of order δ^{n+1} are negligible. To confirm that this indeed was the case, a fourth calculation, with a 61 X 61 grid, was done. Two extrapolated values, computed using results of the first three and the last three grids, were obtained: they were invariant to four significant figures.

The slight discrepancy between the Nusselt numbers predicted by the proposed CVFEM and the FDM of Liang et al. [103] can be partly explained by noting the use of a non-conservative formulation in the FDM [103]. This non-conservative FDM yields different Nusselt numbers at the top and bottom surfaces, while in the proposed conservative CVFEM these Nusselt numbers are the same. In the physical problem, since the lateral wall of the container is insulated, the top and bottom Nusselt numbers should be equal. A difference between the top and bottom Nusselt numbers implies a heat flux through the lateral wall, which is in contradiction with the prescription of the problem.

Scheme	Grid	Iterations	CPU time (s)
FLO	11 X 11	139	7.7
FLO	31 X 31	972	534.3
FLO	51 X 51	2510	3960.2
MAW	11 X 11	158	5.7
MAW	31 X 31	1017	438.0
MAW	51 X 51	2577	3195.1

Table 5.3: Laminar natural convection in a cylindrical enclosure: number of iterations and CPU times

Case	Proposed CVFEM	Liang et al. [103]
upflow	1.768	1.767
downflow	1.765	1.761

Table 5.4: Laminar natural convection in a cylindrical enclosure: average Nusselt number results

5.4 Laminar Flow in a Replica Segment of a Coronary Artery

Problem Statement

In this problem, laminar flow in a replica segment of a mildly atherosclerotic human coronary artery is simulated. Mild atherosclerosis corresponds to a maximum obstruction in the artery of about 50% by cross-sectional area [7]. In the investigation of Back et al. [7], two replicas of a coronary artery were used. The first one was a hollow cast of a segment of the left circumflex coronary artery of a man with mild atherosclerosis. The second was an axisymmetric analogue of the original casting: the analogue casting had a straight axis, and the same cross-sectional area as the original casting at corresponding axial locations. A schematic representation of the analogue casting is presented in Fig. 5.7. More recently, Back et al. [8] did a steady-state flow test in the analogue replica. In this section, a numerical simulation, using the proposed CVFEM, of fluid flow in the analogue replica will be presented, along with a comparison with the experimental results of Back et al. [8].

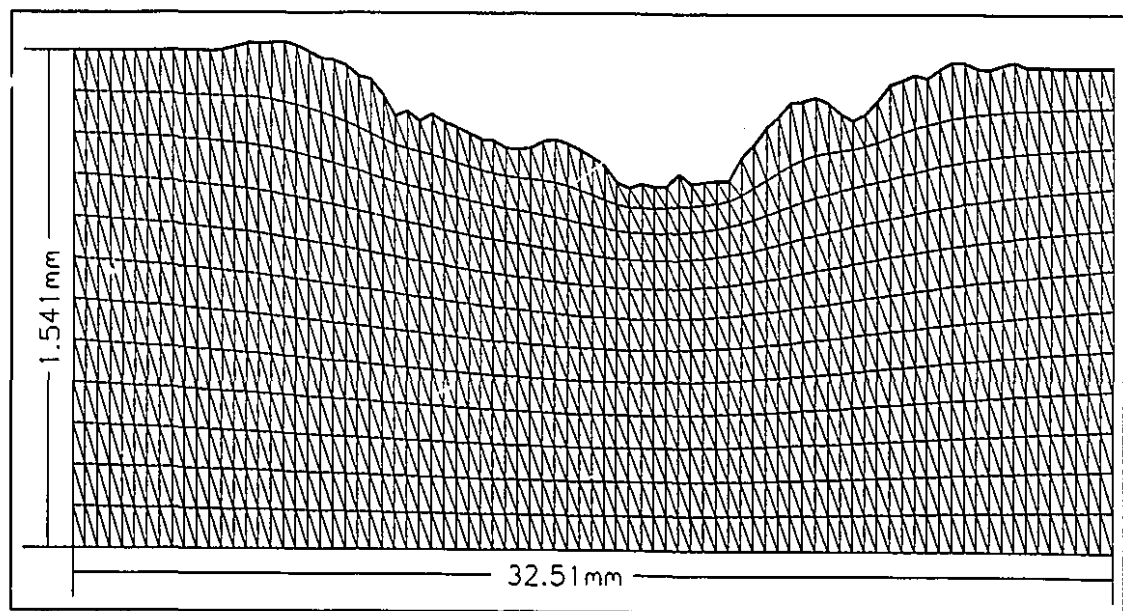


Figure 5.7: Straight axisymmetric analogue casting of a coronary artery and the grid used in the CVFEM simulations: scale in radial direction is ten times that in the axial direction.

Governing Equations

The experiments of Back et al. [8] were done with a 33% sugar-water solution. The resulting fluid can be considered as Newtonian and, therefore, the governing equations are the same as the Navier-Stokes equations enumerated earlier in the context of developing laminar pipe flow.

The boundary conditions are the prescribed Poiseuille velocity profile at the inlet, the outflow treatment at the outlet, and the no-slip condition on the wall.

Results

Fig. 5.7 illustrates the analogue geometry: it is important to note that the scale in the radial direction is ten times bigger than the axial scale. This geometry is clearly irregular, and it has been chosen to illustrate the capability of the proposed CVFEM to simulate flow in a complex geometry. A grid independence analysis was done for a Reynolds number, based on average velocity and diameter at the inlet, of 353. Pressure change coefficients ($= [p^f - p_{z=0}^f] / [0.5\rho^f \bar{u}^f{}^2]$) obtained in this analysis are presented in Figs. 5.8 and 5.9. In Fig. 5.8, it is seen that the results obtained using a 85 X 13 grid is close to that obtained on a 169 X 25 grid. Based on this comparison, the 85 X 13 grid, presented in Fig. 5.7, was used for all the other calculations. Fig. 5.9 presents a comparison between the numerical results obtained using the proposed CVFEM and the experimental data of Back et al. [8] for $Re = 59, 83, 207,$ and 353 . As can be seen from these results, the agreement of the numerical results with the experimental data is good.

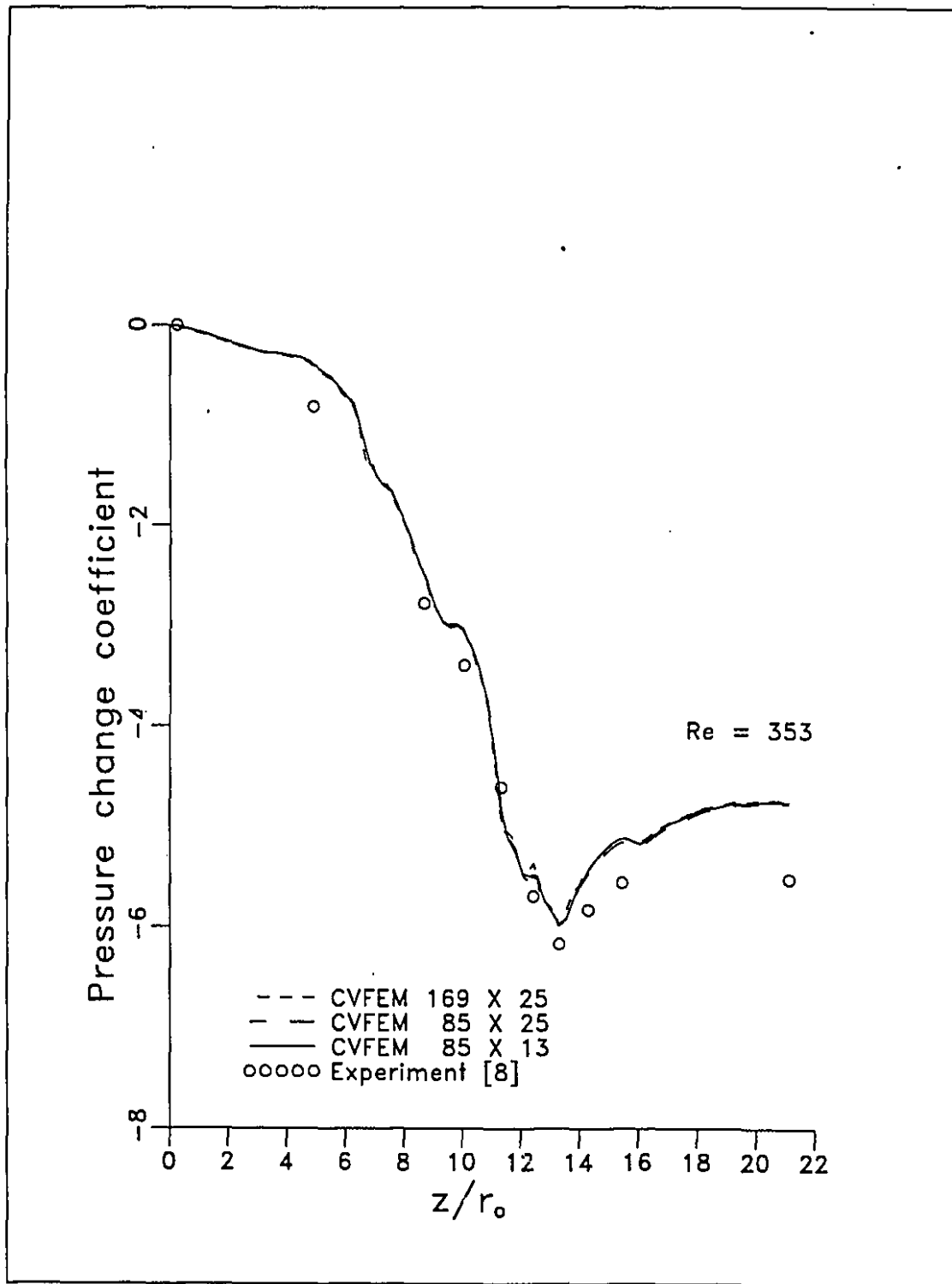


Figure 5.8: Laminar flow in a replica segment of a coronary artery: pressure-change coefficient for different grids

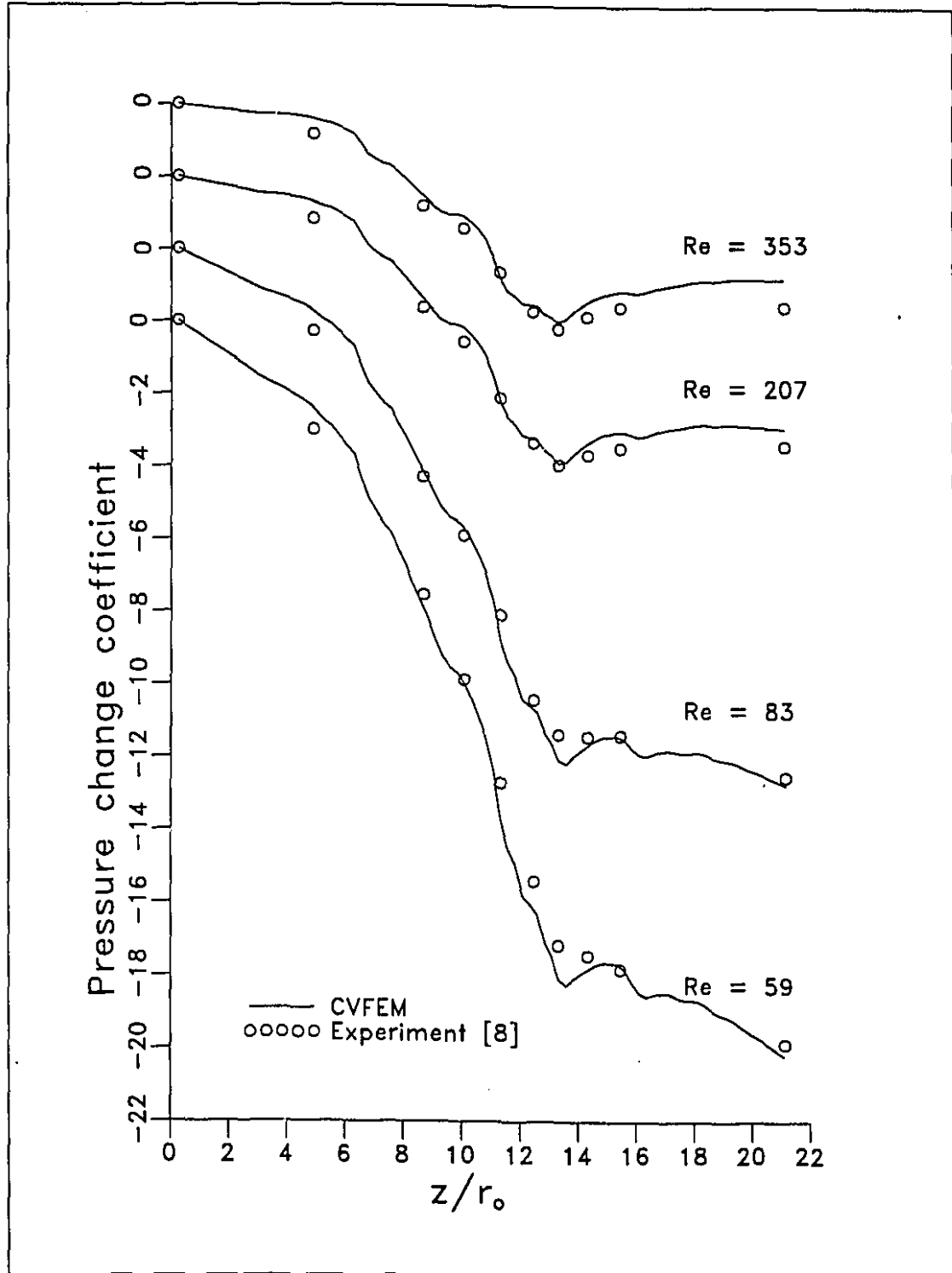


Figure 5.9: Laminar flow in a replica segment of a coronary artery: pressure-change coefficient for different Reynolds numbers

Chapter 6

Dilute Gas-Solid Particle Flow Simulations

The validity of the proposed CVFEM [114, 115, 117] for the simulation of dilute gas-solid particle flows is demonstrated in this chapter. This demonstration is done in three stages: first, the capability of the proposed CVFEM to solve the mathematical model of dilute gas-solid particle flows, Eqs.(3.122)-(3.127), is established by using a *specified solution technique*; then the proposed CVFEM is applied to a problem involving dilute gas-solid particle flows in a channel with a restriction, and the results are compared with other results available in the literature [44] and also results obtained by using a well-established staggered-grid finite-volume method [30, 130]; finally, the proposed CVFEM is used to simulate dilute gas-solid particle flows in an idealized split-flow inertial separator, and the results are discussed.

In the *specified solution technique*, concentration and velocity fields that satisfy the continuity equations for the fluid and solid phases are proposed. In general, these proposed solution fields will *not* satisfy the momentum equations. However, appropriate definitions of the volumetric source terms will ensure that these equations are satisfied. The expressions for these volumetric source terms are obtained by substituting the proposed solution fields into the corresponding governing equations. The proposed solution fields are also used to obtain appropriate boundary conditions. Finally, treating these volumetric source terms and boundary conditions as part of the problem specification, the proposed CVFEM is used to solve the mathematical model, and the results are compared with the *exact solution*, which simply

consists of the proposed concentration and velocity fields. This technique is used to determine whether or not the numerical method is able to solve the mathematical model.

Unless otherwise specified, the $C_D Re^s$ expression of Wallis [186] (see Table 3.1) is used in the following calculations.

6.1 Non-Dimensional Parameters

Before the presentation and discussion of the test problems, it is useful to identify some non-dimensional parameters typically involved in gas-solid particle flows. One parameter is the Reynolds number, $Re = \frac{\rho^f u_{ch}^f L}{\mu^f}$: L is a characteristic length of interest; and u_{ch}^f is a characteristic velocity of the fluid phase. The ratio of the densities of the solid and fluid phases, $\gamma = \frac{\rho^s}{\rho^f}$, is also a parameter. Another important parameter is the ratio of the characteristic times of the two phases [148]. This parameter is called the Stokes number, $Sk = \frac{\tau^s}{\tau^f}$. Each phase has its own characteristic time, denoted here by τ^f and τ^s for the fluid and solid phases, respectively. The fluid-phase characteristic time is given by $\tau^f = \frac{L}{u_{ch}^f}$. The solid-phase characteristic time is taken to be the particle relaxation time, given by [148]:

$$\tau^s = \frac{4}{3} \frac{\rho^s d^2}{\mu^f C_D Re^s} \quad (6.1)$$

The expression for $C_D Re^s$ is typically obtained from theoretical or experimental studies on a single spherical particle. Table 3.1 gives some well-known expressions. The complete description of a test problem must also include the prescription of suitable boundary conditions.

6.2 Specified Solution in a Cartesian Domain

Problem Statement

This first test case has no real physical significance. It was used only to validate the formulation and implementation of the proposed CVFEM. The procedure consists first to propose a concentration distribution, a mass conserving velocity field for each phase, and a pressure field. This ensures that the continuity equations are satisfied. In this test, the calculation domain is a square enclosure of side L . The following steady-state Cartesian solution was proposed:

$$\begin{aligned} u_{ex}^s &= u^{so} & v_{ex}^s &= u^{so} & \alpha_{ex} &= \alpha^o \\ u_{ex}^f &= u^{fo} \frac{y}{L} & v^f &= 0 & p_{ex}^f &= p^{fo} \frac{x+y}{L} \end{aligned} \quad (6.2)$$

where u^{so} , α^o , u^{fo} , and p^{fo} are prescribed constants and $\frac{\rho^s}{\rho^f} = 10^3$. The solution is expressed in term of a (x, y) Cartesian coordinate system. The subscript ex is used to emphasis that the specified solution is the exact solution.

This proposed solution satisfies the momentum equations only for the following non-zero volumetric source terms:

$$S_z^f = p^{fo}(1 - \alpha^o) + K(u^{fo} \frac{y}{L} - u^{so}) \quad (6.3)$$

$$S_r^f = p^{fo}(1 - \alpha^o) - K u^{so} \quad (6.4)$$

$$S_z^s = p^{fo} \alpha^o + K(u^{so} - u^{fo} \frac{y}{L}) \quad (6.5)$$

$$S_r^s = p^{fo} \alpha^o + K u^{so} \quad (6.6)$$

This dilute gas-solid particle flow is governed by Eqs.(3.122)-(3.127), with the volumetric source terms given by Eqs.(6.3)-(6.6). The fluid-phase boundary conditions are: (i) Couette velocity profile at the inlet plane $x = 0$; (ii) outflow treatment [130] at the outlet plane $x = L$; and (iii) given x - and y -components of velocity at planes $y = 0$ and $y = L$. The solid-phase boundary conditions are: (i) uniform inlet velocity and concentration profiles at the inlet planes $x = 0$ and $y = 0$; and (ii) outflow treatment at the outlet planes $x = L$ and $y = L$.

Results

The solutions of this problem produced by the proposed CVFEM, with coarse and fine grids, give the exact solutions (Eq.(6.2)). This behaviour is expected since with this specified solution, the interpolation functions used in the numerical method give exact values of the various fluxes and sources. Nevertheless, this test problem and these successful simulations were very useful: they clearly indicated the validity of the implementation and the capability of the proposed CVFEM to solve the mathematical model of dilute gas-solid particle flows given by Eqs.(3.122)-(3.127).

6.3 Flow in a Channel with a Restriction

Problem Statement

In this test problem, steady, laminar, dilute gas-solid flow in a channel with a restriction is investigated. The influence of gravity is considered negligible. This problem is similar to that proposed and analyzed by Di Giacinto et al. [44]. A schematic illustration of the problem is given in Fig. 6.1. The boundary conditions are: (i) uniform inlet profile for α ; (ii) identical Poiseuille inlet velocity profiles for both phases; (iii) outflow treatment at the outlet plane; (iv) no-slip condition at the walls for the fluid phase; and (iv) *slip* condition at the walls for the *solid phase*. The nondimensional parameters considered in this problem are given in Table 6.1. In the numerical simulations, only one-half channel was modelled, using the symmetry condition at the centerline. The $C_D Re^s$ expression used by Di Giacinto et al. [44] (see Table 3.1) is used in these calculations.

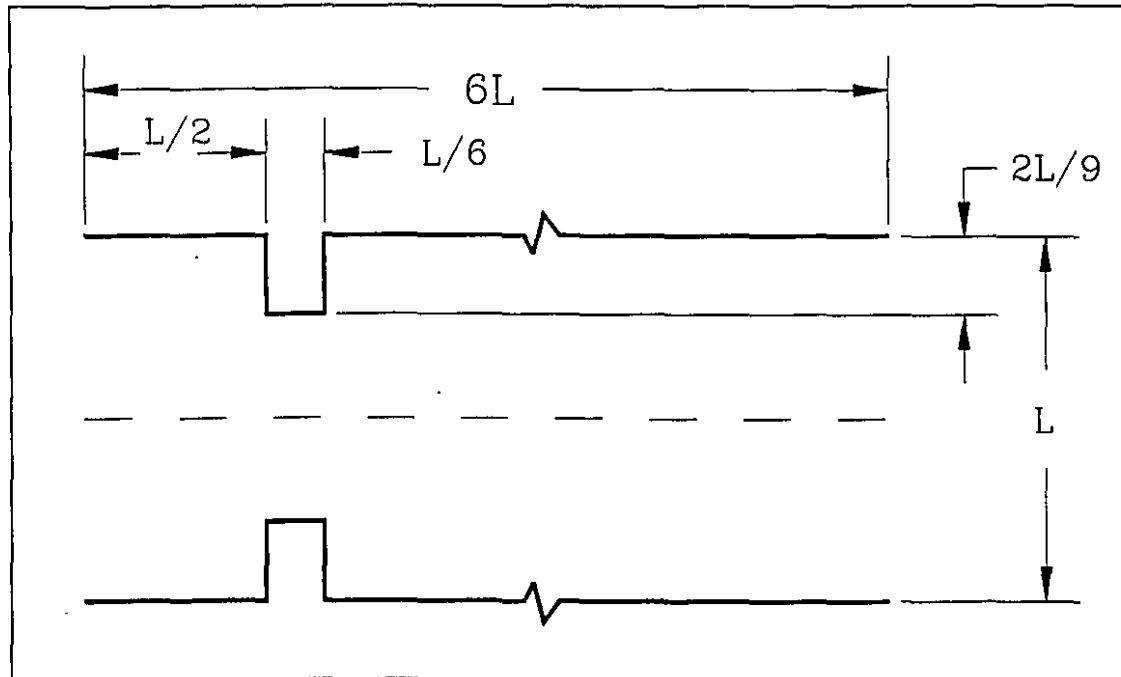


Figure 6.1: Geometry of the channel with a restriction

Results

Three simulations are presented for this test problem (see Table 6.1). They have been selected to illustrate the effects of the Stokes number, Sk , and the inlet concentration, α_{in} , on the flow behaviour. All of the presented results correspond to a Reynolds number of 100, with the channel height (Fig. 6.1) as the characteristic length L , and fluid-phase inlet centerline velocity, u_{cl}^f , as the characteristic velocity, u_{ch}^f . The grid used had 73 X 37 nodes; the results were considered essentially grid independent since calculation on finer grids produced negligible changes in the centerline velocities. Figs. 6.2 to 6.5 present comparisons of the centerline variation of u^f , u^s , p^f , and α computed using the proposed CVFEM and a staggered-grid finite-volume method [30, 130]. Where applicable, the results of Di Giacinto et al. [44] are also shown in these figures.

Re	Sk	α_{in}	γ
100	10^{-2}	10^{-3}	1000
100	10^{-2}	5×10^{-3}	1000
100	10^{-1}	5×10^{-3}	1000

Table 6.1: Values of parameters for flow in a channel with a restriction

As can be observed in Figs. 6.2 to 6.5, the proposed CVFEM and finite-volume/staggered-grid solutions are in good agreement. Quantitative comparisons with the results of Di Giacinto et al. [44] are not very good, but there is agreement in the qualitative behaviour of these solutions as a function of Sk and α_{in} . For $Sk = 10^{-2}$ and $\alpha_{in} = 10^{-3}$, the finite-volume/staggered-grid solution obtained with a 73 X 37 grid is in close agreement with the solution proposed by Di Giacinto et al. [44], while, in the other cases, these solutions are only qualitatively similar. However, for $Sk = 10^{-1}$ and $\alpha_{in} = 5 \times 10^{-3}$, our finite-volume/staggered-grid solution on a coarser grid (37 X 10) was found to be in good agreement with the solution of Di Giacinto et al. [44]. This indicates that some of the results of Di Giacinto et al. [44] may not be grid independent. For $Sk = 10^{-1}$, the CVFEM predicts an outlet concentration 1% larger than the finite-volume/staggered-grid solution (see Fig. 6.5). This difference is not too serious, however, since it does not affect the velocity and pressure distributions, and it is related to the different ways in which

the inlet boundary is treated in the two formulations.

For $Sk = 10^{-2}$, the solid phase is almost in equilibrium with the fluid phase: the results can, therefore, be analyzed using a simple homogeneous two-phase flow theory [186], where suitable average viscosity and density are determined to treat the two phases as a pseudofluid that obeys the usual equations of single-phase flow with the average properties. The density and viscosity of the homogeneous mixture were obtained using

$$\rho_{\text{mix}} = \alpha_{\text{in}}\rho^s + \epsilon_{\text{in}}\rho^f \quad \mu_{\text{mix}} = \mu^f(1 + 2.5\alpha_{\text{in}}) \approx \mu^f \quad (6.7)$$

Therefore, the effects of increasing the solid concentration, with all other conditions unchanged, is similar to the increase of the Reynolds number in single-phase flow when $\gamma = \frac{\rho^s}{\rho^f} \gg 1$. This is exactly the behaviour of the proposed solutions: as the Reynolds number increases, the recirculating zone behind the restriction becomes larger; recovery of the fluid-phase velocity profile takes place over a larger axial length; and the velocity profiles in the core region become flatter, which results in lower centerline velocities. One of the effects of the inlet concentration, α_{in} , can be seen by analyzing the results for $Sk = 10^{-2}$. As the inlet concentration, α_{in} , is increased, the entrance and total pressure drops increase to compensate the augmentation of the drag due to the presence of a larger number of particles.

As the Stokes number increases, the solid phase is no longer in equilibrium with the fluid phase, which can be seen by a larger difference in u^f and u^s in the region of the restriction. At the centerline in the outlet plane, α reaches values bigger than the inlet concentration, α_{in} , which indicates an accumulation of particles in the centre of the channel downstream of the restriction.

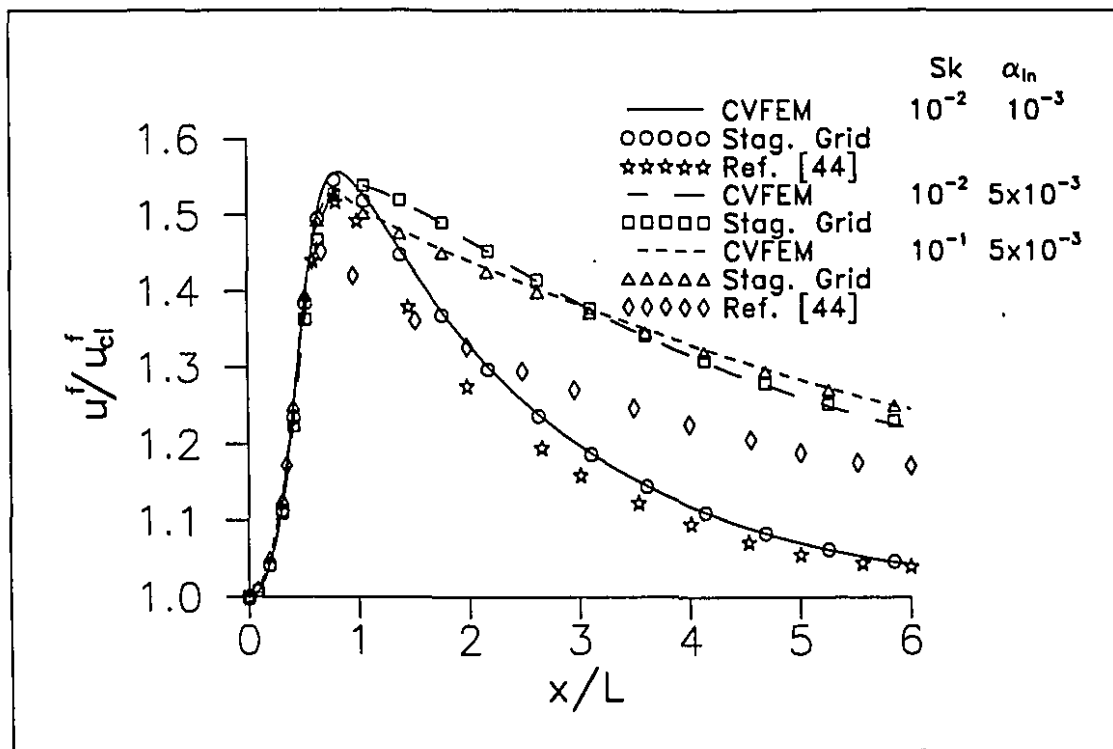


Figure 6.2: Flow in a channel with a restriction: variation of fluid-phase velocity along the centerline

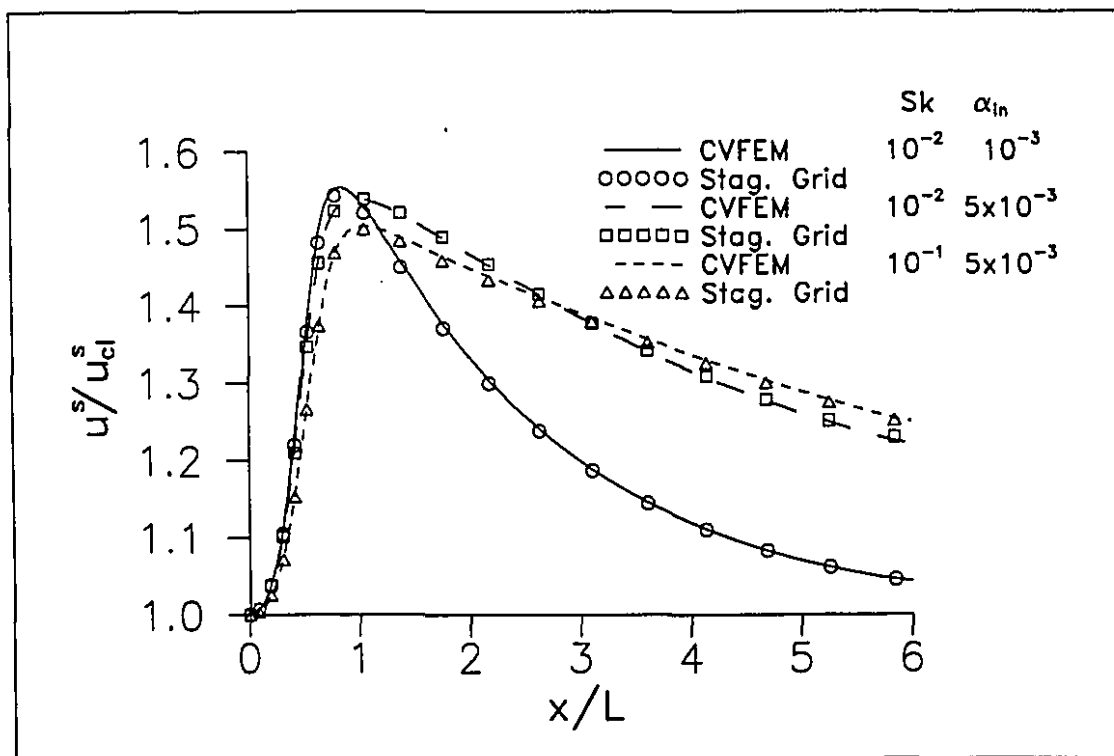


Figure 6.3: Flow in a channel with a restriction: variation of solid-phase velocity along the centerline

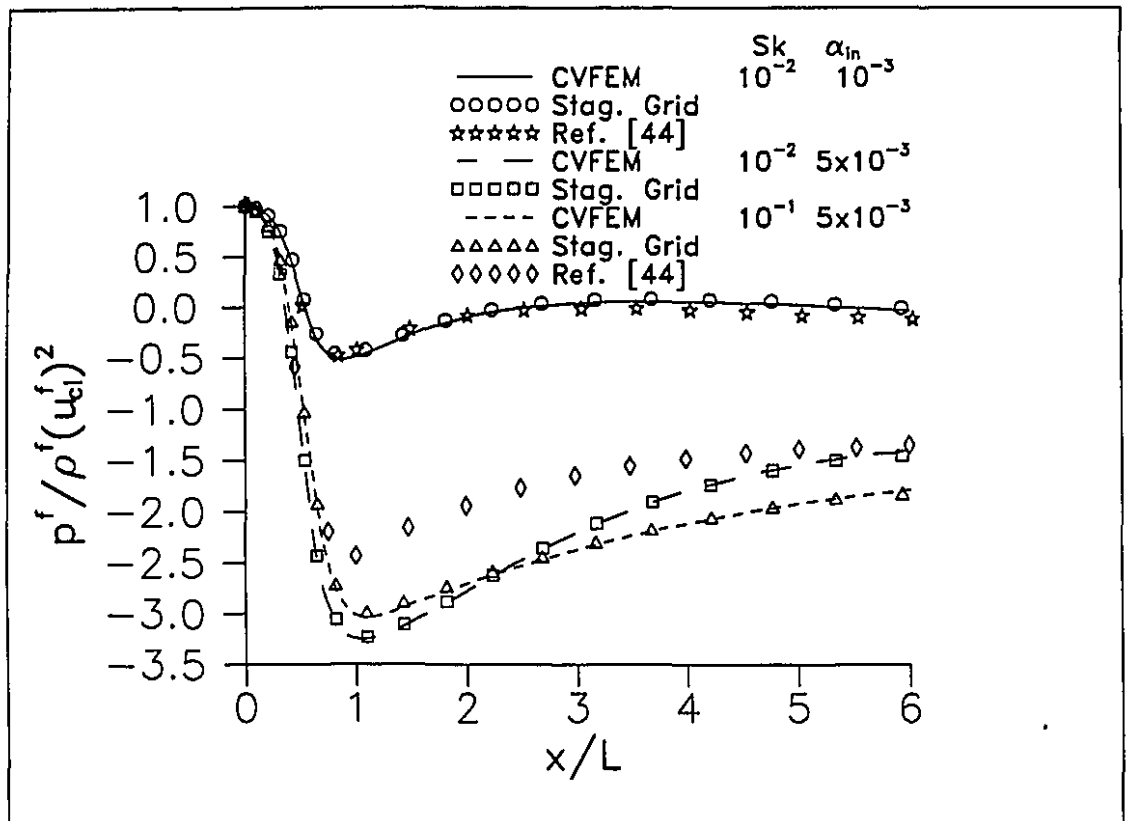


Figure 6.4: Flow in a channel with a restriction: variation of fluid-phase pressure along the centerline

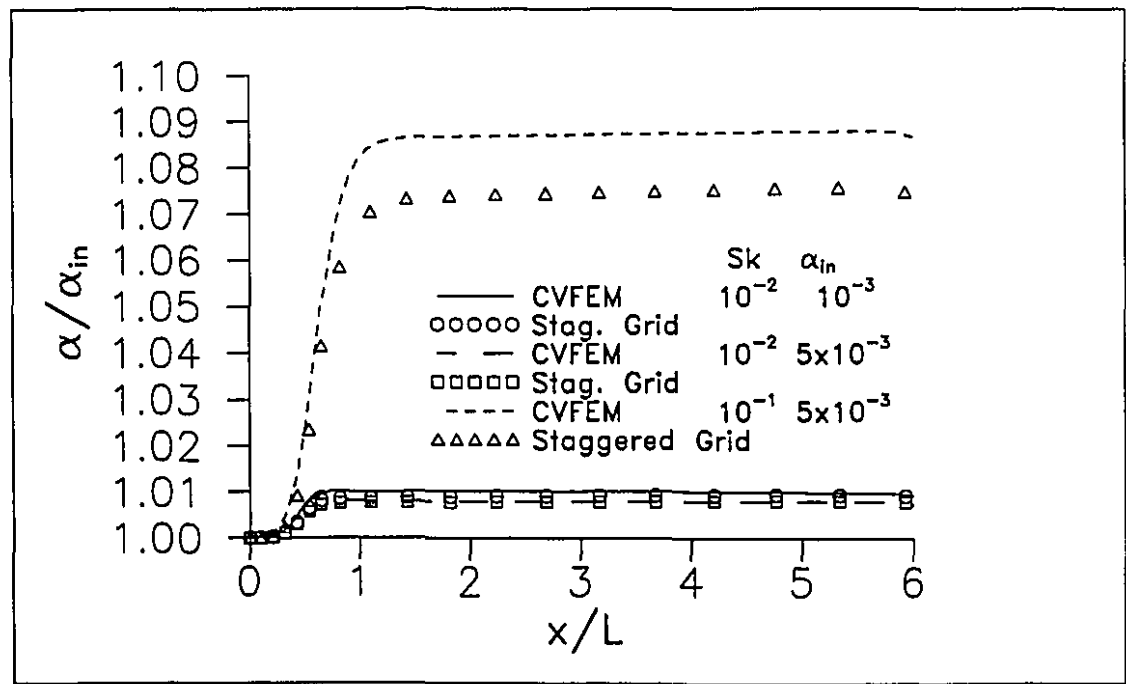


Figure 6.5: Flow in a channel with a restriction: variation of solid-phase concentration along the centerline

6.4 Split-Flow Inertial Separator

This test problem is presented to illustrate the capability of the proposed numerical method to solve problems that involve dilute gas-solid particle flows in complex geometries. The proposed CVFEM is used in this section to simulate steady flows in an idealized split-flow inertial particle separator. Such separators are usually installed at the inlet of helicopter gas-turbine engines in order to prevent ingestion of sand and foreign objects. Such ingestion is responsible for a large proportion of early damage and unscheduled maintenance. The main advantage of such separators is their low-maintenance requirements [195].

In this problem, a dilute gas-solid particle flow in an idealized inertial separator is investigated. The idealization comes from the assumption of zero swirl in the flow and negligible influence of gravity, which allows an axisymmetric analysis. In a real separator, swirl is induced by inlet blades in order to increase the separation efficiency. Furthermore, only laminar flows are considered in this work. Thus, these simulations are *not* intended to model a practical separator. Rather, they are used mainly to demonstrate the capabilities of the proposed CVFEM. It should be noted, however, that this idealized problem is also well-suited for a demonstration of some of the underlying physics of gas-solid particle flows in this geometry. Thus, in the discussion of the results of the CVFEM simulations, an assessment of the effects of the various non-dimensional parameters on overall pressure drop and separation efficiency is included.

Problem Statement

A schematic illustration of the idealized problem is given in Fig. 6.6. The equivalent axisymmetric geometry with swirling flow as been analyzed in the past [22], using a finite element method to solve a one-way coupling model, in which the fluid flow was computed using Euler equations. Viscous flow analysis of a similar Cartesian separator has been realized [197] using one-way coupling and the Lagrangian formulation for the solid phase. In this work, the two-fluid model is used. The inlet is at the left end, and there are two outlets at the right end. The goal is to deviate the particles into the bypass duct, while ensuring only particle-free fluid enters the

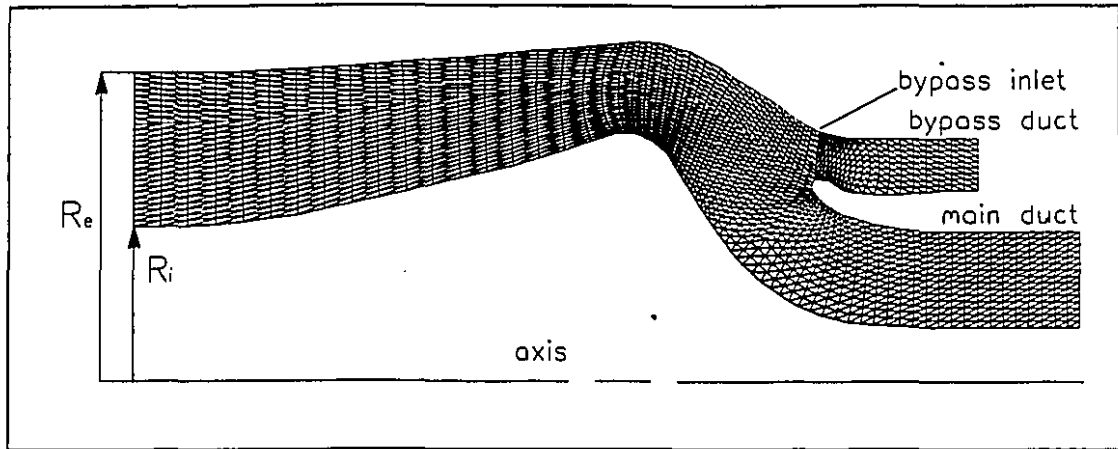


Figure 6.6: Geometry of the separator

main duct. The bypass ratio, b , defined as the ratio of the fluid-phase mass flow rate through the bypass duct to the fluid-phase inlet mass flow rate, is controlled by the pressure difference between the main-duct outlet plane and the bypass outlet plane. The separator efficiency, η_{ef} , indicates, for a given bypass ratio b , the effectiveness of a given separator. This efficiency is defined as the ratio of the solid-phase mass flow rate through the bypass duct to the solid-phase inlet mass flow rate. The boundary conditions are: (i) uniform inlet solid-phase volume concentration, α_{in} ; uniform inlet velocity profiles for u^f and u^s , and $v^f = v^s = 0$; (ii) outflow treatment [130] at the outlet planes, with given pressure difference between the bypass and main outlets; and (iii) no-slip condition at the walls for the fluid phase, and slip condition at the walls for the solid phase.

Non-Dimensional Parameters. The non-dimensional parameters involved in the problem of interest are the Reynolds number, Re , the Stokes number, Sk , the ratio of the densities of the solid and fluid phases, γ , the inlet volume concentration of the solid phase, α_{in} , and the bypass ratio, b . There are also several geometric parameters in this problem. The set chosen for this study is illustrated in Fig. 6.6: the ratio of the inlet external radius, R_e , to the inlet internal radius, R_i , is equal to 2; the other geometric parameters may be obtained from Fig. 6.6, since this figure is drawn to scale. Re is based on D_H , the inlet hydraulic diameter ($=2R_e - 2R_i$). The solid phase enters the separator at the same uniform velocity as that of the fluid phase.

All simulations in this study were done with $Re = 200$. Three different com-

binations of γ and α_{in} were considered: $\gamma = 1000$ and $\alpha_{in} = 10^{-3}$; $\gamma = 100$ and $\alpha_{in} = 10^{-3}$; and $\gamma = 1000$ and $\alpha_{in} = 10^{-4}$. Three values of the bypass ratio were studied: $b = 10\%$, $b = 20\%$, and $b = 30\%$. The influence of the Stokes number was investigated by conducting simulations in the range $10^{-3} \leq Sk \leq 2 \times 10^{-1}$. Values of Sk higher than 2×10^{-1} were not investigated because of the difficulty in obtaining converged solutions. This difficulty is to be *expected*: as Sk increases, for a fixed value of α_{in} , the coupling between the fluid-phase and solid-phase momentum equations becomes progressively weaker; furthermore, at high values of Sk , for a given value of α_{in} , the validity of two-fluid models becomes questionable.

Results

Separator Efficiency. Figs. 6.7a, 6.8a, and 6.9a give the variation of the separator efficiency, η_{ef} , as a function of the Stokes number, Sk , with the bypass ratio, b , as a parameter. The results in Fig. 6.7, which correspond to $\gamma = 1000$ and $\alpha_{in} = 10^{-3}$, will be considered first. At low values of Sk (< 0.01), the particles are relatively very small and almost in equilibrium with the fluid phase. In this regime, therefore, the separator efficiency is essentially equal to the bypass ratio, and the only way to increase η_{ef} , for a given separator geometry, is to increase b . As the Stokes number is increased, the particle size (or inertia) is increased, and the separator efficiency increases: this effect is quite dramatic in the range $0.01 \leq Sk \leq 0.2$. For $Sk > 0.2$, the value of η_{ef} asymptotes to 100% with increasing values of Sk .

A comparison of the results presented in Figs. 6.7a and 6.8a shows that a decrease in γ from 1000 to 100, for $\alpha_{in} = 10^{-3}$, has very little effect on the plot of η_{ef} vs Sk . Similarly, the results in Fig. 6.9a, which pertain to $\gamma = 1000$ and $\alpha_{in} = 10^{-4}$, are very close to those in Fig. 6.7a, which corresponds to $\gamma = 1000$ and $\alpha_{in} = 10^{-3}$. Only a minor difference can be detected: at large values of Sk (> 0.05), heavier particles ($\gamma = 1000$) lead to slightly higher values of η_{ef} than the corresponding values obtained with lighter particles ($\gamma = 100$).

Static-Pressure Drop in the Main Duct. The variation of nondimensionalized static-pressure drop in the main duct, Δp_M^* , with Stokes number, Sk , is presented in Figs. 6.7b, 6.8b, and 6.9b. In each of these figures, the bypass ratio, b ,

is a parameter, and Δp_M^{f*} is defined as follows:

$$\Delta p_M^{f*} = \frac{p_{in,c}^f - p_{out,M}^f}{0.5\rho^f(u_{in}^f)^2}$$

where $p_{in,c}^f$ is the static pressure at the central node in the inlet plane of the separator; $p_{out,M}^f$ is the static pressure at the outlet plane of the main duct; ρ^f is the density of the fluid phase; and u_{in}^f is the prescribed uniform velocity of the fluid phase at the inlet plane of the separator. In all simulations, $p_{in,c}^f$ was essentially equal to the area-weighted average of the static pressure at the inlet plane.

Also presented in Figs. 6.7b, 6.8b, and 6.9b are results pertaining to flow, in the same separator, of a homogeneous mixture (line with long dashes) and a single-phase fluid (line with short dashes). The density and viscosity of the homogeneous mixture were obtained using Eq.(6.7). For the single-phase fluid flow, the density and viscosity were set equal to those of the fluid phase in the gas-solid particle flow.

The results in Fig. 6.7b show that Δp_M^{f*} decreases as b increases, for a fixed Sk . This is to be expected because as b increases, the amount of fluid flow in the bypass duct increases and that through the main duct decreases. For a fixed value of b , Δp_M^{f*} asymptotes to the homogeneous-mixture solution as Sk decreases below a value of 0.01. This is also an expected result: as Sk decreases, the solid and fluid phases move towards equilibrium conditions with one another; and at very small values of Sk , two-fluid models of dilute gas-particle flows become equivalent to the homogeneous-mixture model. At large values of Sk (≥ 0.06), Δp_M^{f*} values given by the two-fluid model fall below those produced by the homogeneous flow model. This is because the separator efficiency increases with increasing Sk ; and for $Sk \geq 0.06$, the concentration of particles in the main duct beyond the split-off point is significantly below the uniform concentration ($= \alpha_{in}$) that is assumed to prevail in the homogeneous flow model.

The results in Fig. 6.7b also show that for a fixed value of b , starting from $Sk = 0.001$, as Sk increases, Δp_M^{f*} first increases until it reaches a maximum, and then it decreases monotonously. This is due to the opposite variations with Sk of the size of the particles (or particle inertia) and the particle number density (or particle-fluid contact surface area). For a fixed α_{in} , at low values of Sk , there is a large amount

of small particles; high values of Sk , on the other hand, correspond to a relatively smaller amount of large particles. High values of Sk are also accompanied by high values of η_{ef} , and this further reduces the particle number density in the main duct beyond the split-off point. *Increases* in size and number density of the particles are *both* accompanied by *increases* in drag force exerted by the particles on the fluid, or vice versa. The results in Fig. 6.7b show that for $0.001 \leq Sk \leq 0.02$, the influence of *increasing particle size* dominates the *opposite* influence of *decreasing particle number density*. The reverse is true for $Sk \geq 0.02$. In the range of parameters considered, the Δp_M^{f*} values for the gas-solid particle flow are all larger than the corresponding values for the single-phase fluid flow, but this difference decreases at high values of Sk . This is also expected, because as Sk increases, for fixed α_{in} and b , η_{ef} increases, so less particles flow through the main duct beyond the split-off point.

The results in Fig. 6.7b pertain to $\gamma = 1000$ and $\alpha_{in} = 10^{-3}$, which corresponds to equal, individual, mass flow rates of the solid and fluid phases at the inlet of the separator. In contrast, the results in Fig. 6.8b apply to $\gamma = 100$ and $\alpha_{in} = 10^{-3}$, and those in Fig. 6.9b correspond to $\gamma = 1000$ and $\alpha_{in} = 10^{-4}$. In both these cases (Figs. 6.8b and 6.9b), the inlet total mass flow rate of the solid phase is ten times smaller than that of the fluid phase. Thus, though the variations of Δp_M^{f*} with Sk in Figs. 6.8b and 6.9b show a pattern that is similar to that in Fig. 6.7b, the various aforementioned features (or trends) are less pronounced. Indeed, there is very little variation of Δp_M^{f*} with Sk in Figs. 6.8b and 6.9b. Another interesting characteristic of the results in Figs. 6.8b and 6.9b is the relatively small difference in the results obtained with the homogeneous-mixture and single-phase models. This shows that when the total inlet mass flow rate of the solid phase is ten times smaller than that of the fluid phase, the influence of the particles on the fluid flow is quite small, or essentially negligible; thus one-way-coupling models [41] could be expected to produce accurate results in such cases, at significantly lower computational costs than those incurred in simulations with two-way-coupling models.

Static-Pressure Drop in the Bypass Duct. The variation of nondimensionalized static-pressure drop in the bypass duct, Δp_{BY}^{f*} , with Stokes number, Sk , is presented in Figs. 6.7c, 6.8c, and 6.9c. In each of these figures, the bypass ratio, b ,

is a parameter, and Δp_{BY}^{f*} is defined as follows

$$\Delta p_{BY}^{f*} = \frac{p_{in,c}^f - p_{out,BY}^f}{0.5\rho^f(u_{in}^f)^2}$$

where $p_{out,BY}^f$ is the static pressure at the outlet plane of the bypass duct; and the physical meanings of $p_{in,c}^f$, ρ^f , and u_{in}^f are the same as those given earlier. Also presented in Fig. 6.7c, 6.8c, and 6.9c are results obtained with a homogeneous-mixture model (line with long dashes) and results pertaining to a single-phase fluid flow (line with short dashes) in the same separator.

The results in Fig. 6.7c show that Δp_{BY}^{f*} increases as b increases, for a fixed Sk. This is expected because with an increase in b , the flow through the bypass duct increases. For a fixed value of b , Δp_{BY}^{f*} asymptotes to the homogeneous-mixture solution as Sk decreases below a value of 0.01. The explanation for this is the same as that provided earlier to explain this feature of Δp_M^{f*} results.

For $Sk \geq 0.01$, the variation of Δp_{BY}^{f*} with Sk is different for different values of b . These differences are caused by the combined influences of the relative speed of the particles with respect to the fluid at the *inlet-plane of the bypass duct* (Fig. 6.6); the particle concentration distribution in the bypass duct; the particle number density in the bypass duct; and the particle size (or inertia). At $b = 10\%$, Δp_{BY}^{f*} decreases with increases in Sk, indicating that the dominant influence is that of the corresponding decrease in particle number density: indeed, for $Sk \geq 0.04$, the two-fluid-model Δp_{BY}^{f*} values are lower than those obtained for single-phase fluid flow. For these particular cases, detailed examinations of the particle- and fluid-phase speeds, $V^f = \sqrt{(u^f)^2 + (v^f)^2}$ and $V^s = \sqrt{(u^s)^2 + (v^s)^2}$, (see Fig. 6.10) showed that the former are significantly larger than the latter at the *inlet-plane of the bypass duct*, just after the split-off point: so the particles facilitate the fluid flow in the bypass duct, rather than impose a drag on it. For $b = 20\%$, Δp_{BY}^{f*} decreases with increases in Sk, but reaches a minimum value in the vicinity of $Sk = 0.08$: this is because the decrease in particle number density caused by increasing Sk (at a fixed α_{in}) is balanced at this point by the increase in this variable produced by increases in η_{ef} . At $b = 30\%$, the influences of the aforementioned factors on Δp_{BY}^{f*} balance each other out very well for $10^{-3} \leq Sk \leq 0.04$, so Δp_{BY}^{f*} is essentially constant in this

range of Sk . However, for $Sk > 0.04$, increases in Sk lead to substantial increases in Δp_{BY}^{f*} . For these particular cases, detailed examinations of the particle- and fluid-phase speeds and volume concentrations (see Fig. 6.11) showed the following: (1) at the *inlet-plane of the bypass duct*, just after the split-off point, the concentration of the solid-phase is very high in the low-velocity region adjacent to the upper wall; (2) downstream of this point, these low-velocity particles move to the central regions of the bypass duct, mainly because of the geometry of this particular separator; (3) this, in turn, causes a considerable drag on the fluid phase, and requires high values of Δp_{BY}^{f*} .

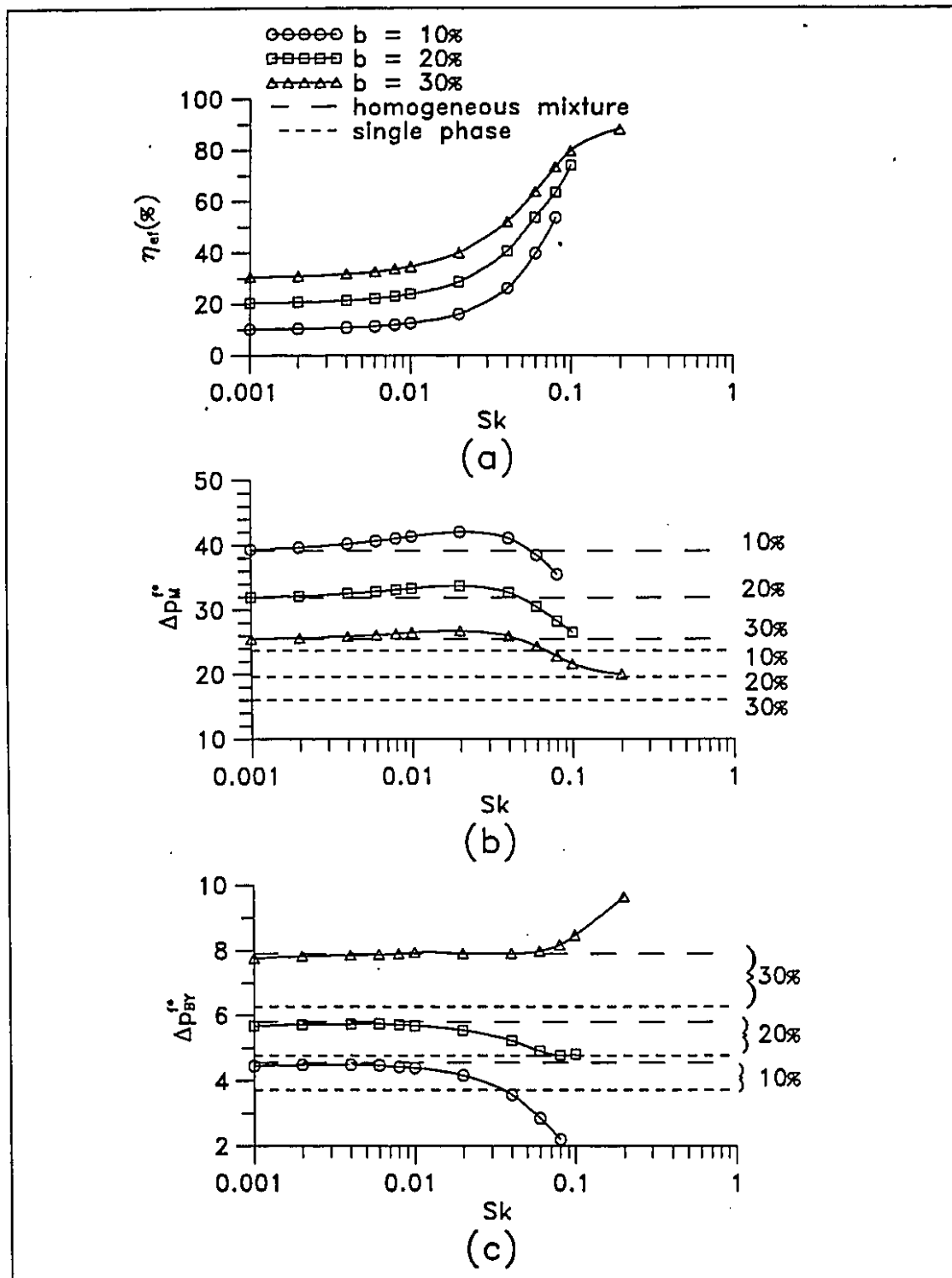


Figure 6.7: Results pertaining to $\gamma = 10^3$ and $\alpha_{in} = 10^{-3}$: (a) separator efficiency; (b) static-pressure drop in the main duct; (c) static-pressure drop in the bypass duct.

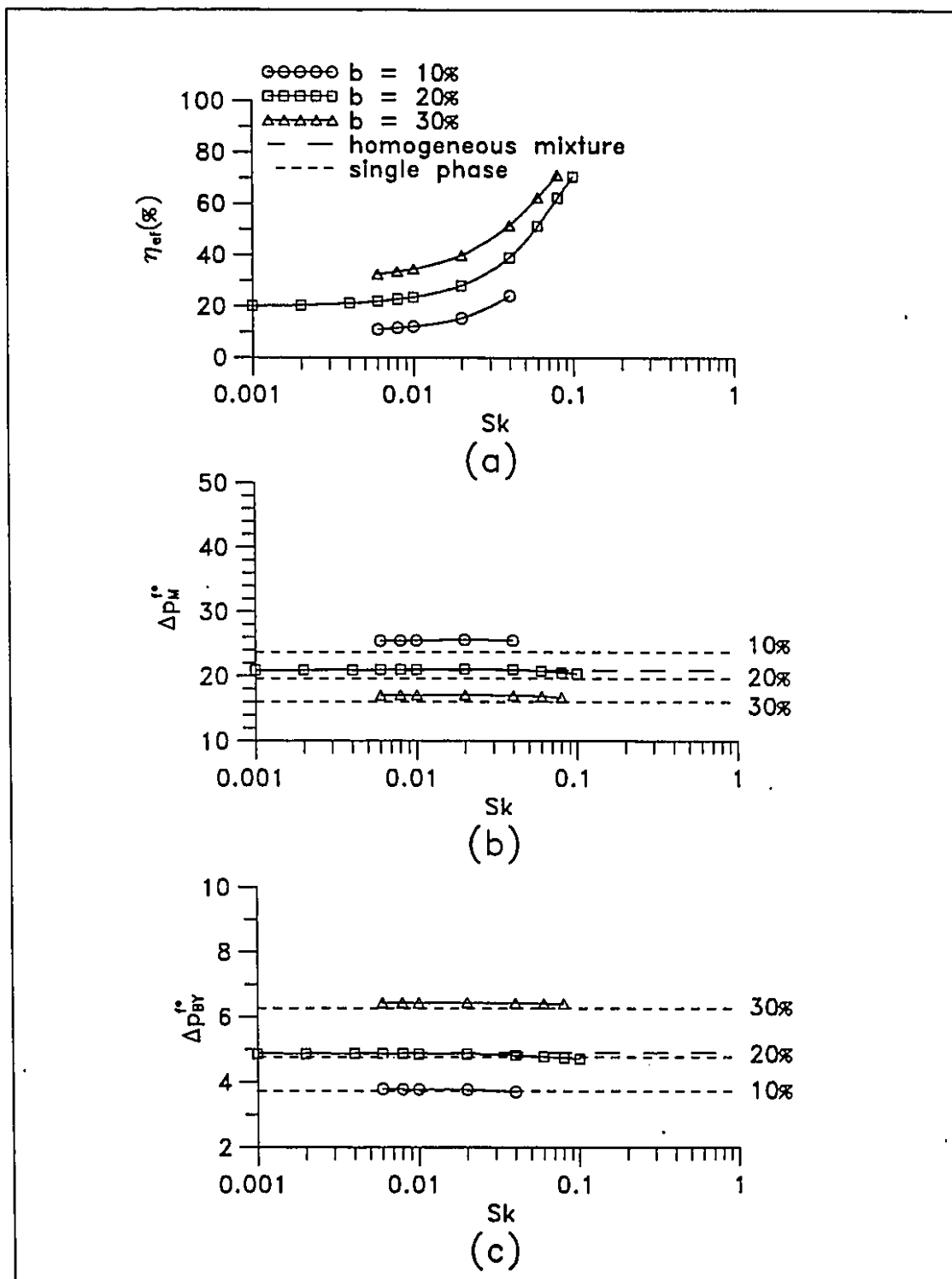


Figure 6.8: Results pertaining to $\gamma = 10^2$ and $\alpha_{in} = 10^{-3}$: (a) separator efficiency; (b) static-pressure drop in the main duct; (c) static-pressure drop in the bypass duct

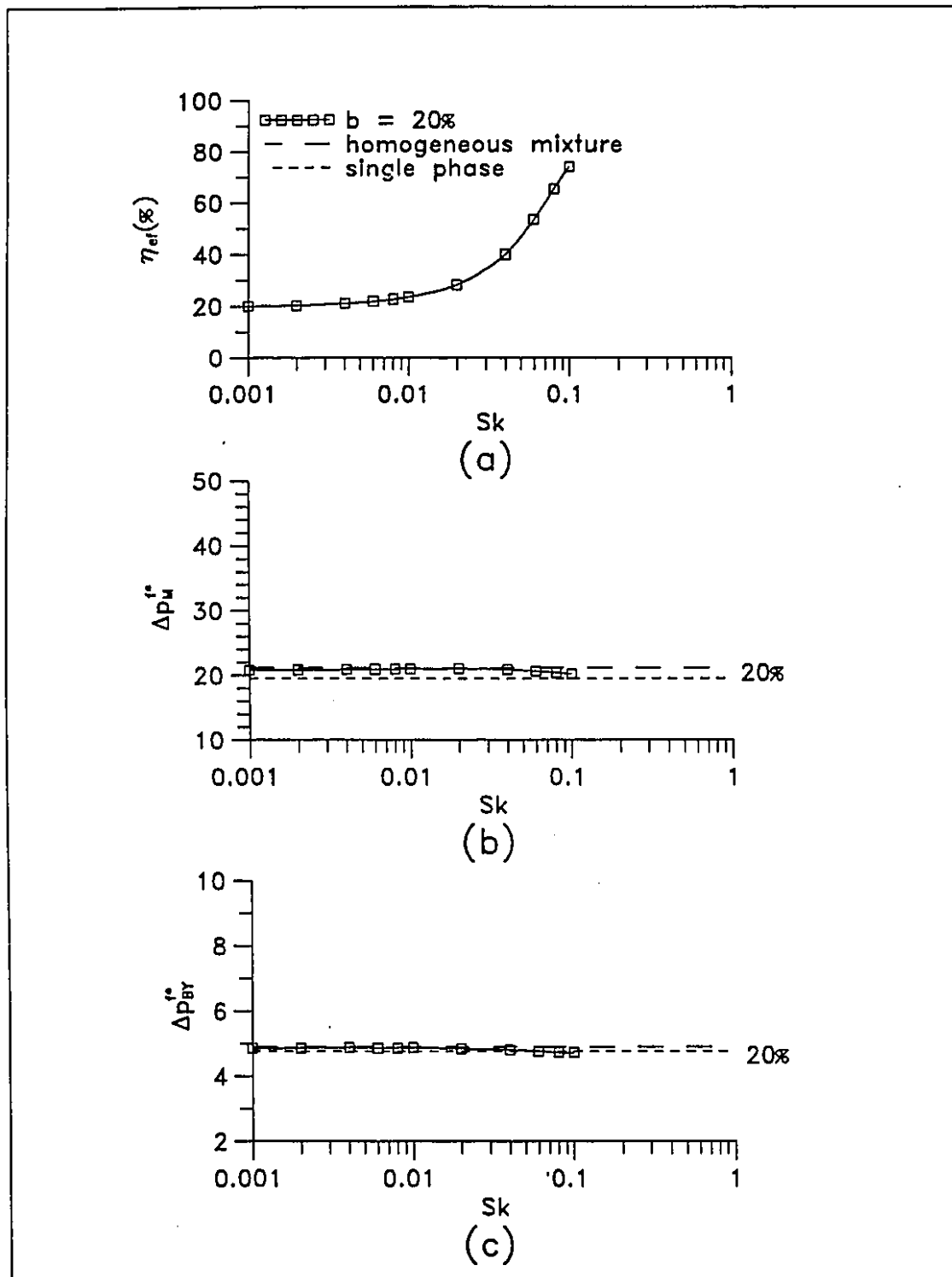


Figure 6.9: Results pertaining to $\gamma = 10^3$ and $\alpha_{in} = 10^{-4}$: (a) separator efficiency; (b) static-pressure drop in the main duct; (c) static-pressure drop in the bypass duct

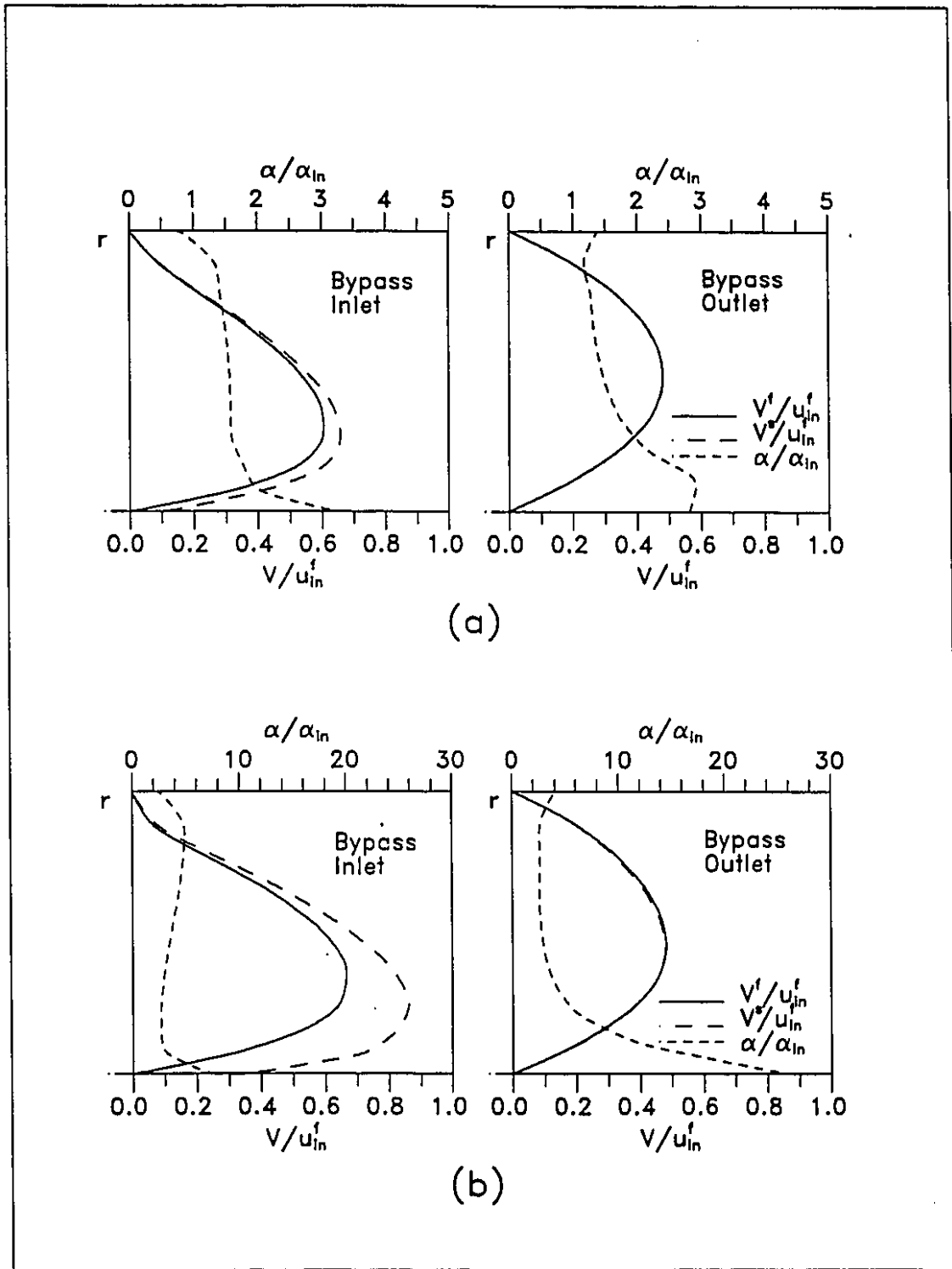


Figure 6.10: Velocity and concentration profiles pertaining to $\gamma = 10^3$, $\alpha_{in} = 10^{-3}$ and $b = 10\%$: (a) $Sk = 2 \times 10^{-2}$; (b) $Sk = 6 \times 10^{-2}$

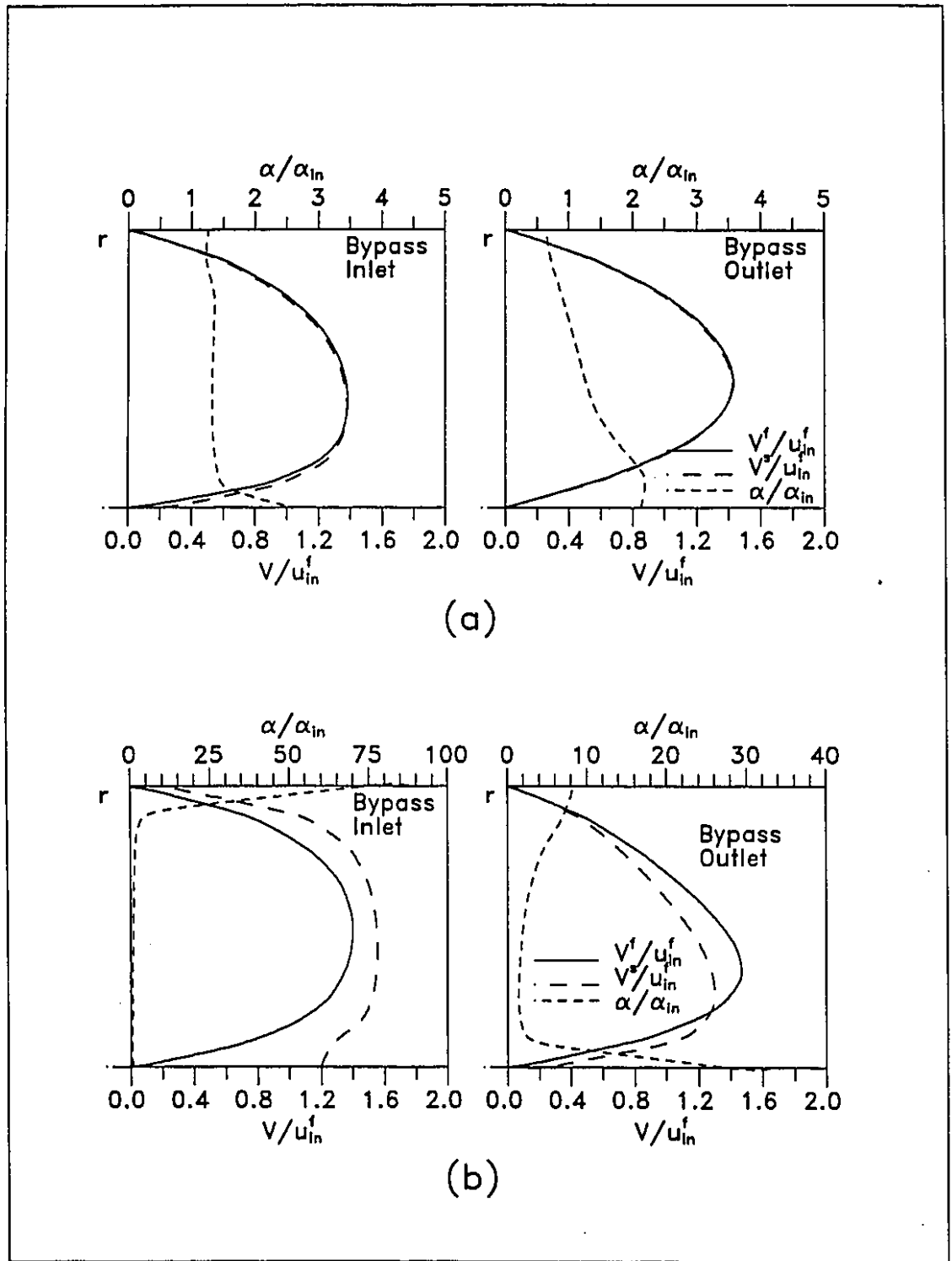


Figure 6.11: Velocity and concentration profiles pertaining to $\gamma = 10^3$, $\alpha_{in} = 10^{-3}$ and $b = 30\%$: (a) $Sk = 2 \times 10^{-2}$; (b) $Sk = 2 \times 10^{-1}$

Chapter 7

Dense Gas-Solid Particle Flow Simulations

The validity of the proposed CVFEM for the simulation of gas-solid particle flows using the general granular temperature model, presented in Chapter 3, is demonstrated in this chapter. Two test cases based on the *specified solution technique* are presented, one using the Cartesian and the other using the cylindrical coordinate systems. Simulations of gas-solid particle flows in a vertical pipe, an annular shear cell apparatus, and in a fluidized bed are also used as test problems, and the results are compared with those of independent numerical and experimental investigations. In another test problem, a dilute-concentration gas-solid particle flow in duct with a sudden contraction is simulated using the general granular-temperature model, and the results are compared with the solution presented earlier in Chapter 6, in order to assess the capabilities of the general granular-temperature model in the dilute concentration regime. Finally, the split-flow inertial separator discussed in Chapter 6 is analyzed using the granular-temperature model. This allow an appreciation of the effects of particle/particle collisions on such a flow.

Unless otherwise specified, $C_D Re^s$, $\mu_r^f(\alpha)$ and g_0 of Wallis [186], Lun and Savage [110], and Sinclair and Jackson [165], respectively, (see Table 3.1) are used in the following calculations.

7.1 Specified Solution in a Cartesian Geometry

The proposed dependent-variable fields used in this problem are:

$$u_{ex}^s = U_0 \quad v_{ex}^s = \frac{U_0}{1 + \frac{y}{L}} \quad \alpha_{ex} = \alpha_0 \left(1 + \frac{y}{L}\right) \quad (7.1)$$

$$u_{ex}^f = U_0 \left(\frac{y}{L}\right) \quad v_{ex}^f = 0 \quad p_{ex}^f = P \left(\frac{x+y}{L}\right), \quad (7.2)$$

$$T_{ex} = T_0 \left(\frac{x+L}{L}\right) \quad (7.3)$$

The solution is expressed in term of a Cartesian coordinate system (x, y) . The subscript ex is used to emphasize that the specified solution is the *exact solution*. L is the dimension of the square calculation domain. This proposed solution satisfies the solid- and fluid-phase momentum equations and the solid-phase fluctuating kinetic energy equation only with specific non-zero volumetric source terms in these equations. The complete expressions for these specific volumetric source terms are fairly involved, so they are presented in Appendix D.

In this test problem, the expressions for solid- and fluid-phase velocities and the granular temperature, given in Eqs.(7.1)-(7.3), were used to generate prescribed values of these dependent variables at the boundaries of the domain. The volume concentration was specified only at the plane $x = 0$ and the plane $y = 0$. The fluid-phase pressure was prescribed at the plane $x = L$.

This problem was solved using the proposed CVFEM and three uniform grids, namely 5 X 5, 11 X 11, and 21 X 21. The CVFEM solutions were compared with the *exact solution*. These comparisons allowed to verify: (i) the capability of the proposed CVFEM to solve the granular-temperature model; (ii) the implementation (or computer coding) of this numerical method; and (iii) the consistency of the Cartesian formulation. As the grid was refined, the average relative error (absolute value) of the CVFEM solution with respect to the *exact solution consistently* decreased: the average relative error in the computed values of v^s was 4.6% on the 5 X 5 grid, 2.3% on the 11 X 11 grid, and 1.3% on the 21 X 21 grid. This trend can be clearly seen in Fig. 7.1 which presents the variation of the solid-phase velocity in the y -direction along the centerline ($x/L = 0.5$) of the computational domain. Fig. 7.2 illustrates the corresponding variation of the solid-phase pressure. The solid-phase pressure results in Fig. 7.2 are also good indicators of the accuracy in the predic-

tions of the volume concentration and granular temperature (see Eq. (3.109)). As is clear from all these results, the solution produced by the proposed CVFEM is in good agreement with the *exact solution*. For all the grids used in this problem, the solid-phase pressure predictions are in better agreement with the *exact solution* than v^s . This can be explained by noting that T and α vary linearly with x and y , while v^s has a non-linear distribution.

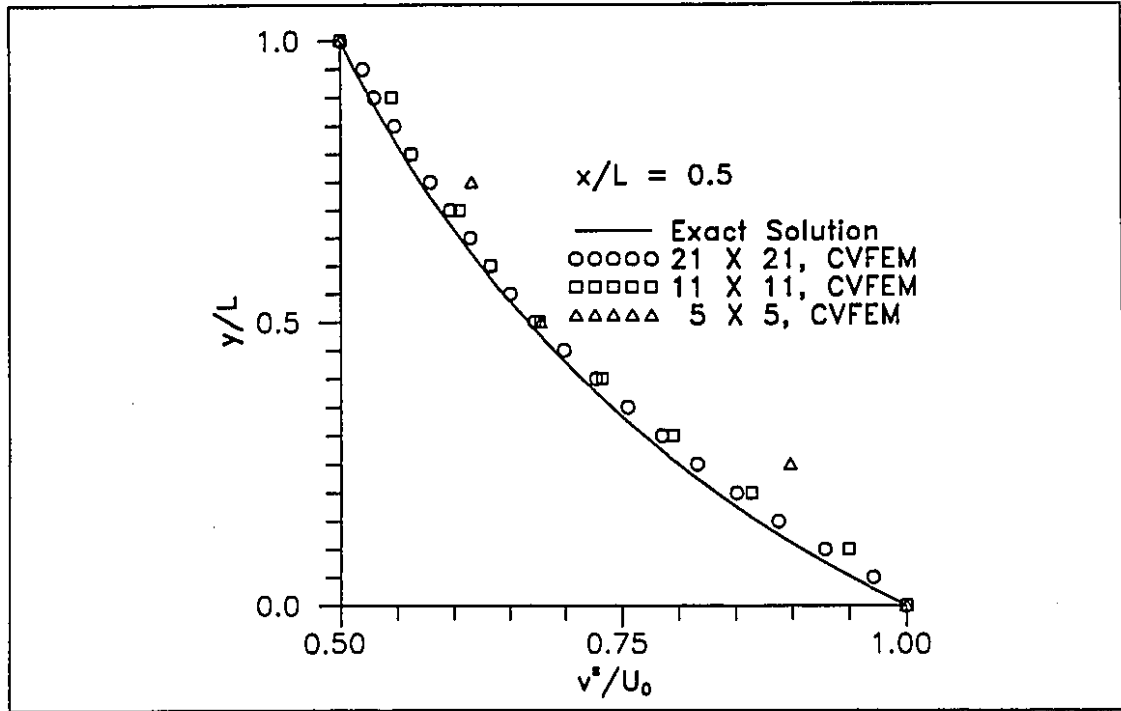


Figure 7.1: Specified solution in the Cartesian geometry: solid-phase velocity in the y -direction along the centerline ($x/L = 0.5$) of the calculation domain.

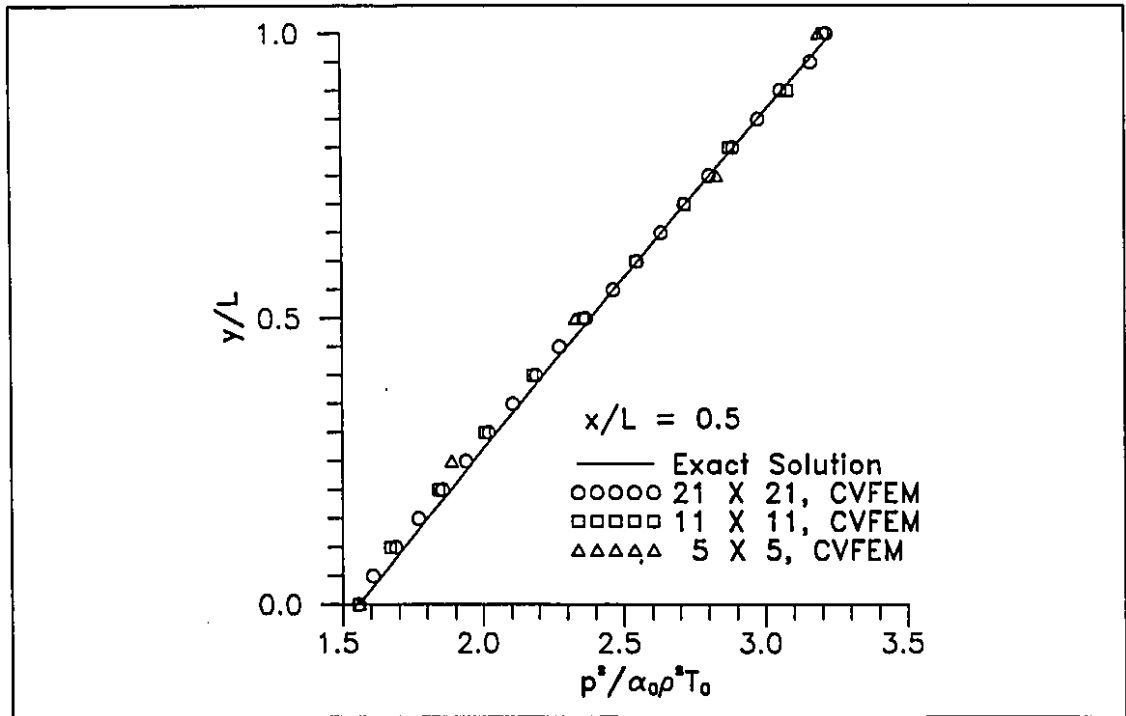


Figure 7.2: Specified solution in the Cartesian geometry: solid-phase pressure along the centerline ($x/L = 0.5$) of the calculation domain.

7.2 Specified Solution in a Cylindrical Geometry

The specified solution used in this problem is given below:

$$u_{cx}^s = U_0 \left(\frac{z}{L} \right) \quad v_{cx}^s = -U_0 \left(\frac{r}{2L} \right) \quad \alpha_{cx} = \alpha_0 \quad (7.4)$$

$$u_{cx}^f = U_0 \left(\frac{r}{L} \right) \quad v_{cx}^f = 0 \quad p_{cx}^f = P_0 \left(\frac{z+r}{L} \right) \quad (7.5)$$

$$T_{cx} = T_0 \quad (7.6)$$

The calculation domain is a cylinder of height L and radius R . The axial and radial velocity components, u and v , respectively, of both the solid and fluid phases, and the granular temperature are considered given on the curved boundary of the cylinder ($r = R$), and the bottom and top faces ($z = 0$) and ($z = L$). The volume concentration is prescribed only on the inflow boundary ($r = R$), while the fluid-phase pressure is prescribed only at the outlet plane, $z = L$. Here again, the proposed solution satisfies the governing equations only with specific non-zero volumetric source terms. The exact expressions for these implied volumetric source terms are quite complex, so they are presented in Appendix D.

This problem was solved using the proposed CVFEM. Again, computations were done with three different, uniform grids, consisting of 5 X 5, 11 X 11, and 21 X 21 nodes. The results were used to evaluate the consistency of the implementation and the capability of the proposed CVFEM to solve gas-solid particle flows in two-dimensional axisymmetric, cylindrical domains. The three calculations were pursued until the residue of the various equations reached zero (to machine precision). No convergence problem were encountered, and the average relative errors of the various dependent variables consistently approached zero as the grid was refined. Table 7.1 gives the value of the average relative errors (absolute values) along with the number of time steps needed to reach complete convergence: the non-linear problem was not solved at each time step since only steady-state solutions were sought (please see details of solution algorithm in Section 4.7).

Grid	time steps	u^f	u^s	v^s	α	p^f	T
5 X 5	100	6×10^{-2}	8×10^{-2}	2×10^{-1}	4×10^{-2}	3×10^{-4}	2×10^{-2}
11 X 11	500	4×10^{-2}	5×10^{-2}	9×10^{-2}	2×10^{-2}	2×10^{-4}	9×10^{-3}
21 X 21	2000	3×10^{-2}	3×10^{-2}	5×10^{-2}	1×10^{-2}	8×10^{-5}	5×10^{-3}

Table 7.1: Specified solution in a cylindrical geometry: absolute values of average relative errors(%).

7.3 Vertical Pipe Flow

Problem Statement

Solutions of gas-solid particle flows in a vertical pipe have been obtained by Sinclair and Jackson [165]. Their mathematical model is quite similar to the one used in this thesis (see Chapter 3). It is based on the kinetic theory of gases, and the granular temperature is a dependent variable that appears in their constitutive equations. However, they have only solved these equations in the fully-developed regime, in which the problem becomes one-dimensional (radial). In the fully-developed regime, Sinclair and Jackson [165] have studied a large variety of flows using a numerical method based on an orthogonal collocation scheme.

In this section, gas-solid particle flows in a vertical pipe (see Fig. 7.3) are investigated using the proposed CVFEM, and the results are compared with the numerical results obtained by Sinclair and Jackson [165]. As was stated before, the fully-developed problem is one-dimensional. However, here this problem was solved using a two-dimensional formulation. This is obviously not the most efficient formulation for this problem, but it allows an appreciation of the two-dimensional capabilities of the proposed CVFEM. The problem is, therefore, formulated over a pipe of finite length. Two types of boundary conditions at the ends of the pipe were tried: (i) periodic boundary conditions; and (ii) prescribed inlet conditions along with the outflow treatment, as discussed in Section 4.6. In the following discussions, the formulation based on the periodic boundary conditions will be referred to the 'periodic' problem, while the formulation based on inflow and outflow boundary conditions will be referred to as the 'inflow-outflow' problem.

The various physical properties of the problem solved by Sinclair and Jackson [165], which corresponds to flow of mineral particles in air at 427°C, are the following:

$$\mu^f = 3.65 \times 10^{-5} Pa \cdot s \quad \rho^f = 4.4 \times 10^{-1} kg/m^3 \quad (7.7)$$

$$\rho^s = 2.5 \times 10^3 kg/m^3 \quad \alpha_{MX} = 0.65 \quad v_t = 1.29 m/s \quad (7.8)$$

$$d = 1.5 \times 10^{-4} m \quad R = 1.5 \times 10^{-2} m \quad (7.9)$$

v_t is the terminal velocity of fall of a single particle under gravity; R is the radius

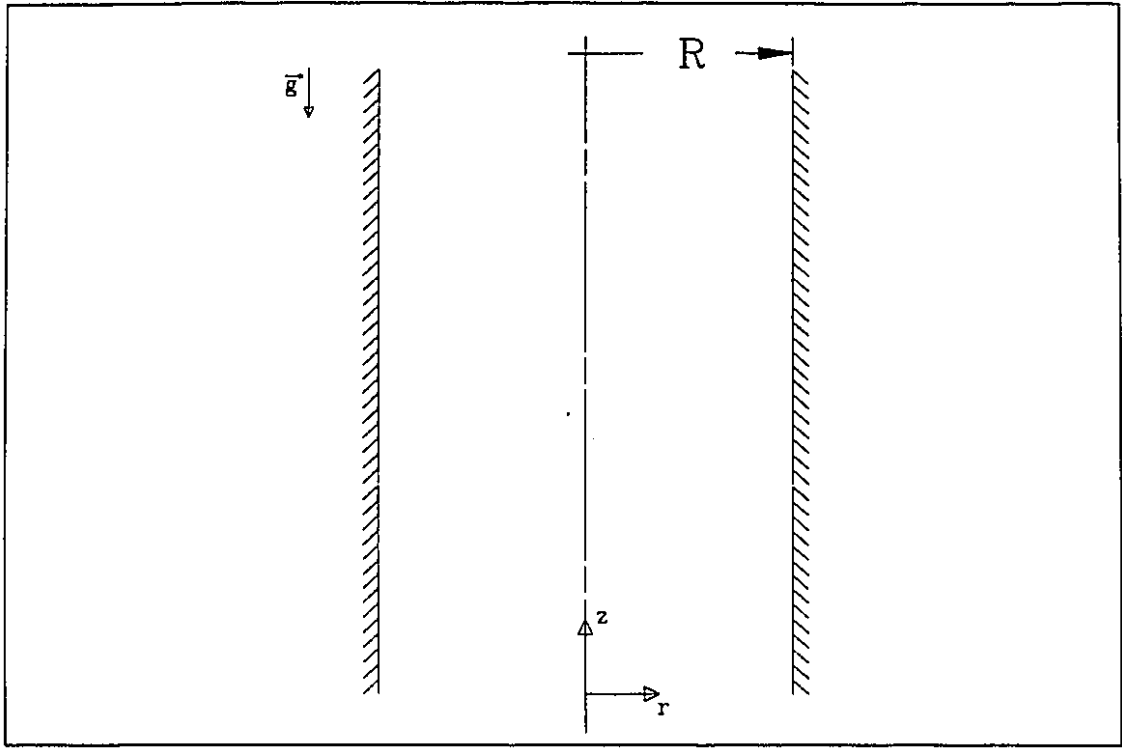


Figure 7.3: Vertical pipe

of the pipe; and α_{MX} is the solid-phase concentration at maximum packing.

Governing Equations

The governing equations for this problem are given by Eqs.(3.95)-(3.101). In order to obtain solutions which correspond to the results of Sinclair and Jackson [165], the following relations for the drag coefficient, the relative viscosity, and g_0 are used:

$$\mu_r^f(\alpha) = (1 + 2.5\alpha + 7.6\alpha^2) \left(1 - \frac{\alpha}{\alpha_{MX}}\right) \quad (7.10)$$

$$C_D Re^s = \frac{4}{3} \frac{\rho^s d^2 g}{v_t \mu_r^f (1 - \alpha)^2} \quad (7.11)$$

$$g_0 = \frac{1}{1 - \left(\frac{\alpha}{\alpha_{MX}}\right)^{\frac{1}{3}}} \quad (7.12)$$

where g is the gravitational acceleration ($g = 9.81 m/s$). With reference to Eq.(3.116), C_s is set to zero since in the formulation proposed by Sinclair and Jackson [165], the Reynolds stress is neglected. Furthermore, the constitutive equations proposed

by Sinclair and Jackson [165] do not include the effects of the drag force. Their simplified constitutive equations can be obtained from the ones proposed in this work by simply setting $\zeta_D = 0$.

The volumetric source terms are given by:

$$S_z^f = -\frac{dP}{dz} \quad (7.13)$$

$$S_r^f = 0 \quad (7.14)$$

$$S_z^s = -\alpha\rho^s g \quad (7.15)$$

$$S_r^s = 0 \quad (7.16)$$

$$S_T^s = 0 \quad (7.17)$$

where $\frac{dP}{dz}$ is the overall fluid-phase effective pressure gradient, in which the gravity term has been absorbed. This overall pressure gradient is a parameter that is specified in the 'periodic' formulation. In the 'periodic' formulation, the mass flow rates of the fluid and solid phases are not known: they have to be calculated. Therefore, another parameter needs to be prescribed in order to assign a specific value to the ratio of the fluid-phase and solid-phase mass flow rates. This additional parameter can be either (i) the average solid-phase concentration, $\bar{\alpha}$; (ii) the fluid-phase mass flow rate; (iii) the solid-phase mass flow rate; or (iv) the value of the solid-phase concentration at one point. In most of the calculation presented in this section, the solid-phase mass flow rate was considered as this additional parameter.

To complete the description of the problem, boundary conditions are required. At the wall of the pipe, both the fluid and the solid phase are allowed to slip, and these slip conditions are expressed through the prescription of appropriate shear stresses at the wall. Sinclair and Jackson [165] used the following expression for solid-phase shear stress at the wall:

$$\sigma_{rz}^s = -\frac{\sqrt{3T_w}\pi\rho^s\alpha_w g_0 u_w^s \phi'}{\alpha_{MX} 6} \quad (7.18)$$

where ϕ' is a specularity factor that is a measure of the fraction of collisions that transfer lateral momentum to the wall. Following the approach proposed by Hui et al. [88], this solid-phase wall shear stress expression was obtained from the rate of transfer of lateral momentum from the particles to the wall. For specular par-

ticle/wall collisions (smooth wall), $\phi' = 0$, while for a rough wall, $\phi' = 1$. In this problem, Sinclair and Jackson used $\phi' = 0.5$.

For the fluid-phase wall shear stress, the following expression has been proposed by Sinclair and Jackson [165]:

$$\sigma_{rz}^f = -\frac{2\mu_e^f \alpha_{MX} T_w u_w^f}{v_t^2 \alpha_w \Delta} \quad (7.19)$$

where Δ is a linear measure of the control-volume at the wall ($\Delta = \mathcal{V}_{cv}^{1/3}$).

The boundary condition for the granular temperature at the wall is expressed in terms of a fluctuating kinetic energy flux. Johnson and Jackson [95] have proposed an expression for this flux, obtained by assuming that the inelastic particle/wall collisions are characterized by a coefficient of restitution e_w . They then used an energy balance to show that the energy flux at the wall is the sum of the rate of dissipation due to particle/wall inelastic collisions, γ_w , and the energy generation by slip:

$$q_r^s = \gamma_w + u_w^s \sigma_{rz}^s \quad (7.20)$$

where

$$\gamma_w = \frac{\sqrt{3T_w} \pi \rho^s \alpha_w g_0 (1 - e_w^2) T_w}{\alpha_{MX} 4} \quad (7.21)$$

In their calculations, Sinclair and Jackson used $e_w = 0.9$.

Solution Procedure

For the case of the 'periodic' problem, a special attention is needed to ensure that the solution will correspond to the fully-developed regime. An additional equation can be derived from the integration of the fully-developed solid-phase momentum equation in the r -direction:

$$p^s(\alpha, T) = \text{constant} = p^s(Q^s) \quad (7.22)$$

This equation simply states that the solid-phase pressure is constant and, for the sake of concreteness in this discussion, this constant is named $p^s(Q^s)$. This equation relates the granular temperature, T , to the solid-phase volume concentration, α , by the use of Eq.(3.109). The granular temperature is given by the solution of the fluctuating kinetic energy equation and, therefore, for a given constant $p^s(Q^s)$, α can be calculated at any point. The constant $p^s(Q^s)$ in Eq.(7.22) is prescribed so as to match the calculated solid-phase mass flow rate, Q^s , with that computed by Sinclair and Jackson [165]: at each time step (or iteration), the solid-phase mass flow rate was computed and compared with the desired solid-phase mass flow rate, in order to propose a correction to the value of $p^s(Q^s)$; and this procedure was continued until the desired solid-phase mass flow rate was obtained. This process is highly implicit and the relationship between p^s , α and T (Eq.(3.109)) is nonlinear, therefore, in most of the calculations using the periodic boundary conditions, under-relaxation was needed to compute α . The notation used to identify the constant in Eq.(7.22) can now be explained to the reader: it emphasizes that this constant is indirectly prescribed by the desired solid-phase mass flow rate Q^s .

Results

Six cases corresponding to six different solid-phase volumetric flow rates were simulated in this test problem. Assuming the various physical properties given before as fixed, each case is characterized by the nondimensional overall pressure gradient $\frac{d\tilde{P}}{dz}$, the nondimensional solid-phase volumetric flow rate, \tilde{Q}^s , and the coefficient of restitution, e , with:

$$\frac{d\tilde{P}}{dz} = \frac{1}{\rho^s g} \frac{dP}{dz} \quad (7.23)$$

$$\tilde{Q}^s = \frac{1}{R^2 v_t} \int_0^R \alpha \rho^s u^s 2\pi r dr \quad (7.24)$$

Using a similar expression, the nondimensional fluid-phase volumetric flow rate \tilde{Q}^f can be calculated. Another quantity of interest that can be computed is the average solid-phase concentration, $\bar{\alpha}$. For each case, the values of \tilde{Q}^f and $\bar{\alpha}$ are computed based on the solutions of the proposed CVFEM and compared with the values obtained by Sinclair and Jackson [165]. Table 7.2 gives the details of this comparison, including absolute values of the relative difference between the proposed solution and

the results of Sinclair and Jackson [165]. The results obtained with the CVFEM are in good agreement with the solutions of Sinclair and Jackson [165]. A grid of 3 X 11 was used. 11 points were used in the r -direction in order to have a grid similar to the one used by Sinclair and Jackson [165]. In the interest of economical computations, only 3 points were used in the z -direction. This does not affect the accuracy of the results, since the solution is strictly one-dimensional. However, it should be noted that for the first case given in Table 7.2, a grid of 11 X 11 was also used and it yielded a converged solution identical to that obtained with the 3 X 11 grid. The sixth case, which corresponds to inelastic particles, needed smaller time step to converge than that used in the first five cases: with larger time steps, in the course of the march towards steady-state solutions, the computed solid-phase volume concentration could achieve values greater than the corresponding value at maximum packing. The time step used for the sixth case was about ten times smaller than for the other cases.

$\frac{dP}{dz}$	e	\bar{Q}^s	Proposed CVFEM		Sinclair and Jackson [165]		Rel. Dif. (%)	
			\bar{Q}^f	$\bar{\alpha}$	\bar{Q}^f	$\bar{\alpha}$	\bar{Q}^f	$\bar{\alpha}$
-0.2	1.0	0.34	4.4	0.19	4.4	0.18	0.0	5.6
	1.0	0.04	1.7	0.25	1.7	0.25	0.0	0.0
	1.0	-0.15	.79	.23	0.83	0.22	4.8	4.5
	1.0	-0.34	-0.023	0.26	-0.022	0.25	4.5	4.0
	1.0	-0.62	-0.61	0.46	-0.61	0.46	0.0	0.0
	.99	-2.10	-2.83	0.36	-2.83	N.A.	0.0	

Table 7.2: Vertical pipe flow: comparative study

The detailed CVFEM results, consisting of the axial velocity, concentration, and granular temperature profiles, corresponding to the various cases described in Table 7.2, are presented in Figs. 7.4- 7.9. In all cases, the CVFEM solutions are in such good agreement with the results of Sinclair and Jackson [165] that they are essentially indistinguishable in a graphical presentation; so the latter are not shown in Figs. 7.4- 7.9. For the first case, a simulation with 21 points in the r -direction was also obtained, and the resulting solution was found to be so close to the 11-point solution that the respective curves presented on plots similar to Fig. 7.4 were indistinguishable.

As was stated before, \tilde{Q}^s was the additional parameter used in the 'periodic' formulation. However, in order to obtain results comparable to Sinclair and Jackson [165], in the third case, the centerline solid-phase concentration was used as the additional parameter, so there is a small difference in the corresponding solid-phase mass flow rates: the proposed CVFEM predicted $\tilde{Q}^s = -0.15$ while the corresponding case in Sinclair and Jackson [165] is $\tilde{Q}^s = -0.16$.

In all the simulations, there is a region of high concentration near the wall, because the particle/wall inelastic collisions have the effect of accumulating particles in the vicinity of the wall. In the case of inelastic particle/particle collisions (case 6), Fig. 7.9, the concentration profile presents a different behaviour than the other cases: the maximum concentration is at the centre of the pipe. This migration of the particle to the centre of the pipe, which is ascribed to shear-induced particle migration in the literature [102], is in qualitative agreement with experiments [85] and Stokesian dynamics simulations [125]. In these studies, a flattening of the velocity profiles in the vicinity of the centerline was also observed. Again, such a flattening behaviour can be noted in the CVFEM solution corresponding to the particle/particle inelastic collisions case, Fig. 7.9a. The shape of the velocity profiles and the direction of the particle migration confirm that the migration goes from high to low shear rate regions [102]. The physical mechanism that explains such a migration is still not well understood [125]. Leighton and Acrivos [102] suggested that the migration is due to the roughness of the particles; Nott and Brady [125] explained this behaviour by the chaotic motion that takes place in a system of more than three particles. Based on the results of this section, all that can be said for sure is that inelastic collisions between the particles clearly induce particle migration to the centre of the pipe.

The results presented so far were obtained using the 'periodic' formulation. However, the fully-developed solution can also be obtained using the 'inflow-outflow' formulation, by prescribing the corresponding solid- and fluid-phase mass flow rates at the inlet. Regardless of the shape of the various prescribed profiles at the inlet, the corresponding fully-developed profiles will be achieved somewhere along the pipe, provided the pipe is long enough. The length between the inlet and the position where the flow is fully-developed is commonly called the entry length. Nott and Brady [125] found that the entry length for gas-solid particle flows is considerably

larger than the entry length for laminar single-phase flow. Using the expression for the entry length proposed by Nott and Brady [125], the entry length of the gas-solid particle mixture used in this simulation is $4 \times 10^4 R$. Thus, the computational domain needed to achieve fully-developed conditions at the pipe exit is far too long. However, if the inlet conditions are prescribed to be close to the fully-developed solution, it is expected that a much smaller length would be needed to reach the fully-developed conditions. Here, in order to illustrate the two-dimensional capabilities of the proposed CVFEM, the 'inflow-outflow' problem was solved in a pipe of length $20R$, with inlet conditions corresponding to a small perturbation of the fully-developed solution obtained with the 'periodic' formulation. At the outlet of the pipe, the outflow treatment of Patankar [130] is used. This treatment is not suitable when backflow exits at the outlet plane. Therefore, the only case that can be successfully simulated with this 'inflow-outflow' formulation is the one illustrated in Fig. 7.4. The assumed perturbed inlet conditions are:

$$u_{in}^f = u_{FD}^f \quad v_{in}^f = 0 \quad \alpha_{in} = \alpha_{FD} \quad (7.25)$$

$$u_{in}^s = u_{FD}^s \quad v_{in}^s = 0 \quad T_{in} = .9T_{FD} \quad (7.26)$$

where u_{FD}^f , u_{FD}^s , α_{FD} , and T_{FD} correspond to the solution obtained with the periodic formulation. The results of this simulation on a 101×11 grid are illustrated in Fig. 7.10. It shows the evolution of the centerline granular temperature as a function of the axial distance from the inlet. The dotted line represents the fully-developed solution obtained with the 'periodic' formulation and the full line is the result of the 'inflow-outflow' simulation. As indicated by Nott and Brady [125], the process to reach the fully-developed regime is very slow: a pipe length of $20R$ is not long enough to reach the fully-developed region, even with the small perturbation imposed at the entrance plane. However, the results in Fig. 7.10 do show that the granular temperature approaches the fully-developed solution as the flow move through the pipe.

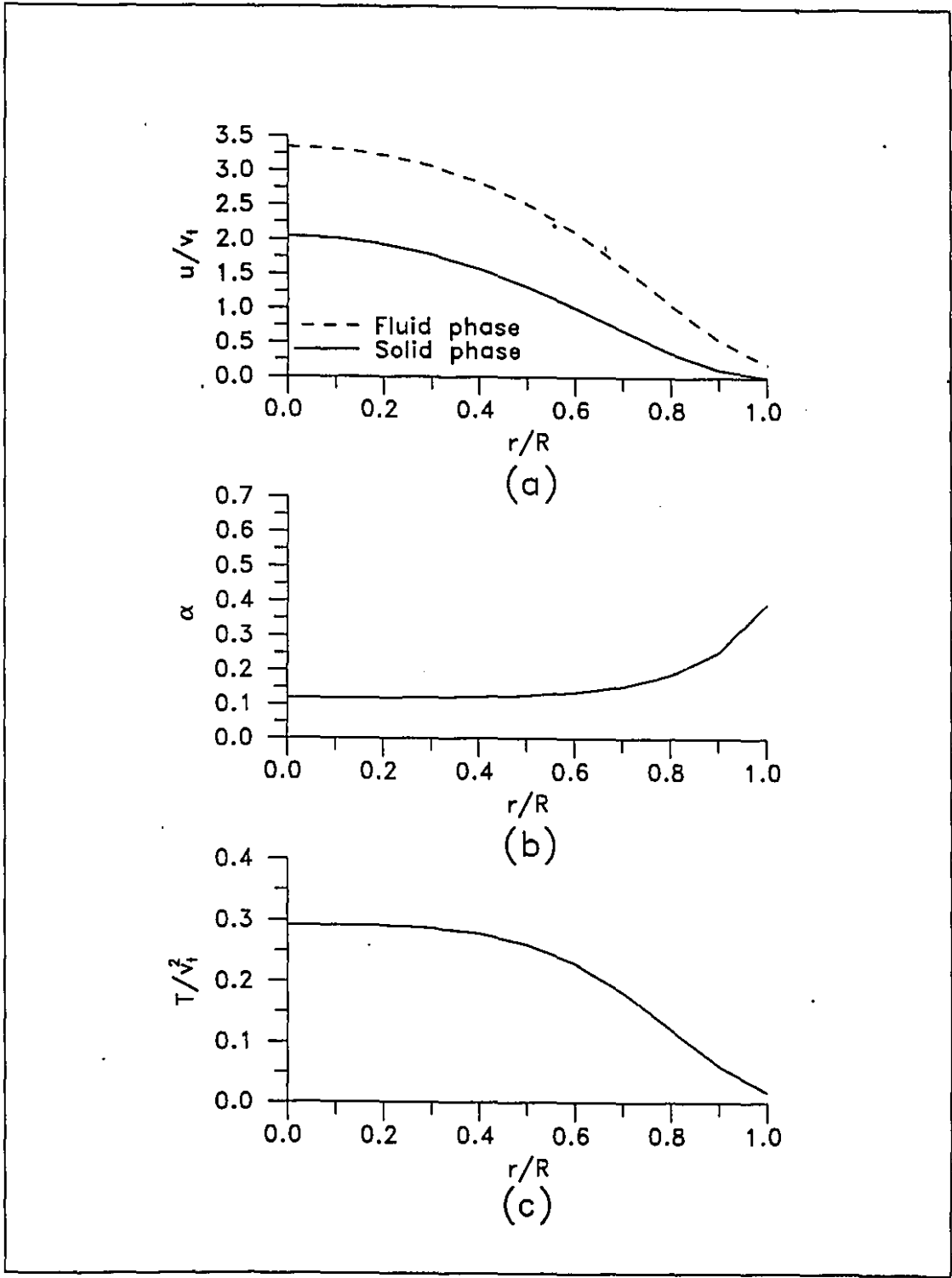


Figure 7.4: Vertical pipe flow : $\frac{d\bar{P}}{dz} = -0.2$; $e = 1.0$; $\tilde{Q}^s = 0.34$

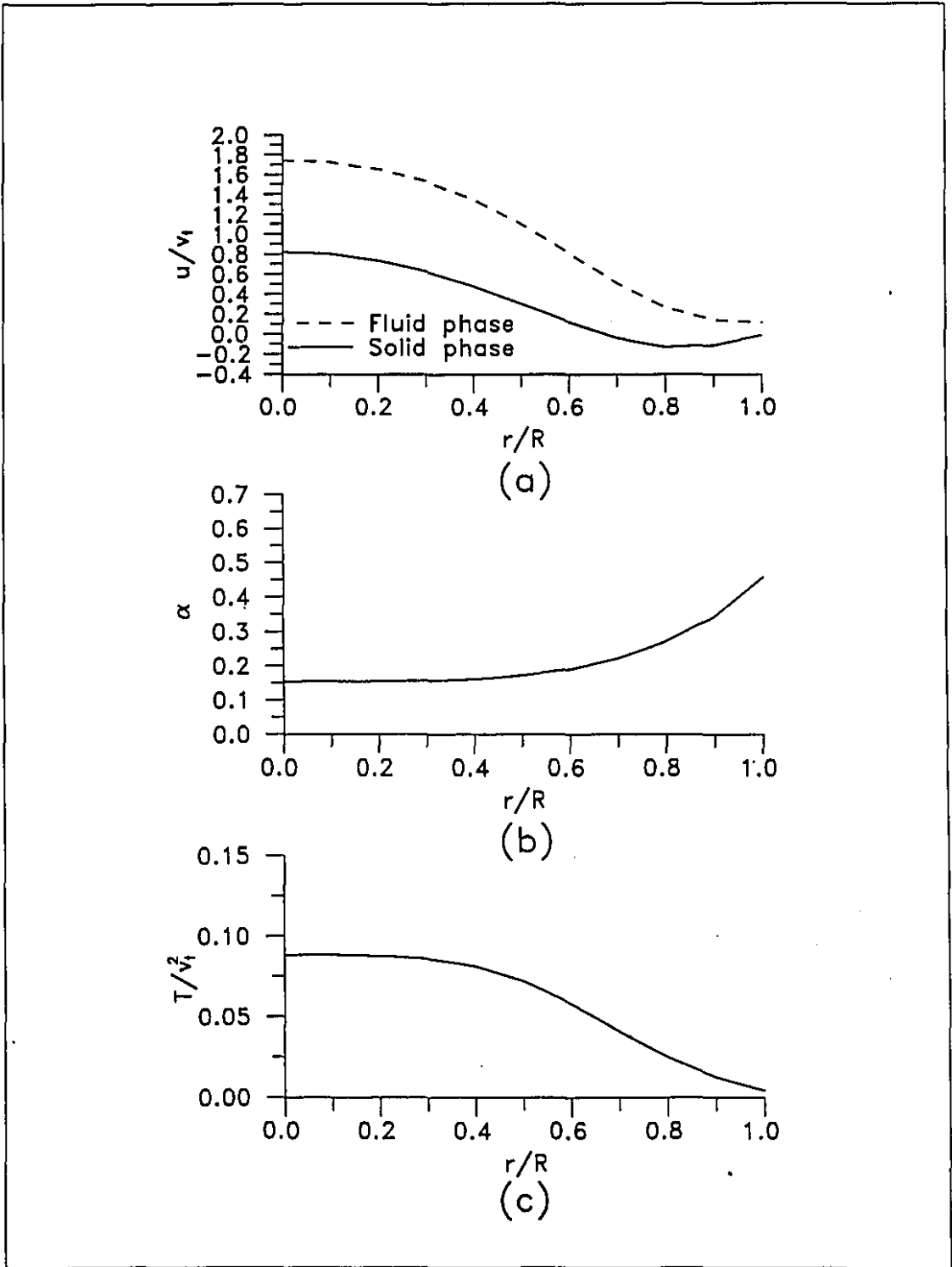


Figure 7.5: Vertical pipe flow : $\frac{dP}{dz} = -0.2$; $e = 1.0$; $\tilde{Q}^s = 0.04$

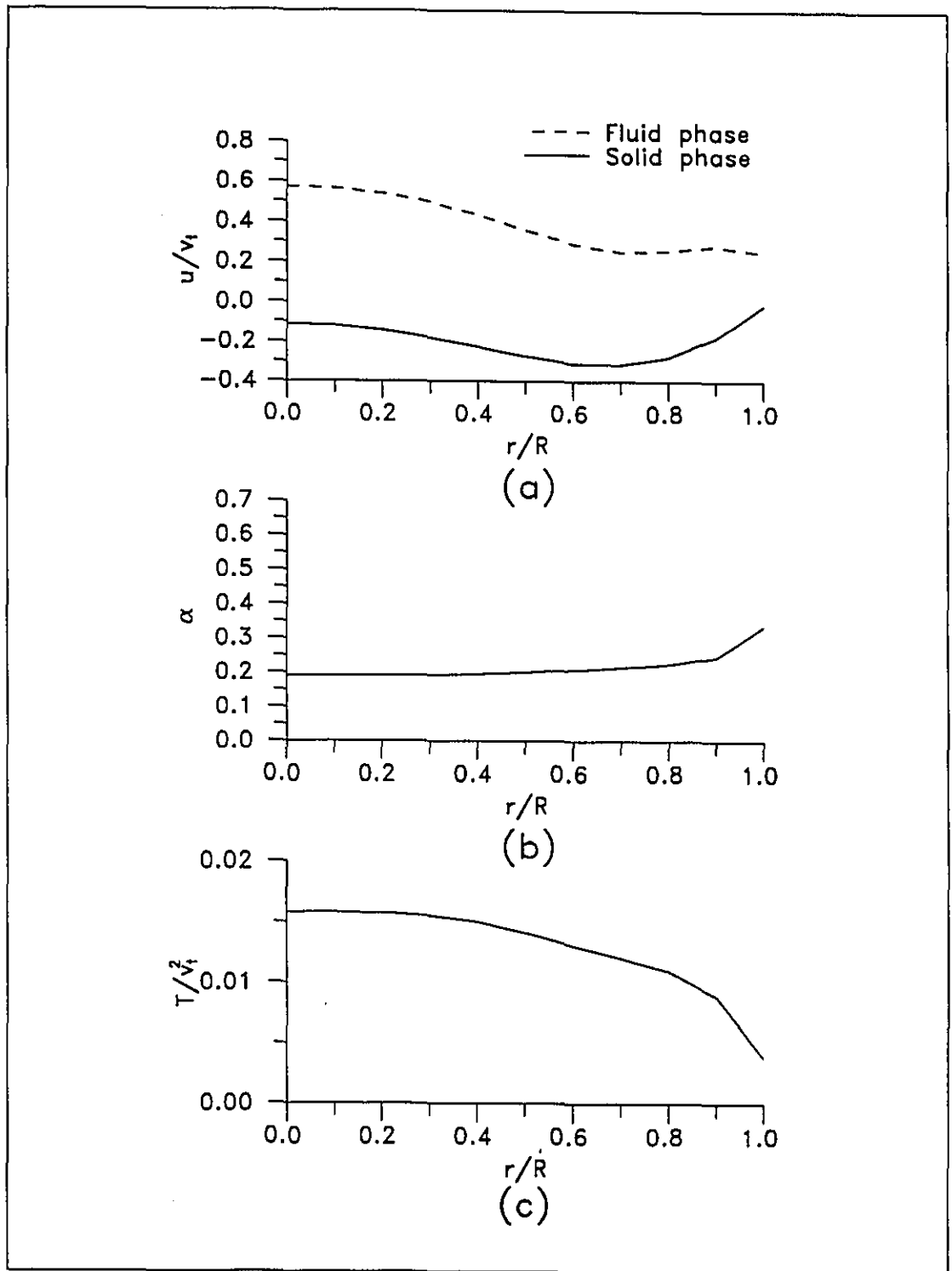


Figure 7.6: Vertical pipe flow : $\frac{d\bar{p}}{dz} = -0.2$; $e = 1.0$; $\tilde{Q}' = -0.15$

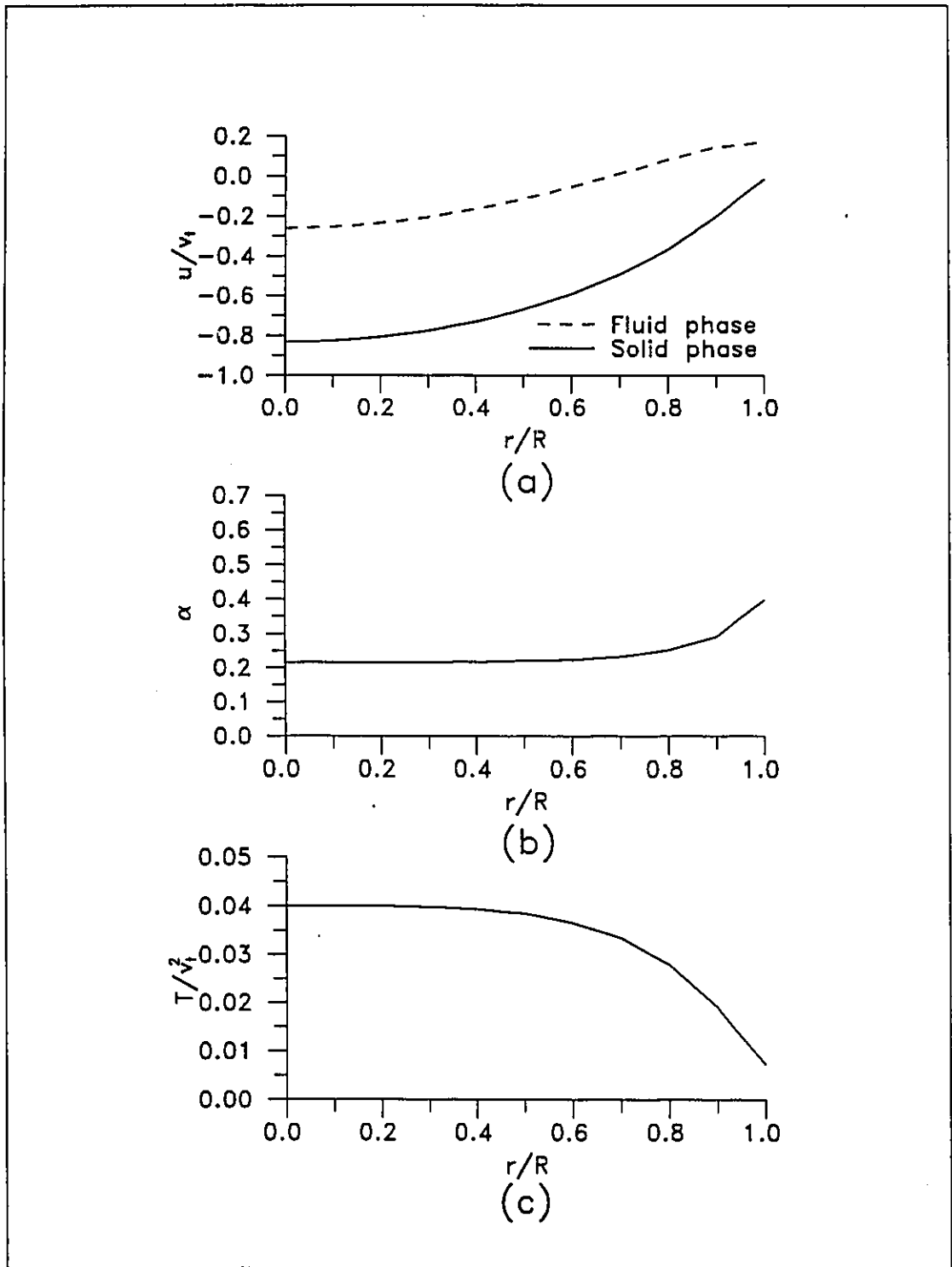


Figure 7.7: Vertical pipe flow : $\frac{d\bar{p}}{dz} = -0.2$; $e = 1.0$; $\bar{Q}^s = -0.34$

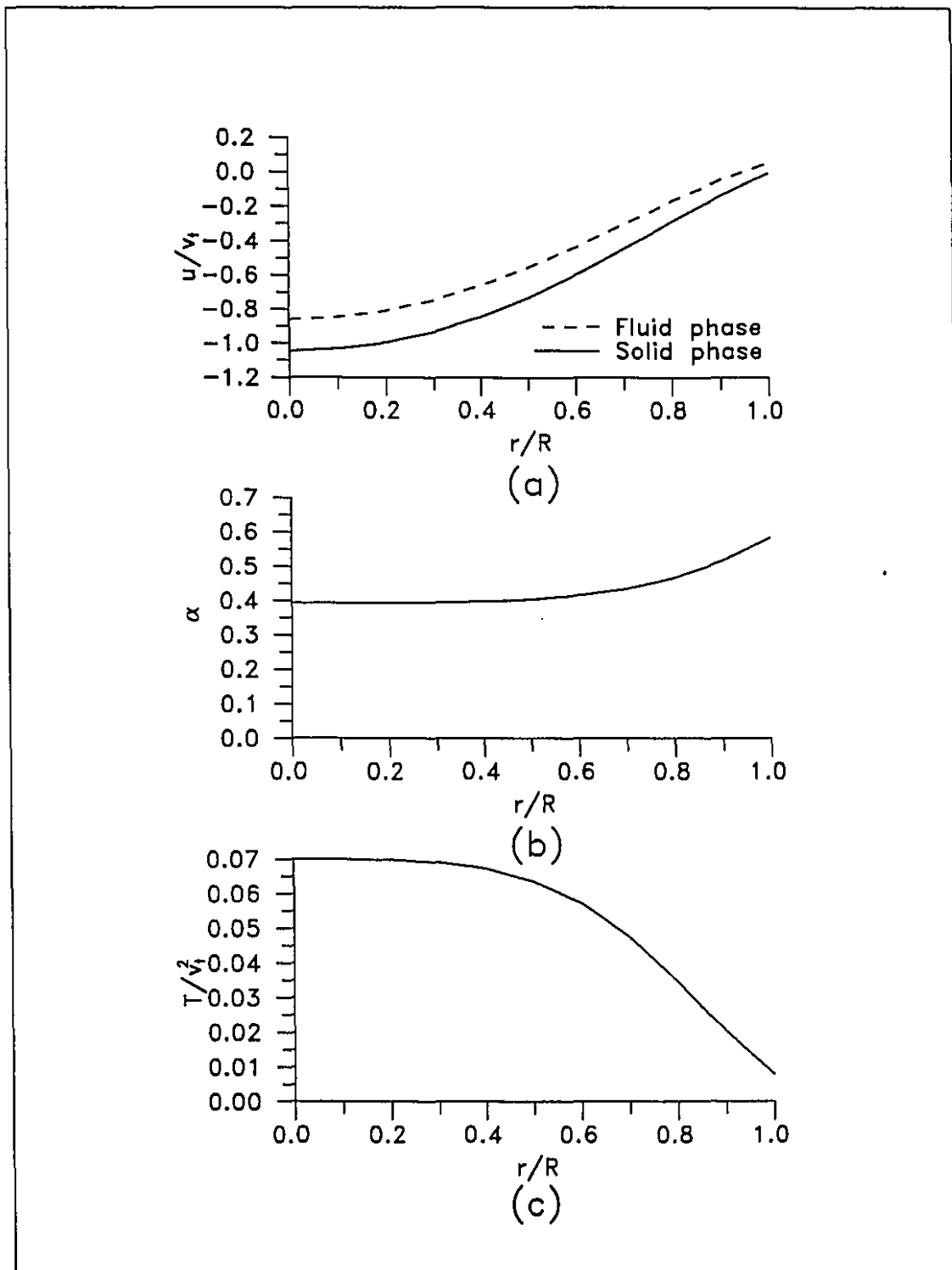


Figure 7.8: Vertical pipe flow : $\frac{d\bar{P}}{dz} = -0.2$; $e = 1.0$; $\bar{Q}^* = -0.62$

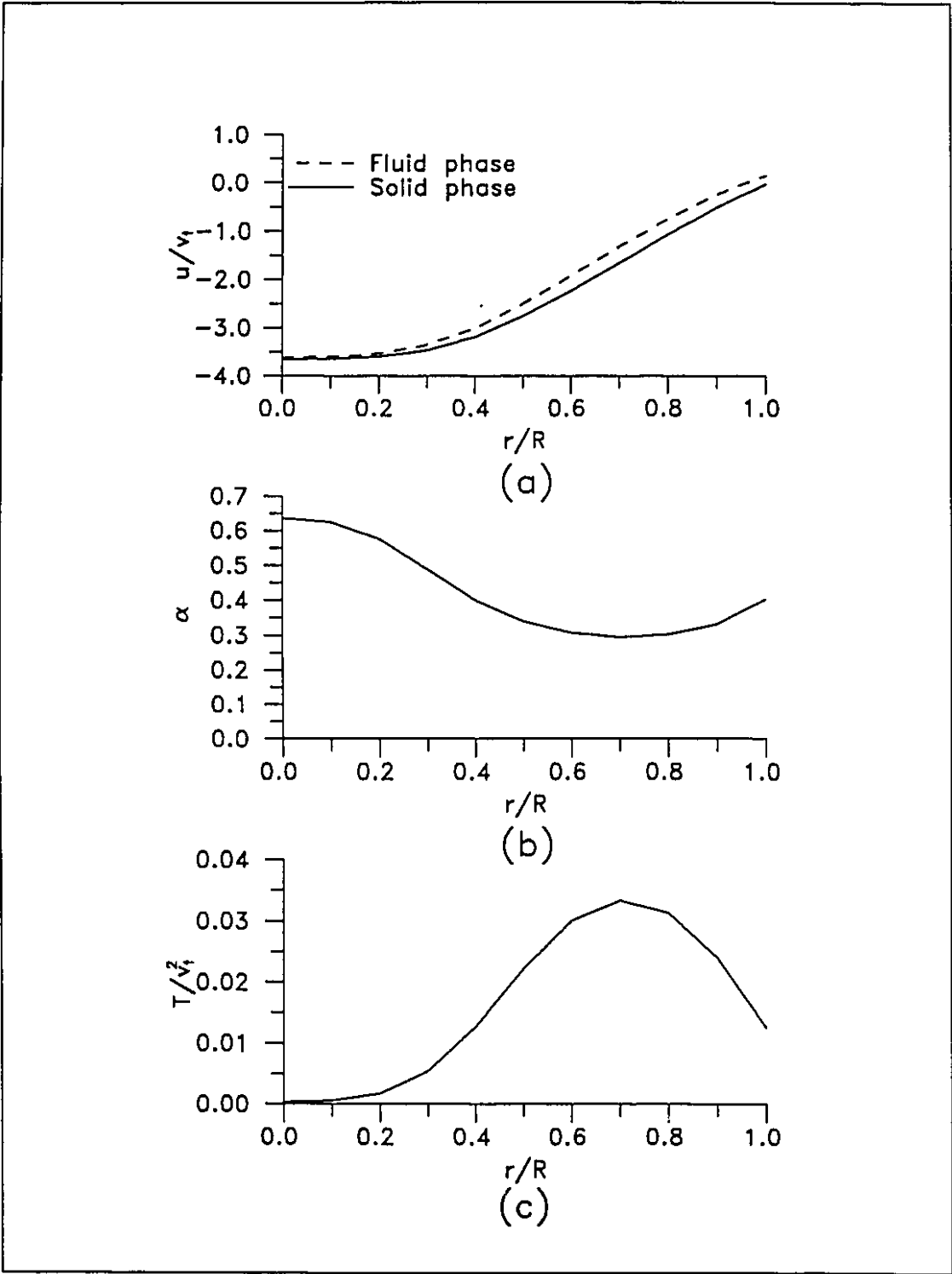


Figure 7.9: Vertical pipe flow : $\frac{d\bar{p}}{dz} = -0.2$; $e = .99$; $\tilde{Q}^s = -2.10$

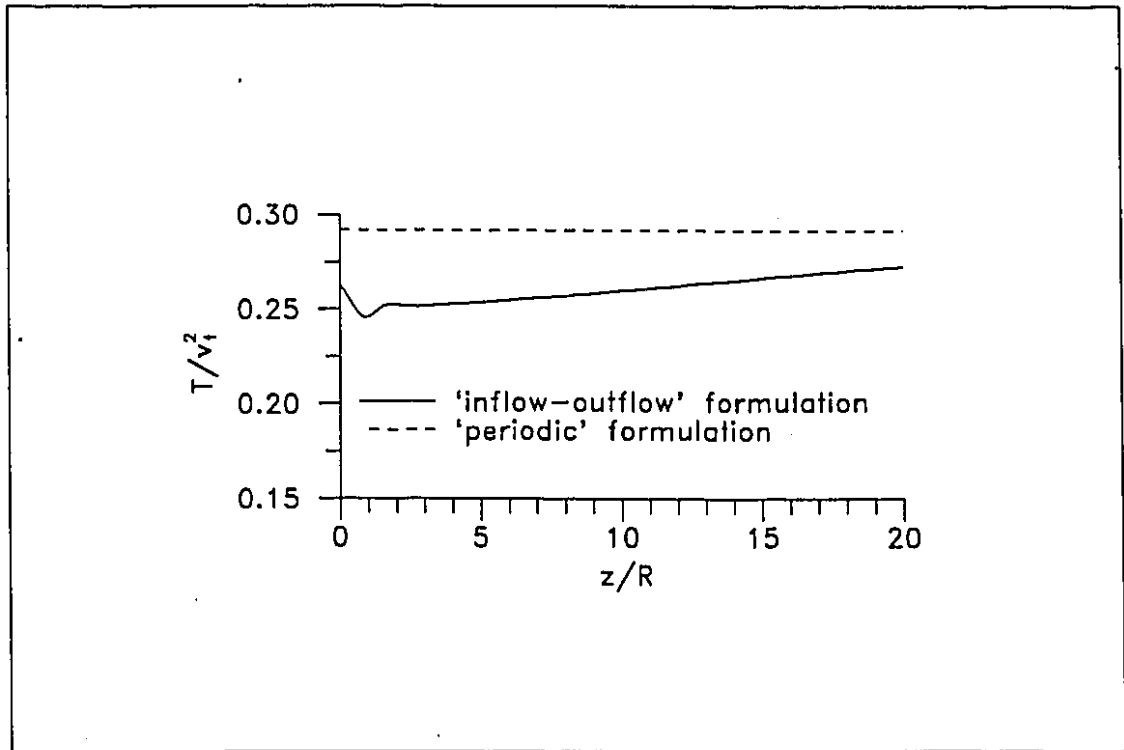


Figure 7.10: Two-dimensional vertical pipe flow : $\frac{d\bar{p}}{dz} = -0.2$; $e = 1.0$; $\hat{Q}^s = 0.34$

7.4 Flow in an Annular Shear Cell Apparatus

Problem Statement

Total normal and shear stresses in gas-solid particle flows have been obtained experimentally by Savage and Sayed [151], and Hanes and Inman [73], using annular shear cell apparatus similar to the one shown in Fig. 7.11a (this is Fig. 1 of Ref. [151]). These experiments provide data that can be used to examine the various mathematical descriptions of the fluid- and solid-phase stress tensors. Savage and Sayed [151] used polystyrene beads, glass beads and crushed walnut in air. Hanes and Inman [73] used glass beads in air and water. These experiments can be described by the simple plane shearing model of Fig. 7.11b if the centrifugal effects are negligible. In the experiment of Savage and Sayed, for example, the centrifugal effects modify the solid-phase stresses by only 1% to 2% [151]. Using this assumption, Johnson and Jackson [95] have solved this problem with the simple plane shearing model. The stress model used in their analysis includes both collisional and frictional contributions. The frictional contribution appears at dense concentrations, close to the maximum packing of the granular material, when particles interact with each other through long-term direct contact. Their evaluation of the frictional contribution included an empirical constant which was calculated to fit the experimental data. Another adjustable parameter was also included in their collisional contribution. Only comparison with the experimental data of Savage and Sayed [151] were presented in the work of Johnson and Jackson [95].

Experiment	$\bar{\alpha}$	$d(mm)$	$\rho^s(kg/m^3)$	$H(mm)$	e	e_w	ϕ'
Savage and Sayed	.477	1.80	2970	11.610	.89	.50	.60
[151]	.507	1.80	2970	10.920	.89	.50	.60
Hanes and Inman	.440	1.85	2780	13.717	.95	.95	-
[73]	.460	1.85	2780	13.121	.95	.95	-
	.490	1.85	2780	12.317	.95	.95	-

Table 7.3: Flow in annular shear cell: various parameters

In this section, numerical solutions of the simple plane shearing model obtained using the proposed CVFEM are compared with some of the experimental data of Savage and Sayed [151] and Hanes and Inman [73]. As was stated earlier, the

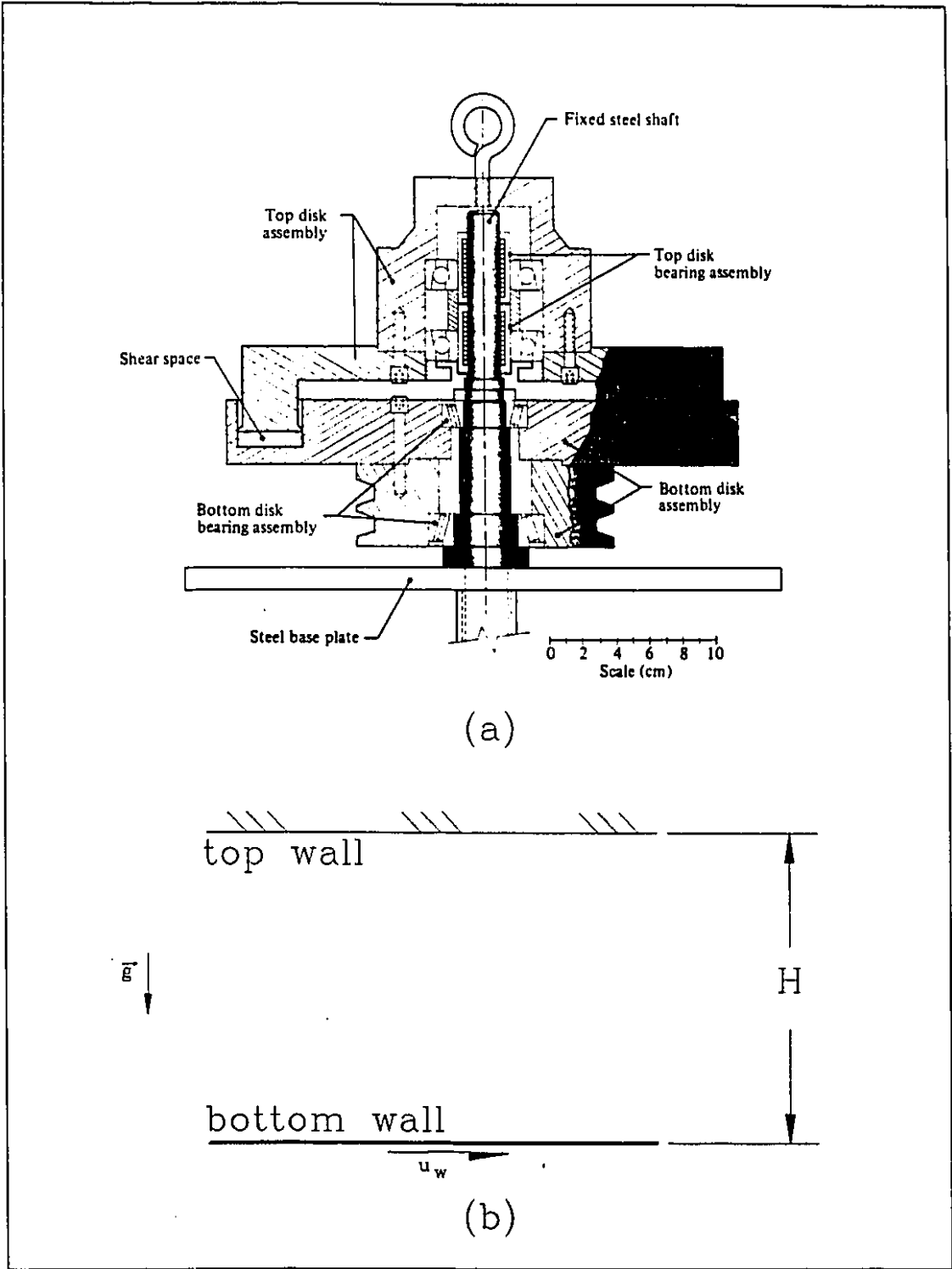


Figure 7.11: (a) Annular shear cell apparatus (Fig. 1 of Ref. [151]); (b) Plane shearing model

frictional contribution becomes significant at very high concentrations, when the concentration is close to the maximum packing of the granular material. At lower concentrations, frictional contribution can also be important when the shearing of the material is very low. In this section, only the relatively high shearing experiments at concentrations far from the close-packing concentration will be presented. No comparison with the numerical solutions of Johnson and Jackson will be presented, since the proposed mathematical model does not include any frictional contribution to the solid-phase stress tensor.

The plane shearing problem solved in this section consists of a fixed top wall and a moving bottom wall separated by a distance H as shown in Fig. 7.11b. The velocity of the bottom wall is denoted u_w and is in the positive x -direction. The bottom wall is located at $y = 0$, and the top wall is located at $y = H$. The experiments of Savage and Sayed [151], and Hanes and Inman [73] were designed to give the normal and shear stresses at the top wall.

Governing Equations

This problem is described by the granular-temperature model, in the Cartesian coordinate system, corresponding to Eqs.(3.95)-(3.101). Strictly, this problem is one dimensional, but in order to test the proposed two-dimensional formulation, a finite length of the plane shearing cell is modelled along with periodic boundary conditions at the inlet and outlet planes of the calculation domain.

The experiments of Savage and Sayed [151], and Hanes and Inman [73] were constructed to minimise the slip of the solid phase at the top and bottom walls of the annular shearing cell: Savage and Sayed used sand paper, while Hanes and Inman cemented a layer of solid particles on each wall. The type of surface roughness used by Hanes and Inman ensures a perfect no-slip condition of the solid-phase. In the case with the sand paper, a slip can exist, and, therefore, the slip boundary conditions proposed by Sinclair and Jackson [165] will be used. Particle/wall collisions are assumed inelastic. In this work, the granular temperature gradients at the walls are prescribed following the analysis proposed by Sinclair and Jackson [165].

Solution Procedure

As was the case in the 'periodic' formulation of the flow in a vertical pipe (Section 7.3), an additional equation is needed to converge to the desired fully-developed solution. This equation is obtained by the integration of the solid-phase momentum equation in the y -direction and is used to compute the solid-phase concentration, α :

$$p^s(\alpha, T) = \left[p^s(\bar{\alpha}_{\text{EXP}}) - (\rho^s - \rho^f) g \int_0^y \alpha dy \right] \quad (7.27)$$

where $p^s(\bar{\alpha}_{\text{EXP}})$ is a constant which has to be prescribed in order to ensure that at convergence, the average volume concentration calculated by the CVFEM corresponds to the experimental one: after each time step (or iteration), the average volume concentration of the CVFEM solution, $\bar{\alpha}_{\text{CVFEM}}$, is computed; then $p^s(\bar{\alpha}_{\text{EXP}})$ is modified so as to meet the requirement that $\bar{\alpha}_{\text{CVFEM}}$ should be equal to the average volume concentration of the experiment, $\bar{\alpha}_{\text{EXP}}$. The concentration is computed using the integrated solid-phase y -momentum equation, Eq. (7.27). This process is highly implicit and α was under-relaxed during the solution process in order to ensure convergence.

Results

The geometrical and physical parameters of the various simulations presented in this section are given in Table 7.3. All the simulations were done for the case of glass particles in air. To simulate the experiments of Hanes and Inman [73], the coefficients of restitution, e and e_w , were set to 0.95. This is the value of the coefficient of restitution of glass particles, e , in vacuum [110]. For the simulation corresponding to the experiments of Savage and Sayed [151], smaller values of e and e_w were used. The smaller value of e_w is justified because of the type of wall surfaces used in their experiment, namely, sandpapered wall: for such a surface, Johnson and Jackson [95] have suggested $e_w = 0.50$ and $\phi' = 0.60$. The use of a smaller e , however, needs more justifications. It is assumed that the sandpapered surfaces scratched the glass particles. Lun and Savage [109] showed that rough particles tend to have more rotational energy than smooth particles, and this, in

turn, leads to lower levels of stresses. The mathematical model proposed in this work assumed that the particles are smooth and, therefore, no rotational energy is included in the analysis. A parametric study of some of the various parameters appearing in the proposed theory was undertaken in order to choose appropriate values of e .

The results of the parametric study are presented in Fig. 7.12 for a case corresponding to an experiment of Savage and Sayed [151]. Fig. 7.12a illustrates the effect of the coefficient of restitution of the particle/particle collisions, e , on the nondimensionalized total shear and normal stresses at the top wall:

$$\tau_s^* = \frac{\tau_s}{\rho^s g d} \quad (7.28)$$

$$\tau_n^* = \frac{\tau_n}{\rho^s g d} \quad (7.29)$$

where τ_n and τ_s are the sum of the solid- and fluid-phase stresses applied normally and tangentially to the top wall, respectively. Only the results with $e > 0.8$ are presented, since the theory is only applicable for slightly inelastic particles. As is clearly seen, there is a significant decrease of the shear and normal stresses as the coefficient of restitution, e , decreases. A variation of 70% is noted between the computed normal stresses corresponding to $e = 0.95$ and $e = 0.80$: the corresponding variation of the shear stress is 50%. This behaviour is associated with the dissipation of fluctuating energy by inelastic collisions, which result in a lower level of granular temperature and, therefore, in smaller values of the solid-phase stresses. These important variations of the stresses illustrate that physically meaningful simulations can be realized only when a good evaluation of e is available. In order to obtain comparable level of stresses between the experiments of Savage and Sayed [151] with rough particles and the smooth-particle simulations done with the proposed CVFEM, a smaller value of e ($= 0.89$) than the one corresponding to glass particle in vacuum ($e = 0.95$) were used in the CVFEM simulations.

A parametric study was also undertaken to quantify the effects of e_w and ϕ' (see Fig. 7.12b and c). The effects of e_w exhibit trends similar to those in the effects of e , but with much smaller variations: between $e_w = 1.0$ and $e_w = 0.0$, a variation of 40% is noted on the normal stress and 20% on the shear stress. Furthermore, most of the variation is noted in the range $0.8 < e_w < 1.0$. The effect of the specular-coefficient ϕ' is illustrated in Fig. 7.12c: there is an increase of the shear and

normal stresses as ϕ' increases. Low values of ϕ' correspond to smooth walls, while large values correspond to rough walls. Rough walls produce solid-phase fluctuating kinetic energy and therefore, the solid-phase stresses increase. Another parameter which significantly influences the level of stress is the radial distribution function g_0 (see Table 3.3). In the present simulations, the radial distribution function was taken as:

$$g_0 = \frac{1}{1 - \left(\frac{\alpha}{\alpha_{MX}}\right)^{\frac{1}{3}}} \quad (7.30)$$

with $\alpha_{MX} = 0.65$. The radial distribution function proposed by Lun [107] (see Table 3.3) produces a decrease of 20% in the stress level.

Fig. 7.13 presents fluid- and solid-phase velocity, solid-phase volume concentration, and granular temperature profiles for the same problem as that corresponding to Fig. 7.12, but with specific values of e , e_w , and ϕ' : $e = 0.89$, $e_w = 0.50$ and $\phi' = 0.6$. The fluid and solid phases are in dynamic equilibrium in almost the entire domain: only slight differences in velocity are noted in regions near the walls. It is also seen that the velocity profiles are not linear, as is the case in the single-phase Couette flow. The concentration profile exhibits accumulation of particles near both the bottom and top walls. The increase in concentration at the bottom is explained by the action of gravity which tends to accumulate particles at the bottom of the shear cell. The migration of particle to the region near the top wall is induced by the inelastic wall/particle collisions. The granular temperature profile shows strong increases of T near the walls, which illustrates that the production of solid-phase fluctuating energy by rough walls is more important than the dissipation by inelastic particle/wall collisions.

Comparisons of the experimental normal and shear stresses with those obtained using the proposed mathematical model are presented in Figs. 7.14 and 7.15. Fig. 7.14 presents a comparison with the results of Savage and Sayed [151] for glass particles of 1.80 mm diameter, and the results in Fig. 7.15 show a comparison with the experimental results of Hanes and Inman [73] for glass particles of 1.85 mm diameter. The experimental and numerical results show fair agreement, with the shear stresses showing a better agreement (see Figs. 7.14a and 7.15a) than the normal stresses (see Figs. 7.14b and 7.15b). Furthermore, the overall trends, in terms of variation with

the apparent shear rate, $\left(\frac{d}{g}\right)^{\frac{1}{2}} \frac{u_w}{H}$, and average concentration, $\bar{\alpha}$, are well predicted.

In conclusion, it should be noted that the experiments of Savage and Sayed [151] and those of Hanes and Inman [73] were done with similar particles, however, the stresses measured by the former are much smaller than those obtained by the latter. This discrepancy is attributed to the different types of wall roughness used in each experiment [73]. Hanes and Inman used a cemented layer of particles, and, therefore, ensured the applicability of the non-slip condition at the wall. Savage and Sayed used sand paper at the wall, which only reduces the slip, and transforms the smooth particles into rough particles.

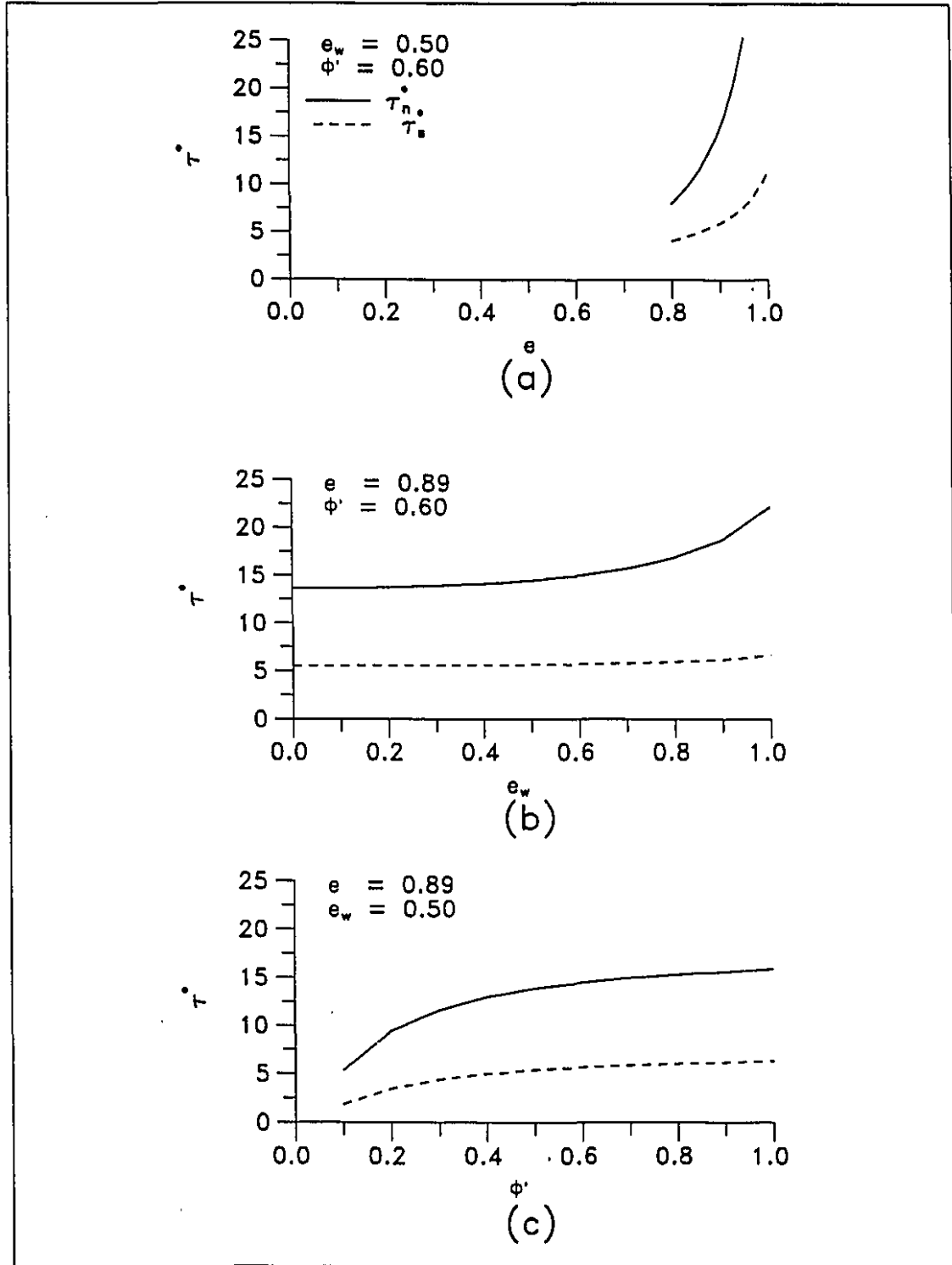


Figure 7.12: Flow in annular shear cell - parametric study : $\bar{\alpha} = 0.477$; $\left(\frac{d}{g}\right)^{\frac{1}{2}} \frac{u_w}{H} = 2.0$

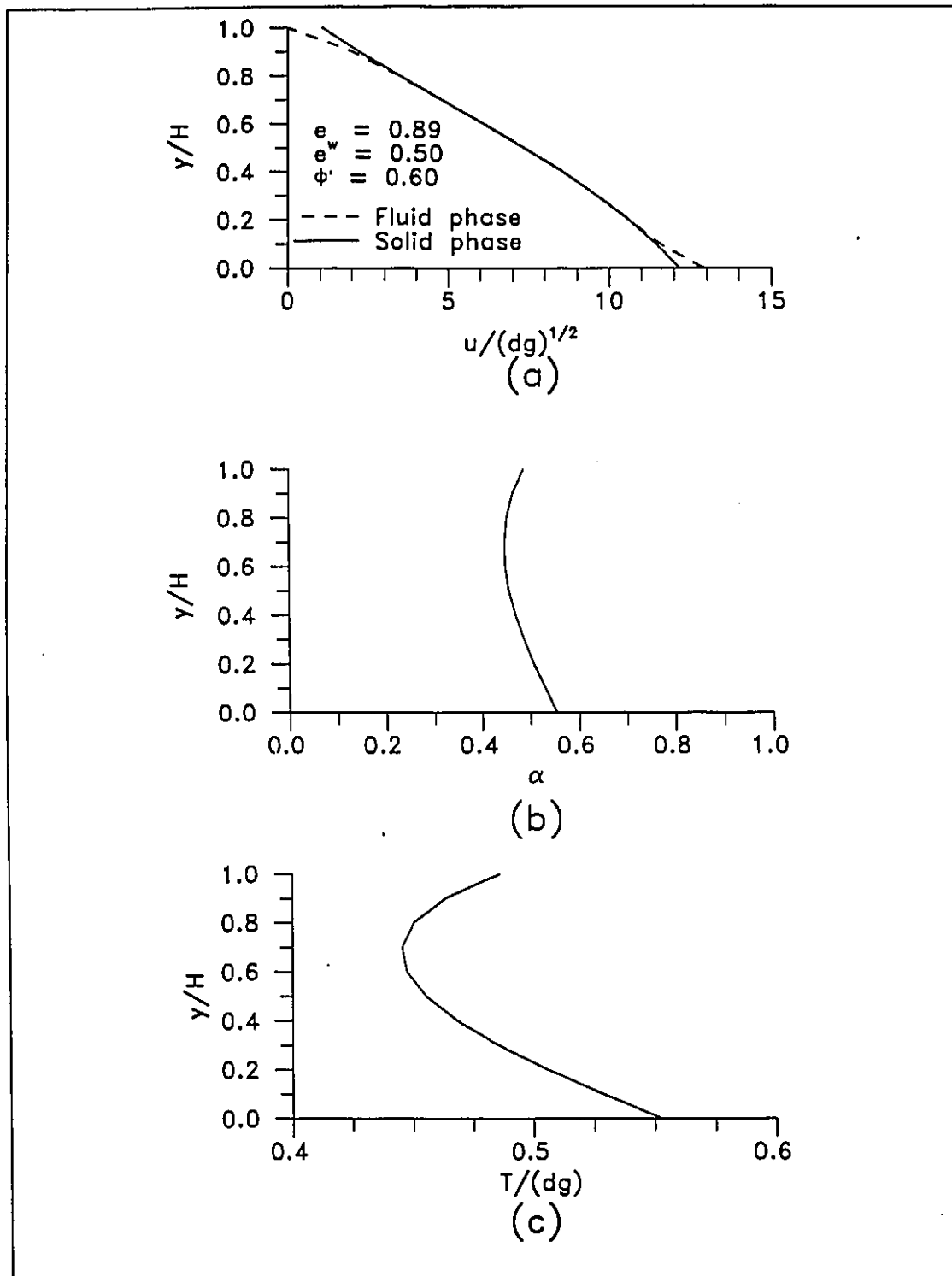


Figure 7.13: Flow in annular shear cell - velocity, concentration and temperature profiles : $\bar{\alpha} = 0.477$; $\left(\frac{d}{g}\right)^{\frac{1}{2}} \frac{u_w}{H} = 2.0$

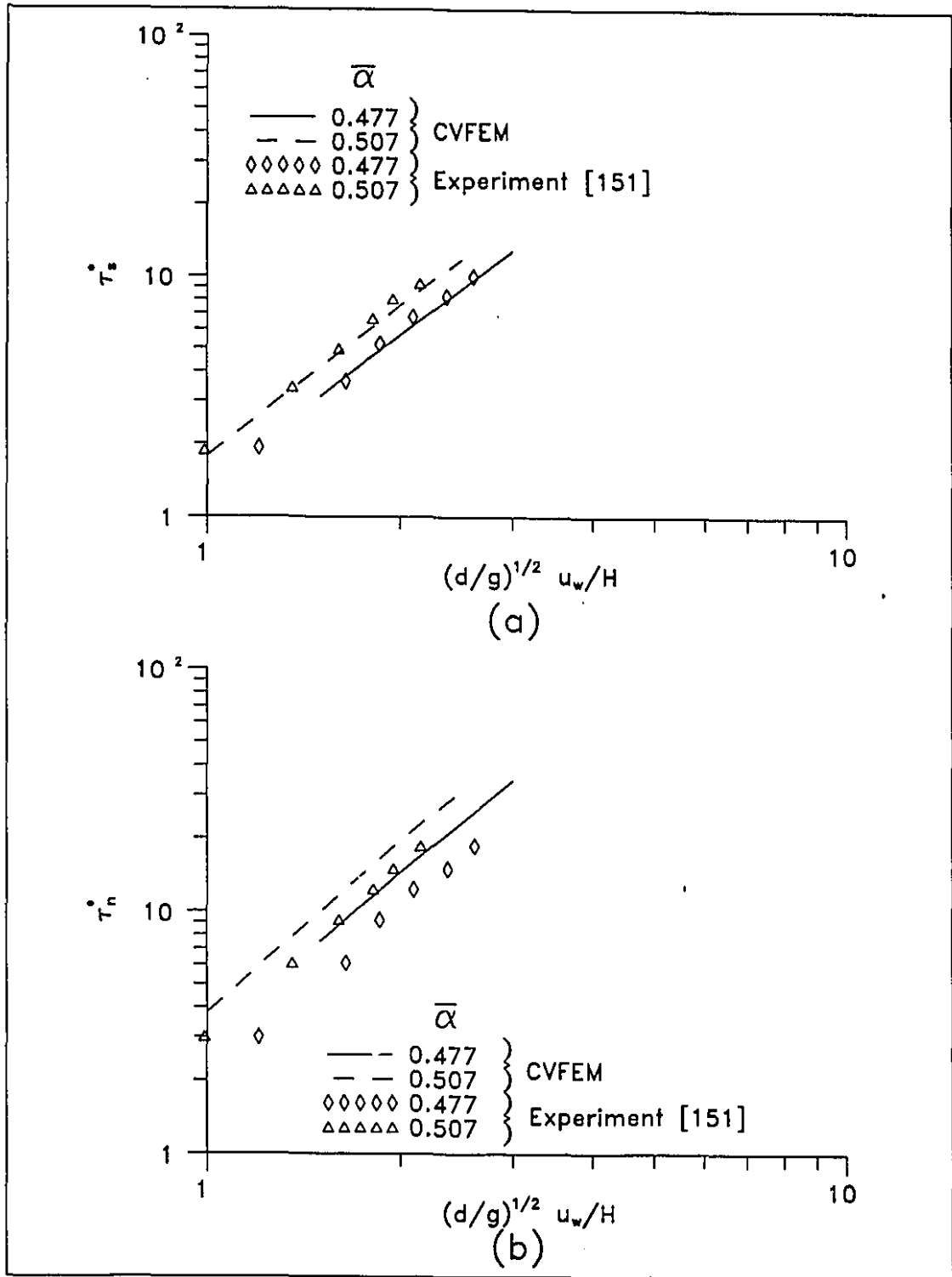


Figure 7.14: Flow in annular shear cell - shear and normal stresses : $e = 0.89$; $e_w = 0.50$; $\phi' = 0.60$

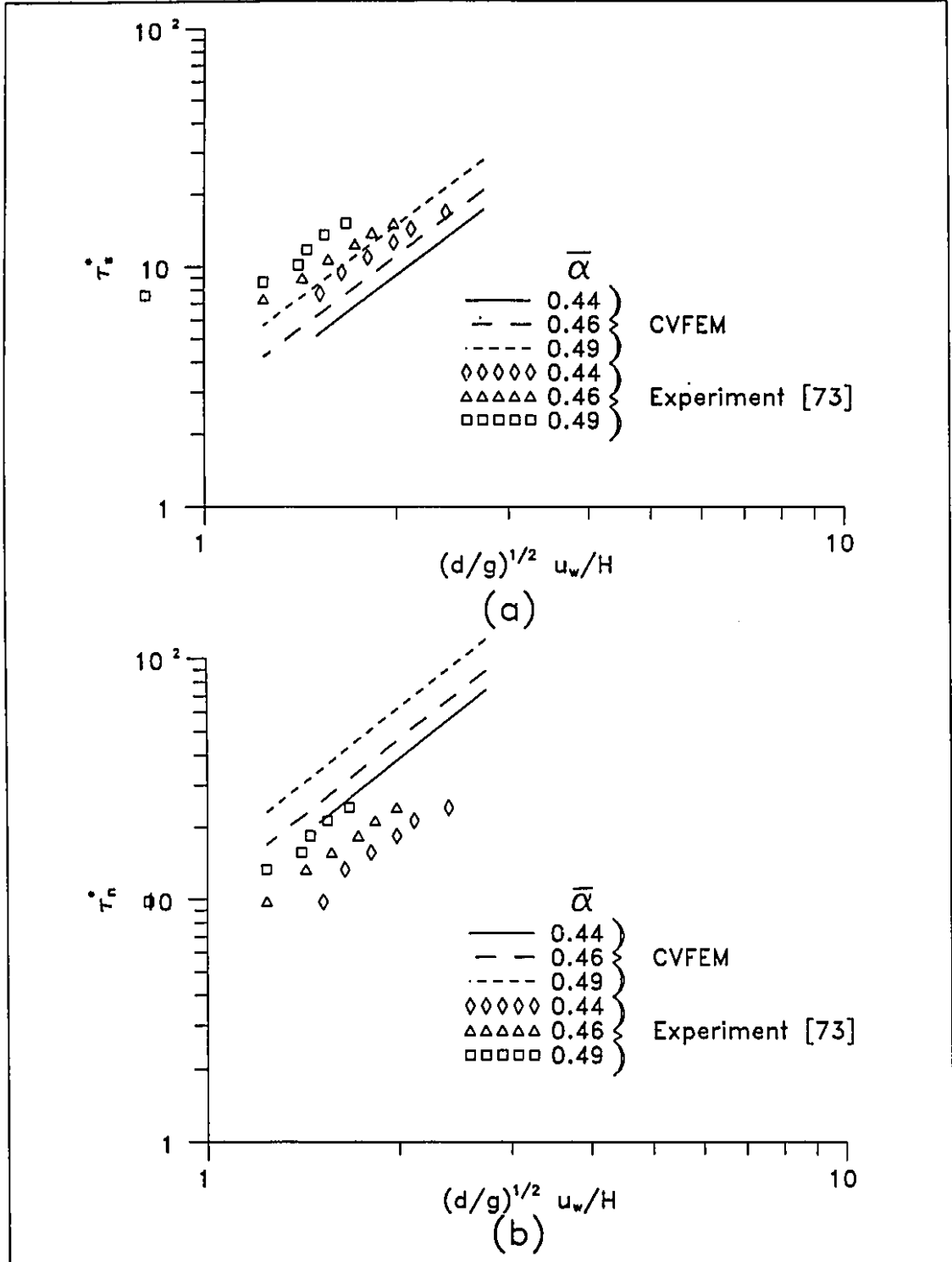


Figure 7.15: Flow in annular shear cell - shear and normal stresses : $e = 0.95$; $e_w = 0.95$; no-slip

7.5 Fluidized Bed

Problem Statement

Fluidization is an important type of gas-solid particle flow that is typically used to enhance heat and mass transfer from the solid particles to the fluid or vice versa. A typical fluidization arrangement is illustrated in Fig. 7.16. It is similar to the vertical pipe flow problem discussed earlier in this chapter. It is possible to obtain a fluidized bed of solid particles by appropriately setting the fluid-phase mass flow rate: for large upward fluid-phase mass flow rates, the fluid/solid interactions are stronger than the gravitational force and an upward flow of particles results; for small upward fluid-phase mass flow rates, the fluid/solid interactions are not strong enough to overcome the gravitational force on the particles, and, therefore, the particles move downward. A fluidized bed is obtained when the fluid/solid interactions balance the gravitational force. In this regime, solid-phase recirculating cells are noted and there is no net transport of particles. The resulting flow is complex, and in some conditions unsteady. Unsteadiness is created by so-called bubbles, or regions of low solid-phase concentrations, that appear at the inlet of the fluidized bed, and rise through the bed. The movement of such bubbles has been analyzed experimentally [105] and numerically [45]. Unsteady analyses of this problem required excessively large times on the computers available for this study (Alacron accelerator board installed in a PC-AT/286, and a Hewlett-Packard HP-720 Unix-based workstation): thus the less demanding steady problem was analyzed. Steady fluidized beds can exist when the minimum fluidization velocity is smaller than the minimum bubbling velocity [64, 69]. Such a fluidized bed has been studied experimentally by Moritomi et al. [120].

In one of the experiments of Moritomi et al. [120], 100 g of glass beads having diameters of 0.163 mm were fluidized with a flow of water in a vertical pipe of 50 mm diameter. At the inlet of the vertical pipe, a screen (see Fig. 7.16), permeable to the water, was installed to prevent any downward flow of the particles. The experiment was designed to obtain a uniform fluid-phase velocity profile at the screen. The quantitative results presented in the paper of Moritomi et al. [120] are the bed height for different fluidization velocities: a sharp horizontal edge between a region of high solid-phase concentration and a clean fluid region was noted at the top of

the fluidized bed, which permitted the definition of the bed height.

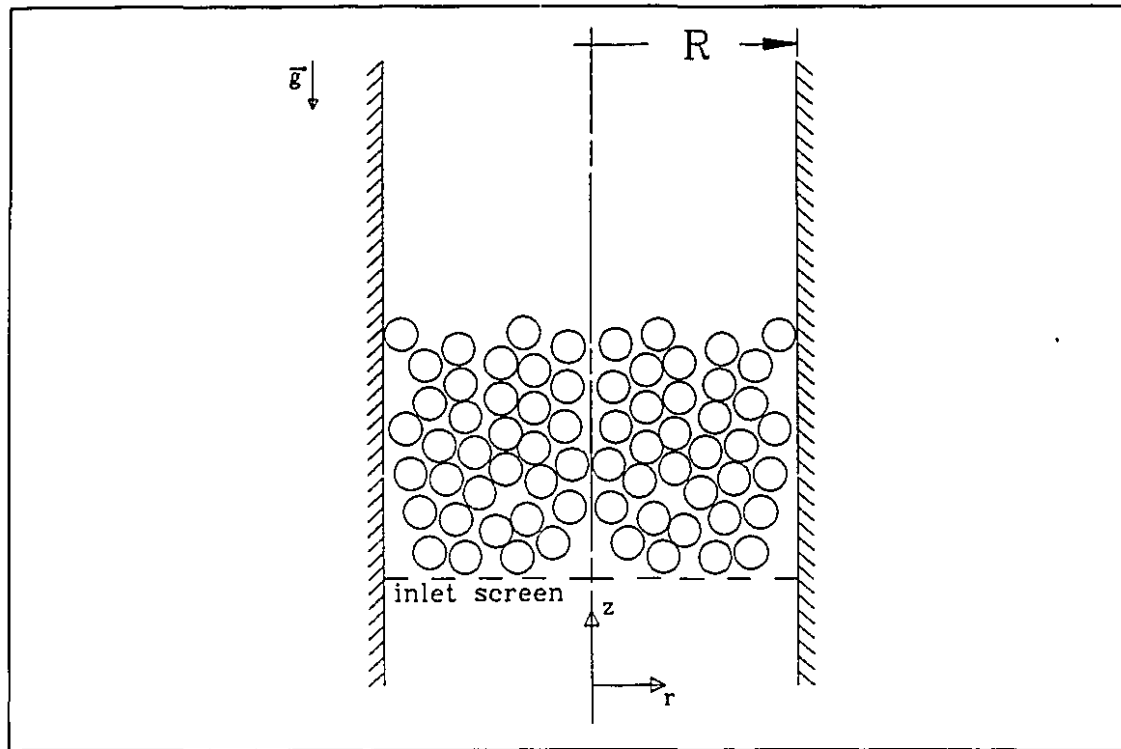


Figure 7.16: Typical fluidized-bed geometry

The numerical simulation of fluidized bed problems involves several challenging features: (i) both dense and dilute concentration regions coexist in the calculation domain, and there is usually a very sharp drop off in the solid-phase concentration at the top of the bed; (ii) both the solid- and fluid-phase flow fields could contain recirculating regions, and these flow fields are often unsteady; (iii) the solid-phase concentration distribution at the inlet is usually not prescribed, rather it has to be calculated as a part of the solution; and (iv) the numerical predictions tend to be extremely sensitive to model parameters such as the restitution coefficients for particle/particle and particle/wall collisions, and drag coefficient. Thus reliable numerical simulations require considerable effort, and even then, careful, and often tedious, “calibration” of model parameters is usually essential for accurate solutions of specific problems of interest.

The work presented in this section is merely intended to demonstrate that the proposed CVFEM can be useful in numerical investigations of fluidized-bed problems. No elaborate fine-tuning or calibration of model parameters was attempted.

The calculations presented here correspond to the fluidized-bed problem of Moritomi et al. [120].

Governing Equations

An attempt was made to simulate the fluidized bed of Moritomi et al. [120] by using the granular temperature model (see Eqs.(3.95)-(3.101)) and the following boundary conditions:

- Fluid phase
 - Prescribed uniform mass flow rate, with zero radial component of velocity, at the inlet.
 - Outflow treatment at the outlet plane for all the fluid-phase dependent variables.
 - No-slip condition at the wall.
- Solid phase
 - Concentration calculated at the inlet plane, assuming zero inflow of the solid-phase.
 - Prescribed zero axial component of velocity at the inlet and outlet planes.
 - Radial velocity and granular temperature computed at the inlet, assuming negligible transport by diffusion.
 - Outflow treatment at the outlet plane for all the solid-phase dependent variables, *except the axial component of velocity*.
 - Inelastic particle/wall collisions on a rough wall: $e_w = 0.9$ and $\phi' = 0.6$.

Solution Procedure

The proposed CVFEM and the solution algorithm described in Chapter 4, along with the mathematical model described in Chapter 3, were used to simulate the fluidized-bed problem of Moritomi et al. [120].

Appropriate initial conditions were essential to achieve convergence of the solution algorithm. It was not possible to start with a packed bed with a clear fluid region on top of it, because of severe convergence problems induced by the sharp discontinuity in the solid-phase concentration at the top of the packed bed. Therefore, the calculations were started with an initial uniform expanded stationary bed extending over the entire computational domain. The initial average volume concentration was prescribed in order to match the amount of solid-phase mass of the experiment (100 g in the experiment of Moritomi et al. [120]). During the solution procedure, no special treatment was needed to keep the solid-phase mass constant.

Results

As was stated earlier, the intention here is to only demonstrate that the proposed CVFEM can be used to investigate fluidized-bed problems. Thus only the results of some rudimentary simulations of the fluidized bed investigated by Moritomi et al. [120] are presented in this section.

The results in Figs. 7.17 and 7.18 correspond to a fluid-phase superficial velocity of 6 mm/s. With reference to Fig. 7.16, the calculation domain extends to 175mm in the z -direction. The grid is uniform with 71 X 11 points. The coefficient of restitution, e , used in this calculation was set to 0.985. This value seems too large since the simulated bed height is significantly higher than the corresponding experimental one (see Table 7.4). However, lower values of e resulted in significant convergence problems, which appear to be caused by the corresponding very low velocities of the solid phase. Nevertheless, this simulation illustrates some of the important features of a fluidized bed. In Fig. 7.17, the recirculating cells of the solid and fluid phases are clearly seen. Near the wall, the fluid-phase velocity is downward except at the top of the bed where the solid-phase concentration is low. The solid-phase flow field also has a low velocity region in the top part of the bed near the axis. Lower values of e (< 0.985) resulted in an increase in the size of this low velocity region. In such a region, calculations of the solid-phase concentration, using the solid-phase continuity equation and the MAW scheme, become questionable. The solid-phase concentration distribution at the axis of the bed is presented in Fig. 7.18. At the bottom, the bed is almost at constant concentration, and there is a relatively

sharp variation of the concentration near the top of the bed, $z/R \approx 5.6$, which also corresponds to the height at which the fluid near the wall starts to move upward.

As stated before, these are only preliminary results, and they are by no means considered as satisfactory predictions. However, this simulation does demonstrate that the proposed CVFEM can produce converged solutions of the granular-temperature model for fluidized-bed problems. These calculations also pointed out limitations of the proposed CVFEM and mathematical model: severe difficulties were encountered in handling the sharp drop of the solid-phase concentration at the top of the bed, and regions of very low solid-phase velocity. It was also found that the value of e can significantly affect the results.

Proposed CVFEM	Moritomi et al. [120]
150	72

Table 7.4: Results of the fluidized-bed problem: bed height in *mm*

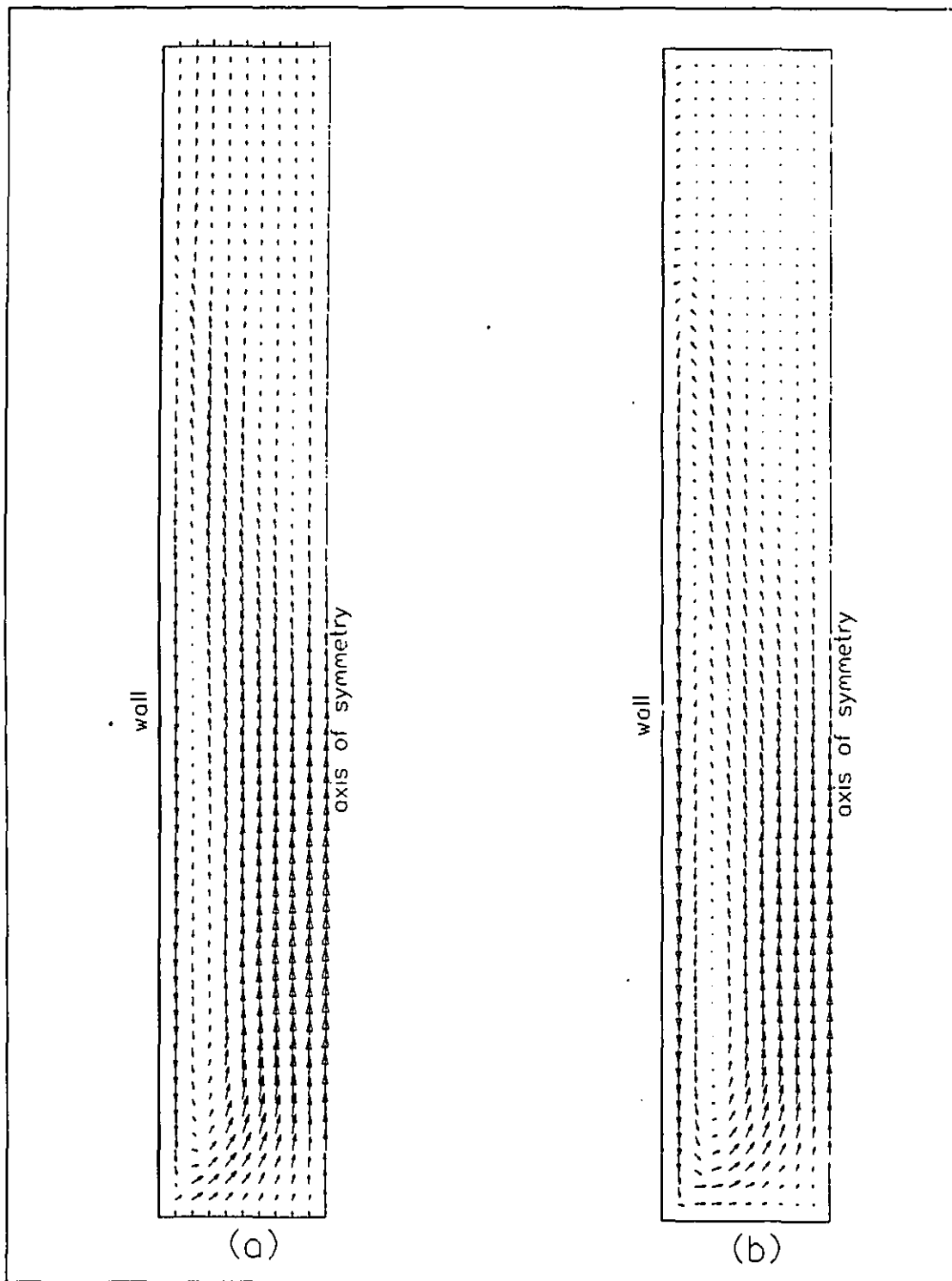


Figure 7.17: Results of the fluidized-bed problem: (a) fluid-phase velocity; (b) solid-phase velocity

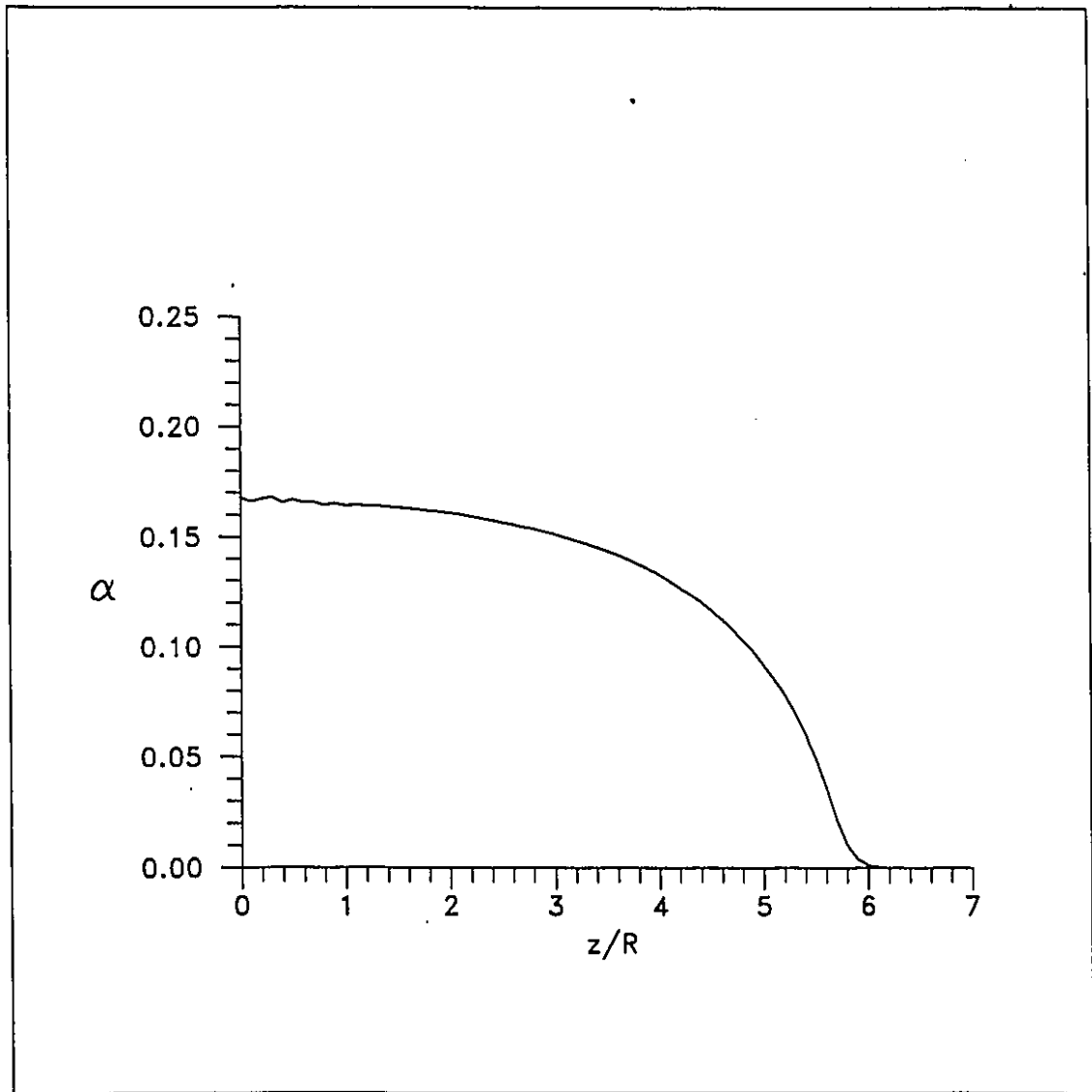


Figure 7.18: Results of the fluidized-bed problem: distribution of the solid-phase concentration along the axis

7.6 Flow in a Channel with a Restriction

Problem Statement

In Chapter 6, dilute gas-solid particle flows in a channel with a restriction were analyzed using the dilute-concentration mathematical model. A schematic illustration of this problem is given in Fig. 6.1. In this section, the granular-temperature model is used to investigate this problem. The use of this general mathematical model for a gas-solid particle flow of dilute concentration is computationally inefficient, since an additional equation, namely the fluctuating kinetic energy equation, needs to be solved. However, this test provides an assessment of the validity of the general mathematical model in the simulation of gas-solid particle flows of dilute concentration. It is necessary to demonstrate this feature of the general mathematical model, before it can be used with confidence in the simulation of gas-solid particle flows that involve a wide range of solid-phase concentration.

Governing Equations

This problem is described by the complete mathematical model given by Eqs.(3.95)-(3.101). The boundary conditions are the same as those used in the corresponding problem described in Chapter 6. It should be noted that these boundary conditions are equivalent to stating that the wall is smooth, or $\phi' = 0$. In addition, the boundary conditions and parameters related to the granular temperature are: (i) zero granular temperature at the inlet plane; (ii) inelastic particle/wall collisions, with $e_w = 0.9$; and (iii) outflow treatment at the outlet planes. The coefficient of restitution for particle/particle collisions, e , is assumed to be 0.9.

Results

The values of the various parameters in this problem are presented in Table 6.1. Figs. 7.19- 7.22 present the solutions based on the dilute concentration model and the general granular-temperature model. All of these results were obtained using a 73 X 37 grid, as described in Chapter 6, Section 6.3. At $Sk = 10^{-2}$, the solutions

are in very good agreement for both $\alpha_{in} = 10^{-3}$ and $\alpha_{in} = 5 \times 10^{-3}$. The results for $Sk = 10^{-1}$ and $\alpha_{in} = 5 \times 10^{-3}$ also compare very well. These successful comparisons demonstrate the validity of the general mathematical model in the dilute concentration regime. At $Sk = 10^{-1}$ and $\alpha_{in} = 5 \times 10^{-3}$, there is a minor discrepancy in the results: the fluid-phase pressure drop, see Fig. 7.21, predicted by the general model is slightly larger than that obtained in the dilute concentration simulation. This may be due to the increasing effects of the particle/particle collisions. For this relatively large value of the Stokes number, the solid phase is not necessarily in dynamic equilibrium with the fluid phase: therefore, the solid-phase concentration could build up in certain regions, such as near the walls, and the effects of the particle/particle collisions could become significant.

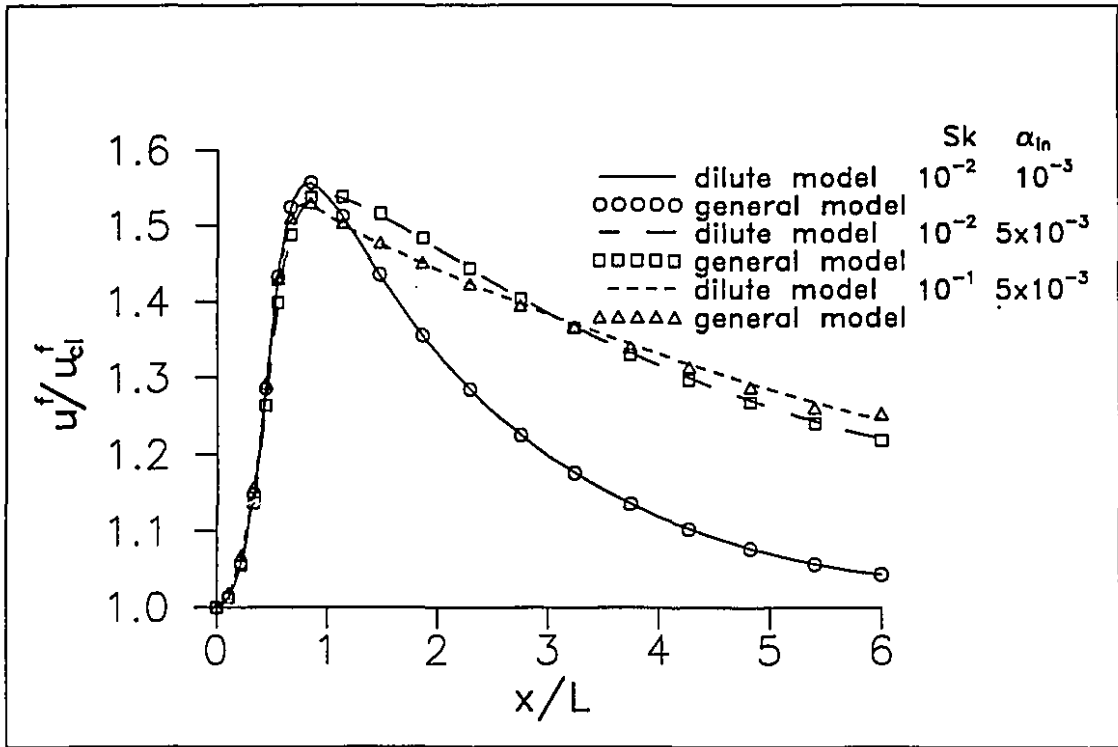


Figure 7.19: Flow in a channel with a restriction: variation of fluid-phase velocity along the centerline

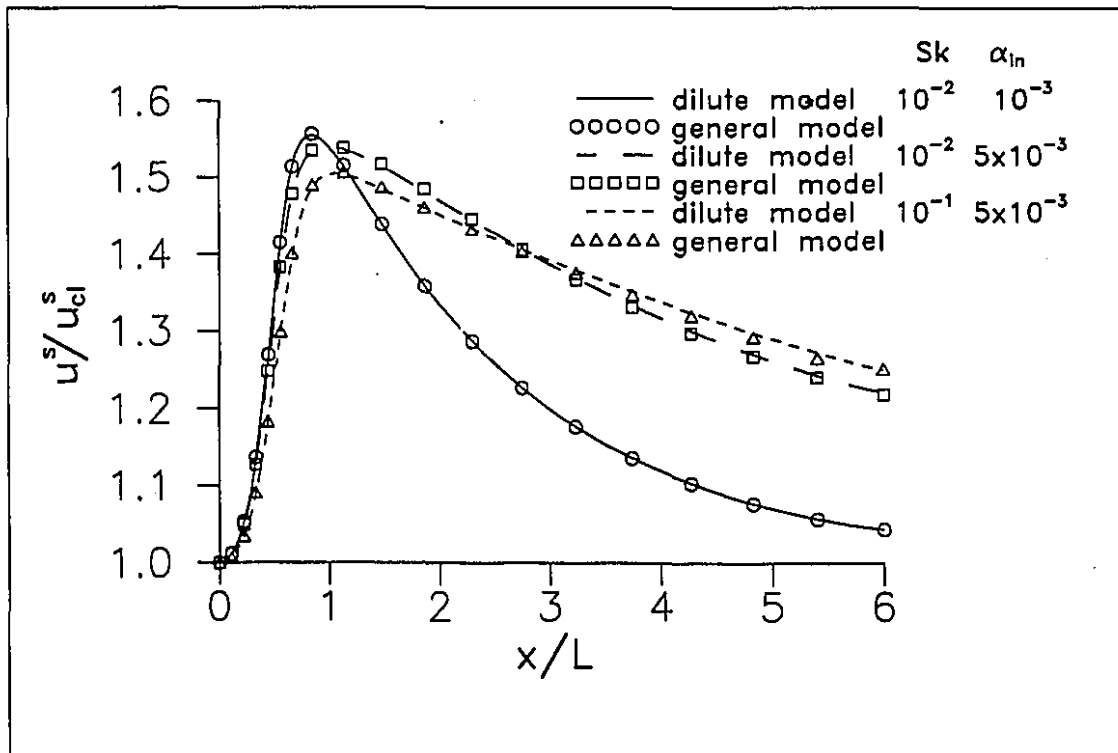


Figure 7.20: Flow in a channel with a restriction: variation of solid-phase velocity along the centerline

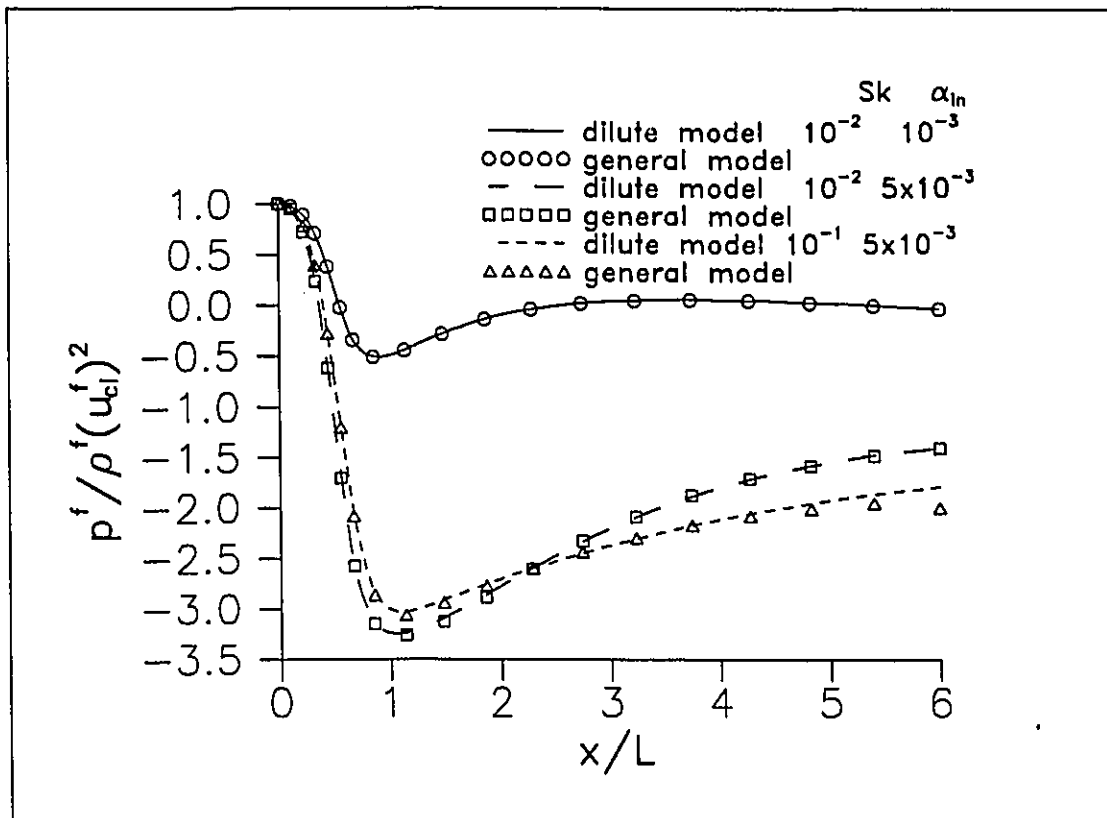


Figure 7.21: Flow in a channel with a restriction: variation of fluid-phase pressure along the centerline

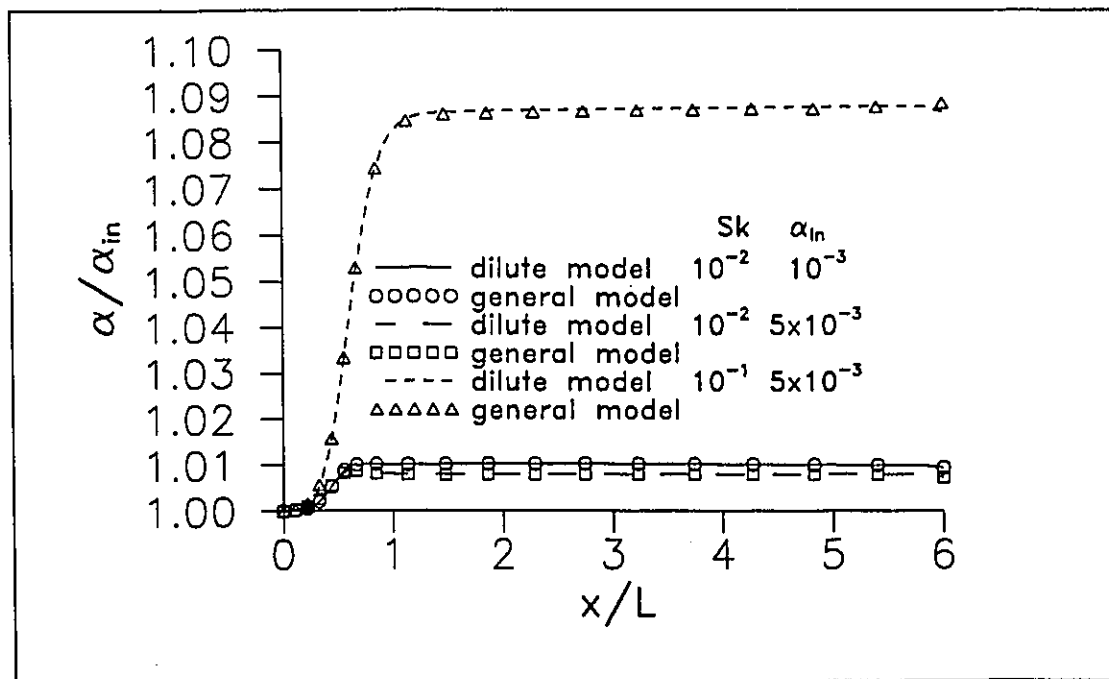


Figure 7.22: Flow in a channel with a restriction: variation of solid-phase concentration along the centerline

7.7 Split-Flow Inertial Separator

Problem Statement

In Chapter 6, dilute gas-solid particle flows in a split-flow inertial separator were analyzed using the dilute-concentration mathematical model. A schematic illustration of this problem is given in Fig. 6.6. In this section, the general granular-temperature model is used to investigate this problem. The separator contains regions of low and high volume concentration of the solid phase. At the inlet and in the main duct, the solid-phase concentration is relatively low. However, when the separator is operating at high efficiency, the solid-phase concentration in the bypass duct may reach values at which the effects of the particle/particle collisions are no longer negligible. The effects of such collisions in a split-flow inertial separator can be illustrated by a comparison between solutions obtained with the dilute-concentration and the general granular-temperature models. The proposed CVFEM was used to solve both these models in this particular application.

Governing Equations

The governing equations and boundary conditions for the dilute-concentration model were presented and discussed in Chapter 6, Section 6.4. The granular-temperature model is given by Eqs.(3.95)-(3.101), and the following boundary conditions were used with this model:

- Fluid phase
 - Prescribed uniform axial velocity and zero radial velocity at the inlet.
 - Outflow treatment at the outlet planes for all the fluid-phase dependent variables.
 - No-slip condition at the wall.
- Solid phase
 - Prescribed concentration, uniform axial velocity, zero radial velocity, and zero granular temperature at the inlet plane.

- Outflow treatment at the outlet planes for all the solid-phase dependent variables.
- Inelastic particle/wall collisions on a smooth wall: $e_w = 0.9$ and $\phi' = 0$.

The assumption of smooth wall leads to solid-phase slip condition at the wall (zero shear stress). This ensures that the boundary conditions of the general model are similar to the ones of the dilute-concentration model. The coefficient of restitution for particle/particle collisions, e , is assumed to be 0.9.

Results

As was discussed in Chapter 6, Section 6.4, the parameters in this problem are the Reynolds number, based on the inlet hydraulic diameter, Re , the Stokes number, Sk , the ratio of the densities of the solid and fluid phases, γ , the inlet volume concentration of the solid phase, α_{in} , and the bypass ratio, b . All the simulations in this comparative study were done with $Re = 200$, $b = 20\%$, $\gamma = 1000$ and $\alpha_{in} = 10^{-3}$. These results were obtained using the same grid as the corresponding dilute-concentration simulation of Chapter 6, Section 6.4 (see Fig. 6.6). The influence of the Stokes number was investigated in the range $10^{-3} \leq Sk \leq 10^{-1}$.

Fig. 7.23a gives the variation of the separator efficiency, η_{ef} , as a function of the Stokes number, Sk : the separator efficiency is defined in Section 6.4. The solid line corresponds to the solution of the dilute concentration model, Eqs.(3.122)-(3.127), and the dashed line represents the solution of the granular-temperature model, Eqs.(3.95)- (3.101). At large Sk , the dilute-concentration model overestimates the separator efficiency, and the difference between the two models reaches a maximum value of 52%. Whenever there is a build up in the concentration of particles, the collisions tend to spread out the particles: thus the effect of collisions is to make the solid-phase concentration more uniform, and decrease the separator efficiency.

The variation of the nondimensionalized fluid-phase static-pressure drop in the main duct, Δp_M^{f*} , with Stokes number, Sk , is presented in Fig. 7.23b. Δp_M^{f*} is defined in Section 6.4. The results obtained with the dilute-concentration and general models show similar behaviour. Δp_M^{f*} asymptotes to the homogeneous-mixture so-

lution as Sk decreases, at low values of Sk . A decrease of Δp_M^{f*} with increasing Sk , at large Sk , is also evident. At an intermediate value of Sk , there is a maximum. However, this maximum does not appear at the same Sk for each model: the granular-temperature model predicts the maximum at a larger Sk than the corresponding value for the dilute-concentration model. Furthermore, Δp_M^{f*} estimated by the granular-temperature model is always greater than that predicted using the dilute-concentration model: particle/particle collisions lead to a viscosity of the solid-phase and the associated stresses, and, therefore, a larger fluid-phase pressure drop is needed to drive the same mass of mixture. The increase in pressure drop is more pronounced at high Sk . This is to be expected since the relaxation time of a particle increases with increasing Sk , while the frequency of collisions is essentially constant for a given inlet concentration. It is also seen that the effects of the collisions are much stronger on the nondimensionalized fluid-phase static-pressure drop in the bypass duct, Δp_{BY}^{f*} , (see Fig. 7.23c). With the granular-temperature model, as Sk increases, Δp_{BY}^{f*} does not decrease, as predicted by the dilute-concentration model, but increases due to the increasing effects of the particle/particle collisions. Furthermore, this increase is amplified by the combined effects of the increasing Sk and increasing solid-phase concentration (associated with the increase in the efficiency). Again, at low Sk , the results of both models asymptote to the homogeneous-mixture solution.

These results show that even at relatively low values of inlet concentrations, α_{in} , the effects of the collisions may not be negligible. This is especially true at large values of the Stokes number and in regions where there is a build up of solid-phase concentration, such as in the bypass duct. These results also clearly illustrate that a mathematical model that includes particle/particle collisions is essential for accurate solutions of gas-solid particle flow problems involving a wide range of solid-phase concentration. Finally, the results of this problem demonstrate that the proposed CVFEM can be successfully used to simulate gas-solid particle flows in complex geometries, over a wide range of solid-phase concentration.

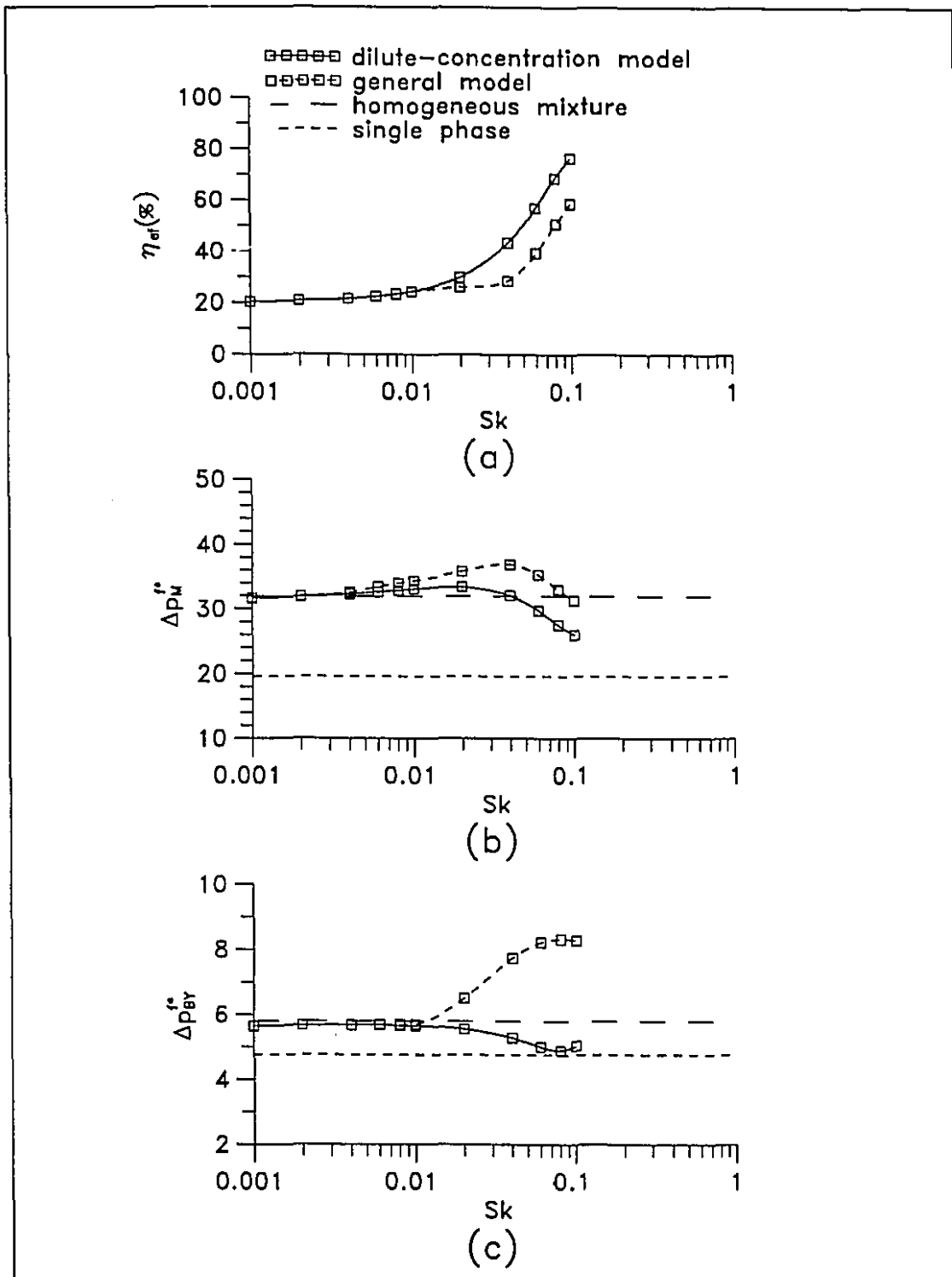


Figure 7.23: Results pertaining to $b = 20\%$, $\gamma = 10^3$ and $\alpha_{in} = 10^{-3}$: (a) separator efficiency; (b) static-pressure drop in the main duct; (c) static-pressure drop in the bypass duct

Chapter 8

Conclusion

8.1 Review of the Thesis

In this thesis, some of the ideas contained in available CVFEMs for single-phase flows [13, 14, 83, 100, 135, 149, 156, 157] have been amalgamated and extended to formulate a co-located, equal-order, CVFEM for the solution of two-fluid models of two-dimensional, planar or axisymmetric, incompressible, gas-solid particle flows in regular- or irregular-shaped geometries. The proposed numerical method has the capability of analyzing gas-solid particle flows over a *wide range of concentration in complex irregular geometries*. The main tasks that were undertaken and completed in this work are summarized below:

- In Chapter 1, the aim and scope of this work were presented. As was stated in this chapter, the research work described in this thesis was primarily aimed at the numerical solution of the mathematical models of laminar gas-solid particle flows, with emphasis on the computer simulation of such flows over a *wide range of concentration* in two-dimensional, planar or axisymmetric, *irregular* geometries. The fundamental concepts used in the mathematical models of gas-solid particle flows were also briefly described in Chapter 1.
- A literature review was presented in Chapter 2. Several available mathematical models of gas-solid particle flows were briefly discussed, with an emphasis on the fundamental differences between dilute-concentration and dense-concentration models. This literature review pointed out that most of the

available mathematical models are applicable only to a narrow range of concentration of the solid phase. Several relevant numerical methods for single-phase and gas-solid particle flows was also reviewed in this chapter. It was demonstrated that most of the available numerical methods for gas-solid particle flows are restricted to problems involving regular-shaped geometries, or calculation domains whose boundaries lie along commonly used orthogonal coordinate axes.

- The chosen mathematical model was presented in Chapter 3. This mathematical description is based on the methodology proposed by Lun [107], and Lun and Savage [110], in which the solid phase is modelled using a theory similar to the kinetic theory of dense gases. This model is appropriate for a wide range of concentration and allows a microscopic interpretation of the solid-phase constitutive equations.
- The various steps in the formulation of the proposed CVFEM were presented in Chapter 4, with emphasis and discussion of features that are particularly relevant, or necessary, in the simulation of gas-solid particle flows. The formulation is presented and implemented in a general manner that allows solution of the mathematical model in two-dimensional planar (Cartesian) and axisymmetric (cylindrical) coordinate systems.
- The capabilities of the proposed CVFEM [116] with regard to the solution of axisymmetric single-phase flows were demonstrated in Chapter 5. Four problems were analyzed in this chapter. The first one involved developing laminar flow in a pipe, and the results were compared with the numerical solution of Friedmann et al. [60]. In the second problem, laminar flow in a pipe with a sudden contraction was considered. For this case, the solutions of the proposed CVFEM were compared with the experimental data of Durst and Loy [52]. Simulations of laminar natural convection in a cylindrical enclosure were also presented in this chapter and the results were compared with the numerical solutions of Liang et al. [103]. Finally, laminar flow in a replica segment of a coronary artery was investigated, and the results were compared with the experimental results of Back et al. [8].
- The validity of the proposed CVFEM [114, 115, 117] for the simulation of dilute gas-solid particle flows was demonstrated in Chapter 6. This demonstration

was done in three stages. First, the capability of the proposed CVFEM to solve a dilute-concentration mathematical model of gas-solid particle flow was established by using a *specified solution technique*. Then the proposed CVFEM was applied to a problem involving dilute gas-solid particle flows in a channel with a restriction, and the results were compared with the results of Di Giacinto et al. [44]. The results produced by the CVFEM were also compared with the results obtained by using a well-established staggered-grid finite-volume method [30, 130]. Finally, the proposed CVFEM was used to simulate dilute gas-solid particle flows in an idealized split-flow inertial separator, and the results were discussed.

- The validity of the proposed CVFEM for the solution of the granular-temperature model, applied to gas-solid particle flows that involve relatively high concentration of the solid phase is presented in Chapter 7. Two test cases based on the *specified solution technique* were presented, one using the Cartesian and another one using the cylindrical coordinate systems. Gas-solid particle flows in a vertical pipe, an annular shear cell, and a fluidized bed were also investigated, and comparisons of the CVFEM results with independent numerical and experimental results were presented. A dilute-concentration gas-solid particle flow in a contraction was simulated using the general granular-temperature model, and the results were compared with the solution obtained with the dilute-concentration model (in Chapter 6). This comparison assessed the applicability of the general granular-temperature model in the dilute concentration regime. Finally, gas-solid particle flows in a split-flow inertial separator, identical to that considered in Chapter 6, was analyzed using the granular-temperature model, and the effects of particle/particle collisions on such a flow were discussed.

In summary, the capabilities of the proposed CVFEM have been assessed by applying it to many test problems and comparing the results with available numerical and experimental results in the literature. These comparisons indicate that the proposed CVFEM can successfully solve gas-solid particle flows in two-dimensional, planar or axisymmetric, regular or irregular geometries, over a wide range of solid-phase concentration.

8.2 Contributions of the Thesis

The main contribution of this thesis is the development of a CVFEM for the solution of two-fluid models of two-dimensional, planar or axisymmetric, incompressible, gas-solid particle flows in irregular-shaped geometries. It should also be noted that this is the first application of CVFEMs to problems involving gas-solid particle flows. The results are quite encouraging.

The steady-state problems were solved through the use of an unsteady formulation. It was found that this approach is more efficient than the use of a steady formulation and an iterative solution algorithm with an under-relaxation scheme [130], since the former ensures similar evolution of the solution of each phase.

The sets of discretized equations for p^f and α are derived from the integral mass conservation equations for the continuous and particulate phases, respectively, rather than a linear combination of these equations, as is done in some available finite volume methods [30, 170]. The reasons for adopting this approach, and the features of the proposed CVFEM that allow this approach without additional special treatments, have been discussed in this thesis.

Novel features of the proposed CVFEM *vis-a-vis* available CVFEMs [13, 14, 83, 100, 135, 149, 156, 157] include the following:

- A formulation that can handle planar or axisymmetric two-dimensional flows.
- Appropriate incorporation of the discretized unsteady terms in the definitions of \hat{u} and \hat{v} .
- A modified MAAss-Weighted skew upwind scheme (MAW) for the interpolation of the volume concentration, α , of the solid phase: this interpolation ensures that all coefficients in the discretized equation for α are positive; at each integration point, the volume concentration of the fluid phase is obtained using $\epsilon = 1 - \alpha$, thus the sum of the fluid- and solid-phase volume concentrations is always unity.
- An iterative variable adjustment algorithm in which linearized discretization equations for u^f and u^s , and v^f and v^s , are solved simultaneously, using a

line Gauss-Seidel algorithm based on a coupled-equation line solver: it was found that the simultaneous solution of the fluid- and solid-phase momentum equations yields a more robust algorithm than one based on a completely segregated (sequential) solution of these equations. It should be noted that this algorithm requires appropriate linearization of the fluid-particle interaction term as discussed in Section 4.5.2 and Appendix C.

8.3 Recommendations for Further Work

- In order to focus attention on the formulation of the proposed CVFEM, the developments in this thesis were conducted in the context of a two-fluid model based on the kinetic theory of granular materials proposed by Lun and Savage [110, 107]. Reference was made to other available models in the literature [89, 5, 193, 167, 48, 35, 94], but a comparative evaluation of these models was not undertaken. However, detailed investigations of the consistency and validity of these mathematical models are needed in order to establish their inherent advantages and weaknesses, and to propose possible improvements. The proposed CVFEM could serve as a useful tool in such comparative evaluations of available two-fluid models of gas-solid particle flows [41, 42, 89, 5, 193, 167, 48, 35, 94].
- The implementation (or computer coding) of the proposed numerical method was based on a structured grid. In order to realize the full geometrical flexibility that the proposed CVFEM allows, implementations on unstructured grids are needed. Such extensions would necessitate modifications of the overall solution algorithm, since the line Gauss-Seidel algorithm would not be appropriate anymore, and approaches such as point-by-point Gauss-Seidel methods, or block-by-block direct solution techniques [49] have to be considered.
- Optimization of the overall algorithm is also an important aspect which was not tackled in this work. Block correction procedures [158], multigrid techniques [21], and enhance sequential solution algorithms [2] can be included to improve the convergence rate of the overall solution algorithm.
- The test problems presented involved only laminar flow. This was done only to focus attention on the testing of the proposed CVFEM, without incorporating

the uncertainties involved in available models of turbulent gas-solid particle flows. The proposed CVFEM has no such limitation in principle. An explicit demonstration of the capability of this CVFEM to solve available models of turbulent gas-solid particle flows [42, 79] would be the next logical step towards the long-term objective of efficient computer simulations of such flows.

- The two-fluid model used in this thesis is limited to gas-solid particle flows in which the particles are of uniform size. Furthermore, the expressions that were used to relate the drag coefficient to the particle Reynolds number are appropriate only for particles of spherical shape. The proposed CVFEM, with some modifications, could serve as a useful tool to test out formulations that relax these limitations.
- Once some of the aforementioned explorations and improvements are completed, the proposed CVFEM, along with a suitable mathematical model, could be used to investigate a wide variety of gas-solid particle flows in engineering and the environment.

In conclusion, the author hopes that this thesis will enable, or at least encourage, other researchers to explore the possibilities offered by CVFEMs in the prediction of practical gas-solid particle flows, and also other two-phase and multiphase flows.

References

- [1] Acharya, S., Moukalled, F.H., An Adaptive Grid Solution Procedure for Convection-Diffusion Problems, *J. Comput. Physics*, Vol. 91, pp. 32-57, 1990.
- [2] Afshar, M., Baliga, B.R., A Sequential Algorithm for the Solution of the Discretized Momentum and Continuity Equations, *Proceedings of the 8th Int. Conf. on Num. Meth. in Laminar and Turbulent Flow*, to be published, Swansea, UK, 1993.
- [3] Amsden, A.A., Hirt, C.W., YAQUI: An Arbitrary Lagrangian-Eulerian Computer Program for Fluid Flow at All Speeds, *Los Alamos Scientific Laboratory Report LA-5100*, 1973.
- [4] Anderson, D.A., Tannehill, J.C., Pletcher, R.H., *Computational Fluid Mechanics and Heat Transfer*, Hemisphere Publ., New York, 599 p., 1984.
- [5] Anderson, T.B., Jackson, R., A Fluid Mechanical Description of Fluidized Beds, *I&EC Fundamentals*, Vol.6, pp.527-539, 1967.
- [6] Aziz, K., Hellums, J.D., Numerical Solution of the Three-Dimensional Equations of Motion for Laminar Natural Convection, *Physics of Fluids*, Vol. 10, pp. 314-324, 1967.
- [7] Back, L.H., Cho, Y.I., Crawford, D.W., Cuffel, R.F., Effect of Mild Atherosclerosis on Flow Resistance in a Coronary Artery Casting of Man, *J. Biomech. Engng.*, Vol. 106, pp. 48-53, 1984.
- [8] Back, L.H., Radbill, J.R., Cho, Y.I., Crawford, D.W., Measurement and Prediction of Flow Through a Replica Segment of a Mildly Atherosclerotic Coronary Artery of Man, *J. Biomechanics*, Vol. 19, pp. 1-17, 1986.

- [9] Bagnold, R.A., Experiments on a Gravity-Free Dispersion of Large Spheres in a Newtonian Fluid under Shear, *Proc. Royal Soc. London*, A223, pp.49-63, 1954.
- [10] Baker, A.J., *Computation of Fluid Flow by the Finite Element Method*, Hemisphere Publishing Corporation, Washington, 1983.
- [11] Baliga, B.R., *A Control-Volume-Based Finite Element Method for Convective Heat and Mass Transfer*, Ph.D. Thesis, Dept. of Mech. Eng., University of Minnesota, 1978.
- [12] Baliga, B.R., Patankar, S.V., A New Finite-Element Formulation for Convection-Diffusion Problems, *Numerical Heat Transfer*, Vol. 3, pp. 393-409, 1980.
- [13] Baliga, B.R., Patankar, S.V., A Control-Volume Finite Element Method for Two-Dimensional Fluid Flow and Heat Transfer, *Numerical Heat Transfer*, Vol. 6, pp. 245-261, 1983.
- [14] Baliga, B.R., Patankar, S.V., Elliptic Systems: Finite Element Method II, in Minkowycz, W.J. et al. (Eds.), *Handbook of Numerical Heat Transfer*, Chap. 11, pp. 421-461, Wiley, New York, 1988.
- [15] Baliga, B.R., Saabas, H.J., Control-Volume Finite Element Methods for Incompressible Fluid Flow, *III Portuguese Conference on Computational Mechanics*, C2.1-C2.20, Coimbra, Portugal, 1992.
- [16] Barth, T.J., On Unstructured Grids and Solvers, *Computational Fluid Dynamics, Von Karman Institute Lecture Series*, 1990-03, 1990.
- [17] Batchelor, G.K., The Effect of Brownian Motion on the Bulk Stress in a Suspension of Spherical Particles, *J. Fluid Mech.*, Vol. 83, pp.97-117, 1977.
- [18] Bedford, A., Drumheller, D.S., Theories of Immiscible and Structured Mixture, *Int. J. Eng. Sci.*, Vol. 21, pp. 863-960, 1983.
- [19] Boll, R.H., Particle Collection and Pressure Drop in Venturi Scrubbers, *Industrial Eng. Chemistry Fundamentals*, Vol. 12, pp. 40-50, 1973.

- [20] Bouillard, J.X., Lyczkowski, R.W., Gidaspow, D., Porosity Distributions in a Fluidized Bed with an Immersed Obstacle, *AICHE J.*, Vol. 35, pp. 908-922, 1989.
- [21] Brandt, A., Multi-Level Adaptive Computations in Fluid Dynamics, *AIAA paper 79-1455*, 1979.
- [22] Breitman, D.S., Dueck, E.G., Habashi, W.G., Analysis of a Split-Flow Particle Separator by Finite Elements, *J. of Aircraft*, Vol. 22, pp. 135-140, 1985.
- [23] Burke, J.P., Berman, N.S., Entrance Flow Development in Circular Tubes at Small Axial Distances, *ASME Paper 69-WA/FE-13*, 1969.
- [24] Buyevich, Y.A., Statistical Hydrodynamics of Disperse Systems. Part 1. Physical Background and General Equations, *J. Fluid Mech.*, Vol. 49, pp. 489-507, 1971.
- [25] Campbell, C.S., Computer Simulation of Granular Flows, *Proc. 10th National Congress of Applied Mechanics*, Austin, Texas, pp. 327-338, 1986.
- [26] Campbell, C.S., Boundary Interactions for Two-Dimensional Granular flows: Asymmetric Stresses and Couple Stresses, in M. Satake and J.T. Jenkins (Eds.), *Micromechanics of Granular Materials*, Amsterdam, pp. 163-174, 1988.
- [27] Campbell, C.S., The Stress Tensor for Simple Shear Flows of a Granular Material, *J. Fluid Mech.*, Vol. 203, pp. 449-473, 1989.
- [28] Campbell, C.S., Rapid Granular Flows, *Annual Rev. Fluid Mech.*, Vol. 22, pp. 57-92, 1990.
- [29] Caretto, L.S., Curr, R.M., Spalding, D.B., Two Numerical Methods for Three-Dimensional Boundary Layers, *Comp. Meth. in Appl. Mech. and Eng.*, Vol. 1, 1972.
- [30] Carver, M.B., Numerical Computation of Phase Separation in Two Fluid Flow, *J. of Fluids Eng.*, Vol. 106, pp. 147-153, 1984.
- [31] Chapman, S., Cowling, T.G., *The Mathematical Theory of Non-Uniform Gases*, Cambridge University Press, 423p., 1939.

- [32] Chen, C.P., Wood, P.E., A Turbulence Closure Model for Dilute Gas-Particle Flows, *Can. J. Chem. Eng.*, Vol. 63, pp. 349-360, 1985.
- [33] Choudhoury, S., Nicolaides, R.A., Discretization of Incompressible Vorticity-Velocity Equations on Triangular Meshes, *Int. J. for Num. Meth. in Fluids*, Vol. 11, pp. 823-833, 1990.
- [34] Costa, V.A.F., Oliveira, L.A., A Control Volume Based Finite Element Method for Two-dimensional Steady Fluid Flow, Heat Transfer, and Related Phenomena, *III Portuguese Conference on Computation Mechanics*, F10.1-F10.15, Coimbra, Portugal, 1992.
- [35] Crapiste, G.H., Rotstein, E., Whitaker, S., General Closure Scheme for the Method of Volume Averaging, *Chem. Eng. Science*, Vol. 41, pp. 227-235, 1986.
- [36] Crowe, C.T., Pratt, D.T., Two-Dimensional Gas-Particle Flow, *Proceedings of 1972 Heat Transfer and Fluid Mechanics Institute*, Stanford University Press, pp. 386-399, 1972.
- [37] Crowe, C.T., Pratt, D.T., Analysis of the Flow Field in Cyclone Separators, *Computers & Fluids*, Vol. 2, pp. 249-260, 1974.
- [38] Crowe, C.T., Stock, D.E., A Computer Solution for Two-Dimensional Fluid-Particle Flows, *Int. J. for Num. Meth. in Eng.*, Vol. 10, pp. 185-196, 1976.
- [39] Crowe, C.T., Sharma, M.P., Stock, D.E., The Particle-Source-In Cell (PSI-CELL) Model for Gas-Droplet Flows, *J. of Fluids Eng.*, Vol. 99, pp. 325-332, 1977.
- [40] Crowe, C.T., On Modelling Spray Air Contact in Spray-Drying Systems, in *Advances in Drying*, Hemisphere Pub., 1980.
- [41] Crowe, C.T., REVIEW - Numerical Models for Dilute Gas-Particle Flows, *J. of Fluids Eng.*, Vol. 104, pp. 297-303, 1982.
- [42] Crowe, C.T., The State-of-the-Art in the Development of Numerical Models for Dispersed Phase Flows, *Proceeding of the International Conference on Multiphase Flows*, Japan, pp. 49-60, 1991.

- [43] Delhaye, J.M., Achard, J.L., On the Averaging Operators Introduced in Two-Phase Flow Modeling, *Transient Two-Phase Flow Proceedings of the CSNI Specialists Meeting*, Vol. 1, Toronto, 1978.
- [44] DiGiacinto, M., Sabetta, F., Piva, R., Two-Way Coupling Effects in Dilute Gas-Particle Flows, *J. of Fluid Eng.*, Vol. 104, pp.304-312, 1982.
- [45] Ding, J., Gidaspow, D., A Bubbling Fluidization Model Using Kinetic Theory of Granular Flow, *AIChE J.*, Vol. 36, pp. 523-538, 1990.
- [46] Ding, J., Lyczkowski, R.W., Burge, S.W., Gidaspow, D., Three-Dimensional Models of Hydrodynamics and Erosion in Fluidized-Bed Combustors, *Fluidized Processes*, AIChE Symposium Series, Vol. 88, pp. 85-98, 1992.
- [47] Drew, D.A., Averaged Field Equations for Two-Phase Media, *Stud. Appl. Math.*, Vol. 50, pp. 133-166, 1971.
- [48] Drew, D.A., Mathematical Modeling of Two-Phase Flow, *Annual Rev. Fluid Mech.*, Vol. 15, pp. 261-291, 1983.
- [49] Duff, I.S., A Survey of Sparse Matrix Research, *Proc. IEEE*, Vol. 65, pp. 500-535, 1977.
- [50] Dukowicz, J.K., A Particle-Fluid Numerical Model for Liquid Sprays, *J. Comput. Physics*, Vol. 35, pp. 229-253, 1980.
- [51] Durst, F., Milojevic, D., Schonung, B., Eulerian and Lagrangian predictions of Particulate Two-Phase Flows: a Numerical Study, *Appl. Math. Modelling*, Vol. 8, pp. 101-115, 1984.
- [52] Durst, F., Loy, T., Investigations of Laminar Flow in a Pipe with Sudden Contraction of Cross Sectional Area, *Computers & Fluids*, Vol. 13, pp. 15-36, 1985.
- [53] Einstein, A., *Investigations on the Theory of the Brownian Movement*, Dover, New-York, 1956.
- [54] El-Bainhawy, V., Whitelaw, J.H., The Calculation of the Flow Properties of a Confined Kerosine-Spray Flame, *AIAA J.*, Vol. 18, pp. 1503-1510, 1980.

- [55] Eldighidy, S.M., Chen, R.Y., Comparin, R.A., Deposition of Suspension in the Entrance of a Channel, *J. Fluid Eng.*, Vol. 99, pp. 365-370, 1977.
- [56] Elghobashi, S.E., Abou-Arab, T.W., A Two-Equation Turbulence Model for Two-Phase Flows, *Physic of Fluids*, Vol. 26, pp. 931-938, 1983.
- [57] Elkaim, D., Reggio, M., Camarero, R., Simulating Two-Dimensional Turbulent Flow by Using the $k - \epsilon$ Model and the Vorticity-Streamfunction Formulation, *Int. J. for Num. Meth. in Fluids*, Vol. 14, pp. 961-980, 1992.
- [58] Farrell, M., Lun, C.K.K., Savage, S.B., A Simple Kinetic Theory for Granular Flow of Binary Mixtures of Smooth, Inelastic, Spherical Particles, *Acta Mech.*, Vol. 63, pp. 45-60, 1986.
- [59] Finlayson, B.A., Scriven, L.E., The Method of Weighted Residuals - A Review, *Appl. Mech. Rev.*, Vol. 19, pp. 735-748, 1966.
- [60] Friedmann, M., Gillis, J., Liron, N., Laminar Flow in a Pipe at Low and Moderate Reynolds Numbers, *Appl. Sci. Res.*, Vol. 19, pp. 426-438, 1968.
- [61] Fromm, J.E., Harlow, F.H., Numerical Solution of the Problem of Vortex Street Development, *Physics of Fluids*, Vol. 6, pp. 975-982, 1963.
- [62] Galpin, P.F., Van Doormaal, J.P., Raithby, G.D., Solution of the Incompressible Mass and Momentum Equations by Application of a Coupled Equation Line Solver, *Int. J. for Num. Meth. in Fluids*, Vol. 5, pp. 615-625, 1985.
- [63] Gauvin, W.H., Katta, S., Knelman, F.H., Drop Trajectory Predictions and their Importance in the Design of Spray Dryers, *Int. J. Multiphase Flow*, Vol. 1, pp. 793-816, 1975.
- [64] Geldart, D., Types of Gas Fluidization, *Powder Technology*, Vol. 7, pp. 285-292, 1973.
- [65] Gidaspow, D., Ding, J., Jayaswal, K., Multiphase Navier-Stokes Equation Solver, *Proceeding of Numerical Methods for Multiphase Flows*, Toronto, pp. 47-56, 1990.
- [66] Gidaspow, D., Hydrodynamic Modeling of Circulating and Bubbling Fluidized Beds, in M.C. Rocco (Ed.), *Particulate Two-Phase Flow*, Butterworth Heine-
mann, 1992.

- [67] Gosman, A.D., Pun, W.M., Runchal, A.K., Spalding, D.B., Woltstein, M., *Heat and Mass Transfer in Recirculating Flows*, Academic Press, 338 p., 1969.
- [68] Gouse, S.W., *An Index to the Two-Phase Gas Liquid Flow Literature*, MIT, Cambridge, Massachusetts, 1966.
- [69] Grace, J.R., Contacting Modes and Behaviour Classification of Gas-Solid and Other Two-Phase Suspensions, *Can. J. Chem. Eng.*, Vol. 64, pp. 353-363, 1986.
- [70] Hackman, L.P., Raithby, G.D., Strong, A.B., Numerical Predictions of the Turbulent Flows over Backward-Facing Steps, *Int. J. for Num. Meth. in Fluids*, Vol. 7, pp. 711-724, 1984.
- [71] Haff, P.K., Werner, B.T., Computer Simulation of the Mechanical Sorting of Grain, *Powder Technology*, Vol. 48, pp. 239-245, 1986.
- [72] Hamed, A., Tabakoff, W., Solid Particle Demixing in a Suspension Flow of Viscous Gas, *J. Fluid Eng.*, Vol. 97, pp. 106-111, 1975.
- [73] Hanes, D.M., Inman, D.L., Observations of Rapidly Flowing Granular-Fluid Materials, *J. Fluid Mech.*, Vol. 150, pp. 357-380, 1985.
- [74] Harlow, F.H., Welch, J.E., Numerical Calculation of Time Dependent Viscous Incompressible Flow of a Fluid with Free Surface, *Physics of Fluids*, Vol. 8, pp.2182-2189, 1965.
- [75] Harlow, F.H., Amsden, A.A., A Numerical Fluid Dynamics Method for All Speeds, *J. Comput. Physics*, Vol. 8, p.197, 1971.
- [76] Harlow, F.H., Amsden, A.A., Numerical Calculation of Multiphase Fluid Flow, *J. Comput. Physics*, Vol. 17, pp. 19-52, 1975.
- [77] Hassan, Y.A., Rice, J.G., Kim, J.H., A Stable Mass-Flow-Weighted Two-Dimensional Skew Upwind Scheme, *Numerical Heat Transfer*, Vol. 14, pp. 395-408, 1983.
- [78] Hetsroni, G., *Handbook of Multiphase Systems*, McGraw-Hill, 1982.
- [79] Hetsroni, G., Particle-Turbulence Interaction, *Int. J. Multiphase Flow*, Vol. 15, pp. 735-746, 1989.

- [80] Hinze, J.O., *Turbulence*, Second Edition, McGraw-Hill, 790 p., 1975.
- [81] Hood, P., Taylor, C., Navier Stokes Equations Using Mixed Interpolation, in J.T. Oden (Ed.), *Finite-Element Methods in Flow Problems*, UAH Press, University of Alabama, Huntsville, pp. 57-66, 1974.
- [82] Hookey, N.A., *Evaluation and Enhancements of Control Volume Finite-Element Methods for Two-Dimensional Fluid Flow and Heat Transfer*, M.Eng. Thesis, Dept. of Mech. Eng., McGill University, Montreal, Canada, 1986.
- [83] Hookey, N.A., Baliga, B.R., Evaluation and Enhancements of Some Control-Volume Finite Element Methods: Part II - Fluid Flow Problems, *Numerical Heat Transfer*, Vol. 14, pp. 273-293, 1988.
- [84] Hookey, N.A., *A CVFEM for Two-Dimensional Viscous Compressible Fluid Flow*, Ph.D. Thesis, Dept. of Mech. Eng., McGill University, Montreal, Canada, 1989.
- [85] Hookham, P., *Concentration and Velocity Measurements in Suspensions Flowing Through a Rectangular Channel*, Ph.D. Thesis, California Institute of Technology, Pasadena, U.S.A, 1986.
- [86] Hotchkiss, R.S., Hirt, C.W., Particulate Transport in Highly Distorted Three-Dimensional Flow Fields, *Proceedings of the 1972 Summer Simulation Conference*, San-Diego, 1972.
- [87] Huebner, K.H., Thornton, E.A., *The Finite Element Method for Engineers*, John Wiley and Sons, New York, 1982.
- [88] Hui, K., Haff, P.K., Ungar, J.E., Jackson, J., Boundary Conditions for High-Shear Grain Flows, *J. Fluid Mech.*, Vol. 145, pp.223-233, 1984.
- [89] Ishii, M., *Thermo-Fluid Dynamic Theory of Two-Phase Flow*, Eyrolles, Paris, 1975.
- [90] Jameson, A., Mavriplis, D., Finite Volume Solution of the Two-Dimensional Euler Equations on a Regular Triangular Mesh, *AIAA Paper 85-0435*, 1985.
- [91] Jenkins, J.T., Savage, S.B., A Theory for the Rapid Flow of Identical, Smooth, Nearly Elastic Particles, *J. Fluid Mech.*, Vol. 130, pp. 187-202, 1983.

- [92] Jenkins, J.T., Richman, M.W., Kinetic Theory for Plane Flows of a Dense Gas of Identical, Rough, Inelastic, Circular Disks, *Physics of Fluids*, Vol. 28, pp. 3485-3494, 1985.
- [93] Jenkins, J.T., Mancini, F., Balance Laws and Constitutive Relations for Plane Flows of a Dense, Binary Mixture of Smooth, Nearly Elastic Circular Disks, *J. Appl. Mech.*, Vol. 54, pp. 27-34, 1987.
- [94] Jiang, T.S., Kim, M.H., Kremese, V.J.Jr., Slattery, J.C., The Local Volume-Average Equations of Motion for a Suspension of Non-Neutrally Buoyant Spheres, *Chem. Eng. Commun.*, Vol. 50, pp. 1-30, 1987.
- [95] Johnson, P.C., Jackson, R., Frictional-Collisional Constitutive Relations for Granular Materials, with Application to Plane Shearing, *J. Fluid Mech.*, Vol. 176, pp. 67-93, 1987.
- [96] Kashiwa, B.A., Gore, R.A., A Four Equation Model for Multiphase Turbulent Flow, *Turbulence Modification in Multiphase Flows*, ASME-FED Vol. 110, pp. 23-28, 1991.
- [97] Koch, D.L., Kinetic Theory for a Monodisperse Gas-Solid Suspension, *Physics of Fluids A*, Vol. 2, pp. 1711-1723, 1990.
- [98] Kunii, D., Levenspiel, O., *Fluidization Eng.*, Wiley, New-York, 1969.
- [99] Lahrmann, A., An Element Formulation for the Classical Finite Difference and Finite Volume Method Applied to Arbitrarily Shaped Domains, *Int. J. for Num. Meth. in Eng.*, Vol. 35, pp. 893-913, 1992.
- [100] LeDain-Muir, B., Baliga, B.R., Solution of Three-Dimensional Convection-Diffusion Problems Using Tetrahedral Elements and Flow-Oriented Upwind Interpolation Functions, *Numerical Heat Transfer*, Vol. 9, pp. 143-162, 1986.
- [101] Lee, J., Crowe, C.T., Scaling Laws for Metering the Flow of Gas-Particle Suspension through Venturi, *Proceedings of Polyphase Flow and Transport Technology Conference*, San Francisco, pp. 245-249, 1980.
- [102] Leighton, D., Acrivos, A., The Shear Induced Migration of particles in concentrated suspensions, *J. Fluid Mech.*, Vol. 181, pp.415-439, 1987.

- [103] Liang, S.F., Vidal, A., Acrivos, A., Buoyancy-Driven Convection in Cylindrical Geometries, *J. Fluid Mech.*, Vol. 36, pp. 239-256, 1969.
- [104] Liljegren, L.M., Ensemble Averaging Applied to the Flow of a Multiphase Mixture, *Gas-Solid Flows*, ASME-FED Vol. 166, pp.73-83, 1993.
- [105] Lin, J.S., Chen, M.M., Chao, B.T., A Novel Radioactive Particle Tracking Facility for Measurement of Solids Motion in Gas Fluidized Beds, *AIChE J.*, Vol. 31, pp. 465-473, 1985.
- [106] Lun, C.K.K., Savage, S.B., Jeffrey, D.J., Chepurnyi, N., Kinetic Theories for Granular Flow: Inelastic Particles in Couette Flow and Slightly Inelastic particles in a General Flowfield, *J. Fluid Mech.*, Vol. 140, pp. 223-256, 1984.
- [107] Lun, C.K.K., *Kinetic Theories of Granular Flow*, Ph.D. Thesis, Dept. of Civil Eng., McGill University, Montreal, Canada, 1985.
- [108] Lun, C.K.K., Savage, S.B., The Effects of an Impact Velocity Dependent Coefficient of Restitution on Stresses Developed By Sheared Granular Materials, *Acta Mech.*, Vol. 63, pp. 15-44, 1986.
- [109] Lun, C.K.K., Savage, S.B., A Simple Kinetic Theory for Granular Flow of Rough, Inelastic, Spherical Particles, *J. Appl. Mech.*, Vol. 54, pp. 47-53, 1987.
- [110] Lun, C.K.K., Savage, S.B., Kinetic Theory for Rapid Flow of Dense Fluid-Solid Suspensions, *submitted to J. Fluid Mech.*, 1993.
- [111] Lyczkowski, R.W., Gidaspow, D., Solbrig, C.W., Hughes, E.D., Characteristics and Stability Analysis of Transient One-Dimensional Two-Phase Flow Equations and Their Finite Difference Approximations, *Nucl. Sci. and Eng.*, Vol. 66, pp. 378, 1978.
- [112] Marble, F.E., Dynamics of Dusty Gases, *Annual Rev. Fluid Mech.*, Vol. 2, pp. 397-446, 1970.
- [113] Marshall, W.R., Seltzer, E., Principles of Spray Drying, Part 1. Fundamentals of Spray Dryers Operation, *Chem. Eng. Science*, Vol. 46, pp. 501-508, 1950.
- [114] Masson, C., Baliga, B.R., A Control-Volume Finite Element Method for Two-Dimensional Dilute Fluid-Solid Particle Flows, *Proceedings of the First European Computational Fluid Dynamics Conference*, Brussels, pp. 541-548, 1992.

- [115] Masson, C., Baliga, B.R., Computer Simulation of Axisymmetric Dilute Gas-Solid Particle Flows in Irregular Geometries, *Gas-Solid Flows*, ASME-FED Vol. 166, pp.31-43, 1993.
- [116] Masson, C., Saabas, H.J. and Baliga, B.R., Co-Located Equal-Order Control-Volume Finite Element Method for Two-Dimensional Axisymmetric Incompressible Fluid Flow, *Int. J. for Num. Meth. in Fluids*, accepted for publication, to appear in 1993 or 1994.
- [117] Masson, C., Baliga, B.R., A Control-Volume Finite Element Method for Dilute Gas-Solid Particle Flows, *Computers & Fluids*, accepted for publication, to appear in 1994.
- [118] Maxey, M.R. and Riley, J.J., Equation of Motion for a Small Rigid Sphere in a Nonuniform Flow, *Physic of Fluids*, Vol. 26, pp. 883-889, 1983.
- [119] Migdal, D., Agosta, D.V., A Source Flow Model for Continuum Gas-Particle Flow, *J. Appl. Mech.*, Vol. 34, pp. 860-865, 1967.
- [120] Moritomi, H., Iwase, T., Chiba, T., A Comprehensive Interpretation of Solid Layer Inversion in Liquid Fluidized Beds, *Chem. Eng. Science*, Vol. 37, pp. 1751-1757, 1982.
- [121] Morsi, S.A., Alexander, A.J., An Investigation of Particles Trajectories in Two-Phase Flow System, *J. Fluid Mech.*, Vol. 55, pp. 193-208, 1972.
- [122] Murray, J.D., On the Mathematics of Fluidization. Part. 1 Fundamental Equations and Wave Propagation, *J. Fluid Mech.*, Vol. 21, pp. 465-493, 1965.
- [123] Ni, J.R., Wang, G.Q., The Kinetic Theory for Vertical Profile of Particle Concentration in Laminar Solid-Liquid Two-Phase Flow, *Proceeding of the International Conference on Multiphase Flows*, Japan, pp. 353-357, 1991.
- [124] Nigmatulin, R.I, 1979, Spatial Averaging in the Mechanics of Heterogeneous and Dispersed Systems, *Int. J. Multiphase Flow*, Vol. 5, pp. 353-385, 1979.
- [125] Nott, P.R., Brady, J.F., Pressure-Driven Flow of Suspensions: Simulation and Theory, *submitted to the J. Fluid Mech.*, 1993.

- [126] Oden, J.T., Finite Element Analogue of Navier-Stokes Equation, *J. Eng. Mech. Div.*, ASCE, Vol. 96, pp. 529-534, 1970.
- [127] Oesterle, B., Petitjean, A., Simulation of Particle-to-Particle Interactions in Gas-Solid Flows, *Proceeding of the International Conference on Multiphase Flows*, Japan, pp. 91-94, 1991.
- [128] Panton, R., Flow Properties for the Continuum Viewpoint of a Non-Equilibrium Gas-Particle Mixture, *J. Fluid mech.*, Vol. 31, pp. 273-303, 1968.
- [129] Patankar, S.V., Splading, D.B., A Calculation Procedure for Heat, Mass and Momentum Transfer in Three-Dimensional Parabolic Flows, *Int. J. Heat Mass Transfer*, Vol. 4, pp. 551-559, 1972.
- [130] Patankar, S.V., *Numerical Heat Transfer and Fluid Flow*, McGraw-Hill, New-York, 1980.
- [131] Peric, M., Kessler, R., Scheuerer, G., Comparison of Finite-Volume Numerical Methods with Staggered and Co-located Grids, *Computers & Fluids*, Vol. 16, pp. 389-403, 1988.
- [132] Pinelli, A., Benocci, C., Large Eddy Simulation of a Fully Turbulent Plane Channel Flow, *Von Karman Institute Technical Note 171*, 1989.
- [133] Pope, S.B., The Calculation of Turbulent Recirculating Flows in General Orthogonal Coordinates, *J. Comput. Physics*, Vol. 26, pp. 197-217, 1978.
- [134] Prakash, C., *A Finite Element Method for Predicting Flow Through Ducts with Arbitrary Cross-Sections*, Ph.D. Thesis, Dept. of Mech. Eng., University of Minnesota, 1981.
- [135] Prakash, C., Patankar, S.V., A Control Volume-Based Finite-Element Method for Solving the Navier Stokes Equations Using Equal-Order Velocity-Pressure Interpolation, *Numerical Heat Transfer*, Vol. 8, pp. 259-280, 1985.
- [136] Prakash, C., An Improved Control Volume Finite-Element Method for Heat and Mass Transfer, and for Fluid Flow Using Equal-Order Velocity-Pressure Interpolation, *Numerical Heat Transfer*, Vol. 9, pp. 253-276, 1986.

- [137] Prakash, C., Examination of the Upwind (Donor-Cell) Formulation in Control Volume Finite-Element Methods for Fluid Flow and Heat Transfer, *Numerical Heat Transfer*, Vol. 11, pp. 401-416, 1987.
- [138] Przekwas, A.J., Singhal, A.K., Lam, L.T., Modeling of Two-Phase Reactive Flows in Swirl Combustion chambers, *Gas-Solid Flows*, ASME-FED Vol. 10, pp. 71-76, 1984.
- [139] Raithby, G.D., Skew Upstream Differencing Schemes for Problems Involving Fluid Flow, *Comp. Meth. in Appl. Mech. and Eng.*, Vol. 9, pp. 153-164, 1976.
- [140] Raithby, G.D., Galpin, P.F., Van Doormaal, J.P., Prediction of Heat and Fluid Flow in Complex Geometries Using General Orthogonal Coordinates, *Numerical Heat Transfer*, Vol. 9, pp. 125-142, 1986.
- [141] Ramadhyani, S., *Solution of the Equations of Convective Heat, Mass and Momentum Transfer by the Finite Element Method using Quadrilateral Elements*, Ph.D. Thesis, Dept. of Mech. Eng., University of Minnesota, 1979.
- [142] Reeks, M.W., On the Continuum Equations for Dispersed Particles in Nonuniform Flows, *Physic of Fluids A*, Vol. 4, pp. 1290-1303, 1992.
- [143] Rhie, C.M., Chow, W.L., Numerical Study of the Turbulent Flow Past an Airfoil with Trailing Edge Separation, *AIAA J.*, Vol. 21, pp. 1525-1532, 1983.
- [144] Rice, S.A., Allnatt, A.R., On the Kinetic Theory of Dense Fluids. VI. Singlet Distribution Function for Rigid Spheres with an Attractive Potential, *J. Chem. Physics*, Vol. 34, pp. 2144-2155, 1960.
- [145] Rice, J.G., Schnipke, R.J., An Equal-Order Velocity-Pressure Formulation that Does Not Exhibit Spurious Pressure Modes, *Comp. Meth. in App. Mech. and Eng.*, Vol. 58, pp. 135-149, 1986.
- [146] Richman, M.W., The Source of Second Moment in Dilute Granular Flows of Highly Inelastic Spheres, *J. Rheology*, Vol. 33, pp. 1293-1306, 1988.
- [147] Rudinger, G., Chang, A., Analysis of Nonsteady Two-Phase Flow, *Physic of Fluids*, Vol. 7, pp. 1747-1754, 1964.

- [148] Rudinger, G., Relaxation in Gas-Particle Flow, in P.P. Wegener (Ed.), *Nonequilibrium Flows*, Vol. 1, 254 p., 1969.
- [149] Saabas, H.J., *A Control Volume Finite Element Method for Three-Dimensional, Incompressible, Viscous Fluid Flow*, Ph.D. Thesis, Dept. of Mech. Eng., McGill University, Montreal, Canada, 1991.
- [150] Savage, S.B., Jeffrey, D.J., The Stress Tensor in a Granular Flow at High Shear Rates, *J. Fluid Mech.*, Vol. 110, pp. 255-272, 1981.
- [151] Savage, S.B., Sayed, M., Stresses Developed by Dry Cohesionless Granular Materials Sheared in an Annular Shear Cell, *J. Fluid Mech.*, Vol. 142, pp. 391-430, 1984.
- [152] Savage, S.B., Rheology of Rapid Granular Flows; Experiments, Kinetic Theories, Computer Simulations and Some Current Issues, *Proceeding of the International Conference on Multiphase Flows*, Japan, pp. 109-125, 1991.
- [153] Savage, S.B., Numerical Simulations of Couette Flow of Granular Materials; Spatio-Temporal Coherence and 1/f noise, in J. Dodds and D. Bideau (Eds.), *Physics of Granular Media*, Nova Scientific Press, New York, 1991.
- [154] Schafflinger, U., Acrivos, A., Zhang, K., Viscous Resuspension of a Sediment within a Laminar and Stratified Flow, *Int. J. Multiphase Flow*, Vol. 16, pp. 567-578, 1990.
- [155] Schlichting, H., *Boundary Layer Theory*, Seventh Edition, McGraw-Hill, 817p., 1979.
- [156] Schneider, G.E., Raw, M.J., A Skewed Positive Influence Coefficient Upwinding Procedure for Control Volume Base Finite Element Convection Diffusion Computation, *Numerical Heat Transfer*, Vol. 9, pp. 1-26, 1986.
- [157] Schneider, G.E., Raw, M.J., Control Volume Finite-Element Method for Heat Transfer and Fluid Flow Using Colocated Variables - 1. Computational Procedure, *Numerical Heat Transfer*, Vol. 11, pp. 363-390, 1987.
- [158] Settari, A., Aziz, K., A Generalization of the Additive Correction Methods for the Iterative Solution of Matrix Equations, *SIAM J. Num. Anal.*, Vol. 10, pp. 506-521, 1973.

- [159] Shah, V.L. et al., Numerical Procedures for Calculating Steady/Unsteady Single/Two Phase Three Dimensional Fluid Flow with Heat Transfer, NUREG-CR-0789, 1979.
- [160] Sharma, M.P., *Numerical and Experimental Study of Gas-Particle Flows in Orifices and Venturis: Application to Flowmeter Design*, Ph.D. Thesis, Washington State University, 1977.
- [161] Sharma, M.P., Cornelius, D.K., Rice, J.G., Dougan, D.R., Numerical Computation of Swirling Gas-Particle Flows: Application to Pulverized Coal Classifiers, *ASME Paper* 80-WA/HT-31, 1980.
- [162] Shyy, W., Vu, T.C., On the Adoption of Velocity Variable and Grid System for Fluid Flow Computation in Curvilinear Coordinates, *J. Comput. Physics*, Vol. 92, pp. 82-105, 1991.
- [163] Simonin, O., Eulerian Formulation for Particle Dispersion in Turbulent Two-Phase Flows, *Proc. 5th Workshop on Two-Phase Flow Predictions*, Erlangen, Germany, 1990.
- [164] Simonin, O., Prediction of the Dispersed Phase Turbulence in Particle-Laden Jets, *Gas-Solid Flows*, ASME-FED Vol. 121, pp. 197-206, 1991.
- [165] Sinclair, J.L., Jackson, R., Gas-Particle Flow in a Vertical Pipe with Particle-Particle Interactions, *AIChE J.*, Vol. 35, pp. 1473-1486, 1989.
- [166] Slattery, J.C., Flow of Viscoelastic Fluids Through Porous Media, *AIChE J.*, Vol. 13, pp. 1066-1071, 1967.
- [167] Slattery, J.C., Momentum, Energy, and Mass Transfer in Continua, Robert E. Krieger, Malabar, 1981.
- [168] Sommerfeld, M., Numerical Simulation of Particle Dispersion in a Turbulent Flow, *Numerical Methods for Multiphase Flow: The Importance of Particle Lift Forces and Particle/Wall Collision Models*, ASME-FED Vol. 91, pp. 11-18, 1990.
- [169] Soo, S.L., *Fluid Dynamics of Multiphase Systems*, Blaisdell, Waltham, Massachusetts, 1967.

- [170] Spalding, D.B., Calculation of Two Dimensional Two-Phase Flows, in F. Durst et al. (Eds.), *Two Phase Momentum, Heat and Mass Transfer in Chemical Process, and Energy Engineering Systems*, Hemisphere Press, Washington, 1979.
- [171] Spalding, D.B., Mathematical Methods in Nuclear Reactor Thermal-Hydraulics, *Proceedings of ANS Meeting on Nuclear Reactor Thermal-Hydraulics*, Saratoga, New York, pp. 1979-2023, 1980.
- [172] Stewart, H.B., Wendroff, B., Two-Phase Flow: Models and Methods, *J. Comput. Physics*, Vol. 56, pp. 363-409, 1984.
- [173] Stock, D.E., Crowe, C.T., Analysis of the Flow Field in Electrostatic Precipitators, *1973 Spring Meeting Midwestern Section of Combustion Inst.*, 1973.
- [174] Syamlal, M., O'Brien, T.J., Simulation of Granular Layer Inversion in Liquid Fluidized Beds, *Int. J. Multiphase Flow*, Vol. 14, pp. 473-481, 1988.
- [175] Swaminathan, C.R., Voller, V.R., Streamline Upwind Scheme for Control-Volume Finite Elements, Part I. Formulations, *Numerical Heat Transfer, Part B*, Vol. 22, pp. 95-107, 1992.
- [176] Tabakoff, W., Hamed, A., Three Dimensional Particles Trajectories in Turbomachinery, *Conference on Gas Borne Particles*, Oxford, England, pp. 21-25, 1981.
- [177] Tanaka, T., Tsuji, Y., Numerical Simulation of Gas-Solid Two-Phase Flow in a Vertical Pipe: On the effect of Interparticle Collision, *Gas-Solid Flows*, ASME-FED Vol. 121, pp.123-128, 1991.
- [178] Taylor, C., Hood, P., A Numerical Solution of the Navier-Stokes Equations Using the Finite Element Technique, *Computers & Fluids*, Vol. 1, pp. 73-100, 1973.
- [179] Thompson, J.F., Warsi, Z.U.A., Mastin. C.W., Boundary-Fitted Coordinate Systems for Numerical Solution of Partial Differential Equations- A Review, *J. Comput. Physics*, Vol. 47, pp.1-108, 1982.
- [180] Trow, M., Particle Trajectories in Uni-Flow Cyclones, *Conference on Gas Borne Particles*, Oxford, England, pp. 31-36, 1981.

- [181] Ushimaru, K., Butler, B., Numerical Simulation of Gas-Particle Flow in an Electrostatic Precipitator, *Gas-Solid Flows*, ASME-FED Vol. 10, pp. 87-96, 1984.
- [182] Vand, V., Theory of Viscosity of Concentrated Suspensions, *Nature*, Vol. 155, pp. 364-365, 1945.
- [183] Van Doormaal, J.P., Raithby, G.D., Strong, A.B., Prediction of Natural Convection in Nonrectangular Enclosures Using Orthogonal Curvilinear Coordinates, *Numerical Heat Transfer*, Vol. 4, pp. 21-38, 1981.
- [184] Van Doormaal, J.P., Raithby, G.D., Enhancements of the SIMPLE Method for Predicting Incompressible Fluid Flows, *Numerical Heat Transfer*, Vol. 7, pp. 147-163, 1984.
- [185] van Leer, B., Towards the Ultimate Conservative Difference Schemes, V. A Second-Order Sequel to Gudunov's Method, *J. Comp. Phys.*, Vol. 32, 101-136, 1979.
- [186] Wallis, G.B., *One Dimensional Two-Phase Flow*, McGraw-Hill, 408 p., 1969.
- [187] Walton, O.R., Computer Simulation of Particulate Flow, *Energy Technol. Rev.*, pp. 24-36, May 1984.
- [188] Walton, O.R., Discrete Particle Computer Methods for Modelling Granular flow, in R.E.A. Arndt et al. (Eds.), *Advancements in Aerodynamics, Fluid Mechanics and Hydraulics*, New York, pp. 264-273, 1986.
- [189] Wang, G.Q., Ni, J.R., Kinetic Theory for Particle Concentration Distribution in Two-Phase Flow, *J. of Eng. Mechanics*, Vol. 116, pp. 2738-2749, 1990.
- [190] Wang, G.Q., Ni, J.R., The Kinetic Theory for Dilute Solid/Liquid Two-Phase Flow, *Int. J. Multiphase Flow*, Vol. 17, pp. 273-281, 1991.
- [191] Westbrook, C.K., Three Dimensional Numerical Modeling of Liquid Fuel Sprays, *Sixteenth Symposium on Combustion*, Pittsburg, 1976.
- [192] Whitaker, S., Diffusion and Dispersion in Porous Media, *AIChE J.*, Vol. 13, pp.420-427, 1967.

- [193] Whitaker, S., The transport Equations for Multiphase Systems, *Chem. Eng. Sci.*, Vol. 28, pp.139-147, 1973.
- [194] Winslow, A.M., Numerical Solution of the Quasilinear Poisson Equation in a Nonuniform Mesh, *J. Comput. Phys.*, Vol. 2, pp. 149-172, 1967.
- [195] Yaffe, M.L., T700 Aims at Low Combat Maintenance, *Aviation Week and Space Technology*, pp. 45-50, January 1974.
- [196] Zienkiewicz, O.C., *The Finite Element Method*, McGraw-Hill, London, 1977.
- [197] Zedan, M., Hartman, P., Mostafa, A., Sehra, A., Viscous Flow Analysis for Advanced Inlet Particle Separators, *AIAA Paper 90-2136*, 8p., 1990.
- [198] Zuber, N., On the Dispersed Two-Phase Flow in the Laminar Flow Regime, *Chem. Eng. Sci.*, Vol. 19, pp. 897-917, 1964.

Appendix A

Ensemble Averages and Collisional Integrals

A.1 Solid-Phase Stress Tensor

A.1.1 Kinetic Contribution

The kinetic contribution of the solid-phase stress tensor is $-\alpha\rho^s \langle C_i C_j \rangle$. It is evaluated using Eq. (3.17) with the velocity distribution function given by Eq. (3.59). The result is the following:

$$-\alpha\rho^s \langle C_i C_j \rangle = -\alpha\rho^s \left\{ T\delta_{ij} + 2a_1 T^2 \left[-\frac{1}{3} \frac{\partial u_k^s}{\partial x_k} \delta_{ij} + \frac{1}{2} \left(\frac{\partial u_i^s}{\partial x_j} + \frac{\partial u_j^s}{\partial x_i} \right) \right] \right\} \quad (\text{A.1})$$

A.1.2 Collisional Contribution

The collisional contribution of the solid-phase stress tensor is given by $-\theta_i(m^p C_j)$ where:

$$\theta_i(m^p C_j) = -\frac{m^p d^3}{2} \int_{\vec{c}_{12} \cdot \vec{k} > 0} (C'_{j1} - C_{j1}) (\vec{c}_{12} \cdot \vec{k}) f(\vec{c}_1, \vec{x} - \frac{d}{2} \vec{k}, t) f(\vec{c}_2, \vec{x} + \frac{d}{2} \vec{k}, t) g_0 k_i d\vec{k} d\vec{c}_1 d\vec{c}_2 \quad (\text{A.2})$$

Using the proposed form of the velocity distribution function, this collisional integral can be evaluated as:

$$\begin{aligned}
-\theta_i (m^p C_j) = & -4\eta g_0 \rho^s \alpha^2 T \delta_{ij} - \frac{8}{5} \alpha^2 g_0 \eta \rho^s \frac{a_1}{2} (2T) \left[\frac{1}{2} \left(\frac{\partial u_i^s}{\partial x_j} + \frac{\partial u_j^s}{\partial x_i} \right) - \frac{1}{3} \frac{\partial u_k^s}{\partial x_k} \delta_{ij} \right] \\
& + \mu_b^s \frac{3}{5} \left[\left(\frac{\partial u_i^s}{\partial x_j} + \frac{\partial u_j^s}{\partial x_i} \right) + \frac{\partial u_k^s}{\partial x_k} \delta_{ij} \right]
\end{aligned} \tag{A.3}$$

where

$$\mu_b^s = \frac{16m^p \alpha^2 \eta g_0}{\pi d^2} \left(\frac{T}{\pi} \right)^{\frac{1}{2}} \tag{A.4}$$

A.2 Interaction Force Term

The ensemble average of the interaction force is simply given by:

$$\alpha \rho^s \langle F_j^f \rangle = \zeta_D (u_j^f - u_j^s) - \alpha \frac{\partial p^f}{\partial x_j} \tag{A.5}$$

A.3 Solid-Phase Heat Flux Vector

A.3.1 Kinetic Contribution

The kinetic contribution of the solid-phase heat flux vector is $\alpha \rho^s \frac{1}{2} \langle C_i C_j^2 \rangle$. The solution is expressed as follow:

$$\alpha \rho^s \frac{1}{2} \langle C_i C_j^2 \rangle = -\alpha \rho^s \frac{5}{2} T^2 \left[\frac{a_2}{T} \frac{\partial T}{\partial x_i} + \frac{a_3}{n} \frac{\partial n}{\partial x_i} \right] \tag{A.6}$$

A.3.2 Collisional Contribution

The collisional contribution of the solid-phase heat flux vector is given by $\theta_i \left(\frac{1}{2} m^p C_j^2 \right)$, where:

$$\theta_i \left(\frac{1}{2} m^p C_j^2 \right) = -\frac{m^p d^3}{4} \int_{\vec{c}_{12} \cdot \vec{k} > 0} (C_{j1}^{2'} - C_{j1}^2) (\vec{c}_{12} \cdot \vec{k}) f(\vec{c}_1, \vec{x} - \frac{d}{2} \vec{k}, t) f(\vec{c}_2, \vec{x} + \frac{d}{2} \vec{k}, t) g_0 k_i d\vec{k} d\vec{c}_1 d\vec{c}_2 \tag{A.7}$$

Using the proposed form of the velocity distribution function, this collisional integral can be evaluated as:

$$\theta_i \left(\frac{1}{2} m^p C_j^2 \right) = -4\eta\alpha^2 \rho^s g_0 d \left(\frac{T}{\pi} \right)^{\frac{1}{2}} \frac{\partial T}{\partial x_i} - \frac{12}{5} \alpha g_0 \eta \frac{1}{2} \alpha \rho^s \frac{5}{4} (2T)^2 \left[\frac{a_2}{T} \frac{\partial T}{\partial x_i} + \frac{a_3}{n} \frac{\partial n}{\partial x_i} \right] \quad (\text{A.8})$$

A.4 Collisional Dissipation

The collisional dissipation is defined as:

$$\gamma_c = -\mathcal{X} \left(\frac{1}{2} m^p c_i^2 \right) \quad (\text{A.9})$$

$$\mathcal{X} \left(\frac{1}{2} m^p c_i^2 \right) = \frac{m^p d^2}{4} \int_{\vec{c}_{12} \cdot \vec{k} > 0} (c_{i1}^2 + c_{i2}^2 - c_{i1}^2 - c_{i2}^2) (\vec{c}_{12} \cdot \vec{k}) f(\vec{c}_1, \vec{x} - d\vec{k}, t) f(\vec{c}_2, \vec{x}, t) g_0 d\vec{k} d\vec{c}_1 d\vec{c}_2 \quad (\text{A.10})$$

The collisional integral is evaluated as:

$$\gamma_c = 48\eta(1 - \eta) \frac{\alpha^2 \rho^s g_0}{d} \left(\frac{T}{\pi} \right)^{\frac{1}{2}} T \quad (\text{A.11})$$

A.5 Interaction-Force Dissipation

The interaction-force dissipation is given by:

$$\alpha \rho^s \langle F_i^f C_i \rangle = -3\alpha \rho^s \zeta_D T \quad (\text{A.12})$$

A.6 Energy Transfer Term

The energy transfer term can be obtained by using the expression of B_{ij} given in Eq. (3.25):

$$\alpha \rho^s \langle B_{ij} \delta_{ij} \rangle = 3\alpha \rho^s \zeta_D T \left(1 + a_0 \alpha^{\frac{3}{2}} \right) \quad (\text{A.13})$$

Appendix B

Some Details of the Implementation of the Proposed CVFEM

B.1 Implementation of the MAW Scheme

The MAW scheme described in Section 4.4.4 can be systematically implemented by using the notation proposed in Fig. B.1. Using such a notation, the MAW scheme is expressed as:

$$\phi_{p1} = \begin{cases} f_1^+ \phi_{p2} + (1 - f_1^+) \phi_{n2} & \text{where } f_1^+ = \min[\max(\frac{\dot{m}_{p2}}{\dot{m}_{p1}}, 0), 1] \text{ if } \dot{m}_{p1} > 0 \\ f_1^- \phi_{p3} + (1 - f_1^-) \phi_{n1} & \text{where } f_1^- = \min[\max(\frac{\dot{m}_{p3}}{\dot{m}_{p1}}, 0), 1] \text{ if } \dot{m}_{p1} < 0 \end{cases} \quad (\text{B.1})$$

$$\phi_{p2} = \begin{cases} f_2^+ \phi_{p3} + (1 - f_2^+) \phi_{n3} & \text{where } f_2^+ = \min[\max(\frac{\dot{m}_{p3}}{\dot{m}_{p2}}, 0), 1] \text{ if } \dot{m}_{p2} > 0 \\ f_2^- \phi_{p1} + (1 - f_2^-) \phi_{n2} & \text{where } f_2^- = \min[\max(\frac{\dot{m}_{p1}}{\dot{m}_{p2}}, 0), 1] \text{ if } \dot{m}_{p2} < 0 \end{cases} \quad (\text{B.2})$$

$$\phi_{p3} = \begin{cases} f_3^+ \phi_{p1} + (1 - f_3^+) \phi_{n1} & \text{where } f_3^+ = \min[\max(\frac{\dot{m}_{p1}}{\dot{m}_{p3}}, 0), 1] \text{ if } \dot{m}_{p3} > 0 \\ f_3^- \phi_{p2} + (1 - f_3^-) \phi_{n3} & \text{where } f_3^- = \min[\max(\frac{\dot{m}_{p2}}{\dot{m}_{p3}}, 0), 1] \text{ if } \dot{m}_{p3} < 0 \end{cases} \quad (\text{B.3})$$

where

$$\dot{m}_{pi} = \int_o^{mi} \beta \rho \vec{V}^m \cdot \vec{n}_{pi} 2\pi r ds \quad (\text{B.4})$$

\vec{n}_{pi} is the unit normal to the surface $o - mi$, as shown in Fig. B.1. Eqs. (B.1)-(B.3) can be cast in a more manageable form by defining the following switch function:

$$\omega_i = \max(0, \text{sign}(\dot{m}_{pi})) \quad (\text{B.5})$$

Using this switch function, the Eqs. (B.1)-(B.3) can be rewritten as:

$$\phi_{p1} = \omega_1 f_1^+ \phi_{p2} + \omega_1 (1 - f_1^+) \phi_{n2} + (1 - \omega_1) f_1^- \phi_{p3} + (1 - \omega_1) (1 - f_1^-) \phi_{n1} \quad (\text{B.6})$$

$$\phi_{p2} = \omega_2 f_2^+ \phi_{p3} + \omega_2 (1 - f_2^+) \phi_{n3} + (1 - \omega_2) f_2^- \phi_{p1} + (1 - \omega_2) (1 - f_2^-) \phi_{n2} \quad (\text{B.7})$$

$$\phi_{p3} = \omega_3 f_3^+ \phi_{p1} + \omega_3 (1 - f_3^+) \phi_{n1} + (1 - \omega_3) f_3^- \phi_{p2} + (1 - \omega_3) (1 - f_3^-) \phi_{n3} \quad (\text{B.8})$$

These three equations contain three unknowns ϕ_{p1} , ϕ_{p2} , and ϕ_{p3} . This system can be solved to obtain:

$$\phi_{pi} = \frac{1}{\text{DET}^\phi} \sum_{k=1}^3 E_{ik}^\phi \left(\sum_{j=1}^3 D_{kj}^\phi \phi_{nj} \right) \quad (\text{B.9})$$

where

$$\text{DET}^\phi = 1 - \omega_1 f_1^+ \omega_2 f_2^+ \omega_3 f_3^+ - (1 - \omega_1) f_1^- (1 - \omega_2) f_2^- (1 - \omega_3) f_3^- \quad (\text{B.10})$$

$$\begin{aligned} E_{11}^\phi &= 1 - \omega_2 f_2^+ (1 - \omega_3) f_3^- & E_{12}^\phi &= \omega_1 f_1^+ + (1 - \omega_1) f_1^- (1 - \omega_3) f_3^- \\ E_{13}^\phi &= \omega_1 f_1^+ \omega_2 f_2^+ + (1 - \omega_1) f_1^- \end{aligned} \quad (\text{B.11})$$

$$\begin{aligned} E_{22}^\phi &= 1 - \omega_3 f_3^+ (1 - \omega_1) f_1^- & E_{23}^\phi &= \omega_2 f_2^+ + (1 - \omega_1) f_1^- (1 - \omega_2) f_2^- \\ E_{21}^\phi &= \omega_2 f_2^+ \omega_3 f_3^+ + (1 - \omega_2) f_2^- \end{aligned} \quad (\text{B.12})$$

$$\begin{aligned} E_{33}^\phi &= 1 - \omega_1 f_1^+ (1 - \omega_2) f_2^- & E_{31}^\phi &= \omega_3 f_3^+ + (1 - \omega_2) f_2^- (1 - \omega_3) f_3^- \\ E_{32}^\phi &= \omega_1 f_1^+ \omega_3 f_3^+ + (1 - \omega_3) f_3^- \end{aligned} \quad (\text{B.13})$$

$$D_{11}^\phi = (1 - \omega_1) (1 - f_1^-) \quad ; \quad D_{12}^\phi = \omega_1 (1 - f_1^+) \quad ; \quad D_{13}^\phi = 0 \quad (\text{B.14})$$

$$D_{22}^\phi = (1 - \omega_2) (1 - f_2^-) \quad ; \quad D_{23}^\phi = \omega_2 (1 - f_2^+) \quad ; \quad D_{21}^\phi = 0 \quad (\text{B.15})$$

$$D_{33}^\phi = (1 - \omega_3) (1 - f_3^-) \quad ; \quad D_{31}^\phi = \omega_3 (1 - f_3^+) \quad ; \quad D_{32}^\phi = 0 \quad (\text{B.16})$$

B.2 Implementation of the Modified MAW Scheme

The implementation of the modified MAW scheme for the interpolation of the volume concentration is very similar to the MAW scheme implementation described in the previous section. Following the derivation of the previous section, it can be shown that:

$$\beta_{pi} = \frac{1}{\text{DET}^\beta} \sum_{k=1}^3 E_{ik}^\beta \left(\sum_{j=1}^3 D_{kj}^\beta \beta_{nj} \right) \quad (\text{B.17})$$

where

$$\text{DET}^\beta = 1 - \omega_1 f_1^+ \omega_2 f_2^+ \omega_3 f_3^+ - (1 - \omega_1) f_1^- (1 - \omega_2) f_2^- (1 - \omega_3) f_3^- \quad (\text{B.18})$$

$$\begin{aligned} E_{11}^\beta &= 1 - \omega_2 f_2^+ (1 - \omega_3) f_3^- & E_{12}^\beta &= \omega_1 f_1^+ + (1 - \omega_1) f_1^- (1 - \omega_3) f_3^- \\ E_{13}^\beta &= \omega_1 f_1^+ \omega_2 f_2^+ + (1 - \omega_1) f_1^- \end{aligned} \quad (\text{B.19})$$

$$\begin{aligned} E_{22}^\beta &= 1 - \omega_3 f_3^+ (1 - \omega_1) f_1^- & E_{23}^\beta &= \omega_2 f_2^+ + (1 - \omega_1) f_1^- (1 - \omega_2) f_2^- \\ E_{21}^\beta &= \omega_2 f_2^+ \omega_3 f_3^+ + (1 - \omega_2) f_2^- \end{aligned} \quad (\text{B.20})$$

$$\begin{aligned} E_{33}^\beta &= 1 - \omega_1 f_1^+ (1 - \omega_2) f_2^- & E_{31}^\beta &= \omega_3 f_3^+ + (1 - \omega_2) f_2^- (1 - \omega_3) f_3^- \\ E_{32}^\beta &= \omega_1 f_1^+ \omega_3 f_3^+ + (1 - \omega_3) f_3^- \end{aligned} \quad (\text{B.21})$$

$$D_{11}^\beta = (1 - \omega_1) (1 - f_1^-) \quad ; \quad D_{12}^\beta = \omega_1 (1 - f_1^+) \quad ; \quad D_{13}^\beta = 0 \quad (\text{B.22})$$

$$D_{22}^\beta = (1 - \omega_2) (1 - f_2^-) \quad ; \quad D_{23}^\beta = \omega_2 (1 - f_2^+) \quad ; \quad D_{21}^\beta = 0 \quad (\text{B.23})$$

$$D_{33}^\beta = (1 - \omega_3) (1 - f_3^-) \quad ; \quad D_{31}^\beta = \omega_3 (1 - f_3^+) \quad ; \quad D_{32}^\beta = 0 \quad (\text{B.24})$$

$$\dot{M}_{pi}^s = \int_o^{mi} \rho^s \vec{V}^s \cdot \vec{n}_{pi} 2\pi r ds \quad (\text{B.25})$$

$$\omega_i = \max(0, \text{sign}(\dot{M}_{pi}^s)) \quad (\text{B.26})$$

$$f_1^+ = \min[\max(\frac{\dot{M}_{p2}^s}{M_{p1}^s}, 0), 1] \quad f_1^- = \min[\max(\frac{\dot{M}_{p3}^s}{M_{p1}^s}, 0), 1] \quad (\text{B.27})$$

$$f_2^+ = \min[\max(\frac{\dot{M}_{p3}^s}{M_{p2}^s}, 0), 1] \quad f_2^- = \min[\max(\frac{\dot{M}_{p1}^s}{M_{p2}^s}, 0), 1] \quad (\text{B.28})$$

$$f_3^+ = \min[\max(\frac{\dot{M}_{p1}^s}{M_{p3}^s}, 0), 1] \quad f_3^- = \min[\max(\frac{\dot{M}_{p2}^s}{M_{p3}^s}, 0), 1] \quad (\text{B.29})$$

B.3 Element Contribution of Diffusion Terms

Algebraic approximations to the surface integrals of diffusion flux appearing in Eqs. (4.40) and (4.41) can be cast in the following general form:

$$\int_o^{mi} \vec{J}_D \cdot \vec{n}_{pi} 2\pi r ds = \sum_{j=1}^3 \text{CD}_{ij} \phi_j \quad (\text{B.30})$$

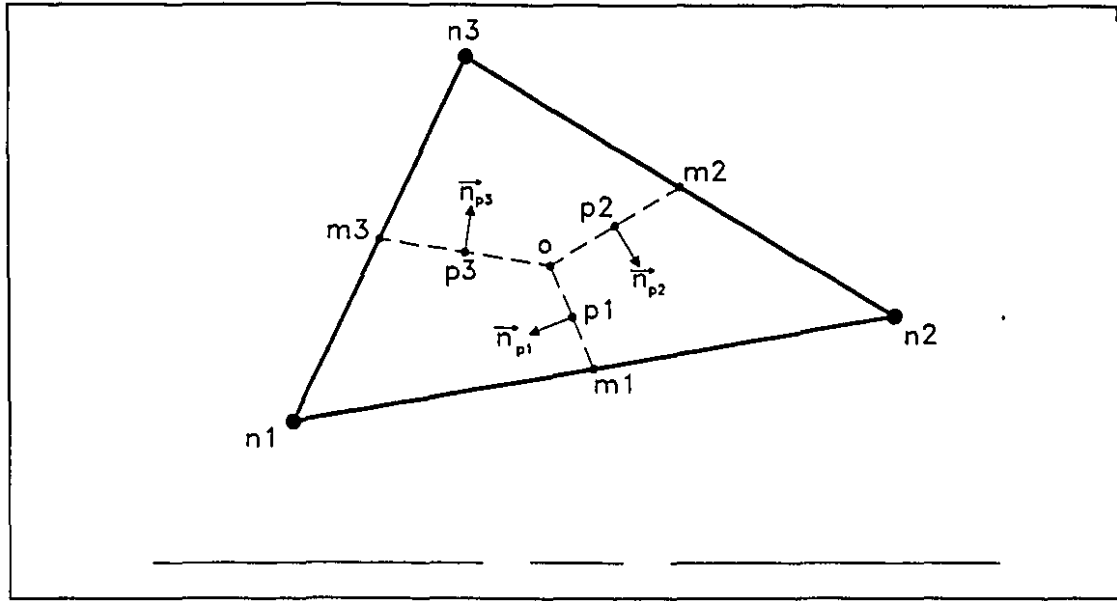


Figure B.1: Typical triangular element - general notation

This integral represents the integrated diffusion flux across the surface $o - mi$ in the direction of the unit normal \vec{n}_{pi} where i can take the value of 1, 2, or 3 (see Fig. B.1). CD_{ij} represents the contribution of node j to the integrated-diffusion flux across the surface $o - mi$. Eq. (4.41) can also be written as:

$$\int_o^{mi} \vec{J}_D \cdot \vec{n}_{pi} 2\pi r ds = 2\pi \bar{\Gamma}_e \frac{r_o + r_{mi}}{2} [Bx_{mi} - Ay_{mi}] \quad (B.31)$$

where

$$\bar{\Gamma}_e = \frac{1}{3} \sum_{j=1}^3 (\Gamma_e)_{nj} \quad (B.32)$$

$$A = -\frac{1}{\text{DET}_{xy}} \sum_{j=1}^3 y \text{MUL}_j \phi_j \quad (B.33)$$

$$B = \frac{1}{\text{DET}_{xy}} \sum_{j=1}^3 x \text{MUL}_j \phi_j \quad (B.34)$$

$$x\text{MUL}_1 = x_{n3} - x_{n2} \quad x\text{MUL}_2 = x_{n1} - x_{n3} \quad x\text{MUL}_3 = x_{n2} - x_{n1} \quad (B.35)$$

$$y\text{MUL}_1 = y_{n3} - y_{n2} \quad y\text{MUL}_2 = y_{n1} - y_{n3} \quad y\text{MUL}_3 = y_{n2} - y_{n1} \quad (B.36)$$

$$\text{DET}_{xy} = (x_{n1}y_{n2} + x_{n2}y_{n3} + x_{n3}y_{n1} - y_{n1}x_{n2} - y_{n2}x_{n3} - y_{n3}x_{n1}) \quad (B.37)$$

The general expression for CD_{ij} can be obtained from the preceding equations:

$$CD_{ij} = 2\pi \frac{r_o + r_{mi}}{2} \frac{\bar{F}_e}{\text{DET}_{xy}} (xMUL_j x_{mi} + yMUL_j y_{mi}) \quad (\text{B.38})$$

B.4 Element Contribution to Convection Terms

The surface integrals of the convection flux appearing in Eqs. (4.44)-(4.45) can be cast in the following general form:

$$\int_o^{mi} \beta \vec{J}_C \cdot \vec{n}_{pi} 2\pi r ds = \sum_{j=1}^3 CC_{ij} \phi_j \quad (\text{B.39})$$

The appropriate form for CC_{ij} depends on the interpolation function that is used to approximate the convection of ϕ .

B.4.1 FLO Scheme

Using the FLO scheme, the integrated convection flux across the surface $o - mi$, in the direction of the unit normal \vec{n}_{pi} , is given by:

$$\int_o^{mi} \beta \vec{J}_C \cdot \vec{n}_{pi} 2\pi r ds = 2\pi \beta_{pi} \left\{ + \frac{y_{mi}}{6} [r_o (J_{Cz})_o + 4r_{pi} (J_{Cz})_{pi} + r_{mi} (J_{Cz})_{mi}] \right. \quad (\text{B.40}) \\ \left. - \frac{x_{mi}}{6} [r_o (J_{Cr})_o + 4r_{pi} (J_{Cr})_{pi} + r_{mi} (J_{Cr})_{mi}] \right\}$$

where

$$J_{Cz} = \rho u^m \phi \quad J_{Cr} = \rho v^m \phi \quad (\text{B.41})$$

$$\phi = A\xi + BY + C \quad (\text{B.42})$$

$$A = -\frac{1}{\text{DET}_{\xi Y}} \sum_{j=1}^3 YMUL_j \phi_j \quad (\text{B.43})$$

$$B = \frac{1}{\text{DET}_{\xi Y}} \sum_{j=1}^3 \xi MUL_j \phi_j \quad (\text{B.44})$$

$$C = \frac{1}{\text{DET}_{\xi Y}} \sum_{j=1}^3 \xi YMUL_j \phi_j \quad (\text{B.45})$$

$$\xi\text{MUL}_1 = \xi_{n3} - \xi_{n2} \quad \xi\text{MUL}_2 = \xi_{n1} - \xi_{n3} \quad \xi\text{MUL}_3 = \xi_{n2} - \xi_{n1} \quad (\text{B.46})$$

$$\text{YMUL}_1 = Y_{n3} - Y_{n2} \quad \text{YMUL}_2 = Y_{n1} - Y_{n3} \quad \text{YMUL}_3 = Y_{n2} - Y_{n1} \quad (\text{B.47})$$

$$\begin{aligned} \xi\text{YMUL}_1 &= \xi_{n2}Y_{n3} - \xi_{n3}Y_{n2} & \xi\text{YMUL}_2 &= \xi_{n3}Y_{n1} - \xi_{n1}Y_{n3} \\ \xi\text{YMUL}_3 &= \xi_{n1}Y_{n2} - \xi_{n2}Y_{n1} \end{aligned} \quad (\text{B.48})$$

$$\text{DET}_{\xi Y} = (\xi_{n1}Y_{n2} + \xi_{n2}Y_{n3} + \xi_{n3}Y_{n1} - Y_{n1}\xi_{n2} - Y_{n2}\xi_{n3} - Y_{n3}\xi_{n1}) \quad (\text{B.49})$$

This yields:

$$\text{CC}_{ij} = \frac{2\pi\beta_{pi}}{6\text{DET}_{\xi Y}} [-\text{YMUL}_j\mathcal{F}(\xi) + \xi\text{MUL}_j\mathcal{F}(Y) + \xi\text{YMUL}_j\mathcal{F}(1)] \quad (\text{B.50})$$

where

$$\begin{aligned} \mathcal{F}(\varepsilon) &= \left(\rho u_o^m r_o \varepsilon_o + 4\rho u_{pi}^m r_{pi} \varepsilon_{pi} + \rho u_{mi}^m r_{mi} \varepsilon_{mi} \right) y_{mi} \\ &\quad - \left(\rho v_o^m r_o \varepsilon_o + 4\rho v_{pi}^m r_{pi} \varepsilon_{pi} + \rho v_{mi}^m r_{mi} \varepsilon_{mi} \right) x_{mi} \end{aligned} \quad (\text{B.51})$$

u_o^m , u_{pi}^m , u_{mi}^m , v_o^m , v_{pi}^m , and v_{mi}^m are computed using linear interpolation of the nodal mass conserving velocities (see Eqs. (4.93) and (4.97)). β_{pi} is calculated using Eq. (B.17).

B.4.2 MAW Scheme

In the MAW scheme, the integrated convection flux across the surface $o - mi$, in the direction of the unit normal \vec{n}_{pi} , is simply expressed as:

$$\int_o^{mi} \beta \vec{J}_C \cdot \vec{n}_{pi} 2\pi r ds = \beta_{pi} \dot{M}_{pi} \phi_{pi} \quad (\text{B.52})$$

Using this general equation along with the expression of ϕ_{pi} , the following expression to CC_{ij} is obtained:

$$\text{CC}_{ij} = \beta_{pi} \dot{M}_{pi} \frac{1}{\text{DET}^\phi} \sum_{k=1}^3 \mathbf{E}_{ik}^\phi \mathbf{D}_{kj}^\phi \quad (\text{B.53})$$

B.5 Element Contribution to the Mass Flow Rates

The surface integrals of the mass flux, Eqs. (4.94), (4.95), (4.98), and (4.99), are expressed in the following general form:

$$\int_o^{mi} \beta \rho \vec{V}^m \cdot \vec{n}_{pi} 2\pi r ds = 2\pi \frac{\beta_{pi}}{6} \{y_{mi} [\rho u_o^m r_o^* + \rho u_{mi}^m r_{mi}^*] - x_{mi} [\rho v_o^m r_o^* + \rho v_{mi}^m r_{mi}^*]\} \quad (\text{B.54})$$

Note that:

$$\dot{m}_{pi} = \beta_{pi} \dot{M}_{pi} = \int_o^{mi} \beta \rho \vec{V}^m \cdot \vec{n}_{pi} 2\pi r ds \quad (\text{B.55})$$

and

$$r_o^* = 2r_o + r_{mi} \quad r_{mi}^* = 2r_{mi} + r_o \quad (\text{B.56})$$

u_o^m , u_{mi}^m , v_o^m , and v_{mi}^m are computed using linear interpolation on the nodal mass conserving velocities (see Eq. (4.93) and (4.97)). β_{pi} is calculated using Eq. (B.17).

Eq. (B.54) can be expressed in terms of the nodal values of the volume concentration β_{ni} , or the fluid-phase pressure p_{ni}^f , in order to derive an equation for β or p^f .

B.5.1 Contribution to the Fluid-Phase Pressure Equation

Using the mass conserved velocity interpolation given by Eq. (4.93) along with the linear interpolation of the fluid-phase pressure (Eq. (4.33)), Eq. (B.54) can be rewritten as:

$$\int_o^{mi} \beta \rho \vec{V}^m \cdot \vec{n}_{pi} 2\pi r ds = \sum_{j=1}^3 CF_{ij}^p p_j^f + BF_i^p \quad (\text{B.57})$$

where

$$CF_{ij}^p = \frac{2\pi \rho \beta_{pi}}{6 \text{DET}_{xy}} [\mathcal{G}(d^v) x \text{MUL}_j x_{mi} + \mathcal{G}(d^u) y \text{MUL}_j y_{mi}] \quad (\text{B.58})$$

$$BF_i^p = \frac{2\pi \rho \beta_{pi}}{6} [\mathcal{G}(\hat{u}) y_{mi} - \mathcal{G}(\hat{v}) x_{mi}] \quad (\text{B.59})$$

$$\mathcal{G}(\varepsilon) = \varepsilon_{mi} r_{mi}^* + \varepsilon_o r_o^* \quad (\text{B.60})$$

B.5.2 Contribution to the Volume Concentration Equation

Contribution to the volume concentration equation can be computed by using Eq. (B.17) in Eq. (B.55):

$$\int_o^{mi} \beta_\rho \vec{V}^m \cdot \vec{n}_{pi} 2\pi r ds = \dot{M}_{pi} \frac{1}{\text{DET}^\beta} \sum_{k=1}^3 E_{ik}^\beta \left(\sum_{j=1}^3 D_{kj}^\beta \beta_{nj} \right) = \sum_{j=1}^3 \text{CF}_{ij}^\beta \beta_j \quad (\text{B.61})$$

Therefore

$$\text{CF}_{ij}^\beta = \dot{M}_{pi} \frac{1}{\text{DET}^\beta} \sum_{k=1}^3 E_{ik}^\beta D_{kj}^\beta \quad (\text{B.62})$$

B.6 Calculation of Element Volumes

The evaluation of the volume occupied by a torus element is done by applying the Pappus theorem. This theorem stipulates that if a planar area is revolved about an axis, the volume so formed is equal to the product of the area and the length of the path traced by the centroid of the area.

The volume occupied by the torus control volume is obtained by an element-by-element procedure. To achieve it, first the torus volumes defined by the rotation of the surfaces $1aoc$, $2boa$ and $3cob$ (see Fig. B.2) are calculated and then assembled appropriately. These three volumes can be obtained using a similar procedure, therefore only the volume defined by the surface $1aoc$, \mathcal{V}_{1aoc} , will be presented in detail.

The surface $1aoc$ can be considered as the sum of two triangles, namely $1ao$ and $1oc$. This is convenient since the position of the centroid \bar{r} of a triangular surface is simply expressed:

$$\bar{r}_{1ao} = \frac{r_1 + r_a + r_o}{3} \quad (\text{B.63})$$

$$\bar{r}_{1oc} = \frac{r_1 + r_o + r_c}{3} \quad (\text{B.64})$$

The triangular surfaces \mathcal{A}_{1ao} and \mathcal{A}_{1oc} are related to the element triangular surface \mathcal{A}_{123} . Since the point o is at the centroid of the triangular element 123 , and the

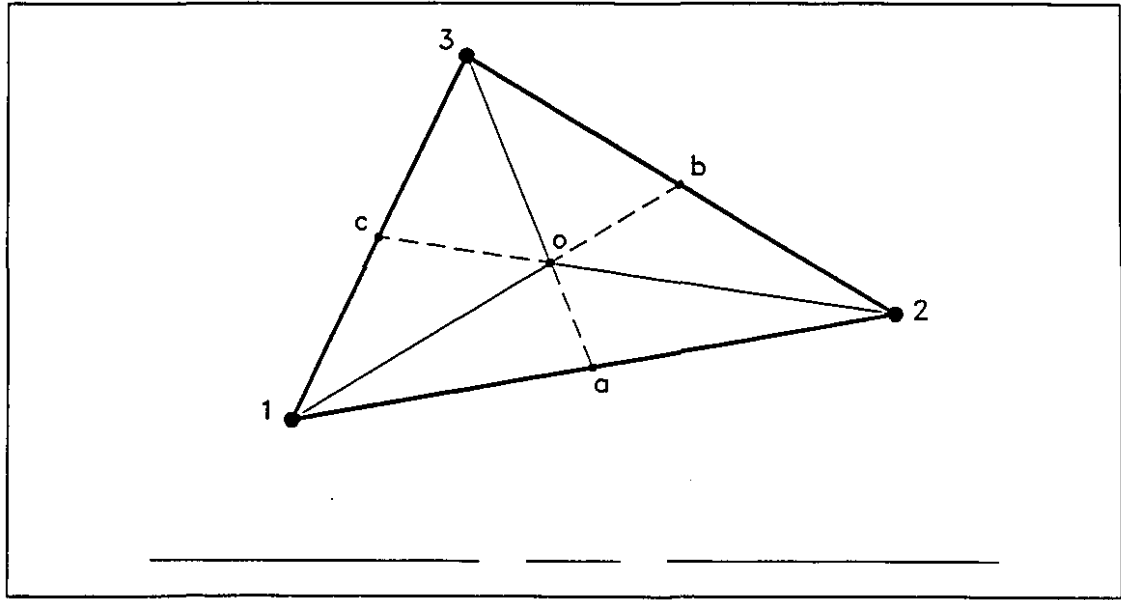


Figure B.2: Typical triangular element - volume calculation

points a , b and c are the mid-points of the corresponding element sides, it follows that:

$$\mathcal{A}_{1ao} = \mathcal{A}_{1oc} = \frac{\mathcal{A}_{123}}{6} \quad (\text{B.65})$$

where

$$\mathcal{A}_{123} = \frac{|\text{DET}|}{2} \quad (\text{B.66})$$

$$\text{DET}_{xy} = (x_1y_2 + x_2y_3 + x_3y_1 - y_1x_2 - y_2x_3 - y_3x_1) \quad (\text{B.67})$$

The torus volumes defined by the rotation of the two triangular surfaces $1ao$ and $1oc$ are obtained by applying the Pappus theorem:

$$\mathcal{V}_{1ao} = 2\pi\bar{r}_{1ao}\mathcal{A}_{1ao} \quad (\text{B.68})$$

$$\mathcal{V}_{1oc} = 2\pi\bar{r}_{1oc}\mathcal{A}_{1oc} \quad (\text{B.69})$$

The torus volume defined by the rotation of the surface $1aoc$ is the sum of \mathcal{V}_{1ao} and \mathcal{V}_{1oc} . Finally, the following expression is obtained:

$$\mathcal{V}_{1aoc} = 2\pi \frac{|\text{DET}|}{36} (2r_1 + 2r_o + r_a + r_c) \quad (\text{B.70})$$

Similarly, it can be shown that:

$$\mathcal{V}_{2bo\alpha} = 2\pi \frac{|\text{DET}|}{36} (2r_2 + 2r_o + r_a + r_b) \quad (\text{B.71})$$

$$\mathcal{V}_{3cob} = 2\pi \frac{|\text{DET}|}{36} (2r_3 + 2r_o + r_b + r_c) \quad (\text{B.72})$$

Appendix C

Linearization of the Momentum Coupling Source Term

The linearization of the momentum coupling term needs to be done appropriately in order to ensure convergence of the proposed algorithm. Several linearizations are possible. In the discussion of the momentum coupling term presented in Section 4.5.2, three linearizations were described:

(i)

$$(S_{Dz})_C^s = K_1 u_1^f \quad (S_{Dz})_P^s = -K_1 \quad (C.1)$$

$$(S_{Dz})_C^f = K_1 u_1^s \quad (S_{Dz})_P^f = -K_1 \quad (C.2)$$

(ii)

$$(S_{Dz})_C^s = K_1 u_1^f \quad (S_{Dz})_P^s = -K_1 \quad (C.3)$$

$$(S_{Dz})_C^f = K_1 (u_1^s - u_1^f) \quad (S_{Dz})_P^f = 0 \quad (C.4)$$

(iii)

$$(S_{Dz})_C^s = K_1 (u_1^f - u_1^s) \quad (S_{Dz})_P^s = 0 \quad (C.5)$$

$$(S_{Dz})_C^f = K_1 (u_1^s - u_1^f) \quad (S_{Dz})_P^f = 0 \quad (C.6)$$

This appendix is intended to give a numerical demonstration of the capabilities and limitations of these three linearizations. For the sake of the argument, the discretized momentum equations for the fluid and solid phases in the z -direction are simplified to:

$$(ac_i^f + K\mathcal{V}_{cv})u_i^f = ac_{nb}^f u_{nb}^f + b^f + Ku_i^s \mathcal{V}_{cv} \quad (C.7)$$

$$(ac_i^s + K\mathcal{V}_{cv})u_i^s = ac_{nb}^s u_{nb}^s + b^s + Ku_i^f \mathcal{V}_{cv} \quad (C.8)$$

These equations can be solved for u_i^f and u_i^s using the linearizations (i), (ii) and (iii). Two different cases will be presented: one typical of low solid-phase concentration; and the other one corresponding to a larger concentration. For the low concentration problem, the various parameters are set to:

$$ac_i^f = ac_{nb}^f = 30 \quad b^f = 100 \quad (C.9)$$

$$ac_i^s = ac_{nb}^s = 20 \quad b^s = 10 \quad (C.10)$$

$$K\mathcal{V}_{cv} = 400 \quad (C.11)$$

The parameters corresponding to the high concentration problem are:

$$ac_i^f = ac_{nb}^f = 30 \quad b^f = 100 \quad (C.12)$$

$$ac_i^s = ac_{nb}^s = 200 \quad b^s = 100 \quad (C.13)$$

$$K\mathcal{V}_{cv} = 4000 \quad (C.14)$$

The boundary conditions for both problem are given by:

$$u_{nb}^f = u_{nb}^s = 1 \quad (C.15)$$

C.1 Linearization (i)

Using the linearization (i), the resulting discretized equations are:

low concentration problem

$$430u_i^f = 30 + 400u_i^s + 100 \quad 420u_i^s = 20 + 400u_i^f + 10 \quad (C.16)$$

high concentration problem

$$4030u_i^f = 30 + 4000u_i^s + 100 \quad 4200u_i^s = 200 + 4000u_i^f + 100 \quad (C.17)$$

Solving the resulting set of two equations yields the exact solutions for this case, namely,

$$\text{low concentration problem} \quad u_i^f = 3.23 \quad u_i^s = 3.15$$

$$\text{high concentration problem} \quad u_i^f = 1.89 \quad u_i^s = 1.87$$

C.2 Linearization (ii)

Using the linearization (ii), the momentum equations reduce to:

low concentration problem

$$30u_i^f = 30 + 400(u_i^{s*} - u_i^{f*}) + 100 \quad 420u_i^s = 20 + 400u_i^f + 10 \quad (\text{C.18})$$

high concentration problem

$$30u_i^f = 30 + 4000(u_i^{s*} - u_i^{f*}) + 100 \quad 4200u_i^s = 200 + 4000u_i^f + 100 \quad (\text{C.19})$$

These sets of equations are solved using an iterative process, where u_i^f is computed first using the values of u_i^{s*} and u_i^{f*} from the previous time step (or iteration); u_i^s is then calculated using the newly computed u_i^f . Starting with the initial guesses $u_i^{s*} = 1$ and $u_i^{f*} = 1$, the results of this iterative processes are

iteration number	u_i^f	u_i^s
0	1.00	1.00
1	4.33	4.20
2	2.53	2.49
3	3.68	3.57

Table C.1: Iterative process for the low concentration problem

iteration number	u_i^f	u_i^s
0	1.00	1.00
1	4.33	4.20
2	-12.93	-
3	-	-

Table C.2: Iterative process for the high concentration problem

An examination of the values in these tables shows that the iterative process for the low concentration problem is converging; for the high concentration problem, the solution is diverging.

C.3 Linearization (iii)

Using the linearization (iii), the momentum equations become:

low concentration problem

$$30u_i^f = 30 + 400(u_i^{f*} - u_i^{f*}) + 100 \quad 20u_i^s = 20 + 400(u_i^f - u_i^{s*}) + 10 \quad (\text{C.20})$$

high concentration problem

$$30u_i^f = 30 + 4000(u_i^{f*} - u_i^{f*}) + 100 \quad 200u_i^s = 200 + 4000(u_i^f - u_i^{s*}) + 100 \quad (\text{C.21})$$

These sets of equations are solved using an iterative process similar to the one described for the linearization (ii). Starting again with the initial guesses $u_i^{f*} = 1$ and $u_i^{s*} = 1$, the results of this iterative processes are

iteration number	u_i^f	u_i^s
0	1.00	1.00
1	4.33	68.17
2	855.44	-
3	-	-

Table C.3: Iterative process for the low concentration problem

iteration number	u_i^f	u_i^s
0	1.00	1.00
1	4.33	68.17
2	8515.44	-
3	-	-

Table C.4: Iterative process for the high concentration problem

These tables show that the iterative process is diverging for both the low and high concentration problems.

These computations clearly indicate that the linearization (i) is the most appropriate, because it allows simultaneous solution of the fluid- and solid-phase momentum equations. Linearization (ii) is limited to low concentration of the solid phase, and linearization (iii) is completely inappropriate.

Appendix D

Implied Source Terms of the Specified Solutions

D.1 Dense Concentration - Specified Solution in a Cartesian Geometry

The proposed dependent-variable fields for the Cartesian geometry are:

$$u_{cx}^s = U_0 \quad v_{cx}^s = \frac{U_0}{1 + \frac{y}{L}} \quad \alpha_{cx} = \alpha_0 \left(1 + \frac{y}{L}\right) \quad (D.1)$$

$$u_{cx}^f = U_0 \left(\frac{y}{L}\right) \quad v_{cx}^f = 0 \quad p_{cx}^f = P_0 \left(\frac{x+L}{L}\right) \quad (D.2)$$

$$T_{cx} = T_0 \left(\frac{x+L}{L}\right) \quad (D.3)$$

This solution is expressed in term of a (x, y) Cartesian coordinate system. The corresponding implied source terms are:

$$S_z^f = (1 - \alpha_{cx}) \frac{P_0}{L} - \frac{5}{2} \left(\frac{U_0}{L}\right) \left(\frac{\alpha_0}{L}\right) \left(1 + \frac{2}{3} \alpha_{cx}\right) (\mu_r^f(\alpha_{cx}))^{\frac{1}{2}} \mu^f + 18 \frac{\alpha_{cx} \mu^f}{d^2} (u_{cx}^f - U_0) \quad (D.4)$$

$$S_r^f = (1 - \alpha_{cx}) \frac{P_0}{L} - 18 \frac{\alpha_0 \mu^f}{d^2} U_0 \quad (D.5)$$

$$S_z^s = \alpha_{cx} \frac{P_0}{L} + \left(\frac{T_0}{T_{cx}}\right) \frac{p^s|_{cx}}{L} - 18 \frac{\alpha_{cx} \mu^f}{d^2} (u_{cx}^f - U_0) \quad (D.6)$$

$$+ \frac{1}{2U_0} \left(\frac{T_0}{T_{cx}}\right) \left(\frac{v_{cx}^s}{L}\right)^2 \left[\frac{3}{5} \mu_b^s|_{cx} + \left(\frac{2}{5} \mu_b^s|_{cx} - \frac{2}{3} \mu_e^s|_{cx}\right) \frac{2\mu^{s'}|_{cx} - \mu^{s''}|_{cx}}{\mu^{s'}|_{cx}} \right]$$

$$S_r^s = \alpha_{cx} \frac{P_0}{L} + 18 \frac{\alpha_0 \mu^f}{d^2} U_0 + \frac{\alpha_0 \rho^s}{L} [T_{cx} (1 + 4\eta\mathcal{F}) - (v_{cx}^s)^2] + \frac{(v_{cx}^s)^2}{(U_0 L)} \left[\frac{4}{3} \mu_e^{s'} + \mu_b^{s'} \right] \quad (D.7)$$

$$\begin{aligned}
& -\frac{2(v_{ex}^s)^3}{(U_0 L)^2} \left[\frac{4}{3} \mu_c^s|_{ex} + \mu_b^s|_{ex} \right] \\
S_T^s = & \frac{3}{2} \alpha_{ex} \rho^s \frac{T_0 U_0}{L} - \left(\frac{\alpha_0}{\alpha_{ex}} \right) \left(\frac{v_{ex}^s}{L} \right) p^s|_{ex} - \frac{(v_{ex}^s)^4}{(U_0 L)^2} \left[\frac{4}{3} \mu_c^s|_{ex} + \mu_b^s|_{ex} \right] \\
& + \gamma_c(\alpha_{ex}, T_{ex}) - a_0 \alpha_{ex}^{\frac{3}{2}} \gamma_D(\alpha_{ex}, T_{ex}) \\
& + \frac{1}{2T_{ex}} \left(\frac{T_0}{L} \right)^2 \left[k_T^s|_{ex} + \frac{k^{s'}|_{ex} - k^{s''}|_{ex}}{k^{s'}|_{ex}} \left(k_T^s|_{ex} - \frac{3}{2} \mu_b^s|_{ex} \right) \right] \\
& + \left(\frac{\alpha_0}{L} \right)^2 \left(\frac{k^{s''}|_{ex}}{\alpha_{ex} g_0(\alpha_{ex})} \right) \left\{ \frac{12}{5} \eta (2\eta - 1) (\eta - 1) T_{ex} \left[\frac{12}{5} \eta \mathcal{F} \alpha_{ex} (\mathcal{F} + g_0(\alpha_{ex})) \right. \right. \\
& \left. \left. + \left(1 + \frac{12}{5} \eta g_0(\alpha_{ex}) \alpha_{ex} \right) \frac{d^2}{d\alpha^2} (\alpha^2 g_0) \Big|_{\alpha=\alpha_{ex}} \right] - \frac{k_\alpha^s|_{ex}}{k^{s'}|_{ex}} \mathcal{F} \right\}
\end{aligned} \tag{D.8}$$

where

$$p^s|_{ex} = p^s(\alpha_{ex}, T_{ex}) \tag{D.9}$$

$$\mu_c^s|_{ex} = \mu_c^s(\alpha_{ex}, T_{ex}) \quad \mu^{s'}|_{ex} = \mu^{s'}(\alpha_{ex}, T_{ex}) \quad \mu^{s''}|_{ex} = \mu^{s''}(\alpha_{ex}, T_{ex}) \tag{D.10}$$

$$\mu_b^s|_{ex} = \mu_b^s(\alpha_{ex}, T_{ex}) \tag{D.11}$$

$$k_T^s|_{ex} = k_T^s(\alpha_{ex}, T_{ex}) \quad k^{s'}|_{ex} = k^{s'}(\alpha_{ex}, T_{ex}) \quad k^{s''}|_{ex} = k^{s''}(\alpha_{ex}, T_{ex}) \tag{D.12}$$

$$k_\alpha^s|_{ex} = k_\alpha^s(\alpha_{ex}, T_{ex}) \tag{D.13}$$

$$\mathcal{F} = \frac{1}{\alpha_{ex}} \frac{d}{d\alpha} (\alpha^2 g_0) \Big|_{\alpha=\alpha_{ex}} - g_0(\alpha_{ex}) \tag{D.14}$$

$$\mu_b^{s'} = \frac{1}{L g_0(\alpha_{ex})} \left(\frac{\alpha_0}{\alpha_{ex}} \right) [\mathcal{F} + g_0(\alpha_{ex})] \mu_b^s|_{ex} \tag{D.15}$$

$$\begin{aligned}
\mu_c^{s'} = & \frac{3}{5} \mu_b^{s'} + \frac{1}{L} \left(\frac{\alpha_0}{\alpha_{ex}} \right) \left[\left(\mu_c^s|_{ex} - \frac{3}{5} \mu_b^s|_{ex} \right) + \mathcal{F} \frac{\mu^{s''}|_{ex}}{g_0(\alpha_{ex})} \right. \\
& \left. \left(\frac{8}{5} \eta \alpha_{ex} \left(\left(1 + \frac{8}{5} \eta (3\eta - 2) \alpha_{ex} g_0(\alpha_{ex}) \right) + (3\eta - 2) \left(1 + \frac{8}{5} \eta \alpha_{ex} g_0(\alpha_{ex}) \right) \right) \right) \right. \\
& \left. \left. - \frac{\mu_c^s|_{ex} - \frac{3}{5} \mu_b^s|_{ex}}{\mu^{s'}|_{ex}} \right) \right]
\end{aligned} \tag{D.16}$$

D.2 Dense Concentration - Specified Solution in a Cylindrical Geometry

The proposed dependent-variable fields for the cylindrical geometry are:

$$u_{ex}^s = U_0 \left(\frac{z}{L} \right) \quad v_{ex}^s = -U_0 \left(\frac{r}{2L} \right) \quad \alpha_{ex} = \alpha_0 \tag{D.17}$$

$$u_{ex}^f = U_0 \left(\frac{r}{L} \right) \quad v_{ex}^f = 0 \quad p_{ex}^f = P_0 \left(\frac{z+r}{L} \right) \tag{D.18}$$

$$T_{ex} = T_0 \tag{D.19}$$

The corresponding implied source terms are:

$$S_z^f = (1 - \alpha_0) \frac{P_0}{L} - \frac{\mu_c^f(\alpha_0, T_0) U_0}{rL} + 18 \frac{\alpha_0 \mu^f}{d^2} (u_{cx}^f - u_{cx}^s) \quad (\text{D.20})$$

$$S_r^f = (1 - \alpha_0) \frac{P_0}{L} - 18 \frac{\alpha_0 \mu^f}{d^2} v_{cx}^s \quad (\text{D.21})$$

$$S_z^s = \alpha_0 \frac{P_0}{L} + \frac{\alpha_0 \rho^s U_0^2}{L^2} z - 18 \frac{\alpha_0 \mu^f}{d^2} (u_{cx}^f - u_{cx}^s) \quad (\text{D.22})$$

$$S_r^s = \alpha_0 \frac{P_0}{L} + \frac{\alpha_0 \rho^s U_0^2}{4L^2} r + 18 \frac{\alpha_0 \mu^f}{d^2} v_{cx}^s \quad (\text{D.23})$$

$$S_T^s = -3\mu_c^s(\alpha_0, T_0) \left(\frac{U_0}{L}\right)^2 + \gamma_c(\alpha_0, T_0) - a_0 \alpha_0^{\frac{3}{2}} \gamma_D(\alpha_0, T_0) \quad (\text{D.24})$$